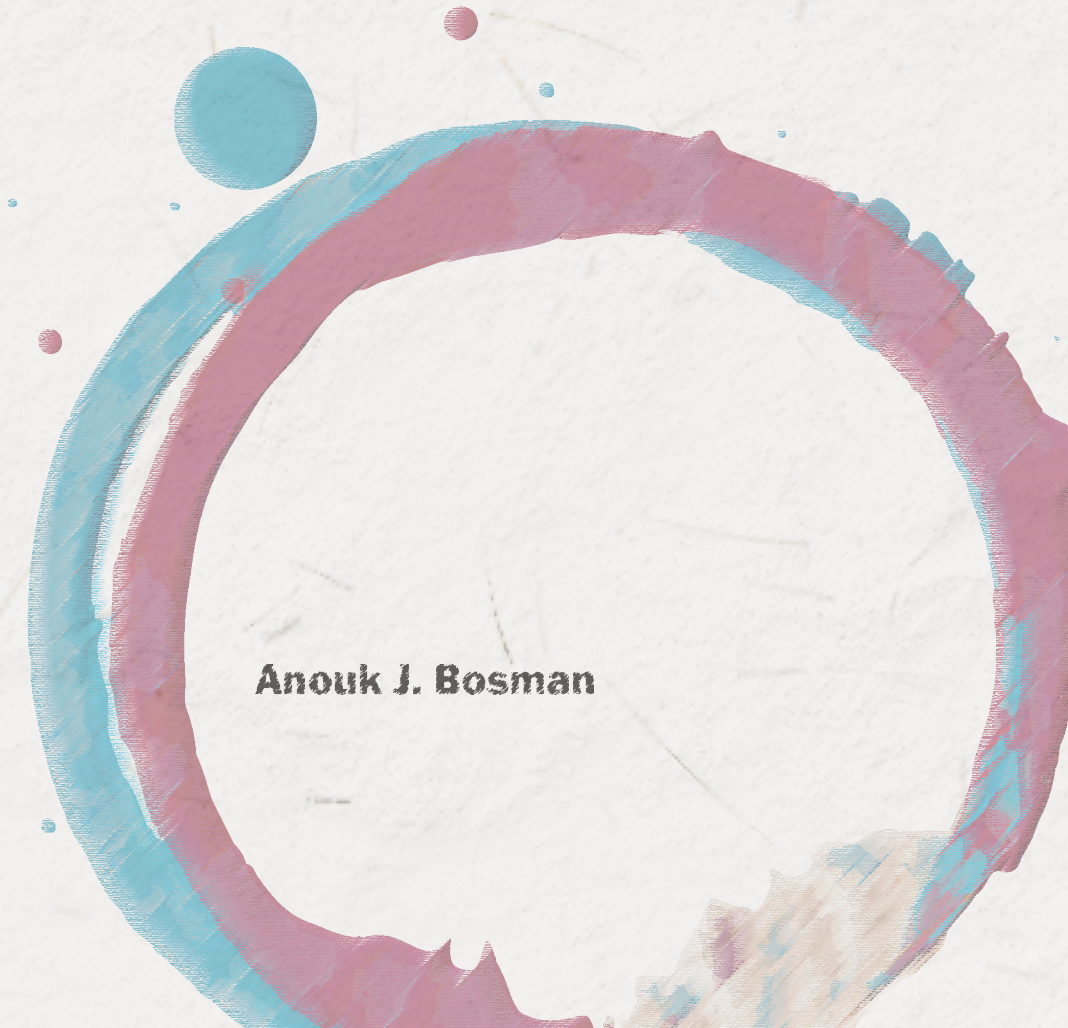
Detecting the Undetectable

DIY sample preparation and infrared spectroscopy for portable mycotoxin analysis



Anouk J. Bosman

Propositions

1. Validation of screening devices without the consideration of end-user sample preparation puts food safety at risk.
   (this thesis)

2. S-PEIRS erases the boundary between screening and confirmation of mycotoxins.
   (this thesis)

3. Misinterpretation of scientific data raises the publication threshold for properly interpreted data.

4. There is no such thing as 'unsupervised' machine learning.

5. Improvements in non-alcoholic beer quality influence drinking behavior more than public health campaigns.

6. Queer parenthood exposes the misalignment between the number of legal parents and actual family structures.

Propositions belonging to the thesis, entitled

Detecting the Undetectable; DIY sample preparation and infrared spectroscopy for portable mycotoxin analysis

Anouk J. Bosman

Wageningen, 2 July 2026

Detecting the Undetectable

DIY sample preparation and infrared spectroscopy for portable mycotoxin analysis

Anouk J. Bosman

Thesis Committee

Promotors
Prof. Dr M.W.F. Nielen
Special Professor in Organic Chemistry
Wageningen University & Research

Prof. Dr J.G.M. Janssen
Special Professor in Organic Chemistry
Wageningen University & Research

Co-promotors
Dr G.IJ. Salentijn
Associate Professor in Organic Chemistry
Wageningen University & Research

Dr F.S. Ruggeri
Associate Professor in Physical Chemistry and Soft Matter
Wageningen University & Research

Other members
Prof. Dr K.A. Hettinga, Wageningen University & Research
Prof. Dr S. de Saeger, Ghent University, Belgium
Prof. Dr J. Oomens, Radboud University, Nijmegen
Dr V. Saggiomo, Wageningen University & Research

This research was conducted under the auspices of the Graduate School VLAG
(Biobased, Biomolecular, Chemical, Food and Nutrition Sciences).

Detecting the Undetectable

DIY sample preparation and infrared spectroscopy for portable mycotoxin analysis

Anouk J. Bosman

Thesis
submitted in fulfilment of the requirements of the degree of doctor
at Wageningen University
by the authority of the Rector Magnificus
Prof. Dr C. Kroeze,
in the presence of the
Thesis Committee appointed by the Academic Board
to be defended in public
on Thursday 2 July 2026
at 3.30 p.m. in the Omnia Auditorium.

Anouk J. Bosman
Detecting the Undetectable
DIY sample preparation and infrared spectroscopy for portable mycotoxin analysis

201 pages

PhD thesis, Wageningen University, Wageningen, the Netherlands (2026)
With references, with summaries in English and Dutch.

DOI: 10.18174/681613

Voor Papa, Mama en Sophie

Contents

Chapter 1	General Introduction	8
Chapter 2	Interconnectable 3D-printed sample processing modules for portable mycotoxin screening of intact wheat	34
Chapter 3	Selective paper-enhanced infrared spectroscopy for molecular detection of deoxynivalenol in wheat	68
Chapter 4	Detection of ochratoxin A in wine at the legal limit via solvent-based enrichment and paper-enhanced infrared spectroscopy	114
Chapter 5	General Discussion and Future Perspectives	150
Appendices	English summary	178
	Dutch summary	182
	Curriculum vitae	186
	Acknowledgements	192



General Introduction

Preface

Access to sufficient and safe food is a fundamental human right. However, despite significant advances in both food production systems and food safety technologies, achieving equitable access to safe food remains a complex global challenge. This challenge arises not solely from limitations in food safety analysis methods, but from a multitude of interconnected factors. These include demographic stability, climate change, infrastructure and logistics along the food value chain, and the stability of national and international economies. Nevertheless, food safety analysis methods serve as the 'eyes and ears' of the food system. They provide essential data on the quality and safety of food products, enabling informed decision-making and regulations. In doing so, they play a critical role in safeguarding public health and maintaining integrity within the global food market.

In this thesis, I address a critical aspect of food safety monitoring: the detection of mycotoxins, a particularly impactful class of food contaminants (Section 1.1). It is very difficult (if not impossible) to prevent mycotoxin contamination of agricultural crops and processed foods completely. While laboratories continue to play a vital role in food safety analysis through comprehensive analytical methods, recent research and technological advancements have increasingly focused on portable analytical solutions and aim to decentralize food testing (Section 1.2). Therefore, methods that incorporate sample preparation in a simple and user-friendly manner are essential as well (Section 1.3). Infrared (IR) spectroscopy has already been implemented as in-line, on-line and on-site detection technology for food quality measurements. More recently, IR spectroscopy has also proven to be a promising technique for portable food safety analysis, yet lacks sufficient selectivity and sensitivity to detect mycotoxin molecules directly at relevant concentration levels for food safety. Therefore, the title 'Detecting the Undetectable' was chosen for this thesis, as IR spectroscopy has been extensively explored with the aim to measure the mycotoxin molecules directly in contaminated foods (Section 1.4). After discussing these topics to introduce the relevant context for this thesis, an outline of the thesis structure is provided (Section 1.5).

1.1 Mycotoxins

Our scientific understanding and characterization of mycotoxins started around the year 1960 [1], but mitigation strategies to prevent fungal damage of food crops dates back much further. This started during the Neolithic revolution (~10000 years ago), a time when humans first attempted to shift from foraging to farming practices [2–4]. The ability to store excess food led to a growing human population, yet at the same time also created a new environment for fungal molds to flourish. Today, many of these fungal molds are known to produce mycotoxins, and finding the best mitigation strategies to minimize the growth of such mycotoxin-producing fungi continues to be a global concern.

Since the 1960's, over 500 different and chemically diverse mycotoxins have been identified, and they can be divided into two groups [5]. The first group are the regulated mycotoxins that are well studied and strictly regulated under global and European Union (EU) legislation. The second group are the emerging mycotoxins that are not (yet) regulated. The majority of mycotoxins have a relatively low molecular weight (<1 kDa) and are toxic to humans and animals when foodstuffs are consumed that contain harmful levels of the toxin, i.e. exceed the maximum levels (MLs) for that particular foodstuff [6,7].

The fungal genera responsible for most mycotoxin contaminations are *Fusarium*, *Aspergillus*, and *Penicillium* [7]. An important class of *Fusarium* mycotoxins are trichothecenes, of which key members are T-2 toxin and deoxynivalenol (DON, Figure 1.1). These non-macrocyclic trichothecene compounds are frequently found in cereals and cereal products, and contamination levels of these mycotoxins in cereals can reach 20 mg/kg. Other *Fusarium* mycotoxins include zearalenone (ZEN) and fumonisin B1 (FUM), which are frequently found in cereals as well (Figure 1.1). *Aspergillus* fungi are known to produce two of the most toxic and strictly regulated mycotoxins; aflatoxin B1 (AFB1) and ochratoxin A (OTA, Figure 1.1). AFB1 is classified as a group 1 carcinogen and OTA as a group 2B carcinogen by the international agency for research on cancer (IARC) [7,8]. Other toxicological consequences related to these mycotoxins include liver damage, kidney damage and immunotoxicity.

Finally, *Penicillium* fungi are also known to produce OTA. Therefore, OTA is produced by multiple fungi and is harmful at very low levels. Moreover, OTA is found in many different commodities, leading to various exposure routes [9]. OTA may have a long-half life in humans [10], and is frequently detected in human urine samples in Nigeria [11], indicating its bio-accumulative stability. Bioaccumulation can affect animal-derived foods such as milk, meat, and fish as well. Mycotoxins in animal feed, often present at higher MLs, may accumulate or metabolize in the animal and transfer as residues into these food products [12–14]. In addition to their stability in

humans and animals, mycotoxins such as OTA are difficult to remove from the food once it has been contaminated, as they exhibit chemical and thermal stability and thus can withstand food processing [15,16].

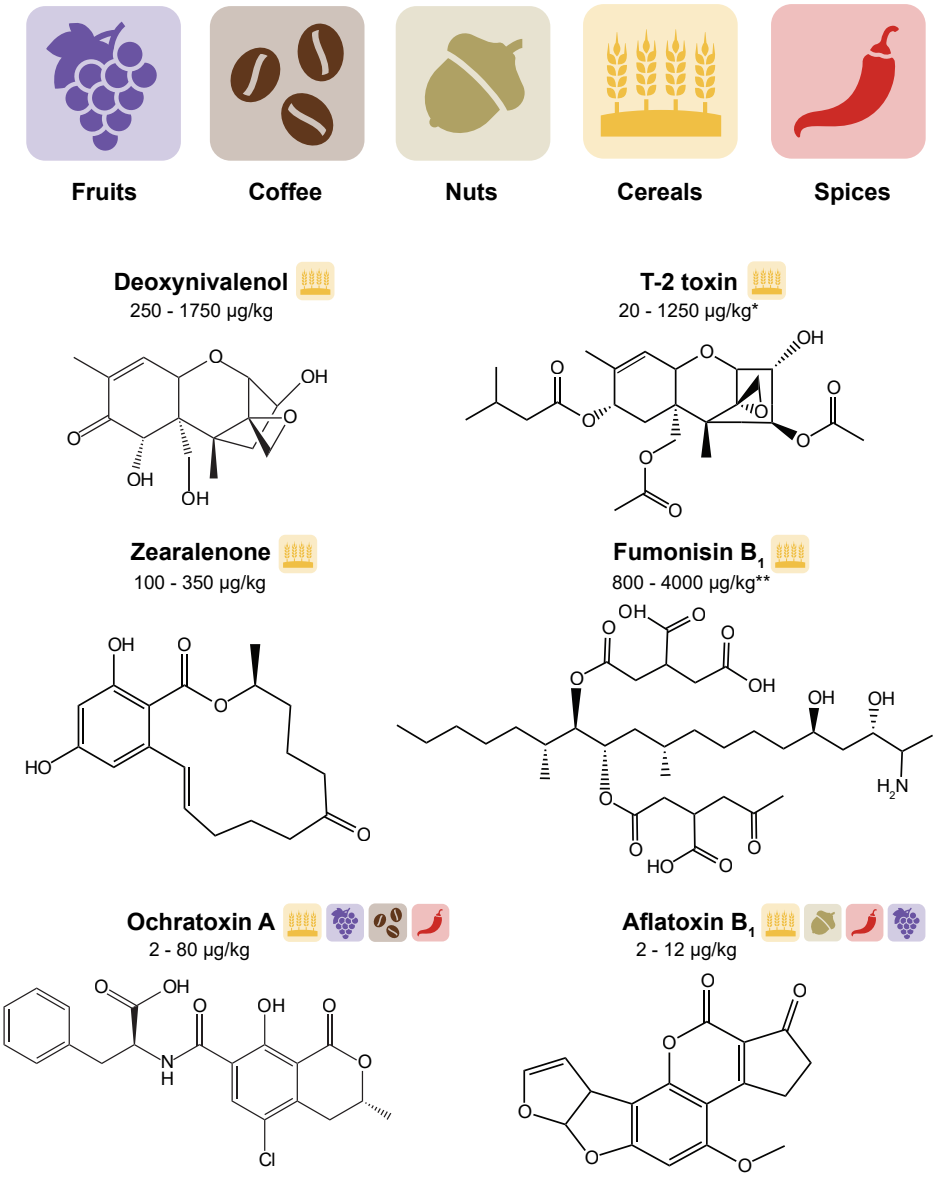


Figure 1.1: *Six regulated mycotoxins, the main commodities in which they are regulated, and the range of maximum levels (MLs) described in EU regulations (* Sum of T-2 and HT-2 toxin; ** Sum of fumonisins B1 and B2).*

1.1.1 Legislation

The MLs that are defined for the regulated mycotoxins described above vary from continent to continent, as well as vary in the degree of legislation. Internationally, the Codex Alimentarius Commission provides standards which are the reference throughout the food supply chain, safeguarding consumer food purchases globally [17,18]. Worldwide, the EU has the strictest regulations for all of the above-mentioned mycotoxins and MLs are sub-divided per foodstuff [19–21]. The US Food and Drug Administration (FDA) has set action levels (i.e. ML) for aflatoxins, advisory levels for DON and guidance levels for fumonisins. The other described regulated mycotoxins are part of the monitoring program but do not have specific action or advisory levels, indicating the diversity in regulations [22]. In Figure 1.1, a range of the MLs for every regulated mycotoxin is listed following the latest EU regulations [19–21], but excluding the ones for baby products as they are not within the scope of the work described in this thesis.

The MLs are revised regularly to include the latest developments with respect to toxicology, occurrence and exposure data evaluating the risks for human and animal health. For example, in 2024, the levels for DON were updated and the EU ML for DON in unprocessed cereals was adjusted from 1250 µg/kg to 1000 µg/kg [20]. The reason for this was the consideration of the scientific opinion from the European Food Safety Authority (EFSA) [23]. Following this opinion, the European Commission (EC) evaluated whether the MLs set for DON should reflect the sum of DON and its modified forms. However, due to the limited amount of occurrence data for these DON derivatives the decision was deferred until more data becomes available from updated routine analysis. Nevertheless, the EC decided to adjust certain DON MLs for unprocessed cereals taking into consideration DON occurrence data.

1.1.2 Occurrence and exposure in a changing climate

Mycotoxin legislation is closely intertwined with occurrence and exposure data. Where occurrence data describes the mycotoxin presence and concentration in certain foodstuffs, exposure data describes the quantity of mycotoxins that a person or animal encounters. Mycotoxin occurrence and exposure can vary from year to year, as well as vary geographically and demographically. One important factor is our changing climate, which is causing more extreme weather events such as heat waves, droughts, heavy rainfall and floods [24–29]. As a result, mycotoxin-producing fungi can migrate depending on such weather events, and manifest in different geographical regions [25–28]. For example, mild temperatures and wet conditions favor the fungus that produces DON and ZEN, *Fusarium graminearum*, while *Aspergillus flavus* is more dominant in geographical regions with a hot and humid climate [26].

It is estimated that 20% of all agricultural crops are contaminated by mycotoxins

above the regulated levels, worldwide [30,31]. Placing this into perspective with the amount of cereals that are produced globally, which is expected to be close to 3000 million tons in 2025 [32], it means that close to 600 million tons of cereals are at risk of mycotoxin contamination exceeding regulatory limits. Annual surveys on the occurrence of mycotoxins are conducted, such as the world mycotoxin survey [33], and provide detailed insights and monitor trends. In 2024, a total of 28,388 samples consisting of wheat, corn and finished feed originating from 95 countries were analyzed and reported in the world mycotoxin survey. The results showed that 70% of the samples contain more than one regulated mycotoxin, that the overall mycotoxin prevalence increased from the year 2023 to 2024, and that DON is the most frequently detected mycotoxin [33]. Around the world, DON is found in cereals such as wheat grains (Table 1.1), and the detected level exceeds the Codex (2000 µg/kg) or EU ML (1000 µg/kg) in some cases.

Table 1.1: *Results of DON contamination in wheat grains around the world as reported in the world mycotoxin survey 2024 from dsm-firmenich [33].*

DON in wheat grains	**Europe**	**Sub-Saharan Africa**	**North America**	**South America**	**Asia**
% contaminated samples	61%	100%	88%	74%	45%
Average of positive (µg/kg)	383	362	1214	1259	667
Maximum (µg/kg)	14667	1264	4526	4070	5348

Next to such surveys focused on raw cereals and feed, the EU has rolled out a Rapid Alert System for Food and Feed (RASFF) that allows food safety authorities to report emerging health risks for a number of food commodities to enable quick action where required [34,35]. Between 2020 – 2024, mycotoxins were the toxins with the most notifications on RASFF, with OTA and aflatoxins frequently exceeding EU MLs [34].

Next to the global health burden, mycotoxins are known to have substantial economic impact [15,36]. Data on wheat production in Europe suggested that between €1.2 and €2.4 billion were lost due to mycotoxin contamination in the year 2015 [36]. Moreover, between 2010 – 2019, an estimated €3 billion was lost due to DON contamination alone, and led to the downgrading of food wheat to feed [28]. Therefore, reducing the losses associated with mycotoxin contamination can have a beneficial economic impact for many countries. In addition, this stresses the importance of the continuous development of analytical tools that can detect the presence of these toxins in agricultural products reproducibly and with certainty.

1.2 Current analytical methods for mycotoxins

Our current understanding of mycotoxins and the ability to monitor them at trace levels can be largely attributed to the continuous development of analytical detection methods. Yet, the chemical diversity of mycotoxins, their co-occurrence, and the wide range of agricultural commodities in which they exist present a challenge for method development. Moreover, the choice of method can largely depend on the stakeholder's motive and the kind of information that is desired from the analysis [37]. Therefore, a broad range of analytical technologies and methodologies are applied for mycotoxin detection [38].

Recently, an 8-level system to categorize such instruments and methodologies was proposed (Figure 1.2) [34]. The methods have been categorized based on the level of measurement uncertainty and the number of analytes included in the analysis. A general distinction can be made between rapid screening methods (groups 1 – 4) and comprehensive lab-based methods (groups 5 – 8). The work described in this thesis relates mainly to technologies and methodologies belonging in groups 2 – 5, which will be further discussed.

Group 2 – *indirect screening* – involves technologies that can determine whether mycotoxin-producing fungi are present in the food sample. Indirect screening approaches include spectral, electrochemical and nucleic acid amplification-based methods [34]. One of the main advantages of indirect screening is that minimal sample preparation is required, resulting in rapid and high-throughput methods. Such methods are important as the number of mycotoxin analyses is likely to further increase in order to comply with regulations and ensure global food safety and security [39]. Recent literature has highlighted the potential of infrared (IR) spectroscopy for mycotoxin screening, since IR spectroscopy can be used to obtain chemical information in a rapid and portable format [34,39,40]. IR spectroscopy relies on the absorption of electromagnetic radiation at frequencies that match molecular vibrations, leading to specific absorptions for certain functional groups that are common in foods (e.g. carbonyls, alcohols, amines and amides) [39]. In IR spectroscopy, the intensity of the absorption depends on the magnitude of the dipole moment change during molecular vibration, and by using Beer's Law (Equation 1.1) the concentration of the molecule can be determined from the absorbance [39,41,42].

$$A = \varepsilon c l \qquad \textit{Equation 1.1}$$

Where, A is the absorbance (a.u.), ε is the molar absorption coefficient ($M^{-1}\ cm^{-1}$) of the analyte, c is the concentration (M^{-1}) and l the path length (cm).

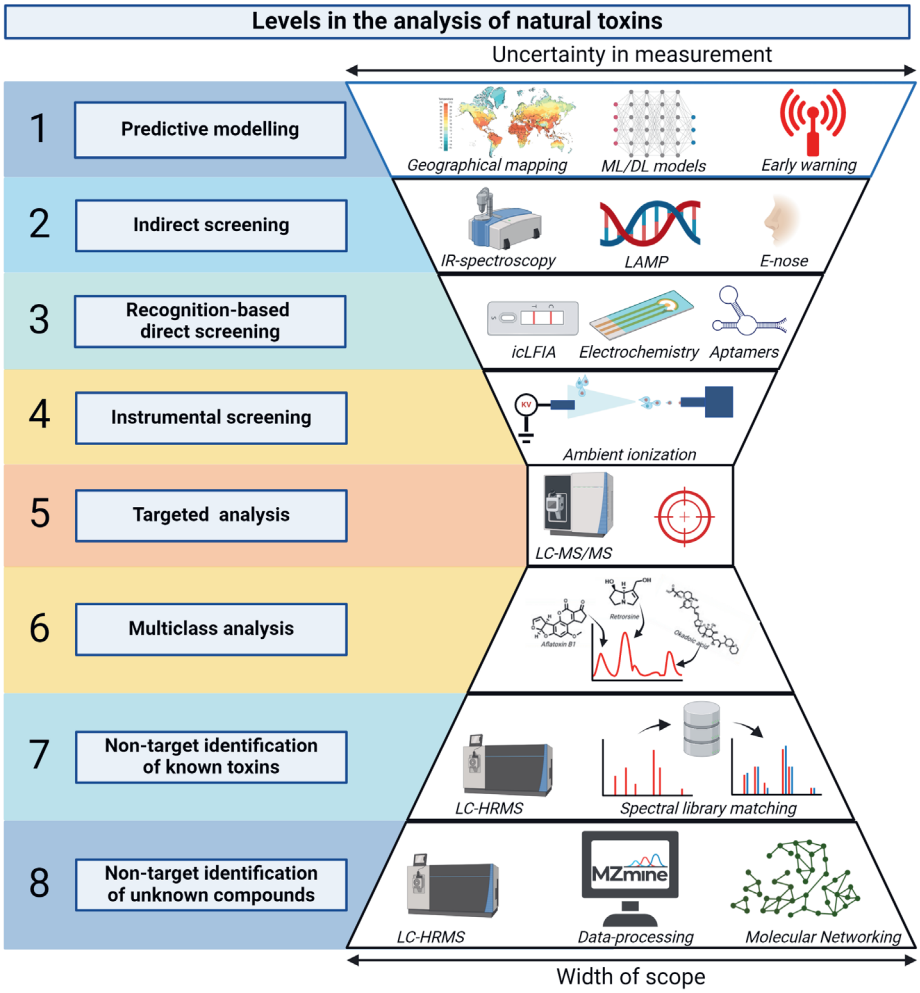


Figure 1.2: *The 8 identified categories of analytical technologies and methodologies described for mycotoxin analysis, reprinted with permission from Ref 34 (Copyright Elsevier 2025).*

Near-IR (NIR) and mid-IR (MIR) spectroscopy as well as hyperspectral imaging (HSI) have been used to measure fungal-induced matrix changes, and have allowed the indirect screening of mycotoxins in food and feed [39]. Monitoring changes in the matrix composition such as protein, carbohydrate or lipid alterations, have shown distinct spectral differences between infected and non-infected samples [39,40,43–45]. These spectra are used as input for chemometric models which can predict mycotoxin contamination [39,40,43]. In general, NIR and MIR spectroscopy are more suitable to predict mycotoxin contamination in solid bulk samples because of their sampling interfaces. However, recently MIR has also been employed for prediction-based mycotoxin screening in food extracts [43,44,46]. HSI on the other hand, is more suitable

for sorting applications because HSI can identify high levels of fungal contamination on single kernels, albeit after more complex data analysis [39]. One major drawback of IR spectroscopic methods for mycotoxin screening is that the molecular fingerprint of the mycotoxin cannot be directly detected. While the molecular fingerprint of the mycotoxin when measured in high concentrations and as pure analytical standard shows unique absorbance features, the detection of the molecules at ML concentrations using routine IR spectrometers is currently impossible. The reason for this is that mycotoxins are occurring and regulated at levels below the detection capability of a typical IR system. Additionally, current IR analyses are not specific towards the mycotoxin molecule(s), as the complete sample composition is used for prediction. This limits the advancement of IR spectroscopy as group 4/5 (portable) food analyzer complying with EU regulation, for which a higher degree of certainty and quantification are required.

Group 3 – *recognition-based 'direct' screening* – involves technologies that use some type of recognition element to measure the mycotoxin. That means that upon interaction between the mycotoxin and the recognition element, a measurable signal is obtained. Most recognition-based screening methods can be defined as a biosensor because they consist of the following components; i) an interaction layer, ii) a transducer surface and iii) an output system [47]. Here, the recognition event (affinity or reaction) is converted at the transducer surface to a measurable output signal. A wide range of biological and biomimetic elements can be used for mycotoxin recognition such as antibodies, aptamers, enzymes and molecularly imprinted polymers (MIPs), of which antibodies are still the golden standard due to their superior specificity especially for regulated mycotoxins [47,48]. The measured signal can be e.g. electrochemical, gravimetric, acoustic or optical [49]. The results thereof can be binary or directly proportional to the concentration of analyte, and sometimes a (bio)chemical label is needed to make the event detectable [47]. Common mycotoxin biosensors include label-free technologies such as Surface Plasmon Resonance (SPR), Quartz-Crystal Microbalance (QCM) and label-based methods such as fluorescence- or colorimetric-based sensing. Even though these recognition-based screening methods are categorized as 'direct' detection in Figure 1.2, such methods do not directly detect a molecular feature of the mycotoxin but rather detect an interaction with the recognition element.

Two classical examples of recognition-based screening for mycotoxins are lateral flow immunoassays (LFIA) and enzyme-linked immunosorbent assays (ELISA), both of which typically use antibodies as recognition element and are colorimetric tests [47,50–52]. Different formats exist, but due to the low molecular weight of mycotoxins a competitive format is usually preferred [53]. In a competitive format, the strength of the signal is inversely proportional to the amount of mycotoxin in the sample. It is

important to note that validated ELISA and LFIA methods are considered official screening methods for mycotoxins by, e.g., the Association of Official Analytical Chemists (AOAC international) and EU regulation. Still, only a small selection of methods has gained this status with the majority of published mycotoxin biosensors being proof-of-concept tests for academic purposes. Overall, recognition-based screening methods are targeted at the regulated mycotoxins, sometimes in multiplex format. These tests are intended for rapid screening and can be used by both experts and non-expert users.

Group 4 – *instrumental screening* – includes other types of screening methods that require more advanced procedures and/or instruments needing a skilled technician to operate. However, instrumental screening methods provide an increased level of confidence over indirect and recognition-based screening methods because the mycotoxin molecule can be identified based on the mass-to-charge ratio (m/z). Over the years, numerous official and non-official instrumental screening methods have been developed for mycotoxins [54,55]. The classical approaches are based on high performance liquid-chromatography (HPLC) coupled with either ultraviolet-visible (UV-VIS), fluorescence (FLD) or mass spectrometric (MS) detection. These methods often require extensive sample preparation which must be carried out in a laboratory environment by trained personnel, which is a significant drawback from the perspective of screening methods. Therefore, other instrumental screening approaches gained popularity, such as (portable) ambient ionization mass spectrometry (AIMS) methods. AIMS-based methods generate ions in ambient conditions, facilitating open-air surface analysis of various surfaces after little or no sample preparation [34,56–59]. Nevertheless, for the detection of mycotoxins sample preparation is needed because they occur, and are regulated, at very low concentrations, as well as in complex matrices [60–63]. This makes their detection directly at the sample surface difficult because of matrix interferences and selectivity and sensitivity issues.

Examples of AIMS methods for mycotoxins include direct analysis in real time mass spectrometry (DART-MS) and (portable) thermal desorption atmospheric pressure chemical ionization (TD-APCI) MS, needing external sample preparation [61,63–66]. Such external sample preparation procedures can include steps like; sample grinding, extraction, centrifugation, filtration, clean-up, drying, reconstitution, dilution, and sometimes an internal standard is needed for analysis. Efforts to reduce the sample preparation for AIMS detection of mycotoxins was achieved using e.g. paper-spray ionization (PSI) and blade-spray ionization (BSI) approaches [67–70]. Researchers developed a coated PSI-based method for the detection of FUM using a cellulose substrate functionalized with FUM-MIPs [68]. Similarly, the coated BSI-based method for DON detection used a plastic blade (a cost-effective alternative to stainless

steel blade spray) modified with DON-antibodies [67]. For both methods the sample preparation steps were reduced, as the extracts can be directly applied to the coated paper or blade, tackling part of the existing limitations of AIMS methods. However, both methods use pre-ground material and therefore do not include a grinding practice of the wheat and maize commodities.

Group 5 – *targeted analysis* – includes the 'golden standard' method for mycotoxin detection [34,38,71]. Moreover, it is the preferred approach for confirmatory analysis and is also used as reference analysis in this thesis. Commission Implementing Regulation 2023/2782 defines confirmatory methods as "methods that provide full or complementary information enabling the mycotoxin to be identified and quantified unequivocally at the level of interest" [72]. However, for such methods to be effective, it is essential that analytical standards are available for the target mycotoxin(s) [34]. In the context of the above described screening methods (groups 2, 3 and 4), confirmatory analysis is needed for those samples that give a 'suspect' result. Whenever a sample gives a 'suspect' result, it must be re-analyzed by a confirmatory method to verify the screening method's result [73]. The most common technique for confirmatory analysis is HPLC-MS/MS, however, techniques such as GC-MS, HPLC-FLD and HPLC-UV are also used [34,72]. An MS/MS system such as a triple quadrupole in single or multiple reaction monitoring (SRM or MRM) mode is used for the highly sensitive, quantitative, and specific analysis of target mycotoxin(s). Here, a precursor ion of a specific m/z is selected and fragmented to produce product ions. The fragment transitions are monitored and thereby the concentration of the mycotoxins can be determined.

In a recent study that explored the demand for mycotoxin analysis along the food supply chain in the EU, an increased interest for rapid, reliable and portable mycotoxin methods was found [74]. Therefore, analytical innovations should strive for end-user-targeted development of (novel) mycotoxin methods.

1.3 Integrated sample preparation

Any analytical workflow starts with proper sample preparation, therefore it is also an essential part in the development of portable food analyzers. However, for integrated sample preparation the aim is to combine (part of) the sample preparation steps by developing analytical tools that allow field-deployable sample preparation, and facilitate the on-site use of LFIAs or biosensors. Typical mycotoxin sample preparation steps include sample grinding, extraction, centrifugation, filtration, clean-up, drying, reconstitution and dilution. The development of such field-deployable tools that integrate these steps is arguably more challenging than developing laboratory-oriented sample preparation tools. All the sophisticated sample work-up methods that are used by experts in the laboratory need to be translated to simplified, miniaturized and integrated formats that are easy and safe to use, in other words; a miniaturized total analysis workflow. Here, the sample preparation should ideally be i) operable by an operator with minimal training, ii) versatile and customizable to specific user needs, and iii) manually- or battery-operable. This set of capabilities have been derived from the ASSURED (affordable, sensitive, specific, rapid, robust, equipment-free, and deliverable to end-users) criteria described by the World Health Organization (WHO) [75]. While these criteria were initially introduced for point-of-care tests targeted at sexually transmitted diseases, they are often also used as guidelines in relation to portable food analyzers (e.g. LFIAs, biosensors and AIMS) [76].

Over the last decade (2015 – 2025), an increasing number of articles described mycotoxin detection using portable food analyzers such as LFIAs and biosensors (Figure 1.3, from Scopus database, last updated December 30th 2025). This suggests that there is an increasing interest for portable sample preparation tools that fit the same purpose as the portable food analyzer, which was also identified by recent studies [73,74]. In order to develop such portable tools with a high degree of design, freedom and customizability, there is one technology that particularly stands out for this; additive manufacturing.

Additive manufacturing is an umbrella term for a set of technologies that allow for the layer-by-layer development of complex three-dimensional (3D) geometries using a wide range of materials. Another, more popular, term for additive manufacturing is 3D-printing, and the combination with the keyword 'biosensor' showed an increasing trend in the number of research articles published on this topic per year (Figure 1.3). This indicates that 3D-printing technologies are increasingly used for biosensor development and could be used for sample handling as well, as identified by several studies [77–80]. The next Section will further elaborate on 3D-printing technologies and their potential use for sample preparation.

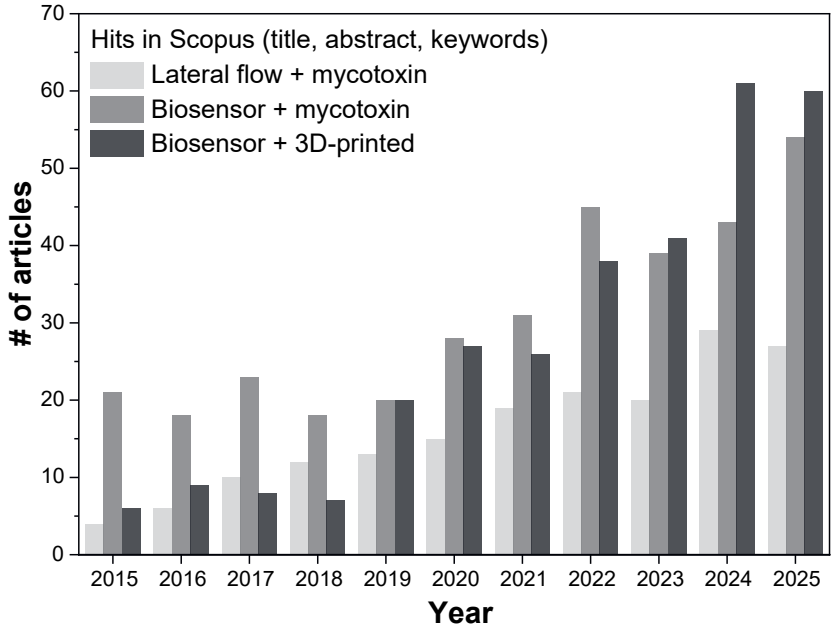


Figure 1.3: *Literature search of title, abstract and keywords in Scopus database between the years 2015 – 2025 for 3 combinations; lateral flow + mycotoxin, biosensor + mycotoxin, biosensor + 3D-printed (last updated 30th of Dec 2025).*

1.3.1 Opportunities for 3D-printed sample preparation

The increase in research articles mentioning the keywords biosensor and 3D-printed can be linked to an increased availability of affordable 3D-printers from 2019 (Figure 1.3). Nowadays, even budget-friendly models (~€200) can produce high-quality parts. Most of the affordable consumer-grade 3D-printers use fused-deposition modelling (FDM) as manufacturing method. The basic principle of FDM is a thermoplastic extrusion of common polymer materials such as polylactic acid (PLA), acrylonitrile-butadiene-styrene (ABS), polyethylene terephthalate (PET), nylon and thermoplastic elastomers (TPE) [78,79]. In order to produce a basic 3D-printed part the following steps are typically needed; (i) computer-aided design (CAD) of the desired part using e.g. SOLIDWORKS or Autodesk Fusion software, (ii) saving the CAD as a universally readable stereolithography format referred to as an .STL file, (iii) uploading of the .STL file in a slicer software which converts it into 2D sections (layers) and (iv) transfer of the resulting .gcode to the 3D-printer. Finally, the 3D-printer moves in xyz directions and thereby a layer-by-layer deposition of heated and extruded thermoplastic forms the complete object [79,81].

Another commonly used manufacturing method for 3D-printers is vat-polymerization, which selectively photopolymerizes (i.e. cures) the desired object

out of a liquid resin, layer-by-layer, using mirrors and a UV laser [81]. One example of vat-polymerization is stereolithography (SLA), and compared to FDM this method typically achieves higher resolution, smooth surfaces and the printing time is faster. Therefore, SLA is a suitable method to produce parts for microfluidics or lab-on-a-chip (LOC) systems. However, post-processing of SLA printed parts is quite cumbersome because the uncured resin needs to be washed off, and a post-cure is needed as well. When the 3D-printed parts need to have a high shore hardness and durability for their application, FDM is more appropriate. FDM is also less expensive and often requires minimal post-processing. Thus, it very much depends on the application of the final parts which 3D-printer is best to be used.

In one study, a transparent 3D-printed (FDM) device for enzymatic assays with UV-VIS detection was developed. In the device, three reaction chambers and an analysis chamber allowed for in-device enzymatic assays and the device was compatible with a UV-VIS spectrophotometer [82]. In another study, (bio)3D-printed polymer scaffolds were developed and functioned as solid-phase extraction (SPE) sorbent. Moreover, MIPs were immobilized on these 3D-printed scaffolds and allowed for the recognition of ergot alkaloids, a group of mycotoxins. Thereby, a 3D-printed example of a common sample preparation approach was established; a MIP-SPE column [83]. A last example includes a 3D-printed total analysis workflow for the smartphone-based detection of allergen proteins (Figure 1.4A) [84]. Here, a 3D-printed unibody lab-on-a-chip (LOC) containing two LFIAs was inserted into a 3D-printed smartphone holder, allowing for the smartphone-based detection of allergen protein in a cookie (Figure 1.4B). The 3D-printed unibody LOC contained a reagent reservoir, a test well and a reference well, and was capable of in-chip, pipette-free dilution (Figure 1.4C) [84]. Both FDM and SLA 3D-printers were used to construct the parts. The FDM printer was used to construct a robust and light-blocking smartphone detection holder, and the SLA printer was used to construct the liquid-handling unibody LOC.

As shown by the unibody LOC, 3D-printing can be used to produce channel structures and fluid handling. Such capabilities also show potential for the fabrication of microfluidic systems [85–88]. Most microfluidic LOC systems are fabricated using soft lithography with polydimethylsiloxane (PDMS). While there are certainly benefits to the use of PDMS for microfluidics, such chips rarely make it out of the research laboratory due to issues with scalability and automation. The ability to 3D-print microfluidic structures allows automated 3D fabrication and improves throughput [85–88]. Therefore, 3D-printing of such structures for the production of e.g. LOC devices is of much interest, until now mostly in the biomedical field but also increasingly for portable food analyzers [87–90].

Typically, liquids are forced through the microfluidic system by a peristaltic pump, a syringe pump or a pressure driven flow controller, connected by tubing

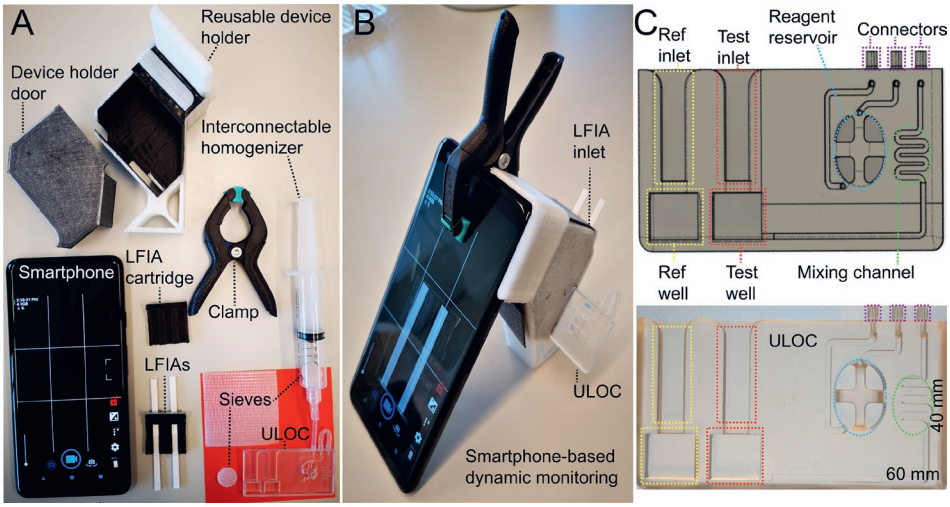


Figure 1.4: *Overview of the 3D-printed smartphone-based device for allergen protein detection. A) Disassembled components of the device. B) Assembled device (side-view) where unibody LOC fits into the smartphone holder. LFIAs are inserted and the analysis progress is recorded by the smartphone. C) CAD design of the unibody LOC and photo of the SLA printed prototype. Reprinted with permission from Ref 84 (Copyright Elsevier 2025).*

to the microfluidic system. In such microfluidic systems it is essential to control the pressure drop, to maintain a consistent flowrate and accurate test results [91–93]. However, the more complex the (3D-printed) microfluidic system, the more complex it becomes to control the pressure drop. Moreover, the use of relatively expensive external pumps and rather complex microfluidics are generally less fitting to the ASSURED concept mentioned earlier. Therefore, fluid handling using a paper-based format is a popular alternative strategy.

1.3.2 Paper-based fluid-handling

Where in microfluidics the control of flow can be very precise when all factors are properly tuned, in paper-based systems the flow is controlled by properties of the paper and it occurs spontaneously [94]. A spontaneous flow can be beneficial for many LOC applications and there is also no need for an external pump, tubing or complex fluidics. This simplicity has led to a rise in paper-microfluidic systems, especially since the seminal publication on patterned paper by the Whitesides group in 2007 [95,96]. However, paper has been utilized in a chemistry context long before that. One very well known example is the Melitta coffee extraction filter that was invented in 1908, and can still be found in every supermarket today [96]. An innovative aspect of the Whitesides group publication was that they used standard chromatography paper as an inexpensive substrate for photolithography, by which a channel-like pattern was developed on paper [95]. Currently, channel-like structures for paper-

based microfluidics are fabricated using methods such as wax printing, inkjet printing, writing (i.e. crayon or marker), mechanical cutting (i.e. scissor or laser), photolithography and etching [97,98]. Next to customizing the channel-structure for the paper-based microfluidics, the paper substrate can be modified to exhibit specific functionalities. For example, paper has been modified with alkyl ketene dimer to exhibit hydrophobic properties and an on-paper liquid-liquid extraction (LLE) was performed [99]. Similarly, paper has been modified with several different hydrophobic reagents and paper-based microfluidic applications were demonstrated such as surface tension measurements, multistep valving, distance-based measurements of alcohol content and on-paper LLE [94]. Other functionalities include affinity-based detection using immobilized recognition elements and, sample collection and storage [96,100,101]. This shows that the tuning of paper properties makes it a versatile microfluidic substrate capable of integrated sample preparation.

As mentioned earlier, the flow in paper occurs spontaneously and this is termed wicking [94]. This wicking is largely governed by capillary action, a phenomenon driven by forces of cohesion (i.e. attraction between liquids) and adhesion (i.e. attraction between substrate and liquid). The wicking of fluid in (dry) paper can be described using the Lucas-Washburn equation (Equation 1.2), which assumes that the paper is a bundle of parallel cylindrical tubes [94,100]. Additionally, as for microfluidic channels, paper-microfluidic channels are characterized by low Reynolds numbers and thus have a laminar flow profile.

$$l(t) = \sqrt{\frac{\gamma r \cos\theta}{2\mu} t} \qquad \textit{Equation 1.2}$$

Where in an ideal example, *l(t)* is the distance travelled by the fluid front, γ is the liquid-air surface tension, r is the effective pore size of the paper, θ is the liquid-paper contact angle, and μ is the fluid viscosity [100]. However, as examples are never ideal in practice, complementary theories such as Darcy's law, which considers flow in a fully wetted paper, should be taken into consideration [102]. Other factors that can influence the fluid flow in paper, and can thus be utilized for integrated sample preparation, include evaporation, geometry and, as already discussed, substrate modification.

1.4 Towards IR-based portable food safety analyzers for direct mycotoxin detection

The current methods used for mycotoxin analysis and the potential of integrated sample preparation were discussed in detail to provide a good understanding of the multidisciplinary field and identify opportunities for the development of portable food safety analyzers. One of the directions to which the opportunities point is towards IR spectroscopy, as was also identified by the stakeholder assessment performed along the European food supply chain [74].

IR spectroscopy is categorized as an indirect screening technique (group 2) for mycotoxins [34]. As discussed, indirect screening means that the macromolecular changes in the matrix upon fungal infestation are linked to mycotoxin contamination via chemometrics [39,43–45,103,104]. To establish such chemometric models, large and diverse sample sets for training and testing of the models are needed. Moreover, reference analysis of the samples using for example LC-MS/MS is essential to develop reliable chemometric models. Therefore, the information that is obtained is prediction-based and not a direct measure of the presence of the mycotoxin. Both NIR and MIR spectroscopy methods have been developed that employ such chemometric models, with wheat and corn as main studied food commodities and the mycotoxin DON as main target [39,45,104]. In these studies, attenuated-total-reflection Fourier-Transform infrared spectroscopy (ATR-FTIR), an extensively used type of MIR spectroscopy, is frequently employed for DON screening. Moreover, efforts to miniaturize ATR-FTIR systems have been reported, suggesting its potential for portable food analysis [46,105].

A standard ATR-FTIR is characterized by an internal reflection element, where an evanescent field penetrates a few μm into the sample (Figure 1.5). At the heart of a typical FTIR system is a Michelson interferometer [41]. A Michelson interferometer contains a radiation source, a beam splitter, a fixed mirror, a moving mirror and a detector (Figure 1.5). The beam splitter divides the radiation to the fixed mirror and to the moving mirror. The moving mirror controls the optical pathlength and upon moving, constructive and destructive interference patterns are obtained when the radiation recombines. This interference pattern is recorded as an interferogram at the detector, which contains information of all IR vibrational frequencies in the source. When the sample is placed in the path of the IR radiation and absorbs part of it, the interferogram alters from its basic form. To interpret this alteration, a seminal mathematical concept is used; the Fourier-Transform (FT). The FT function breaks the interferogram down into individual frequency components (Figure 1.5). This reveals how much of each infrared vibrational frequency was absorbed by the sample, producing a spectrum that shows peaks at specific wavenumbers related

to the molecule(s) present in the sample [41]. As discussed before, Beer's Law can be used to determine the concentration from the specific molecular absorbance features, and which could thus be employed for quantitative mycotoxin detection in a direct format.

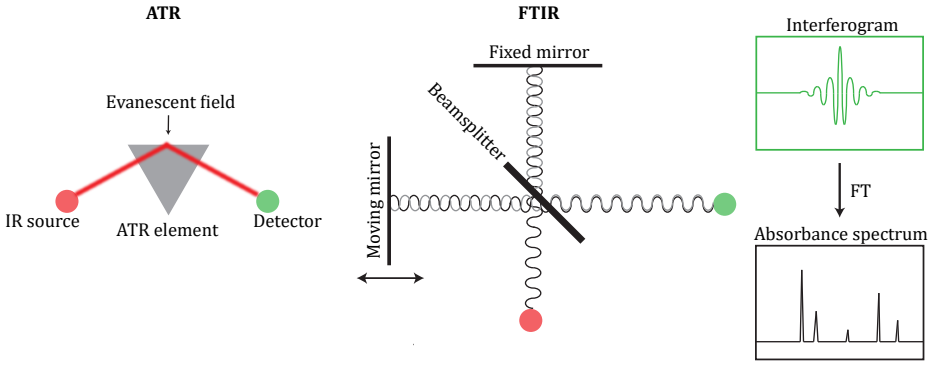


Figure 1.5: *Illustration of the typical components present in ATR-FTIR spectrometers.*

In order to realize the direct detection of mycotoxins in food products the following challenges are identified; (i) the low, yet harmful abundance of mycotoxins in complex food matrices, (ii) the lack of IR method specificity and, (iii) the inadequate sensitivity of routine IR spectrometers for ML concentrations. When these challenges are overcome, ATR-FTIR analysis could provide information on the chemical identity and concentration of the mycotoxin. Then, the presence of mycotoxin is confirmed based on the molecular features and the sample's compliance to regulation can be derived from the concentration. Moreover, ATR-FTIR is already used for differentiating positional isomers [106], something that e.g. LFIA and AIMS technologies struggle with. This is also highly interesting for the differentiation of isomeric mycotoxins such as the acetylated forms of DON, which are known to cause health effects as well [23].

1.4.1 Scope and outline of thesis

To advance towards IR-based portable food safety analyzers that are capable of direct mycotoxin detection, the main focus of this thesis is on integrated sample preparation, specific recognition of mycotoxins in complex food matrices and, molecular detection of mycotoxins using IR. Therefore, the following technologies have been explored; 3D-printing, paper-based microfluidics, immunochemical purification and ATR-FTIR spectroscopy. Such paper-based IR analysis of mycotoxins is expected to allow for a complete sample-to-answer workflow. This novel methodological framework aims to measure regulated mycotoxins from high to low MLs and in different food commodities. To evaluate the capabilities of the proposed methods, two distinct mycotoxin-commodity combinations have been selected; DON

in wheat and OTA in wine (Figure 1.6). This selection includes different mycotoxins and commodity types, as well as a range of MLs from high to low concentration to ensure the proposed methods are tested under relevant conditions.

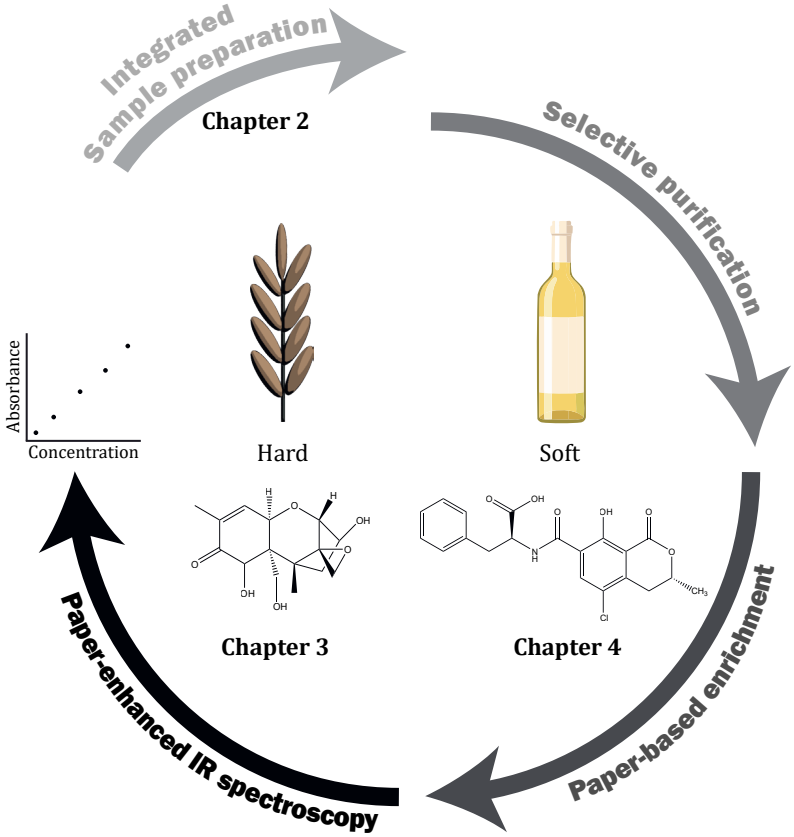


Figure 1.6: *Illustration of the typical components present in ATR-FTIR spectrometers.*

The aim of **Chapter 2** is to investigate if a 3D-printed device could be developed for achieving the grinding of wheat kernels with adequate and reproducible particle sizes for mycotoxin analysis, as well as in-device solid-liquid extraction of DON. It is hypothesized that such a device could lead to increased standardization practices within commercial LFIA workflows. To evaluate the performance of the proposed device, it is benchmarked against a standard laboratory mill and the complete LFIA workflow is validated using LC-MS/MS reference analysis.

The aim of **Chapter 3** is to develop a novel framework for direct mycotoxin analysis of DON in wheat using ATR-FTIR spectroscopy. To address the limitations of indirect ATR-FTIR spectroscopy for mycotoxin detection in food, immunochemical purification and paper-based enrichment of DON are studied. First, to proof the

concept of paper-based ATR-FTIR, a relatively high concentration of DON analytical standard is detected on paper. Secondly, to achieve the detection of DON analytical standard in the ML range (1000 µg/kg), paper-based enrichment of the molecules is studied. Then, immunochemical purification is explored to remove sufficient DON molecules from contaminated wheat extracts and to transfer the DON molecules to a clean solvent for subsequent paper-based enrichment and direct IR analysis of DON. Finally, the complete framework is validated using LC-MS/MS reference analysis and contaminated wheat from field-trials, with the aim to show the method's relevance for food safety analysis.

The aim of **Chapter 4** is to expand the paper-based IR framework of **Chapter 3** to achieve the quantitative detection of OTA in white wine in the range of the very strict ML of 2 µg/kg. To accomplish quantitative OTA detection at these low levels, a pH-dependent solvent extraction is explored that should allow for the pre-enrichment of OTA molecules. The resulting extract with pre-enriched OTA molecules can then be used in a customized IR framework for OTA. It was hypothesized that careful framework optimization with complementary HPLC-HRMS reference analysis should allow for the quantitative detection of OTA in white wine at the ML, showcasing the extended capabilities of the paper-based IR framework for food safety analysis.

Finally, **Chapter 5** provides a general discussion of the methodologies developed in **Chapter 2 – 4** and provides an outlook on the future of integrated sample preparation and paper-based IR spectroscopy in the context of portable food analyzers and beyond.

References

1. Bennett, J. W. & Klich, M. Mycotoxins. Clin. Microbiol. Rev. 16, 497–516 (2003).
2. Salamini, F., Ozkan, H., Brandolini, A., Schäfer-Pregl, R. & Martin, W. Genetics and geography of wild cereal domestication in the near east. Nat. Rev. Genet. 3, 429–441 (2002).
3. Pitt, J. I. & Miller, J. D. A Concise History of Mycotoxin Research. J. Agric. Food Chem. 65, 7021–7033 (2017).
4. Molina, J. et al. Molecular evidence for a single evolutionary origin of domesticated rice. Proc. Natl. Acad. Sci. U. S. A. 108, 8351–8356 (2011).
5. Sulyok, M., Stadler, D., Steiner, D. & Krska, R. Validation of an LC-MS/MS-based dilute-and-shoot approach for the quantification of > 500 mycotoxins and other secondary metabolites in food crops: challenges and solutions. Anal. Bioanal. Chem. 412, 2607–2620 (2020).
6. Muhialdin, B. J., Saari, N. & Meor Hussin, A. S. Review on the Biological Detoxification of Mycotoxins Using Lactic Acid Bacteria to Enhance the Sustainability of Foods Supply. Molecules 25, 2655 (2020).
7. Edite Bezerra da Rocha, M., Freire, F. da C. O., Erlan Feitosa Maia, F., Izabel Florindo Guedes, M. & Rondina, D. Mycotoxins and their effects on human and animal health. Food Control 36, 159–165 (2014).
8. Ostry, V., Malir, F., Toman, J. & Grosse, Y. Mycotoxins as human carcinogens-the IARC Monographs classification. Mycotoxin Res. 33, 65–73 (2017).
9. EFSA Panel on Contaminants in the Food et al. Risk assessment of ochratoxin A in food. EFSA J. 18, e06113 (2020).
10. Li, S., Marquardt, R. R., Frohlich, A. A., Vitti, T. G. & Crow, G. Pharmacokinetics of Ochratoxin A and Its Metabolites in Rats. Toxicol. Appl. Pharmacol. 145, 82–90 (1997).
11. Ezekiel, C. N. et al. Urinary biomarker-based seasonal mycotoxin exposure assessment in rural resident populations of North-central Nigeria. Environ. Int. 203, 109713 (2025).
12. Tolosa, J., Rodríguez-Carrasco, Y., Ruiz, M. J. & Vila-Donat, P. Multi-mycotoxin occurrence in feed, metabolism and carry-over to animal-derived food products: A review. Food Chem. Toxicol. 158, 112661 (2021).
13. Dall'Asta, C. et al. Occurrence of ochratoxin A in raw ham muscle, salami and dry-cured ham from pigs fed with contaminated diet. Food Chem. 120, 978–983 (2010).
14. De Roma, A., Rossini, C., Ritieni, A., Gallo, P. & Esposito, M. A survey on the Aflatoxin M1 occurrence and seasonal variation in buffalo and cow milk from Southern Italy. Food Control 81, 30–33 (2017).
15. Goda, A. A. et al. Global health and economic impacts of mycotoxins: a comprehensive review. Environ. Sci. Eur. 37, 122 (2025).
16. Casu, A., Camardo Leggieri, M., Toscano, P. & Battilani, P. Changing climate, shifting mycotoxins: A comprehensive review of climate change impact on mycotoxin contamination. Compr. Rev. Food Sci. Food Saf. 23, e13323 (2024).
17. FAO - WHO. Codex Alimentarius - General Standard for Contaminants and Toxins in Food and Feed. CXS 193-1995 (1995).
18. Chen, C., Turna, N. S. & Wu, F. Risk assessment of dietary deoxynivalenol exposure in wheat products worldwide: Are new codex DON guidelines adequately protective? Trends Food Sci. Technol. 89, 11–25 (2019).
19. The European Commission. Commission Regulation (EU) 2023/915 on Maximum Levels for Certain Contaminants in Food. (2023).
20. The European Commission. Commission Regulation (EU) 2024/1022 Amending Regulation (EU) 2023/915 as Regards Maximum Levels of Deoxynivalenol in Food. (2024).
21. The European Commission. Commission Regulation (EU) 2024/1038 Amending Regulation (EU) 2023/915 as Regards Maximum Levels of T-2 and HT-2 Toxins in Food. (2024).

22. U.S Food & Drug Administration. Mycotoxins. Toxins found in food infected by certain molds or fungi https://www.fda.gov/food/natural-toxins-food/mycotoxins (2024).
23. EFSA Panel on Contaminants in the Food Chain. Risks to human and animal health related to the presence of deoxynivalenol and its acetylated and modified forms in food and feed. EFSA J. (2017) doi.org/10.2903/j.efsa.2017.4718
24. World Health Organization. Food safety, climate change and the role of WHO. https://iris.who.int/handle/10665/376702 (2018).
25. European Environment Agency. Mycotoxin exposure in a changing European climate. https://www.eea.europa.eu/en/analysis/publications/mycotoxin-exposure-in-a-changing-european-climate (2025).
26. Casu, A., Camardo Leggieri, M., Toscano, P. & Battilani, P. Changing climate, shifting mycotoxins: A comprehensive review of climate change impact on mycotoxin contamination. Compr. Rev. Food Sci. Food Saf. 23, e13323 (2024).
27. Intergovernmental Panel on Climate Change (IPCC). Climate Change 2022 – Impacts, Adaptation and Vulnerability. (Cambridge University Press, Cambridge, 2023). doi:10.1017/9781009325844.
28. Johns, L. E., Bebber, D. P., Gurr, S. J. & Brown, N. A. Emerging health threat and cost of Fusarium mycotoxins in European wheat. Nat. Food 3, 1014–1019 (2022).
29. Chaloner, T. M., Gurr, S. J. & Bebber, D. P. Plant pathogen infection risk tracks global crop yields under climate change. Nat. Clim. Change 11, 710–715 (2021).
30. Eskola, M. et al. Worldwide contamination of food-crops with mycotoxins: Validity of the widely cited 'FAO estimate' of 25%. Crit. Rev. Food Sci. Nutr. 60, 2773–2789 (2020).
31. Park, D. L., Njapau, H. & Boutrif, E. Minimizing risks posed by mycotoxins utilizing the HACCP concept. FAO Food Nutr. Agric. J. (1999).
32. FAO. Food Outlook – Biannual Report on Global Food Markets. (Rome, 2025). doi:10.4060/cd5655en.
33. dsm-firmenich. World Mycotoxin Survey. https://www.dsm-firmenich.com/anh/products-and-services/tools/mycotoxin-contamination/mycotoxin-survey/mycotoxin-survey-report-q4-2024.html (2024).
34. Lemmink, I. B. et al. Recent advances and challenges in the analysis of natural toxins. Adv. Food Nutr. Res. 110, 67–144 (2024).
35. European Comission. RASFF Window. https://webgate.ec.europa.eu/rasff-window/screen/search.
36. Krska, R. et al. Safe food and feed through an integrated toolbox for mycotoxin management: the MyToolBox approach. World Mycotoxin J. (2016) doi:10.3920/WMJ2016.2136.
37. Csenki, E. et al. Stakeholder assessment for mycotoxin analysis: exploring the demand along the European food supply chain. World Mycotoxin J. (2023). doi:10.1163/18750796-20232883.
38. Tittlemier, S. A. et al. Developments in mycotoxin analysis: an update for 2020-2021. World Mycotoxin J. 15, 3–25 (2022).
39. Freitag, S., Sulyok, M., Logan, N., Elliott, C. T. & Krska, R. The potential and applicability of infrared spectroscopic methods for the rapid screening and routine analysis of mycotoxins in food crops. Compr. Rev. Food Sci. Food Saf. 21, 5199–5224 (2022).
40. Freitag, S. Infrared spectroscopy for mycotoxin screening: Advantages and limitations. in Mycotoxins 249–266. Wageningen Academic. (2025). doi:10.1163/9789004724969_012.
41. Stuart, B.H. Infrared Spectroscopy: Fundamentals and Applications. (John Wiley & Sons, 2004).
42. Griffiths, P.R. James A. De Haseth, & James D. Winefordner. Fourier Transform Infrared Spectrometry. (John Wiley & Sons, 2007).
43. Freitag, S. et al. Attenuated total reflection mid-infrared spectroscopy to screen Austrian and French wheat from multiple years for deoxynivalenol. Spectrochim. Acta. A. Mol. Biomol. Spectrosc. 340, 126340 (2025).
44. Femenias, A. et al. Optimizing extraction solvents for deoxynivalenol analysis in maize via infrared attenuated total reflection spectroscopy and chemometric methods. Anal. Methods 15, 36–47

(2023).
45. Öner, T. et al. Machine learning algorithms for the automated classification of contaminated maize at regulatory limits via infrared attenuated total reflection spectroscopy. World Mycotoxin J. (2019) doi:10.3920/WMJ2018.2333.
46. Fomina, P. et al. A Portable Infrared Attenuated Total Reflection Spectrometer for Food Analysis. Appl. Spectrosc. 77, 1073–1086 (2023).
47. Nolan, P., Auer, S., Spehar, A., Elliott, C. T. & Campbell, K. Current trends in rapid tests for mycotoxins. Food Addit. Contam. Part A 36, 800–814 (2019).
48. Wang, Y., Zhang, C., Wang, J. & Knopp, D. Recent Progress in Rapid Determination of Mycotoxins Based on Emerging Biorecognition Molecules: A Review. Toxins 14, 73 (2022).
49. Pisoschi, A. M. et al. Biosensors for Food Mycotoxin Determination: A Comparative and Critical Review. Chemosensors 12, 92 (2024).
50. Song, S. et al. Multiplex Lateral Flow Immunoassay for Mycotoxin Determination. Anal. Chem. 86, 4995–5001 (2014).
51. Kong, Z. et al. Development and application of lateral flow strip with three test lines for detection of deoxynivalenol in wheat. Food Chem. 421, 136114 (2023).
52. van der Fels-Klerx, H. J. & de Rijk, T. C. Performance evaluation of lateral flow immuno assay test kits for quantification of deoxynivalenol in wheat. Food Control 46, 390–396 (2014).
53. Anfossi, L., Baggiani, C., Giovannoli, C., D'Arco, G. & Giraudi, G. Lateral-flow immunoassays for mycotoxins and phycotoxins: a review. Anal. Bioanal. Chem. 405, 467–480 (2013).
54. Pantano, L. et al. QuEChERS LC–MS/MS Screening Method for Mycotoxin Detection in Cereal Products and Spices. Int. J. Environ. Res. Public. Health 18, 3774 (2021).
55. Gilbert, J. & Anklam, E. Validation of analytical methods for determining mycotoxins in foodstuffs. TrAC Trends Anal. Chem. 21, 468–486 (2002).
56. Monge, M. E. & Fernández, F. M. An Introduction to Ambient Ionization Mass Spectrometry. (2014) doi:10.1039/9781782628026-00001.
57. Takáts, Z., Wiseman, J. M., Gologan, B. & Cooks, R. G. Mass Spectrometry Sampling Under Ambient Conditions with Desorption Electrospray Ionization. Science 306, 471–473 (2004).
58. Shiea, J. et al. Electrospray-assisted laser desorption/ionization mass spectrometry for direct ambient analysis of solids. Rapid Commun. Mass Spectrom. 19, 3701–3704 (2005).
59. Meisenbichler, C., Kluibenschedl, F. & Müller, T. A 3-in-1 Hand-Held Ambient Mass Spectrometry Interface for Identification and 2D Localization of Chemicals on Surfaces. Anal. Chem. 92, 14314–14318 (2020).
60. Geballa-Koukoula, A., Gerssen, A. & Nielen, M. W. F. Direct analysis of lateral flow immunoassays for deoxynivalenol using electrospray ionization mass spectrometry. Anal. Bioanal. Chem. 412, 7547–7558 (2020).
61. Maragos, C. M. Application of Ambient Ionization Mass Spectrometry to Detect the Mycotoxin Roquefortine C in Blue Cheese. Food Anal. Methods 15, 751–760 (2022).
62. Maragos, C. M. Detection of T-2 Toxin in Wheat and Maize with a Portable Mass Spectrometer. Toxins 15, 222 (2023).
63. Vaclavik, L., Zachariasova, M., Hrbek, V. & Hajslova, J. Analysis of multiple mycotoxins in cereals under ambient conditions using direct analysis in real time (DART) ionization coupled to high resolution mass spectrometry. Talanta 82, 1950–1957 (2010).
64. Geballa-Koukoula, A., Gerssen, A. & Nielen, M. W. F. From Smartphone Lateral Flow Immunoassay Screening to Direct MS Analysis: Development and Validation of a Semi-Quantitative Direct Analysis in Real-Time Mass Spectrometric (DART-MS) Approach to the Analysis of Deoxynivalenol. Sensors 21, 1861 (2021).
65. Maragos, C. M. Detection of T-2 Toxin in Wheat and Maize with a Portable Mass Spectrometer. Toxins 15, 222 (2023).
66. Maragos, C. M., Barnett, K., Morgan, L., Vaughan, M. M. & Sieve, K. K. Measurement of Fumonisins in

Maize Using a Portable Mass Spectrometer. Toxins 14, (2022).
67. Geballa-Koukoula, A., Gerssen, A., Blokland, M. H. & Nielen, M. W. F. Immunoaffinity Plastic Blade Spray Mass Spectrometry for Rapid Confirmatory Analysis of Food Contaminants. J. Am. Soc. Mass Spectrom. 33, 2038–2045 (2022).
68. Ramalho, R. R. F. et al. Fumonisin B1 analysis in maize by Molecularly Imprinted Polymer Paper Spray Ionization Mass Spectrometry (MIP-PSI-MS). J. Food Compos. Anal. 107, 104362 (2022).
69. Zhao, Y. et al. Sample preparation and mass spectrometry for determining mycotoxins, hazardous fungi, and their metabolites in the environment, food, and healthcare. TrAC Trends Anal. Chem. 160, 116962 (2023).
70. Zhou, W. & Pawliszyn, J. Coated blade spray-mass spectrometry for rapid screening: A tutorial. Anal. Chim. Acta 344458 (2025) doi:10.1016/j.aca.2025.344458.
71. Spanjer, M. C., Rensen, P. M. & Scholten, J. M. LC–MS/MS multi-method for mycotoxins after single extraction, with validation data for peanut, pistachio, wheat, maize, cornflakes, raisins and figs. Food Addit. Contam. Part A 25, 472–489 (2008).
72. The European Commission. Commission Implementing Regulation (EU) 2023/2782 of 14 December 2023 laying down the methods of sampling and analysis for the control of the levels of mycotoxins in food and repealing Regulation (EC) No 401/2006. (2023).
73. Geballa-Koukoula, A. et al. Best practices and current implementation of emerging smartphone-based (bio)sensors - Part 2: Development, validation, and social impact. TrAC Trends Anal. Chem. 161, 116986 (2023).
74. Csenki, E. et al. Stakeholder assessment for mycotoxin analysis: exploring the demand along the European food supply chain. World Mycotoxin J. (2023). doi:10.1163/18750796-20232883.
75. Mabey, D., Peeling, R. W., Ustianowski, A. & Perkins, M. D. Diagnostics for the developing world. Nat. Rev. Microbiol. 2, 231–240 (2004).
76. Jafari, S. et al. ASSURED Point-of-Need Food Safety Screening: A Critical Assessment of Portable Food Analyzers. Foods 10, 1399 (2021).
77. Paul, A. A., Aladese, A. D. & Marks, R. S. Additive Manufacturing Applications in Biosensors Technologies. Biosensors 14, 60 (2024).
78. Gross, B., Lockwood, S. Y. & Spence, D. M. Recent Advances in Analytical Chemistry by 3D Printing. Anal. Chem. 89, 57–70 (2017).
79. Salentijn, G. IJ., Oomen, P. E., Grajewski, M. & Verpoorte, E. Fused Deposition Modeling 3D Printing for (Bio)analytical Device Fabrication: Procedures, Materials, and Applications. Anal. Chem. 89, 7053–7061 (2017).
80. Benjamin Ho, C. M., Huan Ng, S., Holden Li, K. H. & Yoon, Y.-J. 3D printed microfluidics for biological applications. Lab. Chip 15, 3627–3637 (2015).
81. Gross, B. C., Erkal, J. L., Lockwood, S. Y., Chen, C. & Spence, D. M. Evaluation of 3D Printing and Its Potential Impact on Biotechnology and the Chemical Sciences. Anal. Chem. 86, 3240–3253 (2014).
82. Sirjani, E., Migas, M., Cragg, P. J. & Dymond, M. K. 3D printed UV/VIS detection systems constructed from transparent filaments and immobilised enzymes. Addit. Manuf. 33, 101094 (2020).
83. De Middeleer, G., Dubruel, P. & De Saeger, S. Molecularly imprinted polymers immobilized on 3D printed scaffolds as novel solid phase extraction sorbent for metergoline. Anal. Chim. Acta 986, 57–70 (2017).
84. Ross, G. M. S., Filippini, D., Nielen, M. W. F. & Salentijn, G. IJ. Interconnectable solid-liquid protein extraction unit and chip-based dilution for multiplexed consumer immunodiagnostics. Anal. Chim. Acta 1140, 190–198 (2020).
85. Bhattacharjee, N., Urrios, A., Kang, S. & Folch, A. The upcoming 3D-printing revolution in microfluidics. Lab. Chip 16, 1720–1742 (2016).
86. Nielsen, A. V., Beauchamp, M. J., Nordin, G. P. & Woolley, A. T. 3D Printed Microfluidics. Annu. Rev.

Anal. Chem. 13, 45–65 (2020).
87. Mehta, V. & Rath, S. N. 3D printed microfluidic devices: a review focused on four fundamental manufacturing approaches and implications on the field of healthcare. Bio-Des. Manuf. 4, 311–343 (2021).
88. Duarte, L. C., Figueredo, F., Chagas, C. L. S., Cortón, E. & Coltro, W. K. T. A review of the recent achievements and future trends on 3D printed microfluidic devices for bioanalytical applications. Anal. Chim. Acta 1299, 342429 (2024).
89. Chung, S., Sudo, R., Vickerman, V., Zervantonakis, I. K. & Kamm, R. D. Microfluidic Platforms for Studies of Angiogenesis, Cell Migration, and Cell–Cell Interactions. Ann. Biomed. Eng. 38, 1164–1177 (2010).
90. dos Santos, D. M. et al. Advances in 3D printed sensors for food analysis. TrAC Trends Anal. Chem. 154, 116672 (2022).
91. Bruus, H. Theoretical Microfluidics. (Oxford University Press, Oxford, New York, 2007).
92. Su, H. et al. The Characteristics of Pressure Drop in Microchannels. Ind. Eng. Chem. Res. 49, 3830–3839 (2010).
93. Zhao, X. et al. Recent Advances in Microfluidics for the Early Detection of Plant Diseases in Vegetables, Fruits, and Grains Caused by Bacteria, Fungi, and Viruses. J. Agric. Food Chem. 72, 15401–15415 (2024).
94. Aksoy, C., van Kesteren, I., Zuilhof, H. & Salentijn, G. I. Broad Tuning of Paper Microfluidic Properties by Covalent Surface Modification for Precise Flow Control and Sensing. ACS Appl. Bio Mater. 8, 3748–3761 (2025).
95. Martinez, A. W., Phillips, S. T., Butte, M. J. & Whitesides, G. M. Patterned Paper as a Platform for Inexpensive, Low-Volume, Portable Bioassays. Angew. Chem. Int. Ed. 46, 1318–1320 (2007).
96. Salentijn, G. IJ., Grajewski, M. & Verpoorte, E. Reinventing (Bio)chemical Analysis with Paper. Anal. Chem. 90, 13815–13825 (2018).
97. Yamada, K., Henares, T. G., Suzuki, K. & Citterio, D. Paper-Based Inkjet-Printed Microfluidic Analytical Devices. Angew. Chem. Int. Ed. 54, 5294–5310 (2015).
98. Nishat, S., Jafry, A. T., Martinez, A. W. & Awan, F. R. Paper-based microfluidics: Simplified fabrication and assay methods. Sens. Actuators B Chem. 336, 129681 (2021).
99. Salentijn, G. I., Grajewski, M. & Verpoorte, E. Countercurrent liquid–liquid extraction on paper. Lab. Chip 17, 3401–3404 (2017).
100. Gong, M. M. & Sinton, D. Turning the Page: Advancing Paper-Based Microfluidics for Broad Diagnostic Application. Chem. Rev. 117, 8447–8480 (2017).
101. Wang, P., Hettinga, K., Brouwer-Brolsma, E. M., Bijl, E. & Salentijn, G. IJ. Wax-coated dried-milk-spot paper for human milk protein compositional analysis. Food Chem. 470, 142622 (2025).
102. Chakrapani, T. H., Bazyar, H., Lammertink, R. G. H., Luding, S. & Otter, W. K. den. The permeability of pillar arrays in microfluidic devices: an application of Brinkman's theory towards wall friction. Soft Matter 19, 436–450 (2023).
103. De Girolamo, A. et al. Rapid screening of ochratoxin A in wheat by infrared spectroscopy. Food Chem. 282, 95–100 (2019).
104. De Girolamo, A. et al. Fourier transform near-infrared and mid-infrared spectroscopy as efficient tools for rapid screening of deoxynivalenol contamination in wheat bran. J. Sci. Food Agric. 99, 1946–1953 (2019).
105. Baumgartner, B., Freitag, S., Gasser, C. & Lendl, B. A pocket-sized 3D-printed attenuated total reflection-infrared filtometer combined with functionalized silica films for nitrate sensing in water. Sens. Actuators B Chem. 310, 127847 (2020).
106. Verhoeven, M., Bonetti, J., Kranenburg, R. & van Asten, A. Chemical identification and differentiation of positional isomers of novel psychoactive substances – A comprehensive review. TrAC Trends Anal. Chem. 166, 117157 (2023).


2

Interconnectable 3D-printed sample processing modules for portable mycotoxin screening of intact wheat

Adapted from:
A.J. Bosman, S. Freitag, G.M.S. Ross, M. Sulyok, R. Krska, F.S. Ruggeri, G.IJ. Salentijn. Interconnectable 3D-printed sample processing modules for portable mycotoxin screening of intact wheat. Analytica Chimica Acta. 2024. Volume 1285, 342000. doi.org/10.1016/j.aca.2023.342000

Abstract

The increasing demand for food and feed products is stretching the capacity of the food value chain to its limits. A key step for ensuring food safety is checking for mycotoxin contamination of wheat. However, this analysis is typically performed by rather complex and expensive chromatographic methods, such as liquid chromatography-tandem mass spectrometry (LC-MS/MS). These costly methods require extensive sample preparation that is not easily carried out at different points along the food supply chain. To overcome such challenges in sample processing, an inexpensive and portable sample preparation device was needed and that was easy to operate, in order to achieve rapid sample-to-result mycotoxin screening.

In this Chapter, 3D-printed and interconnectable modules for simple, integrated and on-site sample preparation were developed. These modules were capable of the grinding of wheat kernels and solvent-based extraction. We characterized these 3D-printed modules for mycotoxin screening and benchmarked them against a laboratory mill using a commercial lateral flow device (LFD) and an in-house validated LC-MS/MS method. Different integrated sieve configurations were compared based on grinding efficiency, and we selected a sieve size of 2 mm allowing the grinding of 10 g of wheat within 5 min. Moreover, 10 first time-users were able to operate the grinder module with minimal instructions. Screening for deoxynivalenol (DON) in naturally contaminated samples at the DON regulatory limit (1.25 $mg \cdot kg^{-1}$, < 2024) was demonstrated using the developed 3D-printed prototype. The whole process only takes 15 min, from sample preparation to screening result. The results showed a clear correlation ($R^2 = 0.96$) between the LFD and LC-MS/MS.

Our findings demonstrate the potential of 3D-printed sample handling equipment as a valuable extension of existing analytical procedures, facilitating the on-site implementation of rapid methods for the determination of mycotoxins in grains. The presented prototype is inexpensive with material costs of 2.5€, relies on renewable bio-based 3D-printing filament and can be produced with consumer-grade printers everywhere in the world, making the prototype acccessible. As a future perspective, the modular character of our developed tool kit will allow for adaptation to other hard food commodities beyond the determination of DON in wheat.

2.1 Introduction

Ever since human civilization shifted to cultivating and storing food crops from season to season, some 10000 years ago, humanity has had to deal with pathogenic fungi [1]. Such fungi grow on a variety of food crops and can produce toxic secondary metabolites, commonly referred to as mycotoxins. These chemically diverse toxins have caused the deaths of many humans and animals worldwide [1]. Amongst the most well-studied mycotoxins are aflatoxins (AFs), deoxynivalenol (DON), ochratoxin A (OTA), T-2 toxin (T-2), HT-2 toxin (HT-2), zearalenone (ZEN) and fumonisins (FBs).

Fungal contamination can occur in the field, during storage, transportation and food processing [2,3]. Consequently, mycotoxins can be found throughout the entire global food supply chain [4–10]. In the European Union (EU), mycotoxin contamination is among the top three chemical food safety hazards [3,11,12]. Therefore, mycotoxins are strictly regulated by most national and international authorities by means of Maximum Levels (MLs) for different food and feed commodities [13–15]. Whenever the contamination exceeds the ML in that particular food or feed commodity, the entire batch will be downgraded or wasted. Therefore, mycotoxin contamination is associated with economic losses and food waste, and their occurrence is increasing globally as a result of climate change [10,16]. In an estimated 20-25% of global food crops, the mycotoxin contamination exceeded the MLs stipulated by the EU legislation [10]. During the period 2010–2019, DON was the most common mycotoxin in European food and feed wheat. Moreover, 5% of European wheat samples exceeded the ML of DON set for processed cereals for direct human consumption, making it a relevant commodity for this work [17].

Currently, numerous methods for multi-mycotoxin analysis are available, amongst which liquid chromatography-tandem mass spectrometry (LC-MS/MS) is the most extensively used for confirmatory analysis [18–21]. Additionally, chromatographic separation methods coupled to, for example, fluorescence (FLD) or ultraviolet (UV) detectors can also be used for mycotoxin analysis [22,23]. Furthermore, advanced and often large scale laboratory mills capable of grinding and homogenizing the intact samples are indispensable for accurate sample preparation prior to instrumental analysis [24,25]. Despite their unsurpassed performance, such methods are only accessible to laboratories that employ analytically trained personnel and have the resources to purchase such advanced analysis equipment and the needed laboratory infrastructure.

For this reason, integrated (bio)sensing devices for food safety monitoring that can be used at the point-of-need (PON), by an end-user that has limited (or no) analytical training/experience, are of great interest [23,26–29]. Such rapid screening methods are currently recognized as strategic tools for food safety management, as

Commission Regulation (EU) No 519/2014 [30,31] and the Association of Official Analytical Chemists (AOAC) [32]. Specifically, for screening at the PON, commercial mycotoxin screening kits are widely available [23, 33-35], including immuno-based assays such as lateral flow devices (LFDs) and enzyme-linked immuno-sorbent assays (ELISAs). However, the implementation of a full 'sample-to-answer' procedure for the truly on-site analysis of mycotoxins remains difficult due to a lack of appropriate sample handling approaches [36,37].

All of the above-described commercial mycotoxin screening methods require pre-ground material, leading to non-harmonized grinding practices, and thus reduced reproducibility. In lab-based mycotoxin analysis, representative sampling, grinding and extraction of food commodities are pivotal steps, and are therefore performed with industrial laboratory mills. As mycotoxins are heterogeneously distributed throughout typical commodities such as maize and wheat, the sampling error is often reduced by increasing the sample size, and by homogenization through appropriate milling [25, 38-40]. Therefore, the first steps of the analytical procedure are crucial for the validity of the final result, and under-sampling, insufficient processing or inadequate treatment can result in under-estimation of contamination levels [24].

In recent years, 3D-printing has been increasingly employed in the fields of (bio) analytical chemistry and microfluidics to overcome such sample handling challenges [41-46]. For example, 3D-printing has been used for the fabrication of (micro)channels [45], masters for soft lithography [47], sample cartridges [48,49], and for the patterning of paper microfluidics [50]. Notably, 3D-printing offers the capability of in-house and agile fabrication of complex components and integrated systems, which cannot be achieved by conventional manufacturing techniques such as hot embossing or injection molding [41,42]. In recent work, a 3D-printed lab-on-a-chip device for solid-liquid protein extraction and subsequent multiplexed immunodiagnostics was developed to demonstrate the potential for integrated sample preparation in the analysis of allergenic proteins from food products, such as cookies [48]. However, this work only demonstrated analysis of processed food, which is already homogenized. Analysis of harder, heterogeneous and resilient samples, such as intact wheat, remains a key challenge.

In this Chapter, to overcome these challenges and achieve fully integrated on-site sample preparation, we exploited 3D-printing for the development of devices for preparation and extraction of DON in naturally contaminated intact wheat. The 3D-printed devices were benchmarked against a conventional laboratory mill with respect to grinding efficiency, particle size distribution (PSD), extraction efficiency, the influence of sample size and homogenization of the developed prototype, and the screening capability at the relevant ML of DON (1.25 $mg \cdot kg^{-1}$, < 2024). These performance parameters were assessed using a commercially available rapid LFD

screening kit and were confirmed by LC-MS/MS analysis.

2.2 Materials & methods

2.2.1 Reagents & consumables

Acetonitrile (ACN), methanol (MeOH), glacial acetic acid (AcOH), and ammonium acetate were purchased from Sigma-Aldrich (Austria); a Purelab Ultra system (ELGA LabWater, Germany) was used to obtain ultrapure water (UPW). A commercially available rapid screening kit for DON was used (AgraStrip® Pro Deoxynivalenol WATEX®, Romer Labs, Austria) that contained indirect competitive assay LFD strips for DON, proprietary extraction buffer, proprietary dilution buffer, filter bags (Whirl-Pak®, USA), 200 and 1000 µL pipette tips, microcentrifuge tubes for dilution, LFD strip cartridges, and a QR code with calibration information of the specific strip batch.

2.2.2 Sample material

Winter wheat kernels (Trappe variety), were obtained from field-trials performed in 2021 at the Institute for Biotechnology in Plant Production at the Department of Agrobiotechnology, IFA-Tulln, University of Natural Resources and Life Sciences BOKU. LC-MS/MS analysis was used to identify wheat with DON levels exceeding the regulatory limit. Wheat material containing approximately 3.0 $mg \cdot kg^{-1}$ of DON was then used to obtain additional contamination levels, at approximately 0.3 and 1.3 $mg \cdot kg^{-1}$ by mixing with blank material from the same wheat variety and field trial. This mixing method resulted in contamination levels below ML (~0.3 $mg \cdot kg^{-1}$), at ML (~1.3 $mg \cdot kg^{-1}$) and above ML (~3.0 $mg \cdot kg^{-1}$), considering the EU regulatory limit for unprocessed cereals (1.25 $mg \cdot kg^{-1}$).

2.2.3 Instruments

A conventional disc-type laboratory mill (Perten LabMill 3610, PerkinElmer, USA) equipped with a fine grinding, hardened steel disc (type 5) set at distance '0' was used, after which the ground material was collected in a sample cup. A fused deposition modeling (FDM) 3D-printer (Prusa i3 MK3S+, Prusa Research, Czech Republic) was used to fabricate all prototype parts. An analytical sieve shaker (AS 200, Retsch Benelux, NL) was used to sort the particles of the ground material and determine the PSD. An LFD strip reader (AgraVision™ Pro, Romer Labs, Austria) was used to analyze the LFDs. An LC-MS/MS system was used consisting of a 1290 series HPLC (Agilent Technologies, Germany) and a QTrap 5500 MS/MS (Applied Biosystems, USA) with a TurboV electrospray ionization (ESI) source. A Gemini® C18-column (150 × 4.6 mm, 5 µm particle size), and a C18 security guard cartridge, 4 × 3 mm were used (Phenomenex, USA).

Ground wheat for the LFD analysis and for the LC-MS/MS analysis was weighed using precision balances (Kern & Sohn GmbH 572-37 and Kern & Sohn GmbH EG, Germany). A hand drill (Tacklife PCD04C, USA) with one driver setting and a drill clutch set at "1" was used to perform the automatic grinding with the 3D-printed prototypes. This is the lowest torque setting of the drill.

2.2.4 3D-printing settings

All prototype parts and assemblies were designed using computer-aided design (CAD) software SolidWorks 2021 (DSSC, USA) and exported in .STL format. The printing file (.Gcode) was prepared by the open slicer software PrusaSlicer 2.5.0 (Prusa Research, Czech Republic), with the following settings: nozzle diameter 0.4 mm, nozzle temperature 215 °C, bed temperature 60 °C, infill 15%, fill pattern "Gyroid", support on built plate only ("Honeycomb" pattern), and layer height (resolution) 0.2 mm. For more detailed settings refer to the Supporting Information (SI, Table S2.1). All parts were printed with PLA filament (EcoPLA, 3D Jake, Austria). The STL files of these components, as well as the PrusaSlicer configuration can be directly imported in the slicer software, automatically rendering all prototype parts with correct settings for any user (SI Figure S2.1).

2.2.5 DON analysis

2.2.5.1 Rapid mycotoxin screening using LFD kit

The LFDs were used according to the instructions provided by Romer Labs [54]. Ten grams (±0.01g) of ground wheat was transferred to a Whirl-Pak® filter bag. The extraction was carried out by adding an extraction buffer bag and 50 mL of ultrapure water to the filter bag; the filter bag was then manually shaken for 2 min. Subsequently, the sample was allowed to settle for 1 min and 100 µL of extract was diluted with 1000 µL of dilution buffer. The diluted extract was centrifuged (VWR Galaxy Mini Star) for 30 s at 6000 rpm and following this, 100 µL of supernatant was pipetted into a cartridge containing the LFD, which was inserted into the batch-calibrated reader. After 4 min, the reader displayed the result in a concentration range between 0 and 44 parts per million (ppm, $mg \cdot kg^{-1}$) for DON in the starting material [51]. Afterwards, the remaining diluted extract was further diluted using a factor of 1:10 with acetonitrile/ultrapure water/glacial acetic acid (20:79:1, v/v/v), before it was subjected to LC-MS/MS analysis.

2.2.5.2 LC-MS/MS analysis

An LC-MS/MS method that was fully in-house validated for over 500 fungal metabolites was used as confirmatory method during this study. This LC-MS/MS confirmatory method was validated for wheat according to the Eurachem guidelines and has been recently described in detail [21]. The quality of the LC-MS/MS method was assured via a proficiency test organized by BIPEA (France). The test

had a success rate of 96% over 2000 measurements in the past 14 years. Data on intermediate precision over a period of 7 weeks have been described, with 98% of the investigated analytes meeting the within laboratory reproducibility (RSDWLR) criterion of a relative standard deviation (RSD) ≤20% [21]. From this work, all 18 results submitted so far for DON in wheat exhibited a satisfactory z-score of $-2 < z < 2$. In short, 5 g (±0.01g) of pre-ground wheat were extracted in 20 mL of ACN/UPW/AcOH (79:20:1, v/v/v) for 90 min using an overhead shaker (GFL 3017, Germany) and centrifuged (GS-6, Beckman Coulter Inc, USA) for 2 min at 3000 rpm. Thereafter, 350 µL of extract was diluted with 350 µL ACN/UPW/AcOH (20:79:1, v/v/v). The additional dilution step was performed to counteract the difference between the extraction solvent and the chromatographic conditions.

Next, the diluted extract (5 µL) was injected into the LC-MS/MS system. Mobile phases, A (MeOH/UPW/AcOH, 10:89:1 v/v/v) and B (MeOH/UPW/AcOH, 97:2:1 v/v/v), both containing 5 mM ammonium acetate, were used. The gradient started with 100% A for 2 min, after which a proportional linear increase of B to 50% was accomplished within 3 min. Thereafter, within 9 min this increase was continued to 100% B, followed by a hold time of 4 min. The column was re-equilibrated with 100% A, for 2.5 min before the next run. The flow rate was set at 1000 µL/min throughout the run. Scheduled selected reaction monitoring (sSRM), for the transitions of DON, in negative mode was used. The ESI source was used at a temperature of 550 °C, the ion spray voltage was 5500 V, the curtain gas (nitrogen) was 30 psi and, both the sheath gas and drying gas (nitrogen) were 80 psi.

2.2.6 Prototype performance assessment

The 3D-printed prototype for automated grinding was characterized based on the grinding efficiency (2.2.6.1), and the performance was compared to a conventional laboratory mill. The performance was evaluated using a commercial LFD screening kit and LC-MS/MS reference analysis. Additionally, the protoype was benchmarked against the laboratory mill based on particle size distribution (2.2.6.2), extraction efficiency (2.2.6.3), the influence of sample size and homogenization (2.2.6.4), and screening around the DON ML (2.2.6.5). A total of 50 prototype parts were printed over the course of 14 days and all wheat material was ground by a total of three people. The same type of 3D-printer was used throughout all the acquired analysis data presented in this manuscript.

2.2.6.1 Grinding efficiency

Intact wheat kernels, from a non-mycotoxin contaminated batch, were ground with the different 3D-printed prototypes, including sieves with standard mesh sizes of 10 (2 mm), 20 (0.8 mm), and 30 (0.6 mm) and the hand drill.

The grinder prototype was evaluated based on grinding efficiency (weight of ground material per minute). The amount of wheat from the different prototype configurations was measured, at different time points, using a precision balance (Kern & Sohn GmbH, 572-37, Germany). Thereafter, the configuration with the most optimal grinding efficiency was selected for subsequent experiments. The consistency and the repeatability of this selected configuration was evaluated during 2 min of grinding using new parts at each repeat ($n = 9$). This configuration was also subjected to a first-time user trial with 10 participants who operated the 3D-printed prototype with the hand drill for 30 s.

2.2.6.2 Particle size distribution (PSD)

Three batches of ground wheat from the laboratory mill and the selected prototype configuration were characterized based on particle size distribution, using an analytical sieve shaker containing the following pore sizes: 2000, 1250, 1000, 800, 600, 250 and 150 µm. The sieve shaker was set at an acceleration amplitude of 2.00 mm for 2 min and the weight per fraction was measured using a precision balance (TE3102S, Sartorius, Germany). Since the starting weight varied per batch, the relative weight was calculated, and this was plotted against the sieve mesh to obtain a distribution.

2.2.6.3 Extraction efficiency

The extraction efficiency of the material obtained from grinding intact wheat with all available sieve sizes (parts C1/C2/C3) was evaluated by grinding 5 grams of material per sieve part, and from that three times 1 gram was taken to perform the LC-MS/MS analysis (2.2.5.2). This data was compared to wheat ground using the laboratory mill, from which also three times 1 gram was sampled and analyzed. Thereafter, ground kernels, from the 3 $mg \cdot kg^{-1}$ level, from both the laboratory mill and the selected prototype were extracted following the procedures described in 2.2.5.1 and 2.2.5.2.

Ten grams were needed to perform the LFD kit procedure and 5 grams for LC-MS/MS analysis. Nine repetitions were performed for both methods, and therefore 150 grams of material was ground with both the laboratory mill and the selected prototype (SI, Fig. S2.2). The DON content was (semi-)quantified by both procedures. The variance within the analysis method was statistically evaluated using a two-sample F-test with OriginPro2022 (OriginLab Corporation, USA).

2.2.6.4 Influence of sample size & homogenization

The effects of sample size and sample homogenization prior to sampling were investigated by comparing the LFD results of 2.2.6.3 with directly sampling and grinding of 10 g of intact wheat (n = 9). This was evaluated for the 3 $mg \cdot kg^{-1}$ level of contamination (SI, Fig. S2.3). Thereafter, the implementation of the prototype including the extraction module that substitutes part of the LFD screening procedure was assessed by grinding and extracting intact wheat kernels using the 3D-printed prototype (n = 3).

2.2.6.5 Screening DON around the maximum level

300 grams of intact wheat from ~0.3 $mg \cdot kg^{-1}$ (<ML), ~1.3 $mg \cdot kg^{-1}$ (ML), and ~3.0 $mg \cdot kg^{-1}$ (>ML) were sampled, and subsequently each amount was split (2 × 150g) and ground with the laboratory mill or the prototype (SI, Fig. S2.4). The resulting material was analyzed by the entire LFD kit procedure and the residual sample extract was diluted and analyzed by LC-MS/MS (2.2.5.2).

2.3 Results & dicussion

The 3D-printed sample processing module was designed with the aim of enabling user-friendly and fast grinding of intact wheat, with controllable and reproducible particle sizes. Therefore, a rotary "blade and teeth" crushing mechanism was investigated, that was combined with an integrated sieve in order to control the PSD of the collected material. Such a design is schematically depicted in Fig. 2.1.

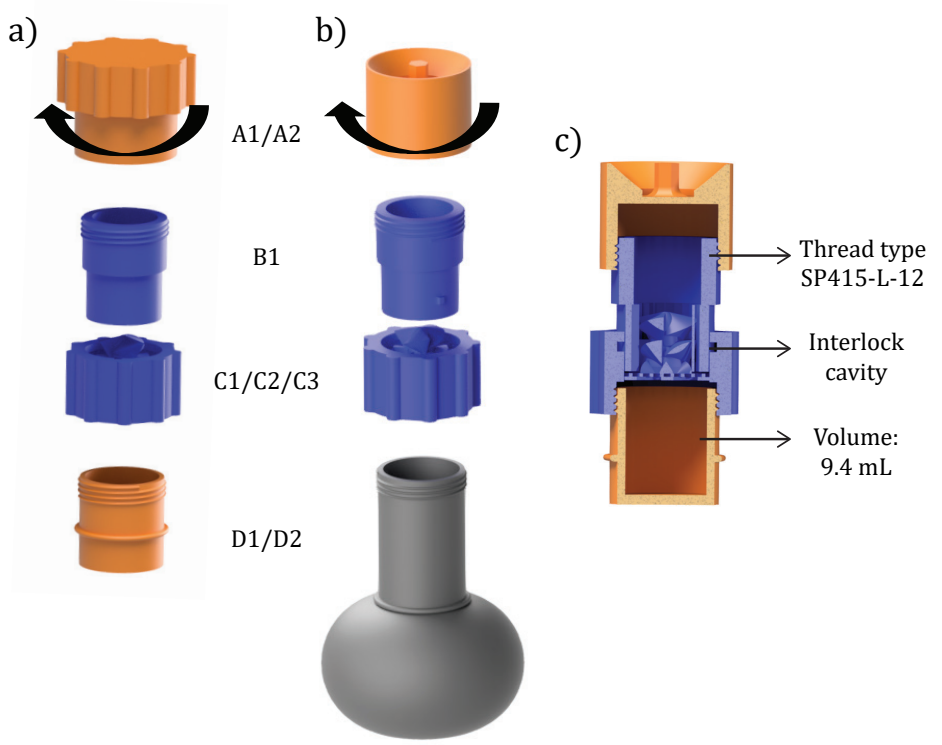


Figure 2.1: *Schematic overview of different configurations of the interconnectable 3D-printed prototype that was developed and investigated during this study. a) (From top to bottom) cap for manual turning of the grinder (A1), grinding compartment with teeth (B1), grinding blades and integrated sieves (3 different sizes; C1/C2/C3) for retention of large particles of unground material, and a collection chamber (D1). b) (From top to bottom) cap for automatic grinding by attaching a battery powered hand drill (A2), grinding compartment with teeth (B1), grinding blades with integrated sieves (different sizes; C1/C2/C3), and collection chamber in which the extraction process can be carried out by addition of extraction solvent (D2). c) Cross-sectional view of parts A2/B1/C1/D1 that are threaded and interlocked.*

2.3.1 Design & development of the 3D-printed prototype

As shown in Fig. 2.1, the device consists of 4 modular parts, namely: (A) a cap for manual grinding (A1) or as interface for a battery powered hand drill (A2) (see Fig. 2.2); (B1) a grinding compartment with teeth; (C) a set of grinding blades on an integrated sieve for particle retention in 3 variations C1, C2, C3, corresponding to mesh sizes of 10 (2 mm), 20 (0.8 mm) and 30 (0.6 mm), respectively; (D) a collection chamber for ground material, to be used with external extraction (D1) or integrated extraction (D2). The prototype was designed for clockwise rotation.

The prototype was improved during several rounds of redesign and optimization, which included: (i) the addition of standard type threads (SP415-L-12) to create a closed system that aids user-safety, (ii) an interlock between grinding parts B and C to ensure robustness, (iii) geared grips for parts C and A1 enabling more ergonomic device handling thus promoting better user experience, and (iv) color-coding of the parts to simplify user instructions. Furthermore, a universal drill extension (A2) was developed to automatically grind intact wheat. Fig. 2.2 shows a photograph of the printed components A2/B1/C1/D1, as schematically depicted in Fig. 2.1c.



Figure 2.2: *Photograph of the 3D-printed prototype connected to a battery powered hand drill for automatic grinding (Fig. 2.1c).*

The choice of parts C and D depends on user preferences. The collection chamber D1 should be chosen when the user solely wants to collect the ground material before an external extraction method. On the other hand, the extraction chamber D2 can be used to adapt the prototype to an existing workflow, for example with a commercially available LFD kit. The choice between C1/C2/C3 depends on the particle size and distribution the user wishes to obtain; the smaller the sieve size, the smaller the particles that reach the collection chamber (D1/D2). Finally, the choice of lid part A1/A2 depends on whether the user wishes to implement a drill for automated grinding. Additionally, part A1 and A2 fit onto part D2, which means that they can also function as a lid for the extraction chamber. The prototype was designed to be disposable, and thus cross-contamination between samples is eliminated. An in-depth discussion regarding the sustainability and costs of 3D-printing with repsect to the prototype was included in the SI Section S2.1.

2.3.2 Prototype performance assessment

2.3.2.1 Grinding efficiency

In Fig. 2.3, grinding efficiency is presented as a function of the sieve mesh size. Different sieve meshes 10 (2 mm), 20 (0.8 mm), and 30 (0.6 mm) were used in parts C1, C2 and C3 (see Fig. 2.3a), respectively. These three parts were compared in terms of grinding efficiency (weight in g of ground material/minute), using the drill extension (part A2, see Fig. 2.2). A larger pore size resulted in more ground material collected per minute (see Fig. 2.3b). Part C1 and C2 showed a proportional increase in the amount of collected material over time, whereas part C3, which has the smallest pore size, showed a decrease in the amount of material obtained per unit time, potentially due to clogging of the pores after approximately 10 min.

Considering the amount of ground material needed for the commercial LFD kit (10 g) and the confirmatory LC-MS/MS procedure (5 g), part C1 in configuration A2/B1/C1/D1 was selected for subsequent studies. Using one prototype with this selected configuration, up to 75.0 g of wheat could be ground in 34 min showing the durability of the prototype. On average, the experienced operator was able to grind 4.09 g with an RSD of 21% in 2 min (SI, Table S2.2). Lastly, this configuration was subjected to the first-time user trials. Here, 10 different first-time users over an age range of 21–66 years tested the prototype for 30 s with minimal instructions. This test resulted in an average of 1.37 g/30 s with an RSD of 38% (SI, Table S2.3). After extrapolation of the data, the experienced operator achieved an estimated amount of 2.05 g/min and the first-time users an estimated amount of 2.74 g/min, showing the robustness of the prototype.

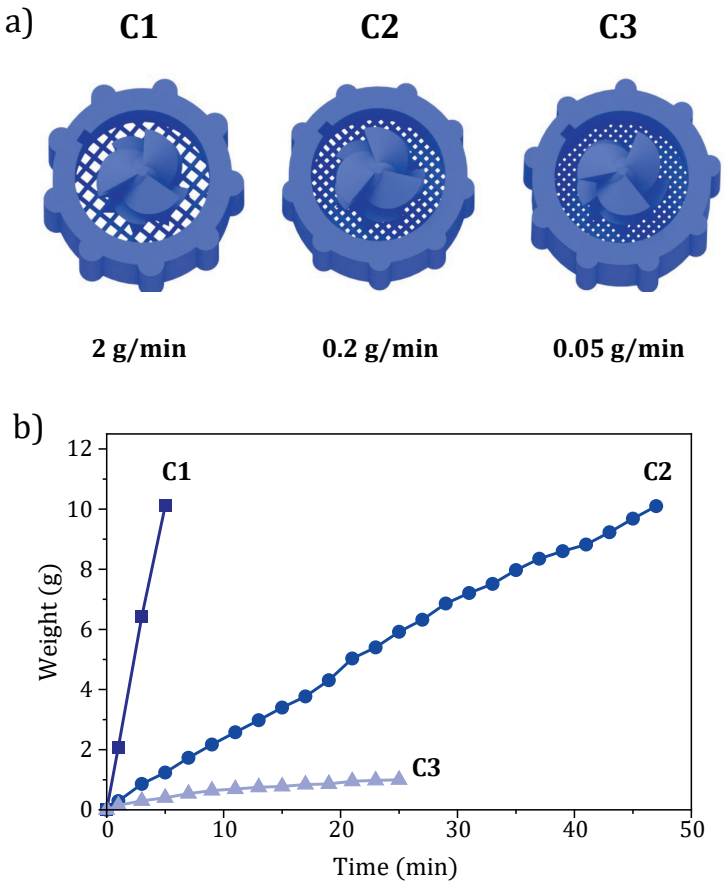


Figure 2.3: *a) 3D-models (top view) of the C1, C2 and C3 parts, which incorporate sieves with mesh 10 (2 mm), 20 (0.8 mm), and 30 (0.6 mm) sizes, respectively. b) the amount of ground material from intact wheat for each of the parts is plotted against time used for automatic grinding with the hand drill (Top part A2, Figure 2.1).*

2.3.2.2 Particle size distribution (PSD)

After sieve mesh 10 (part C1) was selected for subsequent testing, based on its grinding efficiency, the PSD and its reproducibility were evaluated. This was assessed by using an analytical sieve shaker, that incorporates a series of increasingly smaller sieve meshes from top to bottom, and by weighing each material fraction after acceleration. Collected material can thus be classified based on the pore size between two sieve meshes. The results are expressed in weight fraction of the total sample from the laboratory mill and the prototype. Fig. 2.4 demonstrates that the largest amount of particles ground by the prototype fall within the range of 1250–2000 µm, which is in agreement with the used prototype pore size of 2000 µm (mesh 10, 2 mm). This range can be lowered using prototype part C2 (mesh 20; 0.8 mm) or C3 (mesh 30; 0.6 mm), albeit at the expense of grinding efficiency. The largest

number of particles from the laboratory mill fall within the range of 1000–1250 µm. Moreover, the laboratory mill produces smaller particles compared to the prototype (SI, Fig. S2.5), which affects the extraction efficiency [25,39]. All the prototype parts were printed over the course of 14 days and all material was ground by a total of three people. Therefore, the RSD in Fig. 2.4 (on the particle size distribution) includes multiple prototypes (>10 prototypes) and operators (3 persons).

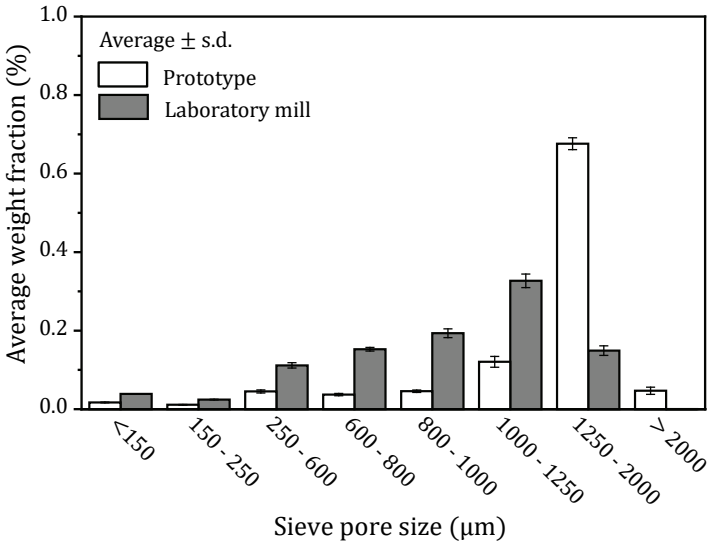


Figure 2.4: *Particle size distribution of the ground wheat from the 3D-printed prototype and the laboratory mill. The average and error bars represent n = 3 separately ground sample batches from both the laboratory mill and the prototype.*

2.3.2.3 Extraction efficiency

The relation between the extraction efficiency and the particle size obtained through the different prototype sieving parts (C1/C2/C3) was investigated. The material obtained by using these devices was analyzed by the LC-MS/MS procedure and compared to material ground with the laboratory mill. In SI Figure S2.6, the results show that there was no significant difference between the laboratory mill and the protoype with sieving part C1 (mesh 10; 2 mm). This result was slightly different than the data shown in Fig. 2.5a, where the LC-MS/MS data (dark grey boxes) shows a significant difference between the prototype (C1) and laboratory mill. This difference is explained by the different sample sizes and repeats, which was 1 g (n = 3) for Figs. S2.6 and 5 g (n = 9) for Fig. 2.5a. The reason for this is the sampling error that is introduced when taking only 1 g and three repeats. However, Fig. S2.6 still shows a lower median value for the prototype compared to the laboratory mill, suggesting that the trend is similar to what was observed in Fig. 2.5a.

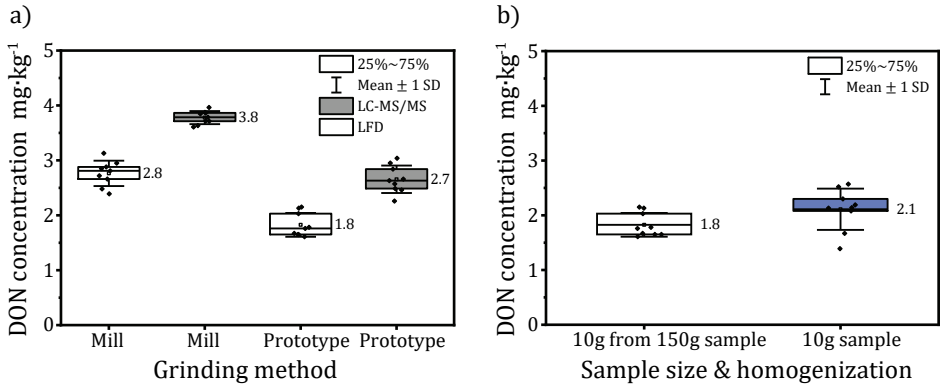


Figure 2.5: *a) 150 g of intact wheat kernels were ground by either the laboratory mill or the prototype and aliquots of ground material were analyzed via either LFD (9 × 10 g) or LC-MS/MS (9 × 5 g) workflows. b) Individual and unmixed aliquots of 10 g were sampled and processed with the prototype grinder (n = 9) for analysis via LFD and compared to 10 g aliquots from 150 g of ground wheat (n = 9).*

In Fig. S2.6, the data related to part C1 of the prototype (3.131 ± 0.809 mg·kg^{-1} DON) showed a larger RSD (25.8% vs 7.1%) when compared to the laboratory mill (3.567 ± 0.254 mg·kg^{-1} DON). By grinding the same material from the prototype configuration with part C1 a second time (3.324 ± 0.443 mg·kg^{-1} DON), the RSD was reduced from 25.8% to 13.3%. However, the improved RSD was as at the expense of time, as well as of an increased amount of sample handling steps.

Furthermore, the data related to part C2 of the prototype with a mesh size of 20 (0.8 mm) resulted in 5.260 ± 0.332 mg·kg^{-1} DON and an RSD of 6.3%. The data related to part C3 of the prototype with a mesh size of 30 (0.6 mm) resulted in 6.687 ± 0.393 mg·kg^{-1} DON and an RSD of 5.9%. The results suggest that the extraction efficiency improved because of the smaller particle sizes that were obtained through the increasingly smaller sieve size of part C. Moreover, both the material obtained from part C2 and C3 showed a better extraction efficiency when compared to the laboratory mill.

Following the result of the grinding efficiency, the selected prototype sieving part for pairing with an LFD for screening DON in wheat was C1, since this part was able to grind the needed amount for the LFD procedure within 5 min. This prototype configuration was benchmarked against the laboratory mill and the LC-MS/MS procedure (Fig. 2.5). The extraction times for the LFD and LC-MS/MS procedure were substantially different, since the LFD procedure only requires a 2-min extraction while the LC-MS/MS procedure requires 90 min, which might explain the difference between obtained results with the two methods from the same exact ground material (either by laboratory mill or prototype grinder). It is

also important to emphasize the different nature of both analytical approaches, with the LFD being designed for immuno-based screening purposes, and the LC-MS/MS for confirmatory analysis. Importantly, when using the prototype for both analysis methods, the contaminated samples could be correctly flagged as suspect according to EU regulations [30,52]. In addition to the difference between the LFD and LC-MS/MS methods, there is also a different amount of DON recovered from the wheat ground by either the lab mill or the 3D-printed prototype plus hand drill, with the latter resulting in lower measured concentrations. This difference can be explained by the difference in particle sizes as shown in Fig. 2.4 and Fig. S2.6. It is well-known that extraction efficiency is improved by reducing the particle size, leading to an increased total surface area available for extraction [25,39].

Finally, Fig. 2.5a demonstrates that by using the prototype the overall error of the LFD and the LC-MS/MS methods does not increase significantly, as the two-sample F-test for variance returned an F-value of 1.226 ($\alpha = 0.05$) against 3.438 of the corresponding F-table. Therefore, with appropriate calibration or correction for a difference in particle size, reliable analysis of DON in wheat can be carried out using the prototype as sample processing unit.

2.3.2.4 Influence of sample size & homogenization

Next, the influence of sampling size and homogenization of the prototype for portable screening methods were evaluated with 3.0 $mg \cdot kg^{-1}$ contaminated wheat. To assess such effects, a comparison was made between $n = 9$ analyses of individual and unmixed aliquots of 10 g, versus $n = 9$ of 10 g aliquots taken from a homogenized lot (Fig. 2.5b). The sample averages were not significantly different when comparing the individually ground and sampled aliquots with the material from the larger batch of 150 g. However, it can be observed that the distribution of the individually sampled 10 g experiment is larger. This can be attributed to the increased homogenization effect when sampling and grinding a larger amount of wheat, which is in good accordance with the scientific literature [25,39].

Within this study the implementation of the prototype in combination with an extraction chamber (part D2) was evaluated, to tailor the prototype to the used LFD kit. The extraction chamber was interconnected with the same type of threads to mesh C1. Thereafter, the naturally contaminated intact wheat (~3.0 $mg \cdot kg^{-1}$) was ground until 10 g were obtained in the extraction chamber. From this point, the LFD kit procedure steps, up until the dilution in running buffer, were performed using the 3D-printed prototype. In short, the extraction of the ground material was carried out by adding an extraction buffer bag and 50 mL of ultrapure water to extraction chamber part D2, which was manually shaken for 2 min, using lid part A1. Thereafter, the sample was allowed to settle for 1 min, a standard filter bag for tea was inserted,

and subsequently 100 µL of extract was transferred for dilution with 1000 µL of dilution buffer. The diluted extract was centrifuged for 30 s at 6000 rpm, and 100 µL of supernatant was pipetted into a cartridge containing the LFD, which was inserted into the batch-calibrated reader.

This integrated grinding and extraction prototype was then used to process the intact wheat kernels, and could achieve results in the same range as the LFD kit procedure (Fig. 2.6a), as no significant difference (t-test, $p>0.05$) was found between LFD and prototype extraction.

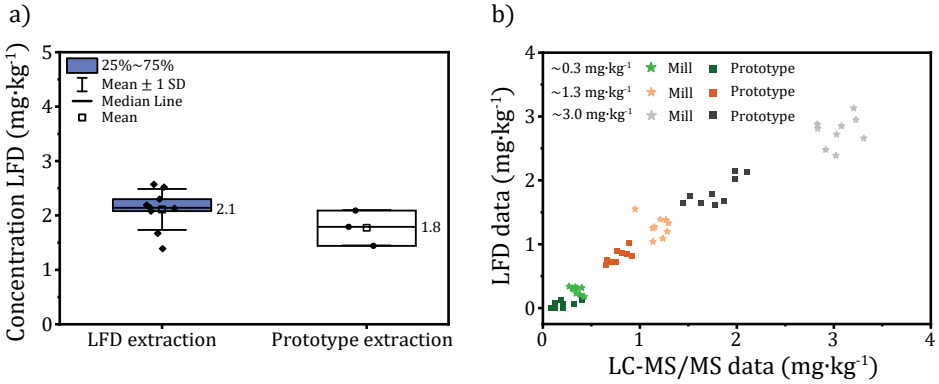


Figure 2.6: *a) comparison between prototype grinding prior to LFD kit procedure and the fully integrated prototype including extraction. b) uncontaminated wheat, and wheat containing DON above ML (~3.0 mg·kg^{-1}) were mixed to obtain batches at two additional levels below ML (~0.3 mg·kg^{-1}) and at ML (~1.3 mg·kg^{-1}). 150 g of wheat kernels from each contamination level were ground either by prototype (square symbols) or by laboratory mill (star symbols). Ground material was extracted via the LFD procedure and these extracts were analyzed by LFD and confirmed by LC-MS/MS. The correlation between concentrations determined via both approaches is plotted.*

2.3.2.5 Screening DON at the maximum level

Previous tests were performed with material that was contaminated above the ML in unprocessed wheat (3.0 mg·kg^{-1}). In order to demonstrate the performance of the developed workflow at and below ML, additional experiments were carried out. The prototype (parts A2/B1/C1/D1) was benchmarked against the laboratory mill at three different contamination levels; extracts of these materials were analyzed by the LFD procedure and confirmed by LC-MS/MS (SI, Table S2.4). This resulted in a clear correlation ($R^2 = 0.96$) between the LFD and the LC-MS/MS data for all samples (Fig. 2.6b). Moreover, the laboratory mill data points were distributed around the contamination levels below, at and above the ML. For the prototype data, an underestimation of the contamination level was observed. While only 60% of the actual content could be recovered after grinding with the prototype, this percentage

has been consistent within and between the different contamination levels. This underestimation can again be explained by the larger particle size obtained with the prototype compared to the mill, which decreases the extraction efficiency. Still, the contamination levels above and below the ML were correctly identified as suspect or compliant, respectively. It is important to consider that the entire LFD kit procedure is calibrated using certified reference material (CRM), which consists of particle sizes that were sieved with a mesh 30 (0.6 mm) using a dedicated laboratory mill. In this regard, the particle size used for calibration of the screening procedure should be in the same range as that of the envisioned grinding method, be it a laboratory mill or a prototype such as the one developed in this work. It is therefore reasonable that if appropriate calibration would be carried out for the developed prototype, such discrepancies will be avoided.

This raises a critical issue in general: when the particle size rendered by the used grinding method has such a significant effect on the final result, then it is necessary to calibrate the screening method with particle sizes in the range as they are generated by the end-user. As explained above, this is true for the prototype reported here, but essentially for any end-user of a commercial kit that relies on pre-ground material.

2.4 Conclusions

The reported 3D-printed prototype allows for novel integration of critical sample work-up procedures including sampling, grinding of intact wheat, and extraction of a target mycotoxin in one portable device. The real-life applicability of this prototype was demonstrated using naturally contaminated wheat kernels at concentration levels below, at and above the EU regulatory limit for DON in unprocessed wheat intended for human consumption (1.25 $mg \cdot kg^{-1}$, < 2024). The prototype was benchmarked against a laboratory mill and DON concentrations were determined using a commercial LFD screening kit with on-site applicability and an LC-MS/MS method for confirmation. The ideal configuration for on-site screening purposes was obtained using sieve mesh 10 (2 mm), which allowed the grinding of 10 g of wheat within 5 min. We found that the particle size range of the envisioned grinder device should be considered for the calibration of the on-site screening method, ideally in a standardized approach.

The presented 3D-printed prototype is inexpensive, with current material costs of 2.5€, a total printing time of 10 h and design files that can be distributed virtually. Anyone with access to an FDM printer should be able to print the exact same designs as used in this work, supporting open-science practices. The printer settings can be optimized towards printing speed in order to decrease the total printing time. The overall costs can be decreased when upscaling the manufacturing, which could be achieved by decentralized manufacturing and upcycling of plastic waste. Additionally, costs could be decreased by further optimizing the grinding and extraction parts.

The next steps to enhance the technological readiness level of this 3D-printed prototype, which is currently in between levels 3 and 4, are validation and demonstration in a relevant environment. Due to the interconnected modules, and exclusive use of aqueous solvent, contamination of other samples or operators during these steps as well as other safety risks are minimalized. Therefore, the developed prototype is affordable, accessible, and integrated for portable sample preparation of intact wheat for the detection of DON, with the potential to be applied for other hard food commodities and target mycotoxins.

Acknowledgements

The authors like to thank prof. dr. Michel Nielen and prof. dr. Hans-Gerd Janssen for the useful discussions, Hannes Gratzl for his assistance during LC-MS/MS analysis and dr. Marc Lemmens from the Institute of Biotechnology in Plant Production (BOKU) for providing the wheat material. The rapid screening kit and reader were kindly provided by our consortium partner Romer Labs. We would like to thank dr. Luis Miguel Fidalgo and dr. Barbara Cvak from Romer Labs for the training on their products.

References

1. Pitt, J. I. & Miller, J. D. A concise history of mycotoxin research. J. Agric. Food Chem. 65, 7021–7033 (2017). https://doi.org/10.1021/acs.jafc.6b04494
2. Alshannaq, A. & Yu, J.-H. Occurrence, toxicity, and analysis of major mycotoxins in food. Int. J. Environ. Res. Public Health 14, 632 (2017). https://doi.org/10.3390/ijerph14060632
3. Pinotti, L., Ottoboni, M., Giromini, C., Dell'Orto, V. & Cheli, F. Mycotoxin contamination in the EU feed supply chain: a focus on cereal byproducts. Toxins 8, 45 (2016). https://doi.org/10.3390/toxins8020045
4. Hussein, H. S. & Brasel, J. M. Toxicity, metabolism, and impact of mycotoxins on humans and animals. Toxicology 167, 101–134 (2001). https://doi.org/10.1016/S0300-483X(01)00471-1
5. Koppen, R. et al. Determination of mycotoxins in foods: current state of analytical methods and limitations. Appl. Microbiol. Biotechnol. 86, 1595–1612 (2010). https://doi.org/10.1007/s00253-010-2535-1
6. van der Fels-Klerx, H. J. et al. Decision support system for integrated management of mycotoxins in feed and food supply chains. World Mycotoxin J. 15, 119–133 (2022). https://doi.org/10.3920/wmj2020.2603
7. Ran, R., Wang, C., Han, Z., Wu, A., Zhang, D. & Shi, J. Determination of deoxynivalenol and its derivatives: current status of analytical methods. Food Control 34, 138–148 (2013). https://doi.org/10.1016/j.foodcont.2013.04.026
8. Ojuri, O. T. et al. Mycotoxicological risk from consumption of complementary foods by infants and young children in Nigeria. Food Chem. Toxicol. 121, 37–50 (2018). https://doi.org/10.1016/j.fct.2018.08.025
9. Logrieco, A. F. et al. The mycotox charter: increasing awareness and action for minimizing mycotoxin exposure worldwide. Toxins 10, 149 (2018). https://doi.org/10.3390/toxins10040149
10. Eskola, M. et al. Worldwide contamination of food crops with mycotoxins: validity of the FAO estimate of 25%. Crit. Rev. Food Sci. Nutr. 60, 2773–2789 (2020). https://doi.org/10.1080/10408398.2019.1658570
11. Moretti, A., Pascale, M. & Logrieco, A. F. Mycotoxin risks under climate change in Europe. Trends Food Sci. Technol. 84, 38–40 (2019). https://doi.org/10.1016/j.tifs.2018.03.008
12. Eskola, M., Elliott, C. T., Hajslova, J., Steiner, D. & Krska, R. Chronic health risks from chemicals in food: a dietary exposome update. Crit. Rev. Food Sci. Nutr. 60, 1890–1911 (2020). https://doi.org/10.1080/10408398.2019.1612320
13. Gruber-Dorninger, C., Jenkins, T. & Schatzmayr, G. Global mycotoxin occurrence in feed: a ten-year survey. Toxins 11, 375 (2019). https://doi.org/10.3390/TOXINS11070375
14. EFSA. Deoxynivalenol in food and feed: occurrence and exposure. EFSA J. 11, 3379 (2013). https://doi.org/10.2903/j.efsa.2013.3379
15. Eskola, M., Altieri, A. & Galobart, J. Activities of EFSA on mycotoxins in food and feed. World

Mycotoxin J. 11, 277–289 (2018). https://doi.org/10.3920/WMJ2017.2270
16. van der Fels-Klerx, H. J., Liu, C. & Battilani, P. Modelling climate change impacts on mycotoxin contamination. World Mycotoxin J. 9, 717–726 (2016). https://doi.org/10.3920/WMJ2016.2066
17. Johns, L. E., Bebber, D. P., Gurr, S. J. & Brown, N. A. Emerging health threat of Fusarium mycotoxins in European wheat. Nat. Food 3, (2022). https://doi.org/10.1038/s43016-022-00655-z
18. Malachova, A. et al. LC–MS-based methods for co-occurring mycotoxins in cereals. Anal. Bioanal. Chem. 410, 801–825 (2018). https://doi.org/10.1007/s00216-017-0750-7
19. Sforza, S., Dall'asta, C. & Marchelli, R. Hyphenated chromatography–mass spectrometry for mycotoxins. Mass Spectrom. Rev. 25, 54–76 (2006). https://doi.org/10.1002/mas.20052
20. Mohamed, R. & Guy, P. A. Role of mass spectrometry in detecting chemical contaminants in foods. Mass Spectrom. Rev. 30, 1073–1095 (2011). https://doi.org/10.1002/mas.20314
21. Sulyok, M., Stadler, D., Steiner, D. & Krska, R. Validation of LC-MS/MS dilute-and-shoot for >500 mycotoxins. Anal. Bioanal. Chem. 412, 2607–2620 (2020). https://doi.org/10.1007/s00216-020-02489-9
22. De Santis, B. et al. LC–MS/MS method for multi-mycotoxin determination in cereals. Toxins 9, 169 (2017). https://doi.org/10.3390/toxins9050169
23. Nolan, P., Auer, S., Spehar, A., Elliott, C. T. & Campbell, K. Trends in rapid mycotoxin tests. Food Addit. Contam. 36, 800–814 (2019). https://doi.org/10.1080/19440049.2019.1595171
24. Whitaker, T. B. Detecting mycotoxins in agricultural commodities. Mol. Biotechnol. 23, 61–71 (2003). https://doi.org/10.1385/MB:23:1:61
25. Spanjer, M. C. et al. Sample comminution for mycotoxin analysis: dry milling vs slurry mixing. Food Addit. Contam. 23, 73–83 (2006). https://doi.org/10.1080/02652030500260439
26. Tsagkaris, A. S. et al. Screening and confirmatory methods for food contaminants and allergens. TrAC Trends Anal. Chem. 121, 115688 (2019). https://doi.org/10.1016/j.trac.2019.115688
27. Jafari, S. et al. ASSURED point-of-need food safety screening. Foods 10, 1399 (2021). https://doi.org/10.3390/foods10061399
28. Griesche, C. & Baeumner, A. J. Biosensors for sustainable agriculture and food safety. TrAC Trends Anal. Chem. 128, 115906 (2020). https://doi.org/10.1016/j.trac.2020.115906
29. Patabadige, D. E. W. et al. Micro total analysis systems: advances and applications. Anal. Chem. 88, 320–338 (2016). https://doi.org/10.1021/acs.analchem.5b04310
30. Lattanzio, V. M. T., Ciasca, B., Powers, S. & von Holst, C. Validation of screening methods: DON in wheat by lateral flow immunoassay. TrAC Trends Anal. Chem. 76, 137–144 (2016). https://doi.org/10.1016/j.trac.2015.10.009
31. The European Commission. Commission Regulation (EU) No 519/2014. Sampling methods for large lots, spices and food supplements and screening performance criteria. (2014). http://data.europa.eu/eli/reg/2014/519/oj
32. AOAC INTERNATIONAL. Guidelines for validation of qualitative binary methods. J. AOAC Int. 97, 1492–1495 (2014). https://doi.org/10.5740/jaoacint.BinaryGuidelines
33. Romer Labs. Mycotoxin test kits. https://www.romerlabs.com/en/products/test-kits/mycotoxin-st-kits/ (accessed 03 Dec 2022)
34. R-Biopharm. Mycotoxin detection tests. https://food.r-biopharm.com/analytes/mycotoxins/ (accessed 03 Dec 2022)
35. FOSS. MycoFoss™ automated mycotoxin testing. https://www.fossanalytics.com/en/products/mycofoss (accessed 03 Dec 2022)
36. Tittlemier, S. A. et al. Developments in mycotoxin analysis: update 2020–2021. World Mycotoxin J. 15, 3–25 (2022). https://doi.org/10.3920/WMJ2021.2752
37. Kumphanda, J., Matumba, L., Monjerezi, M., Whitaker, T. B., De Saeger, S. & Makun, H. A. Sample size and preparation for mycotoxin quantitation. Food Control 130, 108400 (2021). https://doi.org/10.1016/j.foodcont.2021.108400

38. Champeil, A., Fourbet, J.-F. & Doré, T. Effects of grain sampling procedures on Fusarium mycotoxin assays. (2004). https://pubs.acs.org/doi/pdf/10.1021/jf049374s (accessed 03 Dec 2022)
39. Kos, G., Lohninger, H., Mizaikoff, B. & Krska, R. Optimisation of sample preparation for DON assessment in maize using MIR ATR spectroscopy. Food Addit. Contam. 24, 721–729 (2007). https://doi.org/10.1080/02652030601186111
40. Whitaker, T. B. Sampling foods for mycotoxins. Food Addit. Contam. 23, 50–61 (2006). https://doi.org/10.1080/02652030500241587
41. Salentijn, G. I. J., Oomen, P. E., Grajewski, M. & Verpoorte, E. FDM 3D printing for analytical devices. Anal. Chem. 89, 7053–7061 (2017). https://doi.org/10.1021/acs.analchem.7b00828
42. Zhang, Y., Ge, S. & Yu, J. Lab-on-a-chip analysis using 3D-printed platforms. TrAC Trends Anal. Chem. 85, 166–180 (2016). https://doi.org/10.1016/j.trac.2016.09.008
43. Ho, C. M. B., Ng, S. H., Li, K. H. H. & Yoon, Y.-J. 3D-printed microfluidics for biological applications. Lab Chip 15, 3627–3637 (2015). https://doi.org/10.1039/C5LC00685F
44. Capel, A. J., Rimington, R. P., Lewis, M. P. & Christie, S. D. R. 3D printing for chemical, pharmaceutical and biological applications. Nat. Rev. Chem. 2, (2018). https://doi.org/10.1038/s41570-018-0058-y
45. Kabandana, G. K. M., Zhang, T. & Chen, C. Emerging 3D printing technologies for microfluidics. Anal. Methods 14, 2885–2906 (2022). https://doi.org/10.1039/d2ay00798c
46. Agrawaal, H. & Thompson, J. E. Additive manufacturing for analytical chemistry. Talanta Open 3, 100036 (2021). https://doi.org/10.1016/j.talo.2021.100036
47. Comina, G., Suska, A. & Filippini, D. PDMS lab-on-a-chip fabrication using 3D-printed templates. Lab Chip 14, 424–430 (2013). https://doi.org/10.1039/C3LC50956G
48. Ross, G. M. S., Filippini, D. & Nielen, M. W. F., Salentijn, G. I. J. Chip-based dilution for multiplexed immunodiagnostics. Anal. Chim. Acta 1140, 190–198 (2020). https://doi.org/10.1016/j.aca.2020.10.018
49. Salentijn, G. I. J., Permentier, H. P. & Verpoorte, E. 3D-printed paper spray ionization cartridge. Anal. Chem. 86, 11657–11665 (2014). https://doi.org/10.1021/ac502785j
50. Zargaryan, A. et al. Hybrid 3D-printed paper microfluidics. Sci. Rep. 10, 18379 (2020). https://doi.org/10.1038/s41598-020-75489-5
51. Romer Labs. AgraStrip® Pro Deoxynivalenol WATEX®. https://www.romerlabs.com/shop/inter_en/agrastrip-pro-deoxynivalenol-watex/ (accessed 03 Dec 2022)
52. von Holst, C. & Stroka, J. Performance criteria for rapid screening methods for mycotoxins. World Mycotoxin J. 7, 439–447 (2014). https://doi.org/10.3920/WMJ2014.1710

Supplementary information to:

Interconnectable 3D-printed sample processing modules for portable mycotoxin screening of intact wheat

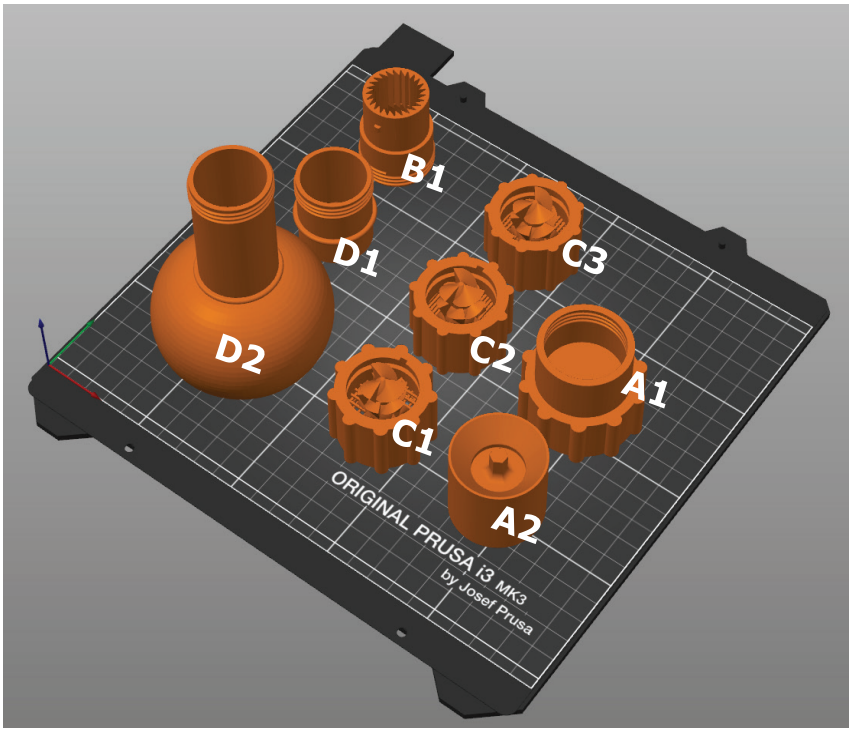


Figure S2.1: *Representation of all the parts in the Slicer software that can be downloaded from the repository with correct settings, ready to print with the Prusa Original MK3S+.*

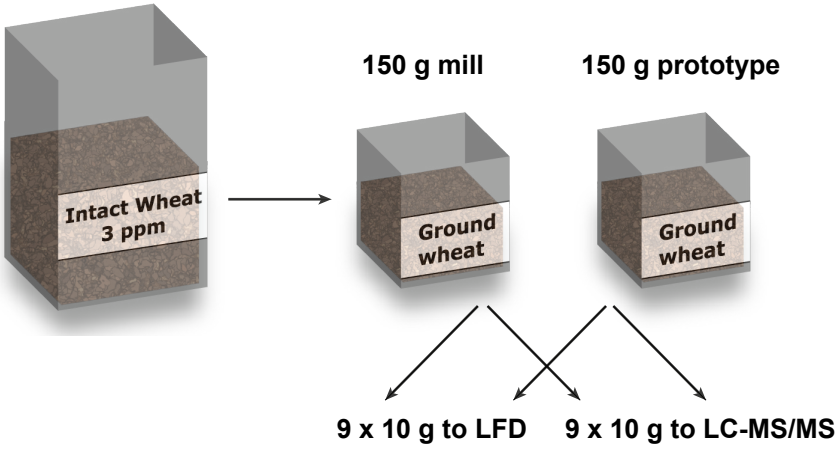


Figure S2.2: *Schematic representation of the sampling methodology for the extraction efficiency experiment. 150 g of intact wheat (3 ppm DON) were ground with both laboratory mill and the prototype, from which nine repetitions were performed for the LFD and LC-MS/MS procedure.*

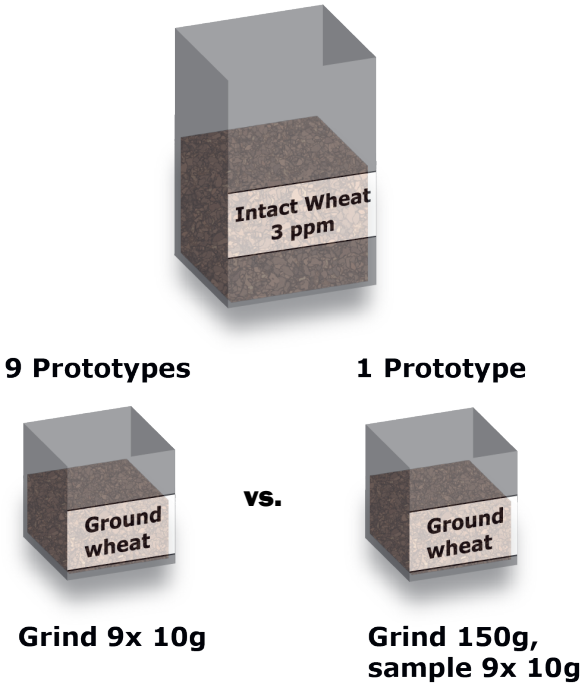


Figure S2.3: *Schematic representation of the sampling method for the sampling size & homogenization experiment. The direct sampling and grinding of 10 g of intact wheat was compared to previous results from 10 g sampled from a 150 g batch of ground wheat with the prototype.*

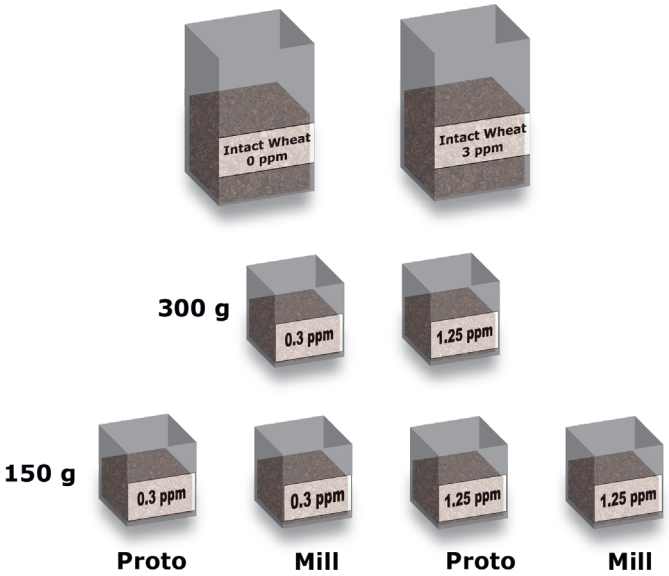


Figure S2.4: *Schematic representation of the sampling method for the screening of DON around the maximum level.*



Figure S2.5: *Visual representation of ground wheat particles from the laboratory mill (left) and prototype (right).*

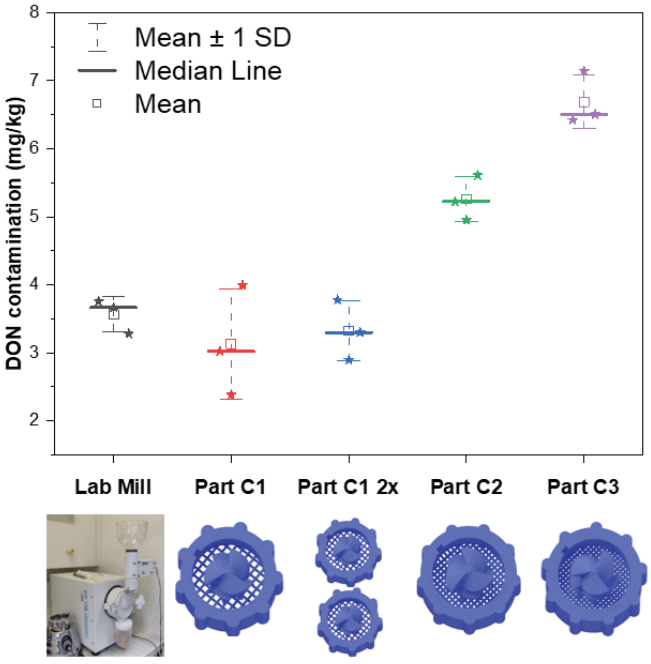


Figure S2.6: *Evaluation of the extraction efficiency comparing ground material obtained by prototype sieving parts (C1/C2/C3) and the laboratory mill. Three times 1 gram of ground material was sampled per sieve size and for the laboratory mill, followed by LC-MS/MS analysis. Note that material from part C1 was also subjected to another grinding round with the same sieve to investigate these effects (part C1 2x).*

Table S2.1: *Prusa Original i3 MK3S+ slicer settings used to print prototype parts.*

Settings	
Layer height	0.2 mm
Solid layers top	6
Solid layers top part A2	40
Solid layers bottom	4
Infill density	15 %
Infill pattern	Gyroid
Support	On built plate only
Filament	PLA
Filament diameter	1.75 mm
Perimenter print speed	45 mm/s
Infill print speed	80 mm/s
Supports print speed	50 mm/s
Bridges print speed	25 mm/s
Nozzle temperature first layer	215 °C
Nozzle temperature	210 °C
Bed temperature	60 °C
Filament cooling	Always on
Nozzle diameter	0.4 mm (standard)
Retraction	0.8 mm
Z-lift	Disabled

Table S2.2: *Consistency and repeatability of grinding using new prototype parts A2/B1/C1/D2 each time and operated by the same user.*

Prototype	**Grams/2 minutes**
1	2.98
2	3.61
3	3.40
4	3.88
5	4.25
6	3.46
7	5.60
8	5.05
9	4.58
Average (g) ± RSD (%)	**4.09 ± 21**

Table S2.3: *First-time user trials with prototype parts A2/B1/C1/D1 and the drill for automatic grinding.*

First-time user	**Age**	**Profession**	**Automatic grinder (grams/30sec.)**
1	31	Start-up manager	1.35
2	43	Coach & consultant	1.34
3	26	PDeng	2.16
4	29	PhD	1.06
5	55	Innovation manager	0.63
6	21	BSc student	1.89
7	66	Associate professor	2.05
8	26	Product manager	1.37
9	28	Truck driver	1.15
10	27	MSc student	0.70
		Average (g)± RSD (%)	**1.37 ± 38**

Table S2.4: *Data of the screening of DON around the ML (Figure 2.6b), showing the correlation between LFD and LC-MS/MS for both the laboratory mill and the prototype.*

Target level (mg/kg)	**LFD Prototype (mg/kg)**	**LC-MS/MS Prototype (mg/kg)**	**LFD Lab. mill (mg/kg)**	**LC-MS/MS Lab. mill (mg/kg)**
0.3	0.0	0.203	0.3	0.303
	0.1	0.186	0.2	0.381
	0.1	0.208	0.3	0.335
	0.1	0.401	0.2	0.426
	0.1	0.316	0.2	0.343
	0.1	0.124	0.3	0.349
	0.0	0.122	0.3	0.271
	0.0	0.127	0.3	0.400
	0.0	0.088	0.3	0.316
Average (mg/kg) ± RSD (%)	**0.1 ± 84**	**0.197 ± 52**	**0.3 ± 21**	**0.347 ± 14**
1.25	1.0	0.883	1.6	0.950
	0.8	0.660	1.4	1.269
	0.7	0.712	1.3	1.151
	0.8	0.862	1.2	1.283
	0.9	0.764	1.3	1.294
	0.8	0.923	1.4	1.212
	0.7	0.650	1.3	1.134
	0.7	0.758	1.0	1.136
	0.9	0.818	1.1	1.236
Average (mg/kg) ± RSD (%)	**0.8 ± 13**	**0.781 ± 12**	**1.3 ± 12**	**1.185 ± 9**
3.0	1.6	1.775	2.5	2.916
	1.7	1.627	2.9	2.831
	1.7	1.443	3.1	3.205
	2.2	1.980	3.0	3.228
	1.8	1.514	2.7	3.029
	1.8	1.746	2.8	2.834
	2.1	2.100	2.7	3.309
	1.7	1.865	2.9	3.079
	2.0	1.978	2.4	3.021
Average (mg/kg) ± RSD (%)	**1.8 ± 12**	**1.780 ± 13**	**2.8 ± 8**	**3.050 ± 6**

Section S2.1: Sustainability and costs of 3D-printing

Currently, 3D-printing technologies, in particular FDM, are widely available and exploited in academia, industry and beyond. As the most common material group for FDM printing are thermoplastic polymers, efforts to make 3D-printing of such materials more sustainable are being made [1]. This consists of several aspects, the first being the type of filament. The developed prototype is currently fabricated with polylactic acid (PLA) filament, which is a common bioplastic sourced from biomass. Essentially, the prototype could be fabricated with any other type of material that is available as filament, such as polyhydroxyalkanoates (PHAs), which are bioplastics produced by fermentation processes and thus have a microbial origin. Therefore, both PLA and PHAs are considered green alternatives to petroleum-based plastics [2]. Moreover, plastic waste can be upcycled to 3D-printing filament with a recyclebot, which is an open-source plastic waste extruder, enabling a circular economy approach [1,3]. This addresses a pressing worldwide challenge, as most of the plastics that were produced until 2010 are being discarded (60%) instead of recycled (9%), and therefore accumulate in the natural environment and landfill [2]. Therefore, Cañado et al. have described the reuse of marine plastic waste as 3D printing filament to reduce environmental impact [1].

In terms of life cycle assessment (LCA), there are three important principles to describe the life cycle or footprint of a product. These are referred to as; cradle-to-grave, cradle-to-gate and, cradle-to-cradle. Ideally, end products should be cradle-to-cradle, which means they can be fully upcycled. However, often this is not the case for rapid screening devices, such as the commercial LFD in this manuscript, where potentially contaminated material is tested and the consumables of the test should be disposed of. Therefore, rapid screening devices are often considered cradle-to-grave. However, when the developed 3D-printed prototype is used prior to the commercial LFD and the result turns out to be non-contaminated, the prototype could either be reused or fully upcycled. When the result of the test states contaminated, it might be possible to first thoroughly clean the prototype parts after which they could be upcycled. However, for the latter a cross-contamination study is necessary to make sure the upcycled material is not introducing toxins to the new product or user.

Another important aspect to consider regarding the upcycling of plastics such as PLA for 3D-printing filament is the resulting thermal, physical and mechanical properties of the recycled filament. The reason for this is that recycling could change the properties of the resulting filament, and thereby change the applicability of the filament for a certain end product functionality [2]. With respect to the developed prototype, an important property that should be considered is the Shore Hardness, which should be comparable to the original PLA filament to maintain performance of the prototype.

Typically, plastic-based end products are mass manufactured in a centralized factory to reduce economic costs, yet not the environmental burden. One potential approach to reduce the environmental impact of plastic products is to decentralize manufacturing using consumer-grade 3D-printers [4–8]. This approach enables the manufacture of end products on the user's demand. Moreover, as 3D-printing allows for more complex structures and control over infill densities, product designs can be optimized to reduce the environmental impact. For example, in our work, part A2 of the prototype has a gradual infill pattern in order to optimize the amount of filament and time needed to print the part, and simultaneously maintain mechanical strength in the drill bit connection. Moreover, the complex geometries that are incorporated in the prototype to provide grinding and particle selection could not be obtained by conventional mass manufacturing techniques such as injection molding or hot embossing. Next to that, most 3D-printers allow for printing with various filament materials within the same part, which could be beneficial for optimizing environmental impact, as well as desired functionality.

Lastly, decentralizing manufacture through 3D-printing allows for the use of green energy sources such a photovoltaic sources to power the 3D-printer [4,9,10]. Thereby, the cumulative energy demand (CED), an important term in LCA analysis, can be reduced significantly compared to conventional mass manufacture [4,9]. Additional energy efficiency can be obtained by optimizing e.g. the nozzle and print bed temperatures, and printing time.

In Table S2.5, a summary of prototype parts, material consumption and costs based on the PLA filament [11,12] that was used are included. One grinding and extraction prototype for automatic grinding with the largest sieve mesh (parts A2/B1/C1/D2) consumed 37.7 m of PLA and costs €2.5. The current market price of the Original Prusa i3 MK3S+ that we used is €754,- with VAT (2023). However, a budget-friendly FDM 3D printer with similar functionalities such as the Ender-3 from Creality costs €169,- including VAT (2023).

The energy consumption of FDM 3D printers ($E_{printing}$) depends on several factors [13]; the heating energy required to transform the thermoplastic filament ($E_{heating}$) this includes the nozzle temperature and the print bed temperature, the energy consumed by all the motors of the printer (E_{motors}) which include the driver motors and the filament feeder motor, and the energy consumed by auxiliary components (E_{aux}) such as pre-heating of the filament, power of the cooling fans and the idle power consumption, as explained in Equation 2.1 [13].

$$E_{printing} = E_{heating} + E_{motors} + E_{aux} \qquad \textit{Equation 2.1}$$

The printing time affects these equation components the most and should therefore be minimalized per 3D-printed part. The average power consumption of the MK3S is 90 W and the current cost (2023) for energy in the Netherlands is €0.4 kW/h. Therefore, to print the grinding and extraction prototype (print time = ~10 hours) the estimated energy costs are €0.4. This is in line with the described energy consumption by Elbadawi et al., who also studied different printer settings and their influence on the energy consumption and carbon footprint [9].

Table S2.5: *Material consumption and costs per prototype part.*

Prototype part	**Material used (including supports)**	**Material costs (€) including support material**
 A1	PLA (7.2 m; 21.47 g)	0.47
 A2	PLA (6.7 m; 19.98 g)	0.44
 B1	PLA (4.51 m; 13.46 g)	0.30
 C1/C2/C3	PLA (Mesh 10: 5.47 m; 16.33 g; Mesh 20: 5.32 m; 15.87 g; Mesh 30: 5.51 m; 16.45 g)	Mesh 10: 0.36 Mesh 20: 0.35 Mesh 30: 0.36
 D1	PLA (4.24 m; 12.63 g)	0.28
 D2	PLA (21.02 m;62.70 g)	1.38

References

1. Cañado, N. et al. 3D printing to enable the reuse of marine plastic waste with reduced environmental impacts. J. Ind. Ecol. 26, 2092–2107 (2022). https://doi.org/10.1111/jiec.13302
2. Naser, A. Z., Deiab, I. & Darras, B. M. Poly(lactic acid) (PLA) and polyhydroxyalkanoates (PHAs) as green alternatives to petroleum-based plastics: a review. RSC Adv. 11, 17151–17196 (2021). https://doi.org/10.1039/D1RA02390J
3. Zhong, S. & Pearce, J. M. Tightening the loop on the circular economy: coupled distributed recycling and manufacturing with recyclebot and RepRap 3-D printing. Resour. Conserv. Recycl. 128, 48–58 (2018). https://doi.org/10.1016/j.resconrec.2017.09.023
4. Kreiger, M. & Pearce, J. M. Environmental life cycle analysis of distributed three-dimensional printing and conventional manufacturing of polymer products. ACS Sustain. Chem. Eng. 1, 1511–1519 (2013). https://doi.org/10.1021/sc400093k
5. Wittbrodt, B. T. et al. Life-cycle economic analysis of distributed manufacturing with open-source 3D printers. Mechatronics 23, 713–726 (2013). https://doi.org/10.1016/j.mechatronics.2013.06.002
6. Gwamuri, J., Wittbrodt, B. T., Anzalone, N. C. & Pearce, J. M. Distributed manufacturing of customizable 3D-printable self-adjustable glasses. Chall. Sustain. 2, 30 (2014). https://doi.org/10.12924/cis2014.02010030
7. King, D., Babasola, A., Rozario, J. & Pearce, J. Mobile open-source solar-powered 3-D printers for distributed manufacturing in off-grid communities. Chall. Sustain. 2, 18 (2014). https://doi.org/10.12924/cis2014.02010018
8. Pearce, J. et al. 3-D printing of open source appropriate technologies for sustainable development. Int. J. Sustain. Dev. 3, 17–29 (2010). https://doi.org/10.5539/jsd.v3n4p17
9. Elbadawi, M., Basit, A. W. & Gaisford, S. Energy consumption and carbon footprint of 3D printing in pharmaceutical manufacture. Int. J. Pharm. 639, 122926 (2023). https://doi.org/10.1016/j.ijpharm.2023.122926
10. Khan, K. Y., Gauchia, L. & Pearce, J. M. Self-sufficiency of 3-D printers using stand-alone photovoltaic systems. Renew. Wind Water Sol. 5, 5 (2018). https://doi.org/10.1186/s40807-018-0051-6
11. Castro-Aguirre, E., Iñiguez-Franco, F., Samsudin, H., Fang, X. & Auras, R. Poly(lactic acid): mass production, processing, industrial applications and end of life. Adv. Drug Deliv. Rev. 107, 333–366 (2016). https://doi.org/10.1016/j.addr.2016.03.010
12. Mikula, K. et al. 3D-printing filament as a second life of waste plastics: a review. Environ. Sci. Pollut. Res. 28, 12321–12333 (2021). https://doi.org/10.1007/s11356-020-10657-8
13. Peng, T. Energy modelling for FDM 3D printing from a life-cycle perspective. Int. J. Manuf. Res. 11, 1–15 (2017). https://doi.org/10.1504/IJMR.2017.10003722


3

Selective paper-enhanced infrared spectroscopy for molecular detection of deoxynivalenol in wheat

This chapter has been published as:
A.J. Bosman, G.M.S. Ross, S. Freitag, M. Sulyok, R. Krska, G.IJ. Salentijn, F.S. Ruggeri. Selective paper-enhanced infrared spectroscopy for molecular detection of deoxynivalenol in wheat. Food Chemistry. Volume 516. 2026. 149360. doi.org/10.1016/j.foodchem.2026.149360.

Abstract

Regulated mycotoxins are food contaminants, whose occurrence is causing economic and health concerns. To ensure food safety, selective and enhanced rapid screening of mycotoxins is of critical importance. Lateral flow immunoassays enable rapid screening of mycotoxins on-site; however, they do not identify and quantify the molecular features of the target analyte. To overcome this challenge, we demonstrate a proof-of-concept for an innovative Selective Paper-Enhanced InfraRed Spectroscopy (S-PEIRS) approach to enhance the sensitivity and selectivity of mid-infrared spectroscopy and allow molecular recognition of mycotoxins in food. Our methodology leverages immunochemistry and paper microfluidics to selectively hyper-concentrate the mycotoxin molecules on a paper-tip.

For the first time, we demonstrate by infrared analysis the direct molecular detection of the mycotoxin deoxynivalenol (DON) in contaminated wheat, in the range of the legal limit (1 $mg{\cdot}kg^{-1}$). These results show the general potential of paper-based IR methods in food safety, as an innovative tool allowing molecular identification of mycotoxins.

3.1 Introduction

Filamentous fungi of the genera *Aspergillus, Fusarium* and *Penicillium* are plant pathogens known to produce mycotoxins, which are a persistent economic and health threat [1–4]. In the last decade, mycotoxins were detected in up to 80% of the food crops, while ~20-25% of the materials sampled at the source contained mycotoxins above the maximum levels (MLs) stipulated by European Union (EU) legislation [2,4–6].

Wheat is an important agricultural crop in Europe but often contaminated with the mycotoxin deoxynivalenol (DON), as a result of Fusarium head blight (FHB) [4]. A study of mycotoxin contamination in the period between 2010-2019 showed that DON was detected in food and feed wheat from all European countries [4]. During this period, an estimated 75 million tonnes of wheat exceeded the legal limit for direct human consumption, which was then downgraded to feed and led to approximately €3 billion of economic loss [4].

Since 2024, the ML for DON in unprocessed cereals has been set by the EU at 1 $mg \cdot kg^{-1}$ [6]. The strict regulations for DON in combination with its high occurrence in cereals require careful food safety monitoring [4,7]. In a recent evaluation of mycotoxin analysis, the demand of different stakeholders along the EU food supply chain has been mapped. The study has demonstrated that a key requirement of stakeholders from agriculture and food processing sectors is a detection tool for on-site analysis with low complexity [8]. While the accurate detection of DON at the EU ML in highly specialized laboratories has been achieved [9–11], the reliable on-site detection of DON remains challenging [12,13].

Currently, on-site detection of DON mainly relies on lateral flow immunoassays (LFIAs), in which user-friendly sample preparation can be achieved with dedicated hardware [14]. The result from an LFIA is typically semi-quantified via optical read-out [15–18]. Numerous LFIA formats for DON have been described that utilize optical labels, such as nanoparticles [19–21], luminescent quantum dots (QDs) [22,23], and metal-organic frameworks (MOFs) [24]. While all these LFIA formats could detect DON at levels below 1 $mg \cdot kg^{-1}$, a key limitation arises from the use of optical labels. Optical read-out does not provide direct molecular identification or quantification of the target analyte, but of the presence of an interaction with an antibody. While highly selective towards the target analyte, the antibodies can cross-react with other mycotoxins or derivatives, which might lead to overestimation of the contamination (false positives) [11,25–28]. Ultimately, on-site detection methods should be able to detect the molecular features of the target analyte; thus, decreasing the chance of overestimation and confirming the presence of the target analyte based on molecular identification.

To achieve molecular identification of analytes in food, it is hypothesized that

infrared (IR) spectroscopy can be employed for the label-free detection of specific molecular features. IR has enabled rapid and environment-friendly analysis of (raw) food materials, and is used to assess the condition of food and feed throughout the supply chain [29,30]. Attenuated Total Reflection Fourier Transform Infrared (ATR-FTIR) spectroscopy is the most widely implemented mid-IR technique [31], as it offers simple sample handling, good sensitivity (1×10^{-4} a.u.) and spectral resolution (<4 cm^{-1}), and relatively small instruments are available [32–36]. However, for mycotoxin analysis, complex chemometric models requiring large data sets for training and analysis are needed. Such methods predict the presence of mycotoxins based on changes in the IR spectrum that correlate to fungal infestation, and thus only indirectly relate to mycotoxin contamination [37–42]. Despite being label-free, these IR platforms using prediction and classification methods still do not offer molecular identification and direct detection of the target analyte.

In this work, we develop a novel method to enhance the specificity and detection capability of IR-based measurements to allow molecular identification and concentration-dependent detection of mycotoxins in food, such as DON in wheat. Our method leverages a paper substrate in which the toxin molecules are hyper-concentrated by adapting the coffee-ring effect, and it is thus called Paper-Enhanced InfraRed Spectroscopy (PEIRS). Dominant features of the molecular fingerprint of DON in mid-IR are used to measure concentrations on paper via the Beer's law. We demonstrate that PEIRS achieves a sensitivity enhancement compared to conventional IR detection methods. Next, we achieve analyte selectivity in PEIRS (S-PEIRS), using immunoaffinity columns (IACs) specific to DON to purify the wheat extracts. S-PEIRS combines analyte identification, enrichment, and selectivity in one method, and for the first time demonstrates the direct molecular detection of DON in naturally contaminated wheat, in the range of the EU ML (1 $mg \cdot kg^{-1}$). Therefore, our results pave the way for the diversification of paper-based IR detection with molecular identification of toxins in food safety.

3.2 Materials & methods

3.2.1 Reagents, consumables & equipment

Chromatography grade ethanol (Supelco® EMSURE, Merck, Germany) and methanol (Supelco® EMSURE, Merck, Germany) were used to perform the IR and paper-based IR experiments. Ultrapure water (Millipore, Merck, Germany) was used for the extraction of wheat samples. These consisted of four types of naturally contaminated quality control (QC) material, (i) a variant that was not contaminated with DON (NC), (ii) a variant with 0.5 mg·kg^{-1} DON contamination (compliant), (iii) and a two variants with 1.8 mg·kg^{-1} and 4.3 mg·kg^{-1} DON contamination (non-compliant) (Trilogy Analytical Laboratory, USA). Additionally, wheat material was obtained from BOKU University (Austria, 2.7.1). Extracts were filtered using 1.2 µm syringe filters (Puradisc, Whatman™, Merck, Germany). Two batches of DON analytical standard (Romer Labs, Austria, 5 mg) were purchased as a solid of which one was dissolved in ethanol and the other in ultrapure water to a stock concentration of 5 mg·mL^{-1}. Immunoaffinity columns (IACs) were purchased from Romer Labs (DONstar™, Romer Labs, Austria), kept in the fridge (4 °C) and allowed to reach room temperature before use. Samples were purified by IAC clean-up. Standard chromatography paper (Whatman™ cellulose Chr1, Merck, Germany) was used for all paper-based IR experiments. A perforator (EAN 7435110290233, 6 mm Ø) was used to cut equally sized paper discs, and a normal scissor was used to cut paper strips for (S-)PEIRS experiments. Samples were measured using a standard FTIR spectrometer (Tensor 27, Bruker, USA), equipped with a single-bounce DiamondATR accessory (2 x 2 mm), a mid-IR source (4000-400 cm^{-1}) and a deuterated triglycine sulphate (DTGS) detector.

3.2.2 ATR-FTIR settings and liquid deposition

All ATR-FTIR spectra were acquired with a scanner velocity of 10 kHz over 3000 – 1000 cm^{-1} and 512 scans. The resolution of the spectrometer was 4 cm^{-1} with an aperture size of the beam of 6 mm. Every sample series consisted of N=3 independent experiments and n=5 replicates, unless stated otherwise. This corresponds to 3 sample or biological replicates and 5 technical replicates. An environmental background spectrum was taken before starting every new sample series and in between each set the prism was cleaned.

For traditional liquid sample deposition, 0.5 µL of sample was deposited and dried on the prism. In dried conditions there is little solvent interference in the absorbance signal and the sample analytes are in close vicinity of the ATR surface where the evanescent electromagnetic field effect is strongest. A DON analytical standard (in ethanol) was diluted to a concentration series of 100 – 5000 µg·mL^{-1}, corresponding to an absolute amount of 50 – 2500 ng dried on the prism. To estimate the limit

of ATR-FTIR signal detection and quantification for liquid deposition, 3x and 10x the baseline of the air vs. air spectra of i) the absorbance and ii) the 2nd derivative were integrated in the range where the C=O of DON occurs (Figure S3.1). Here, the integrated limit of signal detection (3x baseline) was estimated to be $0.0200 \pm 1.0 \cdot 10^{-4}$ a.u. for the absorbance spectra and $3 \cdot 10^{-5} \pm 2 \cdot 10^{-5}$ a.u. for the second derivative spectra. In addition, the integrated limit of signal quantification (10x baseline) was $0.070 \pm 2 \cdot 10^{-3}$ a.u. for the absorbance spectra and $7 \cdot 10^{-5} \pm 6 \cdot 10^{-5}$ a.u. for the second derivative spectra.

3.2.3 Paper-disc ATR-FTIR analysis

A DON analytical standard (in ethanol) was dissolved and diluted in pure ethanol to a concentration series of 100 – 5000 μg·mL^{-1} and 3 μL was deposited on chromatography paper discs having a diameter of 6 mm. The DON solution was drop-casted on one side of the paper disc and was dried to the atmosphere during approximately 1 hour. Thereafter, this side of the paper was pressed onto the ATR prism by the ampul of the Diamond-ATR accessory and a glass slide was placed in between the ampul and the paper to prevent paper deformation (Figure S3.2). The area factor (Equation 3.1) between the ATR prism and the paper disc was 0.14, meaning that 14% of the paper disc area was in contact with the prism. Therefore, the paper disc was slightly moved in between each replicate to represent the absolute amount of DON within the entire disc more accurately and to correct for the accumulation of particles on the paper edges, better known as the coffee-ring effect [43,44]. The estimated absolute amount of DON that was in contact with the ATR prism during this experiment was in the range of 40 – 2120 ng for the corresponding concentration range. A blank paper was prepared by depositing 3 μL of pure ethanol solution, drying and measuring this similarly to the sample papers.

$$\textit{Area factor (\%)} = \frac{Area\ \ ATR\ \ prism}{Area\ \ paper\ \ disc} \times 100 \qquad \textit{Equation 3.1}$$

3.2.4 Paper-enhanced infrared spectroscopy (PEIRS)

To enhance the sensitivity of the ATR-FTIR analysis, chromatography paper was cut into strips of 40 mm x 5 mm, with at one end a tip having an angle of approximately 28°. A concentration range of 0 – 10 μg·mL^{-1} DON analytical standard was prepared in methanol solution and the paper tips were inserted in 1.5 mL aliquots of each concentration with the tip facing up, in triplicate. The solution of DON was passively transported into the paper by capillary action (>12 hours). The DON molecules hyper-concentrated in the paper tip because of evaporation-induced enrichment. The dried tips were positioned and pressed on the ATR prism and measured (Figure S3.3). To estimate the limit of ATR-FTIR signal detection and quantification for PEIRS, 3x and 10x the baseline of the paper vs. paper spectra were used (Figure

S3.4). Thereof, the 2nd derivative spectra were integrated in the region where the C=O of DON occurs and the signal detection and quantification limits were $1 \cdot 10^{-5} \pm 1 \cdot 10^{-5}$ a.u. (3x baseline) and $4 \cdot 10^{-5} \pm 5 \cdot 10^{-5}$ a.u. (10x baseline), respectively.

3.2.5 Calculation of the signal-to-noise ratio

The signal-to-noise ratio (SNR) was estimated according to similar procedures in literature [45]. We first calculated the root mean square (RMS) noise of the IR spectra in the region of interest for DON identification (1800 – 1500 cm^{-1}). We measured the noise for the empty ATR crystal (air background vs air sample, n=10), and for the ATR crystal with paper (paper background vs. paper sample, n=8). This led to an average RMS of $7 \cdot 10^{-5} \pm 3 \cdot 10^{-5}$ a.u. for air vs. air (Figure S3.1) and $6 \cdot 10^{-5} \pm 2 \cdot 10^{-5}$ a.u. for paper vs. paper (Figure S3.4). Then, the absolute signals at 1683 cm^{-1} (C=O) of both the sample containing DON (100 $\mu g \cdot mL^{-1}$) and the blank (0 $\mu g \cdot mL^{-1}$) were determined from the baselined spectra for each method respectively. Finally, we used Equation 3.2 to estimate the SNR as the absolute signal at 1683 cm^{-1} divided by the RMS noise. We evaluated the SNR with a blank solution at 0 $\mu g \cdot mL^{-1}$ and a DON solution 100 $\mu g \cdot mL^{-1}$, for (i) liquid deposition, (ii) drop-casting on paper discs, and (iii) PEIRS.

$$SNR = \frac{Absolute\ \ signal\ \ at\ \ 1683\ \ cm^{-1}}{RMS\ \ noise} \qquad \textit{Equation 3.2}$$

The estimated SNRs per method were used to evaluate the improvement of detection capability for DON using PEIRS compared to the other methods (i) and (ii).

3.2.6 S-PEIRS in DON standard solutions

Ultrapure water, and ultrapure water spiked at 2.0 $\mu g \cdot mL^{-1}$ DON were prepared and referred to as 'blank' and 'pre-IAC spike', respectively. Six IACs were ran using ultrapure water (blank). Then, three IACs were prepared using ultrapure water spiked at 2.0 $\mu g \cdot mL^{-1}$ (4000 ng). All nine IACs were used as follows; (i) loading of IAC by applying 2 mL solution, (ii) washing of the IAC using a total volume of 5 mL ultrapure water, and (iii) the elution from the IAC using 3 x 0.5 mL methanol, following the protocol of the producer. The only difference with the protocol was the washing solution, in the protocol 0.05 M phosphate buffered saline (PBS) solution was used, whereas here ultrapure water was used. The reason for this was to minimize salt residue in the eluate, as this would give interference during IR measurements. Then, in three of the blank eluents, 1.6 $\mu g \cdot mL^{-1}$ DON was spiked (post-IAC spike). Here, ~2500 ng of DON was present in the eluent. Finally, a paper tip was inserted (tip facing up) into each volume of eluent (n=9) which allowed the accumulation of DON (>24 hours). Paper tips were then measured by ATR-FTIR, as described in 3.2.4.

3.2.7 S-PEIRS in wheat

3.2.7.1 Types of wheat material used

Several varieties and origins of wheat material were obtained for the experiments of S-PEIRS. The first group of materials was QC materials (Section 3.2.1) which were naturally contaminated with DON in wheat matrix at different levels (0.5 $mg \cdot kg^{-1}$, 1.8 $mg \cdot kg^{-1}$, 4.3 $mg \cdot kg^{-1}$) and one material that contained no detectable levels of DON referred to as 0 $mg \cdot kg^{-1}$. These materials were homogenized and sieved to the highest degree using a mesh 30 (0.595 mm) sieve size. LC-MS/MS reference analysis was used for certification of these products.

The second group of wheat materials was obtained from BOKU University, Institute for Biotechnology in Plant Production at the Department of Agricultural Sciences. Three types of Austrian wheat were harvested during field trials, two were named 'Trappe' and 'Kronjet' and one variant was named 'non-contaminated' as it contained no detectable levels of DON. These materials were pre-ground with a Perten LabMill 3610 (Perkin Elmer) equipped with a fine grinding, hardened steel disc (type 5) set at a distance '0' and further homogenized using a Blixer 4 V.V mixer (Robo coupe). The contamination levels of these materials were pre-determined using LC-MS/MS analysis [10], and all exceeded the EU regulatory limit for DON in unprocessed wheat, except for the non-contaminated variant (<LOQ, 4 $\mu g \cdot kg^{-1}$). The determined DON contamination levels were 13.3 $mg \cdot kg^{-1}$ for Trappe, and 5.9 $mg \cdot kg^{-1}$ for Kronjet; with an apparent recovery rate for DON in wheat of 101.5% $\pm$ 13.1% using the LC-MS/MS method [10].

A third group of highly contaminated intact Kronjet wheat (6.0 $mg \cdot kg^{-1}$) was mixed with intact and non-contaminated wheat material, to obtain different DON contamination levels of wheat around the ML range of 1 $mg \cdot kg^{-1}$. Subsequently, these mixes mere milled to a fine powder [39].

3.2.7.2 QC wheat protocol

Wheat extracts were prepared by weighing 5.0 grams, which is the minimum sub-sample size according to the supplier, of QC material and were extracted in 25 mL (20% w/v) of ultrapure water for 90 minutes using an overhead shaker. The extracts were centrifuged (3000 rpm, 3 min) and filtered (1.2 μm) to obtain 2 mL of clear solution per extract and subsequently this was applied to individual IACs. After washing using 5 mL of ultrapure water, the bound DON was eluted in a 2 mL Eppendorf tube using 1.5 mL of pure methanol in aliquots of 0.5 mL, of which the first aliquot was allowed to settle into the antibody gel for approximately 3 minutes. Then, as described for PEIRS, a paper tip was inserted into each solution and allowed to accumulate DON (>24 hours), after which the dried tips were analyzed directly by ATR-FTIR. Three full biological replicates (N=3) were prepared per QC variant

and analyzed with n=5 technical replicates. Following this procedure, first, multiple non-contaminated QC extracts were spiked at 5.0 $\mu g \cdot mL^{-1}$, which were then applied to the IACs and compared to the respective non-contaminated sample (0 $\mu g \cdot mL^{-1}$).

Then, another experiment was performed at lower DON concentrations. Here, a single non-contaminated QC extract was aliquoted in 3 volumes of 6 mL, and two of those were spiked at 1.0 and 2.0 $\mu g \cdot mL^{-1}$. All spiked and blank samples were then applied to the IACs in triplicate and per level, and analysed following S-PEIRS. Subsequently, extracts were prepared of the QC wheat levels (0; 0.5 and 4.3 $mg \cdot kg^{-1}$), and analysed by S-PEIRS.

Another experiment with 1.8 $mg \cdot kg^{-1}$ QC wheat was performed. The protocol as described above was followed, except that we now varied the IAC loading volume using 2, 6, and 10 mL. Three full replicates for every loading volume were prepared. A sub-sample of the eluate (0.1 mL) from every sample was measured by LC-MS/MS [10].

3.2.7.3 Field-trial wheat protocol

Wheat extracts were prepared by weighing 20.0 grams of pre-ground wheat material and were extracted in 150 mL of ultrapure water for 30 minutes. Then, 30 mL of extract was centrifuged at 2500 g for 15 minutes. The extract was filtered over a 1.2 µm filter and subsequently 2 mL was applied to every individual IAC, in triplicate per wheat variety. The IACs and the paper tips were prepared in exactly the same way as was described above in 3.2.7.2.

3.2.7.4 Mixed field-trial wheat protocol

Wheat extracts were prepared by weighing 20.0 grams of pre-ground wheat material and were extracted in 100 mL ultrapure water (20% w/v) for 90 minutes. Then, the extracts were centrifuged at 2500 g for 15 minutes, and filtered over a 1.2 µm filter. Subsequently, 10 mL per extract was applied to the IACs, in triplicates and per mix-level. Except for the loading volume, the IACs and paper tips were prepared in exactly the same way as described above in 3.2.7.2. Sub-samples (0.1 mL) of the eluate, and the remaining solid wheat powder per level, were analysed by LC-MS/MS [10].

3.2.8 ATR-FTIR data processing

All measured spectra were analyzed using OPUS (Bruker, USA) and OriginPro (OriginLabs©, 2025, USA). First, the raw data was cut to the fingerprint range (1800 – 1145 cm^{-1}), where the fundamental vibrational modes of DON were most distinct. The raw spectra of the 5 replicates of each individual set were smoothed by Adjacent Averaging (window size 3) and Savitzky-Golay (window size 3, order 2) filters. The 5 replicates of each set were baselined and averaged. The carbonyl stretch mode (C=O) was selected as identifier for DON and the peak area was integrated. A linear regression between the absorbance and the concentration was established based on this peak area integration. Similarly, after the second derivative analysis with a Savitzky-Golay filter (with a window size 9 and an order of 2) a linear regression was established to deconvolve the DON C=O vibration at 1683 cm^{-1}.

For all analyses performed on paper, normalization to a specific point in the spectrum that is related to the C-O symmetric stretch from the hydroxyl of paper at ~1203 cm^{-1} was performed prior to second derivative analysis and integration. Thereby, all signals related to blank paper were converged and the background deviations originating from the paper substrate were corrected.

3.2.8.1 Multivariate analysis of S-PEIRS results

Multivariate analysis of the preprocessed S-PEIRS spectra was performed with Principle Component Analysis (PCA) for Spectroscopy, which is available in the OriginPro software (OriginLabs©, 2025, USA). After the preprocessing as described above in Section 3.2.8, further processing of the spectra was required to prepare the data for PCA. The baselined and normalized absorbance spectra (n=15 per wheat variety) were cut to 1701 – 1639 cm^{-1}. Then, these spectra were baselined again, using interpolation between the two end-points of the spectra, and normalized to 1. A PCA was performed on these preprocessed absorbance spectra. The loadings were smoothed using a 2^{nd} order Savitzky-Golay filter with a 9 points window before plotting.

Next to that, a second derivative analysis (2^{nd} order, 9 points Savitzky-Golay) was performed on the preprocessed absorbance spectra, and the region was cut to 1691 – 1649 cm^{-1}. Finally, PCA was performed on the second derivative spectra and the loadings were smoothed using either a 2^{nd} order Savtizky-Golay filter with a 5 points window (for the field-trial wheat), or adjacent-averaging filter with a 3 points window (for the mixed field-trial wheat), before plotting. Finally, integration of the 2^{nd} derivative DON C=O in the region between 1690-1670 cm^{-1} was plotted for the mixed field-trial wheat material.

3.2.8.2 Statistical analysis of S-PEIRS results

All statistical tests were performed using OriginPro (OriginLabs©, 2025, USA). For the statistical analyses, first, the integrated 2nd derivative areas of the n=5 replicates from the N=3 independent experiments were averaged. Subsequently, a Shapiro-Wilk normality test was performed to determine whether the sample data were drawn from a normally distributed population. A One-way Analysis of Variance (ANOVA) test was used to compare the means of the different sample groups. This analysis integrates a test for the homogeneity of variance (Levene's test), which needs to be equal for ANOVA testing. Additionally, the means were compared using a Fisher's Least Significant Difference (LSD) post-hoc test to identify which group means were significantly different at the 0.05 level. The p-values obtained from this test were represented in the boxplots of the integrated 2nd derivative areas against DON level.

3.3 Results & discussion

3.3.1 Chemical fingerprint and limit of IR detection DON

To achieve the direct detection of the frequently found food mycotoxin DON in unprocessed cereals at the EU limit (1 mg·kg^{-1}, Figure 3.1a), we developed S-PEIRS as an innovative paper-based IR platform combining analyte selectivity, enrichment, and molecular identification (Figure 3.1b).

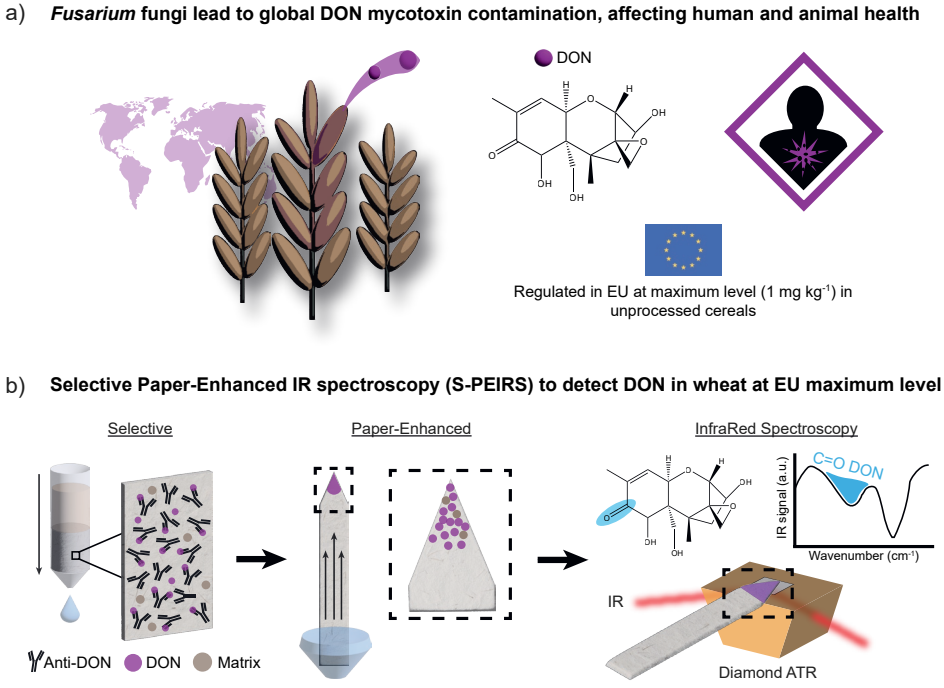


Figure 3.1: *Mycotoxins must be monitored in the global cereal food chain; our developed paper-based IR platform allows direct molecular screening of mycotoxins in food. a) The Fusarium mycotoxin DON is frequently found worldwide on cereals like wheat and can cause health problems in humans and animals. b) Selective paper-enhanced spectroscopy (S-PEIRS) leverages IR detection combined with immunoaffinity columns to gain selectivity towards DON and paper-tips to hyper-concentrate before IR analysis, allowing the detection of DON in naturally contaminated wheat at the EU ML.*

The first step for the development of S-PEIRS was determining the predominant vibrational modes of DON; while using decreasing concentrations of the molecule to assess the detection capability by ATR-FTIR and evaluate which molecular bond could be best used for quantification via Beer's law (Figure 3.2). DON is a polar, cyclic sesquiterpene compound belonging to a group of trichothecene mycotoxins, which has a conjugated ketone (C=O), an ether (C-O-C), one primary alcohol (RCH_2-OH) and two secondary alcohols (R_2CH-OH), and a stable epoxide ring (C_2H_2-O)

(Figure 3.2a). To identify these molecular groups, we measured analytical standard solutions of DON (0.5 µL) at varying concentrations (100 - 5000 µg·mL^{-1}; 50 – 2500 ng) using ATR-FTIR spectroscopy (Figure 3.2b). The predominant vibrational mode of the DON molecule is a carbonyl symmetric stretching (C=O$_{v,s}$) at 1683 cm^{-1} related to the conjugated ketone (Figure 3.2c). Next to that, an ether symmetric stretching (C-O-C$_{v,s}$) is visible at 1168 cm^{-1}. The remaining absorption bands in the region between 1500 cm^{-1} and 1200 cm^{-1} could be related to various carbon-hydrogen (C-H) and carbon-carbon (C-C) vibrational modes.

We then focused on the most prominent molecular feature of DON, the C=O at 1683 cm^{-1}. Here, the second derivatives of the absorbance spectra are calculated. Such analysis is convenient as it avoids baseline effects and is commonly used to deconvolve IR spectra [46–48]. Thereafter, the C=O band is integrated in the range between 1725-1550 cm^{-1} (blue box) in the absorbance spectra (Figure 3.2d), and between 1700-1670 cm^{-1} in the second derivative spectra (Figure 3.2e). The integrated areas are plotted as a function of concentration (Figure 3.2f). The detection capability of the ATR-FTIR towards DON is evaluated by comparing the lower detection range of the integration results for both the absorbance and second derivative data (Figure 3.2g). The instrumental limits of IR signal detection (3x baseline) and quantification (10x baseline) are estimated by integration of the air vs. air spectra in the same C=O range as for the samples (Section 3.2.2, Figure S3.1). The absorbance results (in black) showed that the lowest detected concentration is 250 µg·mL^{-1} (125 ng), and lowest quantified concentration is 500 µg·mL^{-1} (250 ng). The second derivative results (in pink) showed that the lowest detected and quantified concentration is 100 µg·mL^{-1} (50 ng). Indeed, while the second derivative increased the overall noise, it also deconvolved and increased the signal-to-noise ratio (SNR) for the measurements of the C=O of DON, leading to improved detection capability. Nevertheless, this is not sufficient to analyze relevant concentrations of DON in solution down to 1 µg·mL^{-1} (0.5 ng).

Overall, the results show that the C=O at 1683 cm^{-1} is a suitable molecular feature of DON to measure its concentration. However, when the detection limit of such a liquid deposition ATR-FTIR method is compared to the ML of DON in standard solution (1 µg·mL^{-1}; 0.5 ng), an analyte enrichment of at least 100 times is needed.

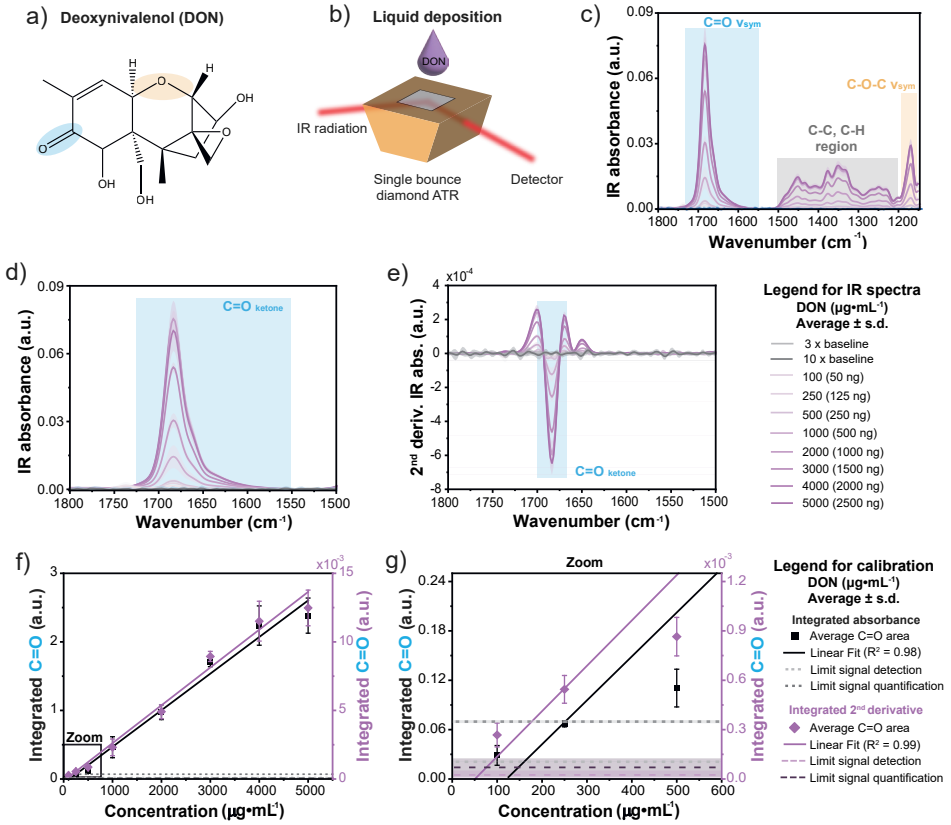


Figure 3.2: *Chemical fingerprint and detection limits of DON standard by ATR-FTIR. a) DON applied to b) the ATR prism by liquid deposition of 0.5 µL over a concentration range of 100 - 5000 µg·mL^{-1} (50 – 2500 ng) and c) analysed consistently by evaluating the spectrum from 1800 – 1145 cm^{-1}. Every sample series consisted of at least N=3 independent experiments of at least n=1 technical replicates. d) The dominant vibrational mode was the carbonyl stretch (C=O$_{v,s}$) related to the conjugated ketone of DON with a peak center at 1683 cm^{-1}. e) A second derivative function is applied to the isolated carbonyl band. f) The absorbance (left ordinate) and the second derivative spectra (right ordinate) in this region are integrated and plotted as a function of DON concentration. g) A zoom of the integration plot for the lowest measured concentrations showed that DON is detected down to 250 µg·mL^{-1} (125 ng) for the absorbance results, and down to 100 µg·mL^{-1} (50 ng) for the 2nd derivative spectra.*

3.3.2 Development of paper-based infrared spectroscopy

The lowest measured concentration of DON by ATR-FTIR (100 µg·mL^{-1}; 50 ng) is not sufficient for molecular identification of DON at relevant concentrations required for food analysis in complex mixtures (1 µg·mL^{-1}; 0.5 ng). Thus, we developed our paper-based microfluidics method by establishment of, (i) a framework for IR detection of DON directly on paper discs (Section 3.3.2.1), and then by (ii) PEIRS (Section 3.3.2.2) to enhance the sensitivity of the IR analysis through hyper-concentrating the target analyte in a paper-tip [49,50].

3.3.2.1 Framework for IR detection of DON on paper discs

Liquid deposition of DON analytical standard showed that the C=O band with a peak centre at 1683 cm^{-1} was directly proportional to the concentration of DON. Next, it was important that the concentration dependency of DON was retained when measuring directly on a paper substrate (Section 3.2.3). A paper disc ATR-FTIR method was developed (Figure S3.2) to (i) establish the framework to detect a specific DON-related signal on paper, (ii) demonstrate that this signal is concentration dependent, (iii) evaluate the minimum concentration that can be detected in this manner, and (iv) to identify which enrichment factor was required to allow the analysis of DON on paper at the ML by ATR-FTIR.

To determine the noise introduced by the possible chemical variability of the paper substrates, we measured the signal of paper using a different paper as background in the spectroscopic range between 1800 – 1500 cm^{-1} (Figure S3.4). The RMS noise from plain paper measurements was of $6 \cdot 10^{-5} \pm 2 \cdot 10^{-5}$ a.u. (n=8, Section 3.2.5). We then investigated the behaviour of paper-based IR detection using paper discs. The paper discs were brought in close contact with the ATR prism (Figure S3.5a). Next, the vibrational modes of the paper itself were identified (Figure S3.5b). As paper is a cellulose polymer the dominant vibrational modes in the range between 1500–1150 cm^{-1}, the fingerprint region, correspond to the repeating units of this network and are mainly assigned to C-O-C symmetric stretching from the ether (blue), C-O symmetric stretching from the hydroxyl (green) and, carbon-hydrogen and carbon-carbon (grey) vibrational modes (Figure S3.5c).

In the spectra of paper containing DON (100 – 5000 $\mu g \cdot mL^{-1}$; ~40 – 2120 ng), the characteristic C=O peak was observed at 1683 cm^{-1} and was partially convoluted with the H-O-H band from the paper. As paper is a hydrophilic material, it absorbs water moisture from the air, resulting in a reoccurring H-O-H band (red box) in all the spectra. The sample spectra were normalized (*) to a specific vibrational mode of paper, which was the C-O symmetric stretch from the hydroxyl at ~1203 cm^{-1}, thereby converging all signals related to paper (Figure S3.5d). Zooming into the region where the DON C=O band (blue) is expected, it can be observed that the band at 1683 cm^{-1} is increasing as a function of DON concentration (Figure S3.5e). While the H-O-H band (red) is not following this trend, the signal intensity was changing due to the inconsistent amount of absorbed water moisture in different paper discs.

To verify that the band at 1683 cm^{-1} originated from DON, the pristine paper spectrum was subtracted from the paper and DON (5000 $\mu g \cdot mL^{-1}$) spectrum, and normalized (*) to the C=O band found for the DON analytical standard after liquid deposition (Figure S3.5f). The suspected DON signal after paper subtraction overlapped perfectly with the C=O from the DON analytical standard, exactly at 1683 cm^{-1}. Finally, a second derivative analysis was used to deconvolve the DON C=O

from the H-O-H band of paper (Figure S3.5g). After second derivative deconvolution, the 1683 cm^{-1} band was integrated, and the peak areas were plotted against DON concentration (Figure S3.5h). The plot showed a linear correlation (R^2= 0.97) of the area as a function of DON concentration, thus allowing the determination of DON concentration on paper using the C=O as molecular identifier. The lowest DON concentration that was detected on the paper disc using this method was 100 $\mu g \cdot mL^{-1}$, which corresponded to an absolute amount of 40 ng. While robust, this methodology does not enhance the detection capability to the required level for analysis of DON down to 1 $\mu g \cdot mL^{-1}$. Therefore, PEIRS was developed, exploiting paper tips that allowed the accumulation of DON molecules prior to ATR-FTIR measurement.

3.3.2.2 Paper-enhanced infrared spectroscopy (PEIRS)

In PEIRS, a large volume (mL-scale) containing a concentration of analyte below the IR detection capability was hyper-concentrated at a triangular shaped edge of a paper strip resulting in continuous deposition of dissolved material in the tip area which is measured by IR (Figure S3.3, Figure 3.3). This analyte hyper-concentration is also illustrated in Figure 3.3a-b and Figure S3.6, using blue dye solution that accumulated in the triangular area of the paper tip because of evaporation-driven capillary action [49,50]. The governing principle behind this effect could be broken down into two parts. First, paper is a hydrophilic porous material that enables fluid transport through capillary action, also known as wicking, which allows dissolved molecules to travel from one side of the paper to the other (Figure S3.6)[44]. Thus, the paper acts as a passive transportation vessel for molecules. Second, when the paper tip is inserted into a solution of methanol with diluted food coloring, and is completely wetted, the molecules move to the area of the paper where the evaporation of methanol is the fastest. The three-phase contact boundary between liquid, solid and vapor is largest in the tip area and leads to continuous deposition of blue dye molecules.

To employ PEIRS for DON, 1.5 mL-aliquots of DON in methanol at the lowest measured concentration by liquid deposition and paper discs (100 $\mu g \cdot mL^{-1}$) were prepared and evaporated in the paper tips. This hyper-concentration in the paper tips at 100 $\mu g \cdot mL^{-1}$ was compared to pure DON analytical standard (5000 $\mu g \cdot mL^{-1}$) and plain paper (0 $\mu g \cdot mL^{-1}$), and is illustrated in Figure S3.7. The spectra of plain paper (grey), pure DON (purple), and hyper-concentrated DON in paper (pink) were stacked to confirm that the C=O of DON was observed on top of the paper background signals. The H-O-H band at 1640 cm^{-1} (red box) originated from water moisture in the air that is absorbed in the paper, as explained before. The dashed line indicates the peak centre of DON molecular vibration at 1683 cm^{-1}, and was

clearly visible for the hyper-concentrated DON in the paper spectrum, in the same position. Moreover, the remaining part of the spectrum between 1500 – 1180 cm^{-1} showed features of both the paper and the DON.

We then hyper-concentrated 1.5 mL-aliquots of DON in methanol for ATR-FTIR analysis at concentrations of DON considerably lower (0–10 $\mu g \cdot mL^{-1}$) than the ones used to measure via liquid deposition (100 $\mu g \cdot mL^{-1}$; ~50 ng), or using the paper discs (100 $\mu g \cdot mL^{-1}$; ~40 ng) (Figure 3.3c). When normalized to the typical absorption of paper (1203 cm^{-1}), the results showed that the C=O signal of DON at 1683 cm^{-1} (blue box) could be observed over the H-O-H signal from water moisture in the paper at 1640 cm^{-1} (red box, Figure 3.3c, Figure S3.7). Indeed, while the concentrations of DON are well below 100 $\mu g \cdot mL^{-1}$, the relatively large volume that had wicked into the paper led to substantial accumulation of toxin molecules in the paper tip. Hence, the absolute quantity of enriched DON molecules is estimated between 1500-15000 ng; allowing the ATR-FTIR detection of DON. The time in which the tip is dried and the DON molecules accumulate could be optimized by active drying methods such as using compressed air or heat [49]. We further used second derivative analysis to deconvolve the C=O peak of DON from the H-O-H peak of water (Figure 3.3d). The integration of the C=O peak, between 1700 – 1670 cm^{-1}, showed a strong linear relationship (R^2= 0.99) as a function of DON concentration (Figure 3.3e). Thus, PEIRS allowed the enrichment and direct molecular detection of DON on paper at relevant concentrations for food analysis.

When the same concentration of DON was applied on paper (100 $\mu g \cdot mL^{-1}$, Figure 3.3f), a comparison between the IR signal of DON for paper discs vs. tips confirmed that the absorbance of the tip-based measurements increased significantly at 1683 cm^{-1}, in the C=O of DON (blue box). We estimated the SNR for the three different methods by comparing the absolute absorbance value of DON at 1683 cm^{-1} against the absolute absorbance of the blank (0 $\mu g \cdot mL^{-1}$) for every method independently (Section 3.2.5, Figure 3.3g). The triangular tips of PEIRS showed the strongest increase of SNR by a factor of ~8.5 when compared to the blank background signal. Overall, we proved that PEIRS allowed enrichment of DON molecules leading to an improvement of the detection capability of ATR-FTIR by a factor ~40, when comparing the lowest detected concentrations using both methods, which were 100 $\mu g \cdot mL^{-1}$ and 2.5 $\mu g \cdot mL^{-1}$. We then further optimized these novel capabilities to detect DON in complex food matrices, such as wheat.

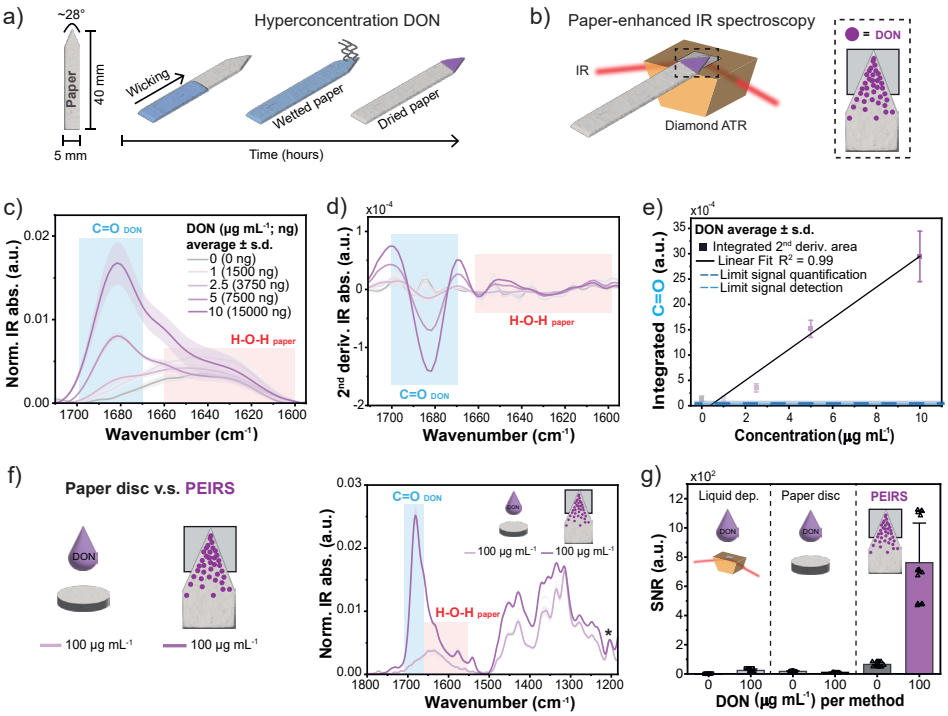


Figure 3.3: PEIRS for detection and analysis of DON. *a) Hyper-concentrating DON in paper-tip by passive wicking and continuous deposition of DON through evaporation in a triangular tip area. b) ATR-FTIR analysis of the paper tip leading to enhanced measurement sensitivity. c) Measurement of different concentrations (0-10 µg·mL^{-1}) of DON, hyper-concentrated in paper tips. Every sample series consisted of N=3 independent experiments of n=5 technical replicates. d) Second derivative analysis was used for deconvolution of DON signal in the C=O peak, and e) the integrated area was plotted as a function of concentration. f) Comparison between the paper disc and tip-based PEIRS method showed that triangular paper tips resulted in a significant increase of the DON C=O signal and g) this was reflected when the signal-to-noise (SNR) was estimated per method (liquid, disc, tip), showing clear signal enhancement for PEIRS.*

3.3.3 Selective paper-enhanced infrared spectroscopy (S-PEIRS)

Next, the PEIRS methodology was implemented to detect DON in a complex food matrix, namely in wheat (Figure 3.4). However, a means for selective purification was required to decrease matrix interference of major food components such as proteins, carbohydrates and lipids. Immunoaffinity is a robust method for selective purification of analytes in complex matrices [51,52], and was used in this work to selectively purify wheat extracts, thus expanding the method to Selective-PEIRS (S-PEIRS). During the loading of an IAC, DON molecules selectively bind to the antibodies in the IAC, while most non-specific matrix constituents are removed during washing.

S-PEIRS was used for DON detection in (i) solutions without wheat matrix,

(ii) spiked QC wheat extracts, (iii) naturally contaminated QC wheat, and (iv) contaminated wheat from field-trials.

3.3.3.1 S-PEIRS using DON standards

The ability of S-PEIRS to achieve molecular identification of DON was initially evaluated using extraction solvent (ultrapure water) without any wheat matrix present (Figure S3.8). These measurements allowed to obtain information on IAC performance and background interference. DON standard was spiked either in the 2 mL loading solution (pre-IAC spike) or in the 1.5 mL eluate (post-IAC spike), and compared to the blank eluate (Figure S3.8a).

The maximum loading capacity of the IAC, given by the producer, is 2500 ng [53]. Thus, only quantities of DON (possibly cross-reacting conjugates) of approximately 2500 ng can be captured in one IAC. In the pre-IAC sample, 2 mL of loading solution spiked at 2 $\mu g \cdot mL^{-1}$ contained 4000 ng of DON, thus the IAC capacity was reached. On the other hand, in the post-IAC spiking 1.5 mL of eluate at 1.6 $\mu g \cdot mL^{-1}$ amounts to ~2500 ng DON. After spectral preprocessing, the typical vibrational mode of DON (C=O, 1683 cm^{-1}, blue) was similarly observed in the pre- and post-IAC spike spectra (Figure S3.8b). The region related mainly to paper between 1500 – 1145 cm^{-1} converged after normalization to a specific peak of paper (1205 cm^{-1}), while between 1600 – 1500 cm^{-1} material that co-eluted from the IAC was visible. Fortunately, this did not interfere with the DON C=O region. Closer investigation of the DON C=O region showed that the pre- and post-IAC spike samples overlapped within the standard error in the typical peak at 1683 cm^{-1}, while being clearly different from the blank. This gave an estimation about the recovery of DON using the IAC at full loading capacity and was close to a 100% (Figure S3.8c).

3.3.3.2 S-PEIRS to detect DON spiked in QC extracts

In a first set of experiments using wheat, we evaluated the performance of S-PEIRS on non-contaminated (NC) QC wheat (0 $mg \cdot kg^{-1}$), and on multiple NC extracts spiked with DON analytical standard (5.0 $\mu g \cdot mL^{-1}$, Figure S3.9). The IACs were loaded with the extracts, in triplicate. Here, the capacity of the IAC column was exceeded by applying 5.0 $\mu g \cdot mL^{-1}$ (>2500 ng of DON). The bound DON was dissociated and eluted from the IAC using 1.5 mL of methanol. A PEIRS paper tip was inserted in the eluted volume and DON was hyper-concentrated in the tip area (Figure S3.9a). The spectra showed a clear protein signature of the amide I band (brown box, 1656 cm^{-1}), because of the residues of wheat matrix components that co-eluted from the IAC, and that were hyper-concentrated as well. Regardless, a difference in the typical peak associated with DON at 1683 cm^{-1} (blue box, Figure S3.9b) was observed. Furthermore, the second derivative spectra of the residual matrix components well

overlapped in the 1670 – 1600 cm^{-1} region. This coherence can be explained since the same non-contaminated QC wheat material was used to prepare both the 0 and 5 $\mu g \cdot mL^{-1}$ samples. ANOVA statistical testing (Section 3.2.8.2) showed that the means of the integrated area of the molecular signature of DON at 1683 cm^{-1} were significantly different ($p=0.036$), and that the difference between non-contaminated 0 $\mu g \cdot mL^{-1}$ and contaminated samples 5 $\mu g \cdot mL^{-1}$ was statistically significant (Figure S3.9c).

In a second set of experiments, non-contaminated QC wheat extract was spiked with DON standard at 1.0 $\mu g \cdot mL^{-1}$ and 2.0 $\mu g \cdot mL^{-1}$, and the full S-PEIRS procedure was repeated (Figure S3.10a). The absolute DON loading quantity of 1.0 $\mu g \cdot mL^{-1}$ was 2000 ng, and of 2.0 $\mu g \cdot mL^{-1}$ was 4000 ng, which means that for the latter maximal IAC loading was reached. After spectral preprocessing and 2^{nd} derivative analysis, the spiked samples showed the vibrational signature of DON in the C=O mode at 1683 cm^{-1}, which was absent in the non-contaminated material (Figure S3.10b). Additionally, the amide I band of the co-eluted wheat proteins was visible around 1656 cm^{-1}. These results were in line with the previous experiment of spiked QC wheat. Moreover, the molecular signature of DON at 1683 cm^{-1} increased from 1.0 $\mu g \cdot mL^{-1}$ to 2.0 $\mu g \cdot mL^{-1}$ (Figure S3.10c). ANOVA statistical testing (Section 3.2.8.2) on the means of the integrated areas were compared resulted in significant difference between 0 and 1.0 $\mu g \cdot mL^{-1}$ ($p=0.0323$), 0 and 2.0 $\mu g \cdot mL^{-1}$ ($p=0.0004$), and 1.0 and 2.0 $\mu g \cdot mL^{-1}$ ($p=0.0053$). These results show potential for future quantitative analysis of DON by probing its molecular identifier peak.

3.3.3.3 S-PEIRS to detect DON in naturally contaminated QC wheat

S-PEIRS was employed to detect DON in naturally contaminated milled wheat (Figure 3.4). Therefore, non-contaminated (0 $mg \cdot kg^{-1}$) and naturally-contaminated QC wheat with two different levels of contamination (0.5 $mg \cdot kg^{-1}$; 4.3 $mg \cdot kg^{-1}$) were used to prove the detection of DON. One of the naturally contaminated QC wheat materials was contaminated below ML and thus compliant with EU regulation (0.5 $mg \cdot kg^{-1}$; light pink), while the other was above ML and thus non-compliant (4.5 $mg \cdot kg^{-1}$; dark pink). The absolute DON quantity in the 2 mL of loading, for both contaminated materials after extraction (20% w/v), was maximally 200 ng and 1720 ng. Therefore, the 0.5 $mg \cdot kg^{-1}$ samples most likely did not contain sufficient DON to measure the C=O vibrational mode.

All samples were first purified with the IACs, enriched with PEIRS and then analyzed by ATR-FTIR (Figure 3.4a). When normalized to the typical absorption of paper (1203 cm^{-1}, indicated by *), the absorbance spectra indeed show the characteristic amide I (~1655 cm^{-1}) and amide II (~1550 cm^{-1}) vibrations of proteins (Figure 3.4b) [35,47], due to matrix residues that co-eluted from the column.

The amide I region convoluted the specific C=O vibration of DON and is indicated by a dashed box. The second derivative spectra show that the C=O signature of the DON molecule (blue, Figure 3.4c) could be deconvoluted and differentiated from residual absorption originating from the amide I band of protein in the wheat matrix (brown, Figure 3.4c). The results showed an increased area related to the presence of DON in the peak related to the DON C=O at 1683 cm^{-1} (blue box) for the non-compliant material (dark pink) when compared to the non-contaminated material (grey). To quantify these differences, the C=O peak at 1683 cm^{-1} is integrated and plotted as a function of contamination level, showing an increasing trend (Figure 3.4d). The non-contaminated sample showed a lower value for the integrated area in the peak of DON at 1683 cm^{-1} with a mean level of $1.1 \cdot 10^{-3} \pm 4 \cdot 10^{-4}$ a.u. The compliant material showed a slight increase in integrated area to $1.5 \cdot 10^{-3} \pm 1 \cdot 10^{-4}$ a.u. mean level. The non-compliant material showed an increase of the mean level to $1.9 \cdot 10^{-3} \pm 4 \cdot 10^{-5}$ a.u. ANOVA statistical testing (Section 3.2.8.2) showed that the difference between the negative control and non-compliant material is significant with $p=0.0065$. The difference between compliant and non-compliant showed a trend toward significance with a $p=0.055$. The negative control and compliant material could not be clearly differentiated ($p = 0.142$, Figure 3.4d).

Finally, the peak at 1657 cm^{-1} related to the amide I (brown box) showed a change in intensity with increasing DON contamination. This difference might be explained by changes in the composition of the plant upon fungal infestation affecting major matrix constituents, such as proteins [29,33,38,40].

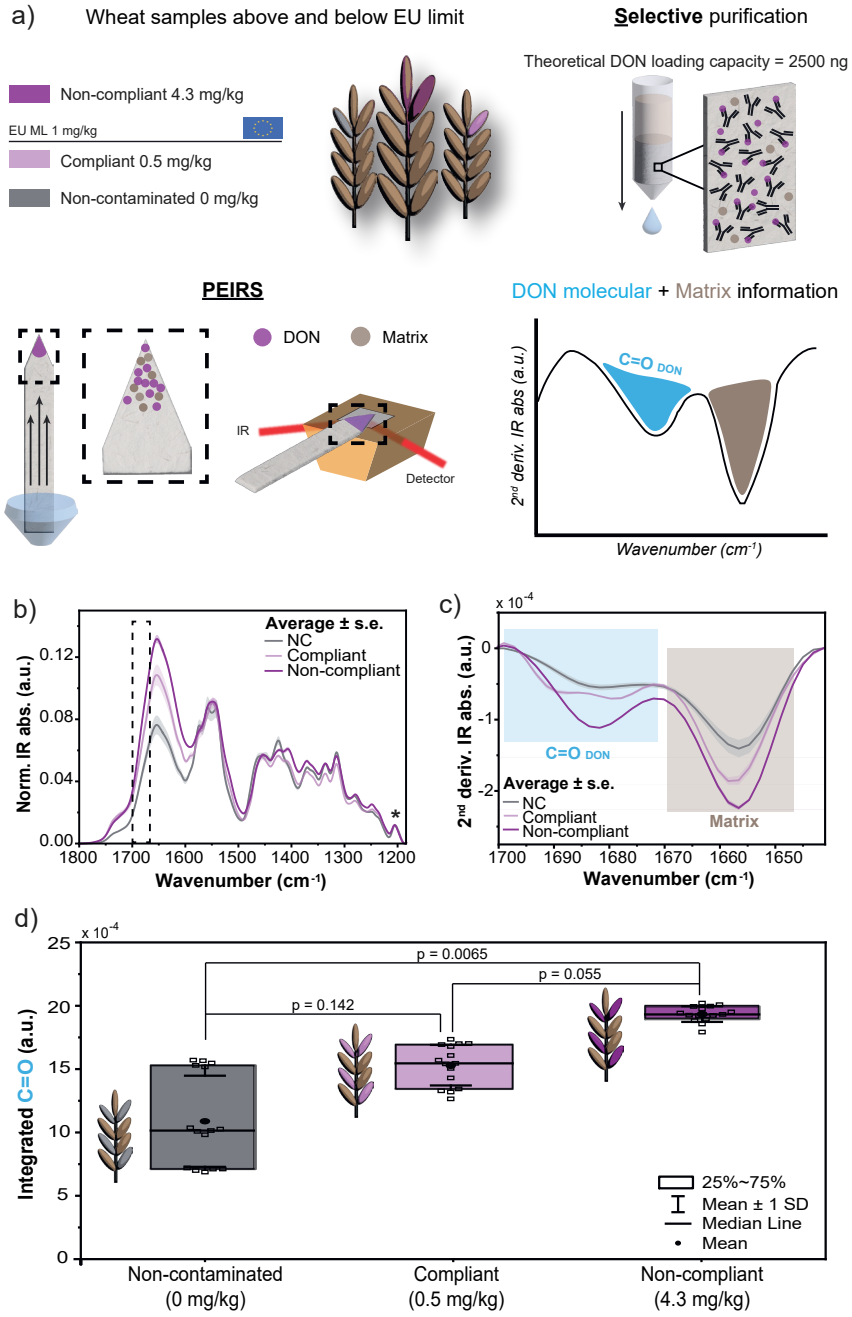


Figure 3.4: *S-PEIRS detection of DON mycotoxin in naturally contaminated QC wheat. a) non-contaminated wheat used as negative control (NC; mg·kg^{-1}) and two levels of contaminated wheat (0.5 and 4.3 mg·kg^{-1}) were extracted with water and applied to immunoaffinity columns; after which PEIRS was performed. Every sample series consisted of N=3 independent experiments of n=5 technical replicates. b) Normalized (*) absorbance spectra showed the characteristic*

amide I and amide II vibrations of proteins from matrix residues between ~1700 – 1500 cm^{-1}. This protein region overlapped with the DON C=O region, indicated by the dashed box. c) When this region was subjected to second derivative analysis, an increasing signal by increasing contamination was found in the DON C=O region (blue box). The region between 1670 – 1640 cm^{-1} (brown box) originated from protein matrix residues that co-eluted from the column. d) The 2nd derivative IR absorption of the DON C=O region was integrated and plotted as a function of contamination level. ANOVA identified significant difference between the negative control and non-compliant material (p=0.0065), and a trend toward significance between compliant and non-compliant material (p=0.055). The negative control and compliant material could not be clearly differentiated (p=0.142).

3.3.3.4 S-PEIRS for DON detection in wheat from field-trials

Once it was proved that S-PEIRS can successfully detect DON in QC wheat, we employed it to evaluate different types of highly contaminated wheat from field-trials (Figure 3.5).

The main difference between QC wheat and wheat from these field-trials is the higher heterogeneity, with overall larger particle size and distribution. This difference occurs due to the milling procedure. QC wheat is milled and subsequently sieved by a highly specialized laboratory to the highest degree of homogeneity using 0.595 mm meshes (mesh 30); whereas the wheat kernels harvested from the field-trials were milled, but not sieved to a specific average particle size. To decrease the influence of heterogeneity, a larger starting material weight (20 g) and extraction volume (150 mL) were used (~13% w/v).

S-PEIRS analysis was conducted for non-contaminated, Trappe (13.3 mg·kg^{-1}, max quantity = 3550 ng) and Kronjet (5.9 mg·kg^{-1}, max quantity = 1570 ng) wheat that were locally harvested during field-trials at BOKU University (Austria) (Figure 3.5a). As these wheat varieties were expected to have increased variation in the matrix, we performed an additional normalization step, and employ PCA to prove that they might exhibit small but clear differences in the DON region of the IR (Figure 3.5b). This additional normalization step allowed us to correct for the differences in wheat protein, which can occur due to difference in variety and fungal infestation [29,33,38,40]. The molecular signature of DON C=O was visible for Trappe and Kronjet spectra (green box). PCA was performed and the scores and loadings indicated that Trappe and Kronjet were different (Figure S3.11). However, the degree of separation was not clearly related to the DON feature.

Therefore, the 2nd derivative spectra were calculated and again PCA was performed (Section 3.2.8.1). The score plots with 95% confidence ellipsoids showed separation in the multidimensional space of the principle components (PCs) between the non-contaminated and the DON contaminated samples (Figure 3.5c). Accordingly, the loadings showed that the region of DON was a main feature responsible for the degree of separation in the scores (green box, Figure 3.5d). These results proved

that DON could be detected in Trappe and Kronjet against the blank, by probing the C=O feature at 1683 cm^{-1}.

To quantify this result, the 2nd derivative spectra were calculated identically as described in previous paragraphs. The spectra showed a statistically significant difference in the typical DON C=O vibrational mode at 1683 cm^{-1}, between the non-contaminated wheat against all wheat samples with levels of DON exceeding the EU limit (Figure 3.5e). This difference was quantified by the integration of the C=O band between 1702–1672 cm^{-1} which showed that this difference was significant compared to the non-contaminated wheat, for Trappe ($p=0.009$) and Kronjet ($p=0.016$), after ANOVA statistical testing (Section 3.2.8.2, Figure 3.5f).

We further proved intra-experiment variation and intra-day repeatability of S-PEIRS for this set of experiments (Figure S3.12). The intra-experiment variation was assessed by calculating the relative standard deviation (RSD) of the n=5 technical replicates which were 5%, 18% and 7% for NC, for Trappe 1%, 5%, and 11%, and for Kronjet 6%, 6% and 20%. The intra-day repeatability was assessed by calculating the RSD of the pooled data of the N=3 and n=15 analyses per variety, which was 11% for the NC, 7% for Trappe and 17% for Kronjet.

Overall, S-PEIRS could accurately and robustly distinguish non-compliant contaminated wheat from non-contaminated wheat. However, the individual differences between Trappe and Kronjet could not clearly be quantified. Thus, to assess (semi-)quantitative performance of S-PEIRS, a final set of experiments was conducted with contaminated wheat closer to the ML.

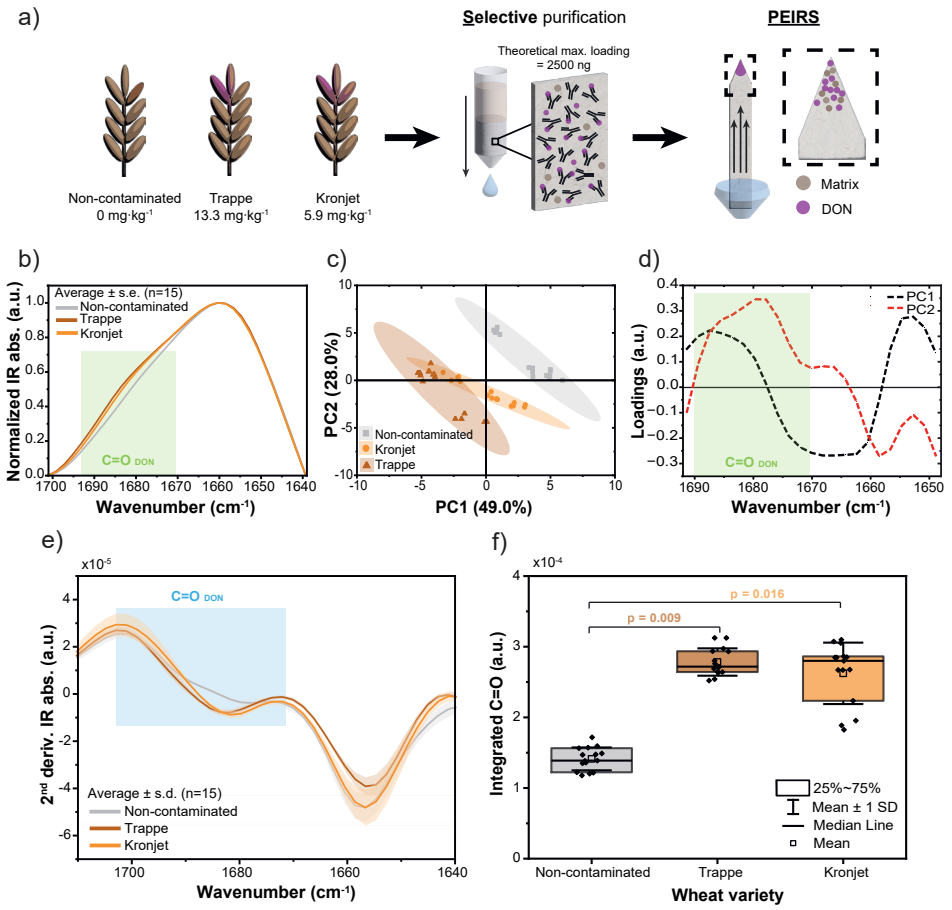


Figure 3.5: *Evaluation of S-PEIRS using wheat from field-trials. a) Austrian field-trial wheat varieties ('Trappe', and 'Kronjet') contained DON at levels exceeding the EU regulatory limit in unprocessed wheat. These wheat varieties were compared with a non-contaminated wheat that had no detectable levels of DON as determined by LC-MS/MS. N=3 IACs and paper tips per sample extract were prepared and measured using n=5 technical replicates (n=15 spectra per variety). b) The amide I band and DON region was baselined and the absorbance spectra were normalized to 1. The DON C=O signal was visible in the spectra of Trappe and Kronjet (green box) outside of the standard error of the non-contaminated. Thereof, 2nd derivative spectra were calculated and c) the PCA scores and 95% confidence ellipsoids showed separation of the non-contaminated (grey) and the DON containing samples (brown and orange) in PC1 (49.0%) and PC2 (28.0%). d) The loadings of PC1 and PC2 against wavenumber show which variables were responsible for the greatest degree of separation, clearly showing the contribution of the DON region (green box). e) The vibrational mode specific for DON (C=O, 1683 cm-1, blue) was identified in the 2nd derivative of all spectra of the DON containing wheat samples. f) After integration of the C=O peak between 1702 – 1672 cm-1, the mean areas of Trappe and Kronjet showed significant difference compared to the non-contaminated (ANOVA, p=0.009 and p=0.016, respectively)*

3.3.3.5 High volume S-PEIRS to achieve DON detection around ML

S-PEIRS has proven qualitative detection capability of a molecular feature of DON in wheat; differentiating highly contaminated QC wheat (4.3 $mg \cdot kg^{-1}$) and field-trial wheat (5.9 and 13.3 $mg \cdot kg^{-1}$) via the vibrational mode of the C=O of DON at 1683 cm^{-1}. Yet, further optimization of S-PEIRS was required to achieve DON detection at the legal limit of 1 $mg \cdot kg^{-1}$ in contaminated wheat materials. This limit was related to the maximum quantity of DON that could wick into the paper tip, which could maximally reach 400 ng in the conditions above (following a 20% w/v extraction). Thus, we hypothesized that applying a larger loading volume could increase the quantity of DON recovered after sample preparation.

To test this hypothesis, we: i) measured the recovery of the sample preparation using different loading volumes (2, 6, 10 mL) with extracts from QC wheat contaminated at 1.8 $mg \cdot kg^{-1}$; ii) evaluated which of these volumes allowed for the IR detection of the DON C=O.

We present, in Table S3.1, the LC-MS/MS results of DON after loading 2, 6 or 10 mL of extract to the IACs, showing a recovery rate of 91 ± 3%, 84 ± 7% and 77 ± 9%, respectively. In Figure S3.13, the results of LC-MS/MS and S-PEIRS against the different loading volumes are presented. The quantity of DON in the eluate was proportional to the loading volume (Figure S3.13b, $R^2 = 0.998$), verifying that increasing the loading volume allowed to maximize DON enrichment. Moreover, the eluate of the 10 mL loading volume contained DON quantities in the range of the maximum capacity stated by the producer (~2500 ng). After LC-MS/MS analysis, the residual eluate volume (~1.4 mL) was used to perform S-PEIRS analysis of the same sample set. The results showed a monotonic trend of the integrated IR spectral areas of the DON C=O vibration as a function of the loading volume (Figure S3.13c). A blank QC wheat material data set, obtained using the standard 2 mL procedure (Section 3.2.7.2, Figure S3.10), was added to compare the sample responses to a typical background signal. The average DON quantity present in the total eluate volume after loading 2 mL (655 ± 25 ng) could not be used to differentiate the sample from the blank by S-PEIRS. On the other hand, the higher loading volumes of 6 and 10 mL showed that DON could be detected based on the C=O feature. Care should be taken with this comparison, as also the amount of matrix loaded onto the IAC was variable between the experiments. Still, the MS and IR data suggested that loading 10 mL of extracts from contaminated wheat around the ML (1 $mg \cdot kg^{-1}$) could allow the detection of the C=O vibration of DON using S-PEIRS.

To prove the hypothesis stated above, milled blank wheat was mixed with highly contaminated milled Kronjet wheat (Section 3.2.7.4). The obtained DON contamination levels were 0, 0.6, 2.2, 2.5, 3.9 and 4.3 $mg \cdot kg^{-1}$, as determined by LC-MS/MS analysis (Table S3.2). To minimize the influence of sample heterogeneity

on the S-PEIRS results, for each extraction a triplicate was considered (Figure 3.6). Aliquots of 0.1 mL were used for LC-MS/MS analysis, and 1.4 mL were used to perform S-PEIRS as illustrated in Figure 3.6a. As in Section 3.3.3.4, we processed the spectra in the region of the amide I band of protein and the C=O of DON (Figure 3.6b). The molecular signature of the DON C=O was visible in the normalized spectra (Figure 3.6b) and the 2nd derivative spectra (Figure 3.6c, green box). We in turn utilized PCA to show that contaminated samples group separately from blank material, as shown in the score plot (Section 3.2.8.1, Figure 3.6d). The score plot also showed proportionality of the mixed wheat samples along the diagonal of the first and fourth quadrant; this trend was related to the DON region in the loadings plot, suggesting that DON content allows to differentiate the levels of contamination (Figure S3.14). Thus, similar as in previous paragraphs, we performed the integration of the 2nd derivative of the spectra in the range of the C=O of DON (Figure 3.6c, green box). The integration showed a monotonic trend of the integrated area of the C=O of DON as a function of the contamination level (Figure 3.6e). The differences between the blank and the contaminated materials were identified (Section 3.2.8.2) and showed significances of $p=0.11$, $p=0.0024$, $p<0.0001$, $p=0.00039$ and $p<0.0001$ for 0, 0.6, 2.2, 2.5, 3.9 and 4.3 mg·kg^{-1}, respectively. Thus, DON could be successfully detected in a the range around the ML of 1 mg·kg^{-1}.

The integrated S-PEIRS signal (from the paper substrate) and MS-determined DON concentrations (in solution) were plotted against the DON contamination (Figure 3.6f). The comparison of the two approaches showed a similar monotonic trend, confirming that both IR and MS can detect the increasing level of DON contamination in mixed Kronjet wheat. However, we must note that MS shows a plateau above 2.2 mg·kg^{-1} (1711 $\pm$ 150 ng·mL^{-1}; 3295 $\pm$ 210 ng) because of reaching the maximum IAC capacity (Table S3.2); while the IR results of 3.9 and 4.3 mg·kg^{-1} were most likely influenced by other matrix effects as a result of the mixing. It is plausible that such limitations could be overcome by i) simple dilution of the highly contaminated extract prior to application to the IAC in order to not exceed the maximum loading capacity of the IAC [51] and decrease matrix-mixing influence, or ii) alternative paper-based and cost-effective sample processing circumventing the need of an IAC altogether [54,55].

Overall, the direct IR detection of DON in the range of the ML was achieved using S-PEIRS marking a unique development in the field of IR spectroscopy and food safety analysis.

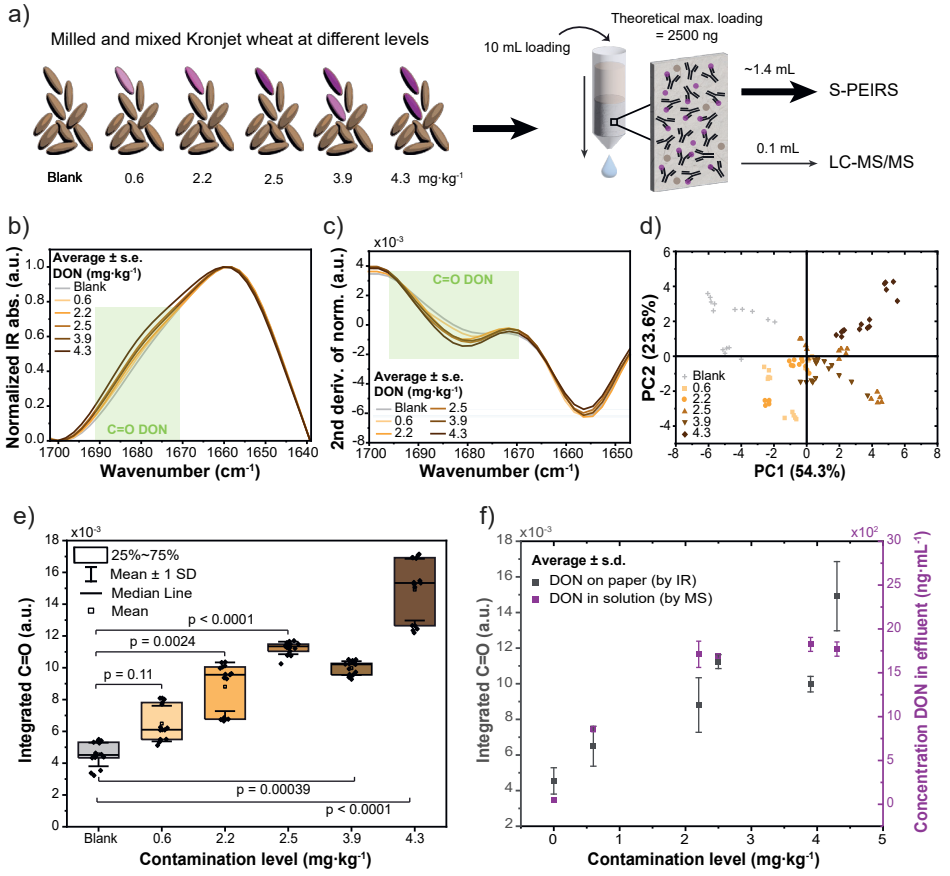


Figure 3.6: *Evaluation of linear performance of DON detection in field-trial wheat by S-PEIRS. a) Illustration of the experimental workflow to analyze different contamination levels, in triplicates. b) Cut, baselined and normalized [0-1] S-PEIRS spectra (N=3, n=5), in the region of the amide I band of protein and the DON C=O (green box). c) S-PEIRS spectra after 2nd derivative analysis showing the C=O signature of DON (green box). d) PCA score plot of the 2nd derivative spectra between 1700-1670 cm-1, with PC1 and PC2 explaining 54.3% and 23.6% of the variance, respectively. e) Integration of the 2nd derivative area, in the same region as for PCA of the DON C=O. p-values were evaluated following statistical testing. f) Average concentration of DON measured in the eluate by LC-MS/MS (purple) and average integrated DON C=O area detected following S-PEIRS (dark grey), against the determined contamination of DON in the starting material (mixed field-trial wheat).*

3.4 Conclusions

In this work, S-PEIRS is presented as a novel IR-based method to allow molecular identification of toxins in food at relevant levels. The developed strategy combines selectivity, enrichment and analyte identification in one method to achieve molecular identification of DON in multiple wheat varieties by ATR-FTIR.

The method leverages the enrichment of the DON toxin in a paper substrate, and then uses its predominant molecular feature for direct analysis. The intensity of the C=O molecular signature of DON is indeed directly proportional to the concentration of the toxin, and is used to develop a paper-based framework, termed here PEIRS; which allows improving the detection capability of ATR-FTIR by a factor 40, from 100 $\mu g \cdot mL^{-1}$ to 2.5 $\mu g \cdot mL^{-1}$. Immunoaffinity columns are then introduced to gain selectivity, here defined as S-PEIRS. Independently from wheat matrix impurities that co-eluted from the column, S-PEIRS achieves the successful differentiation in the ML range (1 $mg \cdot kg^{-1}$) between compliant and non-compliant mixed wheat material from field-trials which were naturally contaminated with DON. Thus, for the first time, IR is used to detect a molecular feature of DON in non-compliant wheat directly, with high sensitivity, selectively, and with robustness; as demonstrated via comparison with LC-MS/MS analysis.

The developed S-PEIRS concept opens new possibilities for label-free target analyte screening based on the actual molecular feature of the contaminant via mid-IR spectroscopy. In the field of mycotoxin analysis, other DON-conjugates are known to cross-react in IACs, such as DON-3-glucoside, 15-acetyl-DON, and 3-acetyl-DON. Although the prevalence of these conjugates is often much lower than that of DON itself. The molecular identification of S-PEIRS paves the way for their future differentiation from DON. Furthermore, different IACs could be employed to study other (myco-)toxins in different commodities, since the hyper-concentration by (S-)PEIRS is universal. Other paper-based purification and enrichment strategies may be explored to circumvent the need for IACs and to improve the usability of the method while reducing costs. Additionally, efforts towards on-site applicability should include optimization of paper tip drying time by active evaporation mechanisms.

Altogether, S-PEIRS and its further development shows potential for the implementation of paper-based IR as (semi-)quantitative tool with molecular identification power in food safety analysis to analyze a wide range of contaminants in different matrices.

Acknowledgements

The authors like to thank Barend van Lagen for his assistance with the FTIR instruments and Marc Lemmens for supplying the wheat material. The authors thank the support and funding of the Shared Research Facilities (SRF) of Wageningen University and Research (The Netherlands). The authors gratefully acknowledge the facility NanoFACT (Wageningen, The Netherlands) for the support and assistance in undertaking this work.

References

1. Pitt, J. I. & Miller, J. D. A Concise History of Mycotoxin Research. J. Agric. Food Chem. 65, 7021–7033 (2017).
2. Eskola, M. et al. Worldwide contamination of food-crops with mycotoxins: Validity of the widely cited 'FAO estimate' of 25%. Crit. Rev. Food Sci. Nutr. 60, 2773–2789 (2020).
3. El-Sayed, R. A., Jebur, A. B., Kang, W. & El-Demerdash, F. M. An overview on the major mycotoxins in food products: characteristics, toxicity, and analysis. J. Future Foods 2, 91–102 (2022).
4. Johns, L. E., Bebber, D. P., Gurr, S. J. & Brown, N. A. Emerging health threat and cost of Fusarium mycotoxins in European wheat. Nat. Food 3, 1014–1019 (2022).
5. The European Commission. Commission Regulation (EU) 2023/915 of 25 April 2023 on maximum levels for certain contaminants in food and repealing Regulation (EC) No 1881/2006. (2023).
6. The European Commission. Commission Regulation (EU) 2024/1022 of 8 April 2024 amending Regulation (EU) 2023/915 as regards maximum levels of deoxynivalenol in food. (2024).
7. van Der Fels-Klerx, H. J., Van Asselt, E. D., Madsen, M. S. & Olesen, J. E. Impact of Climate Change Effects on Contamination of Cereal Grains with Deoxynivalenol. PLoS ONE 8, e73602 (2013).
8. Csenki, E. et al. Stakeholder assessment for mycotoxin analysis: exploring the demand along the European food supply chain. World Mycotoxin J. 16, 287–299 (2023).
9. Sulyok, M., Suman, M. & Krska, R. Quantification of 700 mycotoxins and other secondary metabolites of fungi and plants in grain products. Npj Sci. Food 8, 1–8 (2024).
10. Sulyok, M., Stadler, D., Steiner, D. & Krska, R. Validation of an LC-MS/MS-based dilute-and-shoot approach for the quantification of > 500 mycotoxins and other secondary metabolites in food crops: challenges and solutions. Anal. Bioanal. Chem. 412, 2607–2620 (2020).
11. The European Commission. Commission Implementing Regulation (EU) 2023/2782 of 14 December 2023 laying down the methods of sampling and analysis for the control of the levels of mycotoxins in food and repealing Regulation (EC) No 401/2006. (2023).
12. Jafari, S. et al. ASSURED Point-of-Need Food Safety Screening: A Critical Assessment of Portable Food Analyzers. Foods 10, 1399 (2021).
13. Geballa-Koukoula, A. et al. Best practices and current implementation of emerging smartphone-based (bio)sensors - Part 2: Development, validation, and social impact. TrAC Trends Anal. Chem. 161, 116986 (2023).
14. Bosman, A. J. et al. Interconnectable 3D-printed sample processing modules for portable mycotoxin screening of intact wheat. Anal. Chim. Acta 1285, 342000 (2024).
15. Nolan, P., Auer, S., Spehar, A., Elliott, C. T. & Campbell, K. Current trends in rapid tests for mycotoxins. Food Addit. Contam. Part A 36, 800–814 (2019).
16. Majdinasab, M., Aissa, S. Ben & Marty, J. L. Advances in Colorimetric Strategies for Mycotoxins Detection: Toward Rapid Industrial Monitoring. Toxins vol. 13 (2021).
17. Di Nardo, F., Chiarello, M., Cavalera, S., Baggiani, C. & Anfossi, L. Ten Years of Lateral Flow Immunoassay Technique Applications: Trends, Challenges and Future Perspectives. Sensors 21, 5185 (2021).

18. Xing, K.-Y., Shan, S., Liu, D.-F. & Lai, W.-H. Recent advances of lateral flow immunoassay for mycotoxins detection. TrAC Trends Anal. Chem. 133, 116087 (2020).
19. Yu, Q. et al. Gold nanoparticles-based lateral flow immunoassay with silver staining for simultaneous detection of fumonisin B1 and deoxynivalenol. Food Control 54, 347–352 (2015).
20. Huang, X., Huang, X., Xie, J., Li, X. & Huang, Z. Rapid simultaneous detection of fumonisin B1 and deoxynivalenol in grain by immunochromatographic test strip. Anal. Biochem. 606, 113878 (2020).
21. Zhang, X. et al. Multiplex Lateral Flow Immunoassays Based on Amorphous Carbon Nanoparticles for Detecting Three Fusarium Mycotoxins in Maize. J. Agric. Food Chem. 65, 8063–8071 (2017).
22. Foubert, A. et al. Development of a Rainbow Lateral Flow Immunoassay for the Simultaneous Detection of Four Mycotoxins. J. Agric. Food Chem. 65, 7121–7130 (2017).
23. Li, R., Meng, C., Wen, Y., Fu, W. & He, P. Fluorometric lateral flow immunoassay for simultaneous determination of three mycotoxins (aflatoxin B1, zearalenone and deoxynivalenol) using quantum dot microbeads. Microchim. Acta 186, 748 (2019).
24. Li, R. et al. Polydopamine coated zirconium metal-organic frameworks-based immunochromatographic assay for highly sensitive detection of deoxynivalenol. Anal. Chim. Acta 1131, 109–117 (2020).
25. Nguyen, N. T. et al. Cross-reactivity of commercial and non-commercial deoxynivalenol-antibodies to emerging trichothecenes and common deoxynivalenol-derivatives. World Mycotoxin J. 12, 45–54 (2019).
26. Ruprich, J. & Ostrý, V. Immunochemical methods in health risk assessment: cross reactivity of antibodies against mycotoxin deoxynivalenol with deoxynivalenol-3-glucoside. Cent. Eur. J. Public Health 16, 34–37 (2008).
27. Tangni, E. K., Motte, J.-C., Callebaut, A. & Pussemier, L. Cross-reactivity of antibodies in some commercial deoxynivalenol test kits against some fusariotoxins. J. Agric. Food Chem. 58, 12625–12633 (2010).
28. Gonçalves, C. & Stroka, J. Cross-reactivity features of deoxynivalenol (DON)-targeted immunoaffinity columns aiming to achieve simultaneous analysis of DON and major conjugates in cereal samples. Food Addit. Contam. Part A 33, 1053–1062 (2016).
29. Freitag, S., Sulyok, M., Logan, N., Elliott, C. T. & Krska, R. The potential and applicability of infrared spectroscopic methods for the rapid screening and routine analysis of mycotoxins in food crops. Compr. Rev. Food Sci. Food Saf. 21, 5199–5224 (2022).
30. Lemmink, I. B. et al. Chapter Two - Recent advances and challenges in the analysis of natural toxins. in Advances in Food and Nutrition Research (ed. Toldrá, F.) vol. 110 67–144 (Academic Press, 2024).
31. Ramer, G. & Lendl, B. Attenuated Total Reflection Fourier Transform Infrared Spectroscopy. in Encyclopedia of Analytical Chemistry (John Wiley & Sons, Ltd, 2013). doi:10.1002/9780470027318.a9287.
32. Hinkov, B. et al. A mid-infrared lab-on-a-chip for dynamic reaction monitoring. Nat. Commun. 13, 4753 (2022).
33. Fomina, P. et al. A Portable Infrared Attenuated Total Reflection Spectrometer for Food Analysis. Appl. Spectrosc. 77, 1073–1086 (2023).
34. Sieger, M. et al. Portable Infrared Laser Spectroscopy for On-site Mycotoxin Analysis. Sci. Rep. 7, 44028 (2017).
35. Etezadi, D. et al. Nanoplasmonic mid-infrared biosensor for in vitro protein secondary structure detection. Light Sci. Appl. 6, e17029–e17029 (2017).
36. Kim, S.-S., Young, C. & Mizaikoff, B. Miniaturized mid-infrared sensor technologies. Anal. Bioanal. Chem. 390, 231–237 (2008).
37. De Girolamo, A. et al. Rapid screening of ochratoxin A in wheat by infrared spectroscopy. Food Chem. 282, 95–100 (2019).

38. Femenias, A. et al. Optimizing extraction solvents for deoxynivalenol analysis in maize via infrared attenuated total reflection spectroscopy and chemometric methods. Anal. Methods 15, 36–47 (2023).
39. Fomina, P. et al. Prediction of Deoxynivalenol Contamination in Wheat via Infrared Attenuated Total Reflection Spectroscopy and Multivariate Data Analysis. ACS Food Sci. Technol. 4, 895–904 (2024).
40. Freitag, S. et al. Attenuated total reflection mid-infrared spectroscopy to screen Austrian and French wheat from multiple years for deoxynivalenol. Spectrochim. Acta. A. Mol. Biomol. Spectrosc. 340, 126340 (2025).
41. Kos, G. et al. A novel chemometric classification for FTIR spectra of mycotoxin-contaminated maize and peanuts at regulatory limits. Food Addit. Contam. Part A 33, 1596–1607 (2016).
42. Öner, T. et al. Machine learning algorithms for the automated classification of contaminated maize at regulatory limits via infrared attenuated total reflection spectroscopy. World Mycotoxin J. 12, 113–122 (2019).
43. Mampallil, D. & Eral, H. B. A review on suppression and utilization of the coffee-ring effect. Adv. Colloid Interface Sci. 252, 38–54 (2018).
44. Paper Microfluidics: Theory and Applications. (Springer, Singapore, 2019). doi:10.1007/978-981-15-0489-1.
45. Ruggeri, F. S., Mannini, B., Schmid, R., Vendruscolo, M. & Knowles, T. P. J. Single molecule secondary structure determination of proteins through infrared absorption nanospectroscopy. Nat. Commun. 11, 2945 (2020).
46. Jansson, P. A. Deconvolution: With Applications in Spectroscopy. (Academic Press, 1984).
47. Dong, A., Huang, P. & Caughey, W. S. Protein secondary structures in water from second-derivative amide I infrared spectra. Biochemistry 29, 3303–3308 (1990).
48. Ruggeri, F. S. et al. Infrared nanospectroscopy characterization of oligomeric and fibrillar aggregates during amyloid formation. Nat. Commun. 6, 7831 (2015).
49. Salentijn, G. Ij. & Hoekstra, M. H. Sensor cartridge for chemical assays of a liquid sample containing analyte molecules. (2018).
50. Cheng, H. et al. Drug preconcentration and direct quantification in biofluids using 3D-Printed paper cartridge. Biosens. Bioelectron. 189, 113266 (2021).
51. MacDonald, S. J. et al. Determination of Deoxynivalenol in Cereals and Cereal Products by Immunoaffinity Column Cleanup with Liquid Chromatography: Interlaboratory Study. J. AOAC Int. 88, 1197–1204 (2005).
52. Şenyuva, H. Z. & Gilbert, J. Immunoaffinity column clean-up techniques in food analysis: A review. J. Chromatogr. B 878, 115–132 (2010).
53. Romer Labs. DonStar Immunoaffinity columns. Romer Labs https://www.romerlabs.com/shop/inter_en/donstar-immunoaffinity-columns/ (2025).
54. Lemmink, I. B., Bosma, S., Bovee, T. F. H., Zuilhof, H. & Salentijn, G. IJ. Paper-immobilized liquid-phase microextraction for direct paper spray mass spectrometry and immuno-detection of atropine in baby food, buckwheat cereals, and edible oils at regulatory levels. Anal. Chim. Acta 343823 (2025) doi:10.1016/j.aca.2025.343823.
55. Lemmink, I. B. et al. Modular Point-of-Need Tropane Alkaloid Detection at Regulatory Levels: Combining Solid–Liquid Extraction from Buckwheat with a Paper-Immobilized Liquid-Phase Microextraction and Immuno-Detection in Interconnectable 3D-Printed Devices. Anal. Chem. 96, 16462–16468 (2024).

Supplementary information to:

Selective paper-enhanced infrared spectroscopy for molecular detection of deoxynivalenol in wheat

SI Tables

Table S3.1: *LC-MS/MS results and recovery of different IAC loading volumes using QC wheat material contaminated at 1.8 mg·kg^{-1} (Three full replicates per volume, N=3).*

Loading volume (mL)	Measured DON concentration in eluate (ng·mL^{-1})	DON quantity in eluate (ng)	Recovery (%)
2	437 ± 17	655 ± 25	91 ± 3
6	1214 ± 99	1821 ± 149	84 ± 7
10	1861 ± 211	2792 ± 316	77 ± 9

Table S3.2: *LC-MS/MS analysis of different mixed and contaminated field-trial wheat levels used for loading onto the IACs using 10 mL extract volume in triplicate (n=3).*

Accurate contamination level mixed wheat (µg·kg^{-1})	Contamination level reported (mg·kg^{-1})	Measured DON concentration in eluate (ng·mL^{-1})	Proportion of theoretical IAC capacity (%)	DON quantity in 1.4 mL eluate (ng)
29	0	50 ± 2	3	69 ± 3
575	0.6	858 ± 30	52	1201 ± 42
2248	2.2	1711 ± 150	103	2395 ± 210
2503	2.5	1690 ± 25	101	2366 ± 34
3902	3.9	1824 ± 80	109	2553 ± 112
4307	4.3	1770 ± 81	106	2478 ± 125

SI Figures

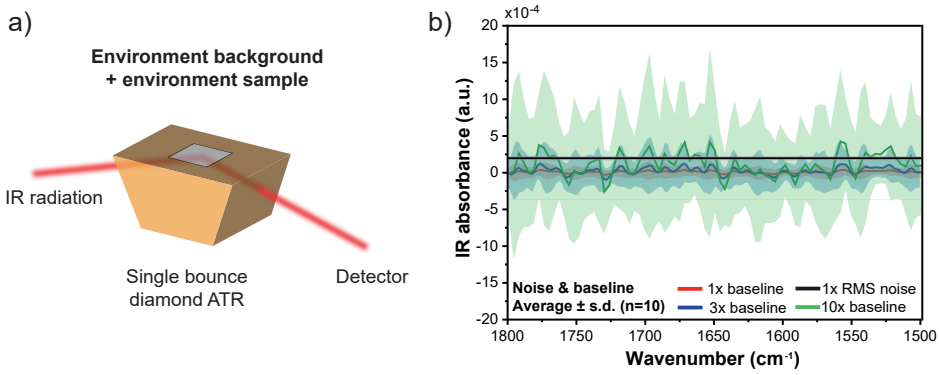


Figure S3.1: *Evaluation of the ATR-FTIR instrument sensitivity by characterizing the noise floor. a) The background of a clean and empty ATR prism was measured, followed by acquiring the sample spectrum of the same clean and empty ATR prism (n=10). b) The resulting baseline spectrum was plotted (red) and multiplied by 3x (blue) and 10x (green). The instrument noise floor was calculated based on the RMS noise between 1800-1500 cm^{-1} and was 7 ·10^{-5} ± 3 ·10^{-5} a.u.*

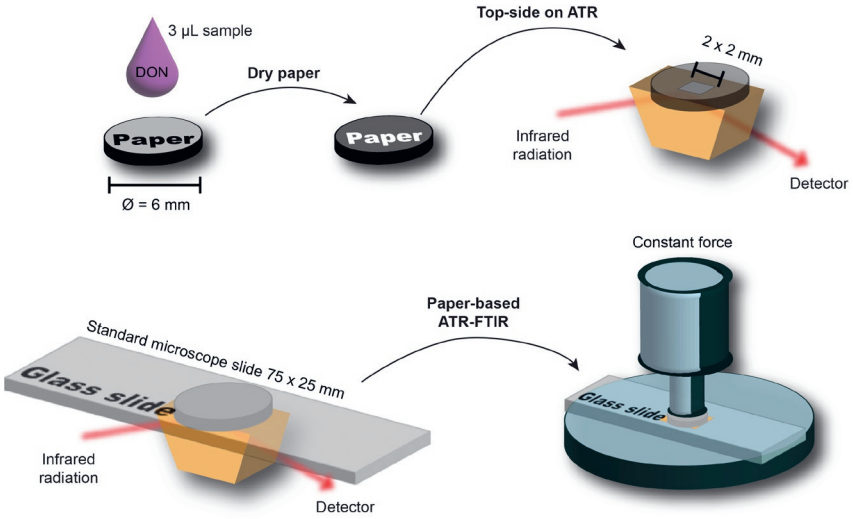


Figure S3.2: *Methodology of paper-based IR with paper discs to detect DON. Sample was drop-casted on a paper disc and dried under laboratory standard conditions for ≥1 hour to ensure full drying. The top-side of the paper was placed on the ATR prism and a standard microscope glass slide was placed on the paper. The ampul ensured close contact of sample and ATR prism.*

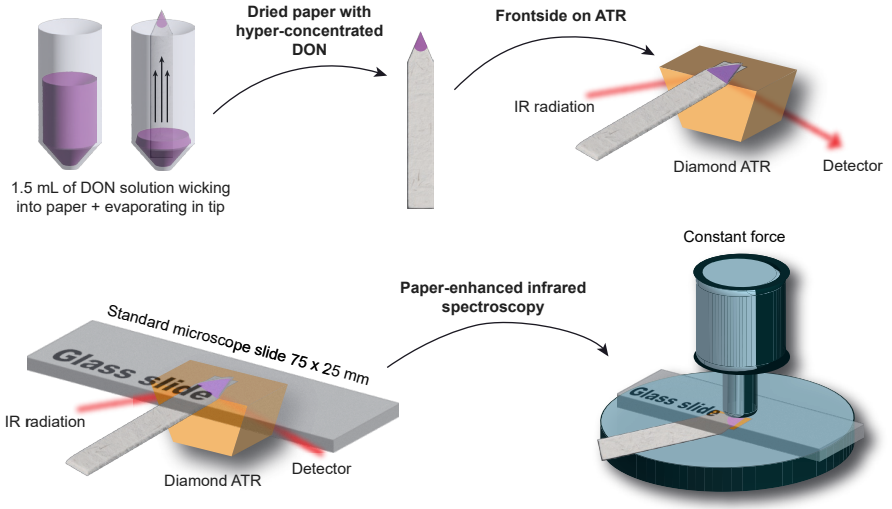


Figure S3.3: *Methodology of paper-enhanced infrared spectroscopy (PEIRS) with paper tips to hyper-concentrate and detect DON. A volume of 1.5 mL of DON at different concentrations (0 – 100 µg·mL-1) was hyper-concentrated in the PEIRS paper tips by inserting the tip in the solution and waiting for the tips to be completely dried (overnight). The frontside of the paper tip was placed on the ATR prism and a glass slide ensured uniform pressure between ATR ampul and prism, without damaging the paper. Then, ATR-FTIR analysis was performed to measure DON directly on the paper tip.*

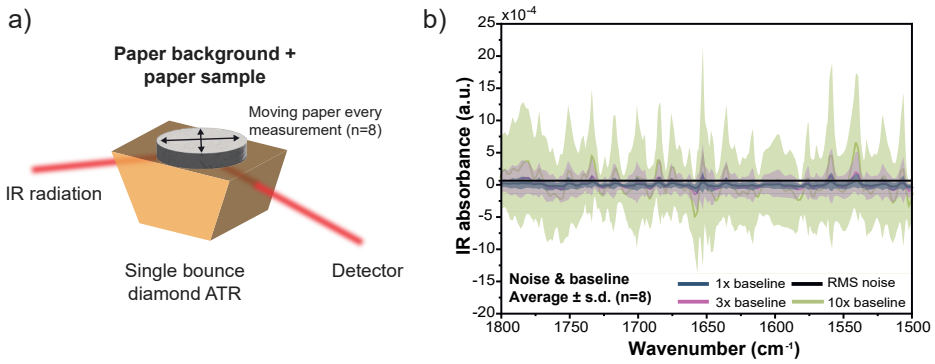


Figure S3.4: *Evaluation of the chemical variability by characterizing background noise of paper. a) The background of a clean paper was measured, followed by acquiring the sample spectrum of the same clean paper. We acquired n=10 technical replicates but for every new measurement the paper was slightly moved to account for its variability in composition. b) The resulting baseline spectra were plotted (blue) and multiplied by 3x (pink) and 10x (green). The noise floor with paper was calculated based on the RMS noise between 1800-1500 cm^{-1} and was 6 · 10^{-5} ± 2 ·10^{-5} a.u.*

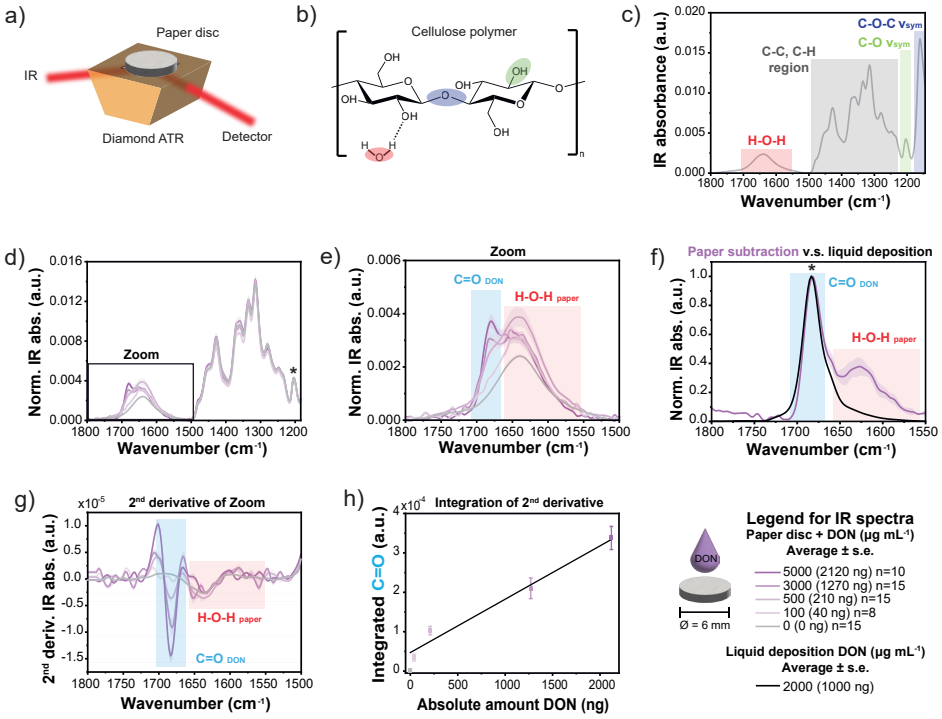


Figure S3.5: *Paper-based IR spectroscopy using paper discs for the detection of DON. a) The paper discs (6 mm Ø) used in this work were directly pressed onto the ATR prism. b) paper consists of the natural polymer cellulose which has characteristic hydroxyl (green) and ether (blue) groups. It is also hygroscopic (red). c) IR vibrations from these characteristic functional groups were identified and highlighted in similar colors. d) After normalisation to 1203 cm^{-1} (*), the region where paper IR signal dominates (1500 – 1145 cm^{-1}) overlaps. e) Zooming into the relevant region of the DON C=O, its IR signature was found over the IR background signal of paper for all concentrations, although convolution with the water IR band of paper occurred. f) To avoid false detection of the C=O of DON, the paper background was subtracted from the highest concentration DON on paper and compared to pure DON dried on the ATR prism, matching exactly in 1683 cm^{-1} after normalization (*) to 1. g) the C=O of DON was deconvoluted from the paper water band by second derivative analysis and h) the integrated areas were plotted as a function of concentration showing concentration dependency, and the error bars show the standard error.*

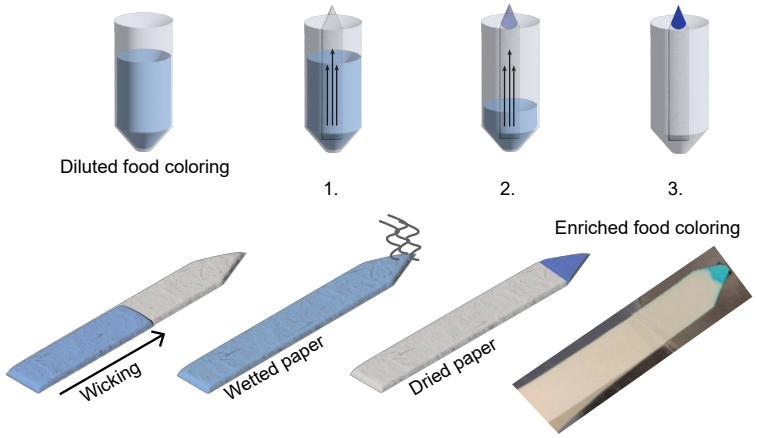


Figure S3.6: *Evaporation-induced enrichment in paper. An Eppendorf tube with blue dye in methanol was prepared and (1.) a PEIRS paper tip was inserted; (2.) the solution wicked into the paper and blue dye was enriched in the tip area due to increased evaporation in this three-phase contact boundary; (3.) after the paper tip was dried, it was clearly visible where the dye molecules were enriched at the tip. The same steps were also illustrated on the bottom, focusing on the paper enrichment mechanism in the tip area.*

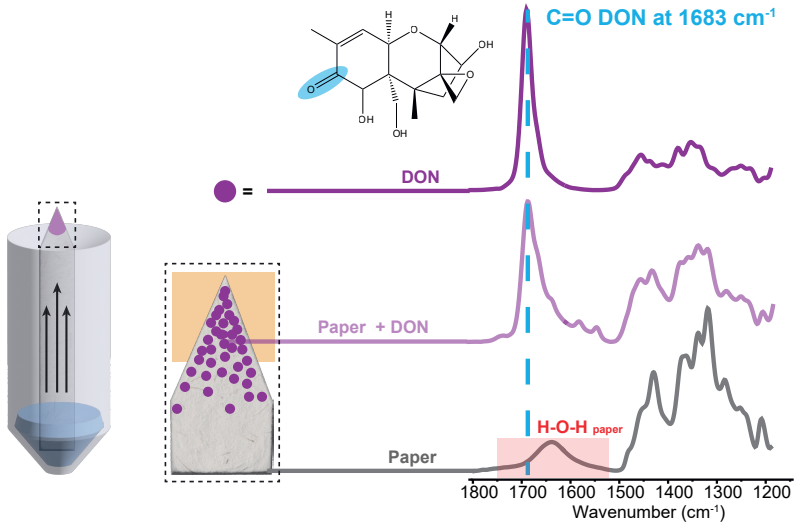


Figure S3.7: *DON hyper-concentration by PEIRS at 100 µg·mL^{-1}. The individual spectra of paper (grey) and pure DON analytical standard (purple) showed that the characteristic C=O vibration of DON (dashed blue line) occurred in an area of minimal paper absorbance. The peak centre of the characteristic DON C=O was at 1683 cm^{-1} for both the pure DON (purple) and hyper-concentrated DON (pink). This confirmed that the C=O of DON could be observed on top of the paper background signals, specifically the H-O-H band at 1640 cm^{-1} (red) that originates from water moisture in the air that is absorbed in the paper. The remaining part of the spectrum between 1500 – 1180 cm^{-1} showed features of both the paper and DON.*

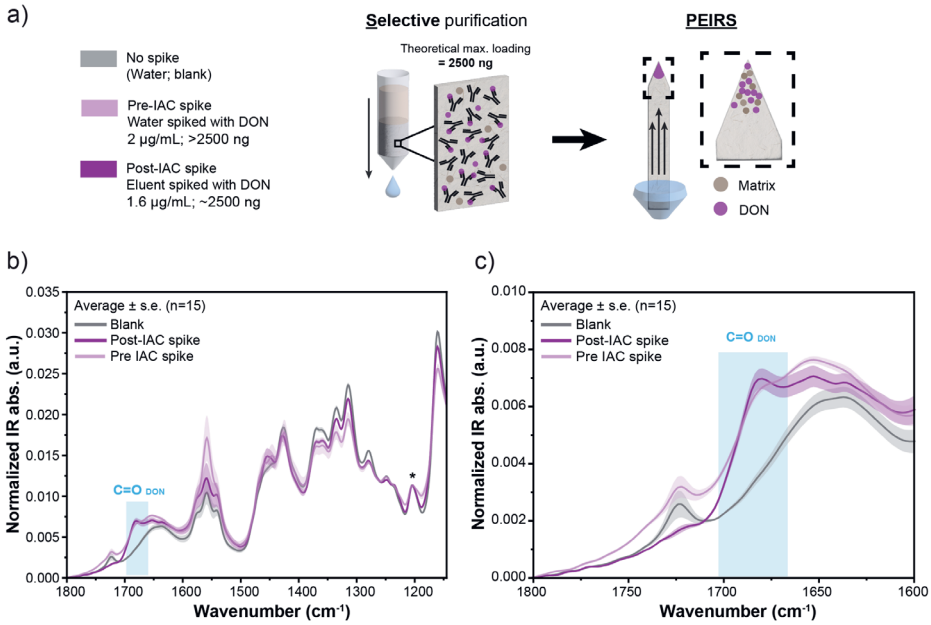


Figure S3.8: *Evaluation of S-PEIRS using DON standards in water. a) Blanks were prepared by applying 2 mL of ultrapure water to the IACs (n=6). Three blank eluents were used as is, to represent the background IR signal from running an IAC using 1.5 mL of methanol. Three blank eluents were spiked with 1.6 µg·mL^{-1} of DON (post-IAC spike), representing 100% recovery from the IAC. Three IACs were loaded with 2.0 µg·mL^{-1} of DON (pre-IAC spike), washed, and eluted in methanol, representing actual recovery from the IAC. All extracts were then hyper-concentrated and measured via S-PEIRS methodology. All paper tips (N=3) were analyzed using n=5 repeats leading to 15 spectra per experimental condition. b) the typical vibrational mode of DON, the C=O at 1683 cm^{-1}, was visible in the absorbance spectra for the samples containing DON, and not in the blanks. The IR signal between 1600-1500 cm^{-1} originated from the background of the IAC. c) The IR signal of the pre- and post-IAC spike clearly overlaps in the C=O vibration of DON, indicating that the recovery of DON is close to 100%.*

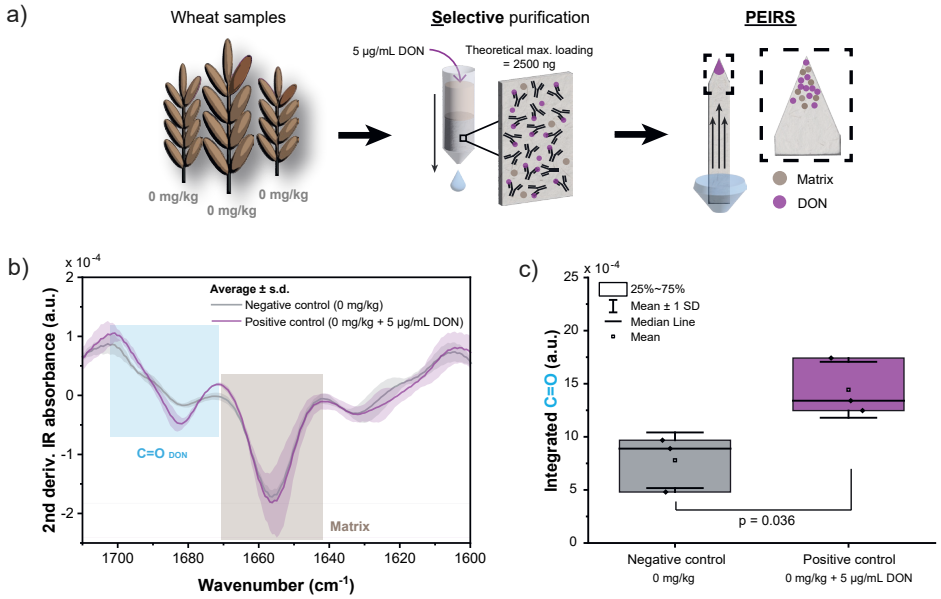


Figure S3.9: *Evaluation of S-PEIRS using spiked Quality Control (QC) wheat. a) Non-contaminated (NC) QC wheat (0 mg·kg^{-1}) was used as negative control (blank) and by spiking several NC extracts with DON analytical standard (5.0 µg·mL^{-1}), a positive control was prepared and analyzed following S-PEIRS. Every sample series consisted of N=3 independent experiments of n=5 technical replicates, which were averaged per experiment, to ensure statistical significance. b) For the relevant IR region, a second derivative analysis was performed. A difference in the C=O of DON (blue box) was observed between the blank and spiked sample. The region between 1670 – 1640 cm^{-1} (brown box) originated from matrix residues that retained and co-eluted from the column. c) The signals in the DON C=O region were integrated and plotted for the negative and positive control, showing an increasing trend. High significant difference (p=0.036) was found between the samples by one-way ANOVA with Fisher's LSD.*

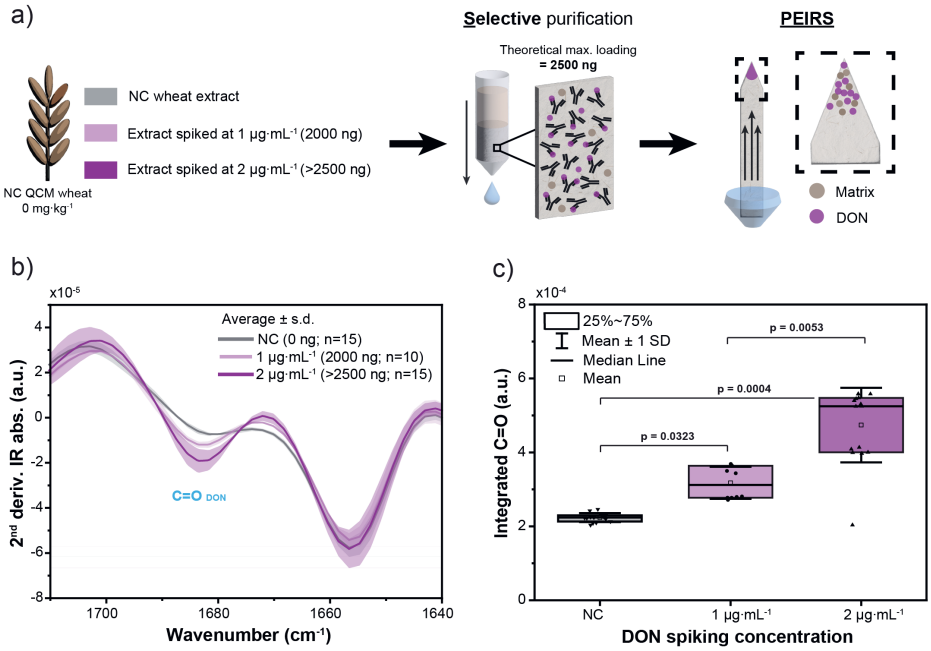


Figure S3.10: *Evaluation of S-PEIRS using spiked Quality Control Material (QC) wheat from 0- 2.0 µg·mL^{-1}. a) Non-contaminated (NC) QC wheat (0 mg·kg^{-1}) and two separate aliquots (2 x 6 mL) of this NC extract were spiked with DON analytical standard (1.0 and 2.0 µg·mL^{-1}). Every sample series consisted of N=3 independent experiments of n=5 technical replicates, except 1.0 µg·mL^{-1} (N=2; n=5). b) The relevant region of the DON C=O at 1683 cm^{-1} was subjected to second derivative analysis. The region between 1670 – 1640 cm^{-1} originated from matrix residues that retained and co-eluted from the column. c) The signals in the DON C=O region were integrated and plotted, showing significant differences (p=0.0323 and p=0.0004) between the means of 0 µg·mL^{-1} and the means of the spiked samples (1.0 and 2.0 µg·mL^{-1}) by one-way ANOVA with Fisher's LSD.*

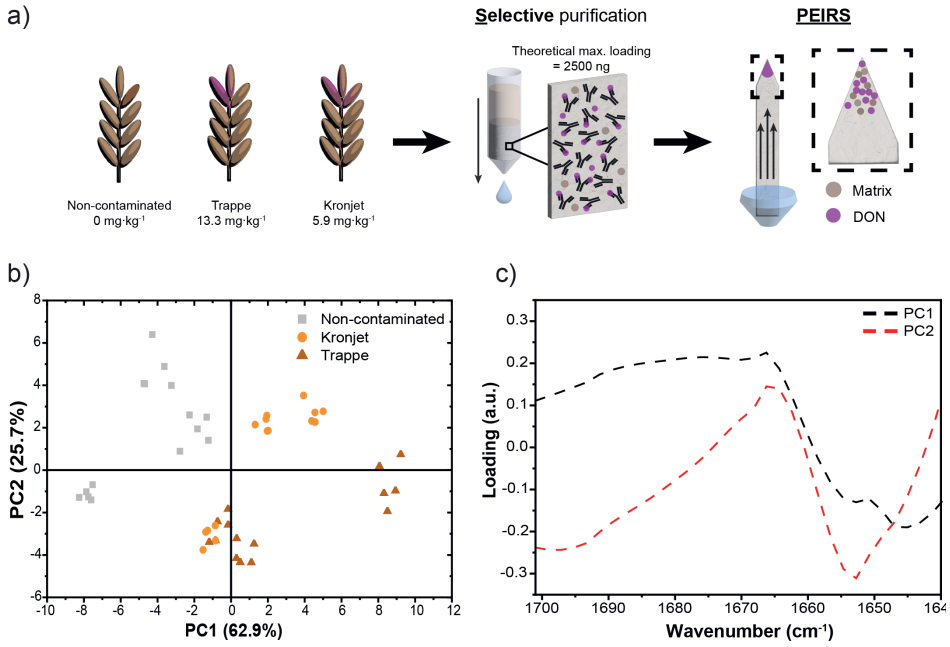


Figure S3.11: *Evaluation of S-PEIRS using wheat from field-trials. a) Austrian field-trial wheat varieties named 'Trappe', and 'Kronjet' contained 13.3 mg·kg^{-1} and 5.9 mg·kg^{-1} DON, respectively. Trappe and Kronjet were compared with a non-contaminated wheat (0 mg·kg^{-1}), as determined by LC-MS/MS. N=3 IACs and paper tips per sample extract were prepared and measured using n=5 technical replicates (n=15 spectra per variety). b) the PCA scores showed a difference between the non-contaminated (grey) and, Kronjet and Trappe (brown and orange) in PC1 (62.9%) and PC2 (25.7%). c) The loadings of PC1 and PC2 (smoothed with 9 pts 2nd order Savitzky-Golay filter) against wavenumber showed contribution to the separation from the DON region in PC1. Separation in PC2 was not specifically related to DON contribution.*

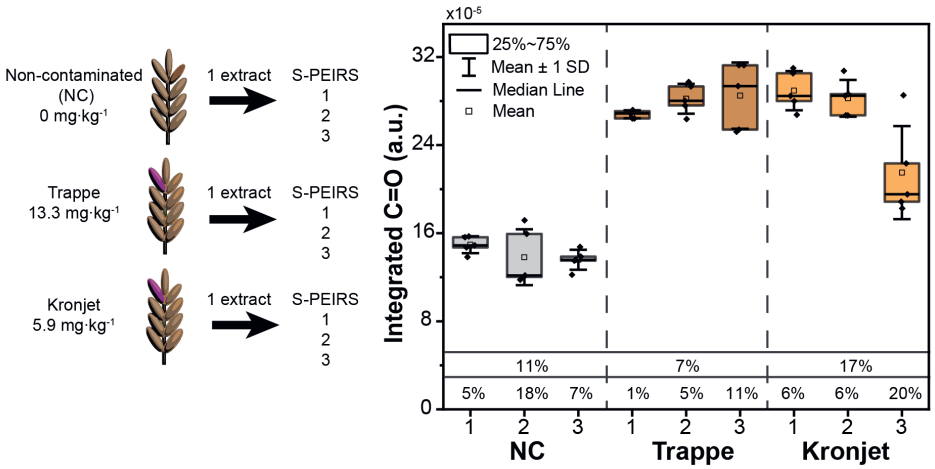


Figure S3.12: *Evaluation of intra-experiment variation and intra-day repeatability S-PEIRS for field-trial wheat samples. One extract per variety was prepared and N=3 S-PEIRS samples were analyzed using n=5 technical replicates. Every set of technical replicates was plotted to show the three intra-experiment variations per variety, which was expressed using the relative standard deviation. Then, the intra-day repeatability RSD (%) of the NC, Trappe and Kronjet experiments was 11%, 7% and 17% respectively.*

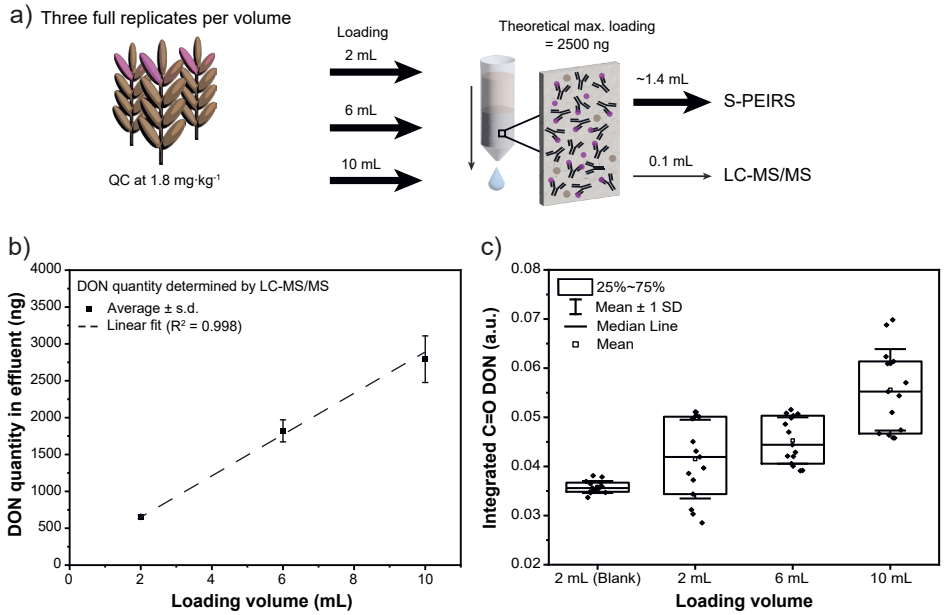


Figure S3.13: *Evaluation of the influence of loading volume on the DON quantity recovered after S-PEIRS. a) An illustration of the experimental workflow, for the different loadings on the IACs using full replications per volume. b) Results of the LC-MS/MS analysis (N=3, n=1) where loading volume was plotted against the determined average DON quantity (ng) in the eluate after the IAC. c) Results of the S-PEIRS analysis (N=3, n=5) where the loading volume was plotted against the integrated area of the DON C=O at 1683 cm^{-1}.*

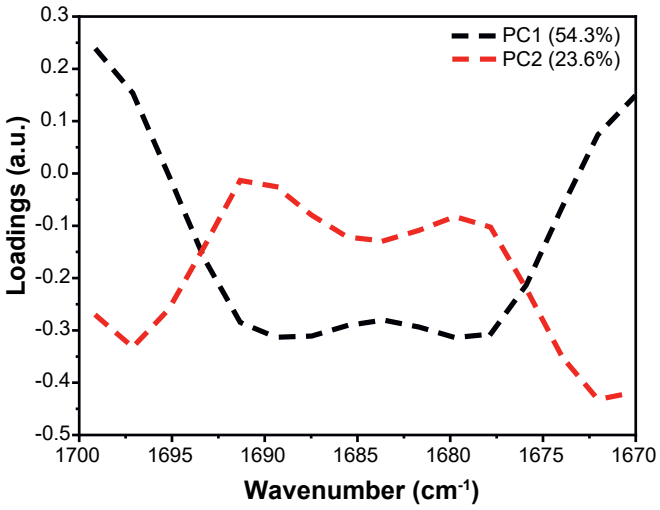


Figure S3.14: *PCA loading plot corresponding to the evaluation of milled and mixed Kronjet field-trial wheat.*


4

Detection of ochratoxin A in wine at the legal limit via solvent-based enrichment and paper-enhanced infrared spectroscopy

This chapter has been published as:
A.J. Bosman, I.B. Lemmink, F.S. Ruggeri, G.IJ. Salentijn.
Detection of ochratoxin A in white wine at the legal limit via solvent-based enrichment and selective paper-enhanced infrared spectroscopy.
Journal of Hazardous Materials. Volume 511. 2026. 142248.
doi.org/10.1016/j.jhazmat.2026.142248.

Abstract

Ochratoxin A (OTA) is a mycotoxin that occurs in many food products including cereals and wine, and is regulated at strict $\mu g \cdot kg^{-1}$ levels. Spectroscopy-based methods have shown potential for mycotoxin detection but have limitations regarding selectivity, sensitivity and molecular identification. Here, we present a method that combines a 2-step pH-dependent liquid-liquid extraction with our recently developed selective paper-enhanced infrared spectroscopy (S-PEIRS), to empower label-free, selective and concentration-dependent detection of OTA contamination in wine at the legal limit. This combination allowed for the purification and enrichment of OTA, from white wine spiked at 2, 6 and 20 $\mu g \cdot kg^{-1}$ into a focused area of a paper tip. A 2-step pH-dependent liquid-liquid extraction was optimized for OTA and benchmarked against high-performance liquid chromatography high-resolution mass spectrometry (HPLC-HRMS), showing extraction recoveries of ~70% per extraction, and an average enrichment factor (EF) of 40. The extracts were further divided in 2 mL aliquots and applied to immunoaffinity columns (IACs) showing recoveries >80%. Then, our approach leveraged the infrared detection of OTA on the paper tip, via the direct and linear detection of one of its molecular fingerprints (C=O, 1660 cm^{-1}).

Overall, our approach represents the first demonstration of concentration-dependent detection of OTA contamination in white wine, with an estimated detection limit at the legal limit of 2 $\mu g \cdot kg^{-1}$, an estimated limit of quantification of 6.7 $\mu g \cdot kg^{-1}$ and strong correlation with independent HPLC-HRMS analysis ($R^2 = 0.963$).

4.1 Introduction

The World Health Organization (WHO) estimated that annually one in ten people become ill as a result of contaminated food [1]. One major class of chemical food contaminants is mycotoxins, which is a group of naturally occurring toxins produced by fungi that can occur on many different agricultural products [2]. It has been reported that approximately 20% of these crops contain mycotoxin levels above the EU regulatory limits [2,3], while 60-80% of crops contained detectable levels of mycotoxins [2,4]. The most common regulated mycotoxins are produced by filamentous fungi of the genus *Fusarium*, *Aspergillus* and *Penicillium*, and their occurrence is expected to change as a result of global warming [4–7]. Worldwide, regulations are in place to monitor and control human and animal exposure to mycotoxins.

Sophisticated analytical methods for quantitative mycotoxin detection using liquid chromatography-mass spectrometry (LC-MS) are typically used [8]. Such comprehensive procedures are needed to accurately measure all regulated toxins ranging from relatively high maximum levels (MLs) of deoxynivalenol (DON, 600 – 1750 $\mu g \cdot kg^{-1}$ in unprocessed or milled cereals), down to low MLs (0.5 – 2 $\mu g \cdot kg^{-1}$) set out for highly toxic compounds such as ochratoxin A (OTA) and aflatoxin B1 (AFB1) [3,8,9]. While established analytical methods are necessary for confirmatory analysis [8,10–12], they require expert operation and sample preparation, are expensive and laboratory-bound [13]. Therefore, different spectroscopy-based analytical techniques are emerging in the field of food safety monitoring [14–16]. Spectroscopic analyses are typically fast, easy-to-operate, relatively inexpensive, considered environment-friendly, and in many cases (trans)portable [16]. These benefits are promising for the development of portable detection methods for mycotoxin monitoring [13].

Examples of spectroscopy methods that have been used to predict mycotoxin contamination are based on near- and mid-infrared (NIR and MIR) radiation, and allow detection of matrix changes that occur when produce is infected with fungi [16–18], which is an indirect approach to predict the occurrence of mycotoxins. NIR and MIR spectroscopy are ideally suited for high-throughput sample screening, and allow for the collection of large sample sets on which the success of the prediction models relies. While powerful for rapid pre-screening, these methods do not possess the capability of direct molecular identification of mycotoxins and thus cannot be used for confirmation and quantification [16–18]. Additionally, surface-selective spectroscopy platforms such as surface-enhanced Raman scattering (SERS) have been reported for sensitive and semi-quantitative mycotoxin detection [19–24]. However, reproducible and robust development of such surface-selective platforms has been a challenge for the field, which can be related to the (nano)fabrication of transducer surfaces, functionalization of affinity elements to transducer surfaces, prevention

of non-specific binding and regeneration of the surface in between consecutive experiments [25,26]. Similar challenges arise in related surface-selective spectroscopy platforms such as surface-enhanced infrared absorption spectroscopy and localized surface plasmon resonance spectroscopy [19,27–29].

To overcome the challenges related to the need of large sample sets, molecular identification, and (nano)fabrication of surface-selective substrates, a novel paper-based IR method was pioneered in our group recently [30]. This method, named selective paper-enhanced infrared spectroscopy (S-PEIRS), leverages capillary action and evaporation mechanisms to enrich solutes in a in tip-shaped chromatography paper. Subsequently, a spectral feature of the mycotoxin in the mid-infrared is measured for direct molecular detection. The implementation of an immunoaffinity column (IAC) allows for selective purification of the mycotoxin from a food commodity, resulting in a unique method capable of direct molecular detection without the need of (bio) chemical labels. This approach has been demonstrated for the detection of DON in wheat at the ML of 1000 $\mu g \cdot kg^{-1}$ [30]. However, mycotoxins like OTA are regulated at more strict MLs, such as those stipulated for OTA in wine (2 $\mu g \cdot kg^{-1}$). Thus, to enable the detection of mycotoxins at such strict limits, further advances towards enrichment are required.

In this work, these limitations are addressed by introducing a 2-step liquid-liquid extraction (LLE) for pH-dependent purification and enrichment of OTA prior to S-PEIRS, as OTA is weakly acidic and can become negatively charged in alkaline conditions [31,32]. In this study, we propose that the combination of selective enrichment by solvent-based clean-up and S-PEIRS is suitable for the concentration-dependent and linear detection of OTA in wine, via its molecular signature and down to the ML of 2 $\mu g \cdot kg^{-1}$ [3].

4.2 Materials & methods

4.2.1 Experimental design

The objective of this work was to develop a method that can detect a molecular feature of OTA in wine at or above the legal limit of 2 μg·kg^{-1} using attenuated total reflection Fourier Transform infrared (ATR-FTIR) spectroscopy. This strategy consisted of the following steps: i) studying the IR spectral signature of OTA, ii) selecting an OTA molecular feature for IR detection, first without the IAC (PEIRS), iii) defining the detection capability of S-PEIRS first from standard solutions and subsequently with wine matrix, and finally iv) establish an additional enrichment method prior to S-PEIRS to reach detection at ML. In the first three steps, the framework of S-PEIRS pioneered in our previous work [30], was tailored to OTA. In the final step, a two-step pH-dependent solvent extraction was developed. OTA is a weak organic acid with estimated pKa values of 4.3 and 7.2, and exists in neutral or negatively charged form depending on the pH (Figure 4.1a) [31,32]. In the first extraction step the wine, that is characterized by its acidic pH (~pH 2.5), contained neutral OTA. Therefore, the OTA was expected to favor partitioning to an apolar organic phase.

In the second step, alkaline aqueous solution was mixed with the organic phase leading to negatively charged OTA molecules, and hence OTA was expected to favor partitioning to the polar aqueous phase. Next to tuning the solubility of OTA using pH, the volume of the liquid-phase that contained OTA was minimized (Figure 4.1b). This was designed to achieve enrichment of OTA in the final extraction solution and was expected to be sufficiently concentrated for S-PEIRS at ML.

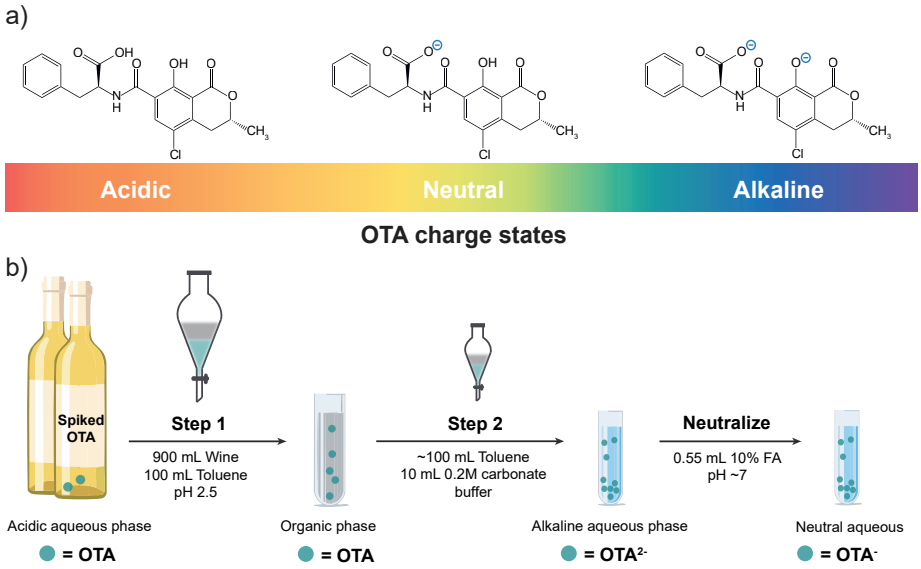


Figure 4.1: *S-PEIRS assisted by a 2-step pH-dependent solvent extraction to purify, enrich and detect OTA in wine at the ML of 2 µg·kg^{-1}. a) OTA has two acidic functional groups that allow pH-dependent solvent extraction. b) Complete workflow of pH-dependent solvent extraction and S-PEIRS for the direct detection a molecular feature of OTA in wine at ML. FA = formic acid.*

4.2.2 Reagents & consumables

Two types of white wine were purchased from a local grocery store in the Netherlands, a biological white wine (12.5% v/v, Spain), and a dealcoholized white wine (0.0% v/v, Italy). OTA analytical standard (BiopureTM, 5 mg, Romer Labs, Austria) was purchased as a solid with a purity of 97.6 ± 2.4%, and was dissolved in 1 mL chromatography grade methanol (Supelco® EMSURE, Merck, Germany) to obtain 5 mg·mL^{-1} stock solution and stored in the fridge (4 °C) until use. Chromatography grade ethanol (Supelco® EMSURE, Merck, Germany) was used to prepare water/ethanol solutions (15% v/v). Immunoaffinity columns (IACs) for OTA (OchraStarTM, Romer Labs, Austria) were kept in the fridge (4 °C) and were taken out of the fridge at least 15 min before use. The producer stated a loading capacity of 2000 ng for the OTA IACs.

Plastic stopcock luer valves (CHROMABOND®, laboratoriumdiscounter, Netherlands) were used to control the flow of the IACs. Deionized water was purchased from Merck (Millipore, Germany). Chromatography grade methanol was purchased from Merck (Supelco® EMSURE, Germany), and toluene (HPLC-grade) was purchased from Actu-All chemicals (Oss, The Netherlands). Carbonate buffer (pH 9.5, 0.2M) was prepared by mixing 0.2M sodium carbonate (Merck, Germany) and sodium bicarbonate (Merck, Germany) solutions. The pH was measured using

a pH-electrode (inoLab® pH7110, WTW, Germany). Formic acid (FA, ≥ 95%) was purchased from Sigma Aldrich (USA). Standard chromatography paper (Whatman® cellulose Chr1, 250 x 250 mm) was purchased from Merck (Germany).

4.2.3 Instruments & settings

4.2.3.1 High-pressure liquid chromatography high-resolution mass spectrometry

A high-pressure liquid chromatography high-resolution mass spectrometry (HPLC-HRMS) method was used as benchmark for the quantification of OTA in different samples and extracts. For the HPLC-HRMS method, an HPLC (1290 Infinity II LC; Agilent Technologies, USA), equipped with a ZORBAX SB-C18 column (3.0 × 250 mm, 5 µm; Agilent Technologies, USA) and a 1290 infinity II photodiode array detector (Agilent Technologies, USA) was coupled to a Q-Exactive quadrupole orbitrap HRMS (Thermo Fischer Scientific, USA). The column oven was set at 50 °C. The mobile phase consisted of 0.1% (v/v) FA in both water (mobile phase A) and methanol (mobile phase B), and the flow rate was 0.6 mL·min^{-1}, using an isocratic elution (0-10 minutes 70% B) followed by flushing of the column (10-10.30 minutes linear ramping to 90% B; 10.30 - 16 minutes 90% B) and re-equilibration (16-16.10 minutes linear decrease to 70% B; 16.10-21 minutes at 70% B). MS was performed in positive mode with a scan range of m/z 393-413 and a mass resolution of 70.000 full width at half maximum (FWHM, Table S4.1), a sheath gas flow rate of 10 L·min^{-1}, an auxiliary gas flow rate of 10 L·min^{-1}, a capillary temperature of 320 °C, an S-lens RF level of 90, an ion source interface voltage of 4 kV, and a heating block temperature of 400 °C were used.

Using these settings, the calibration curve for OTA was constructed between m/z 404.085-404.095. Therefore, 50 mg·L^{-1} OTA stock solution was diluted in water:methanol (1:1, v/v) to obtain calibration solutions with concentrations of 0, 0.5, 1, 5, 10, 50, 100 and 500 ng·mL^{-1} OTA. From each solution, 10 µL was injected, in triplicate. The constructed calibration curve was used as external standard to quantify the concentration of OTA in all samples and extracts prepared in this work (Figure S4.1). The limit of detection (LOD, Equation 4.1) and limit of quantification (LOQ, Equation 4.2) were estimated following:

$$LOD = 3 \times \frac{\sigma_{lowest}}{S} \qquad \textit{Equation 4.1}$$

$$LOQ = 10 \times \frac{\sigma_{lowest}}{S} \qquad \textit{Equation 4.2}$$

Where S is the slope of the calibration curve and σ_{lowest} is the standard deviation of the response at the lowest measured OTA concentration.

4.2.3.2 Precision-cutting of S-PEIRS tips

Chromatography paper was cut automatically into paper tips using an open-source 2D design software (Silhouette Studio® 4.5, USA) and a precision cutting device (Silhouette Curio 2, USA). The Silhouette Curio 2 was equipped with a flatbed cutting surface able of cutting in the XY direction. The flatbed surface was electrostatic, to hold the paper in place by electrostatic forces that did not alter the paper. The Silhouette Curio 2 was used to cut 64 tips from one sheet of paper (Figure S4.2) in less than 5 minutes. The paper tips were cut into strips of 40 mm x 5 mm, with at one end a tip having an angle of approximately 28°. The Silhouette Studio software settings that were used to operate the device are included in Table S4.2.

4.2.3.3 ATR-FTIR measurements

An FTIR spectrometer (Tensor 27, Bruker, USA) equipped with a single-bounce DiamondATR accessory (2 x 2 mm), a mid-IR source (4000-400 cm^{-1}) and a deuterated triglycine sulphate (DTGS) detector were used in this work. The FTIR spectrometer was operated using OPUS software (version 7.8, Bruker, USA). All the raw spectral data were analyzed using OriginPro (OriginLabs©, 2025, USA). The spectra were recorded using 512 co-averages, a scanner velocity of 10 kHz, a resolution of 4 cm^{-1}, an aperture of 6 mm, and atmospheric compensation was applied. Between every new set of measurements, a new background spectrum was recorded to correct for drifts in the background environment. For liquid deposition of OTA standard solution, N=3 individual depositions of 0.5 µL with n=3 technical replicates were measured, unless stated otherwise. For the dried PEIRS and S-PEIRS tips N=3 independent experiments and n=5 technical replicates were measured, unless stated otherwise. All the dried tips were positioned on the active area of the single-bounce ATR accessory of the FTIR. A glass slide was used to distribute the pressure applied by the ampul of the accessory evenly on the tip and to prevent damaging the paper.

4.2.3.4 ATR-FTIR data analysis

All recorded IR spectra were analyzed using a semi-automated analysis workbook via OriginPro. First, the raw data were cut to the fingerprint range (1800 – 1000 cm^{-1}) in which the fundamental vibrational modes of OTA were most distinct. The raw spectra were smoothed by Adjacent Averaging (window size 3) and Savitzky-Golay (window size 3, order 2) filters, and subsequently baselined (constant linear baseline).

For the PEIRS and S-PEIRS tip measurements, the single spectra were normalized to a point where paper showed a clear feature and OTA had minimal absorbance at 1315 cm^{-1}. Thereby, all signals related to the chromatography paper converged

and background deviations originating from the paper substrate were corrected. The normalized absorbance spectra were averaged per concentration level of OTA. A second derivative analysis (Savitzky-Golay filter of window size 9 and order 2) was used to deconvolve the molecular feature of OTA in all the single spectra in order to evaluate concentration-dependency. The OTA feature in every individual 2nd derivative spectrum was integrated, and the areas were plotted (boxplot) as a function of concentration.

The normality (Shapiro-Wilk) and variance (Two-Sample Test for Variance) of the data were tested prior to performing a Two Sample t-test for statistical analysis. Either equal or unequal variance were assumed depending on the result of the variance test, and the statistical significance of the results were evaluated.

4.2.4 Development of pH-dependent solvent extraction

4.2.4.1 Partitioning of OTA under different phase ratios

To optimize the first solvent extraction of OTA from acidic aqueous to organic solution, different phase ratios were evaluated. First, a large stock solution of 0.1% FA in water (pH ~ 2.7) containing 50 ng·mL^{-1} OTA was prepared. Subsequently, in a 50 mL falcon tube, this acidic aqueous solution was mixed in 1:1, 3:1, 7:1, 16:1, and 40:1 ratios with butyl acetate ensuring that the final volume of the mixture remained constant at 40 mL. Subsequently, the falcon tubes were vortexed for 2 minutes to ensure the two phases were properly mixed. Then, the falcon tube was centrifuged for 8 minutes at 2800 revolutions per minute (rpm), to ensure the phases were separated again. After this, 0.5 mL of the organic phase and 0.5 mL of the aqueous phase were collected. The 0.5 mL of the organic phase was evaporated under a gentle nitrogen flow, and redissolved in 1 mL MeOH:H_2O (1:1 v/v) to be analyzed with HPLC-HRMS (Section 4.2.3.1). Separately, to the 0.5 mL of collected aqueous solution 0.5 mL of MeOH was added to obtain MeOH:H_2O (1:1 v/v), after which it was analyzed with HPLC-HRMS (Section 4.2.3.1). The concentration of OTA (ng·mL^{-1}) in each phase was quantified using an external standard method (Figure S4.1). Subsequently, the amount of OTA in each phase was calculated.

4.2.4.2 Stability of OTA under different alkaline conditions

For the development of the second step of the solvent extraction, where OTA partitions from the organic to the alkaline aqueous solution, the stability of OTA in different alkaline conditions was assessed. HPLC-vials were filled with either 1 mL ultrapure water (pH ~ 7), 0.05M carbonate buffer (at pH ~ 9, 9.5, 10, 10.5, 11 or 12), or 0.05M NaOH (pH ~ 12.5). Subsequently, the alkaline solution was spiked with 10 µL of a 10 µg·mL^{-1} OTA solution in methanol and kept at room temperature (RT) for 12 hours. After 12 hours, the solution in each vial was analyzed using HPLC-HRMS.

Subsequently, after another 4 hours (t = 16 hours), the solution in each vial was analyzed again using HPLC-HRMS. The concentration of OTA ($ng \cdot mL^{-1}$) in each vial was quantified (Section 4.2.3.1, Figure S4.1).

4.2.4.3 Partitioning of OTA under different alkaline conditions

To optimize transfer of OTA from the organic to the alkaline aqueous solution, different alkaline conditions were evaluated. Therefore, 0.7 mL butyl acetate was mixed with 0.7 mL of ultrapure water (pH ~ 7), or 0.05M carbonate buffer at pH ~8.3, 9, 9.5, 10, or 10.5 containing 125 ng mL^{-1} OTA in a 2 mL Eppendorf tube. The 2 mL Eppendorf tube was vortexed for 2 minutes to ensure the phases were mixed. After this, the 2 mL Eppendorf tube was centrifuged for 8 min at 2800 rpm to ensure the phases were separated. Subsequently, 0.3 mL of the organic phase and 0.1 mL of the aqueous phase were collected. The collected organic phase was evaporated under a gentle nitrogen flow, and redissolved in 0.45 mL MeOH:H_2O (1:1 v/v) to be analyzed with HPLC-HRMS. The collected aqueous phase was diluted with 0.1 mL MeOH, to be analyzed with HPLC-HRMS. The concentration of OTA ($ng \cdot mL^{-1}$) in each phase was quantified. Subsequently, the recovery of OTA was calculated.

4.2.4.4 Toluene as organic phase

To further optimize the solvent extraction, besides butyl acetate used in the previous experiments, also toluene was tested. For this, a 15 mL falcon tube containing 1990 µL toluene was spiked with 10 µL of a 100 $\mu g \cdot mL^{-1}$ OTA solution in methanol. Subsequently, 0.5 mL of toluene was collected, evaporated under a gentle nitrogen flow, and redissolved in 1 mL MeOH:H_2O (1:1 v/v) to be analyzed with HPLC-HRMS. Then, 10 mL of 0.1% FA in H2O, dealcoholized wine, or regular wine was added to the falcon tube. The falcon tube was vortexed for 2 minutes to mix both phases. After this, the falcon tube was centrifuged for 8 minutes at 2800 rpm, to ensure the phases were separated again. Subsequently, 0.5 mL of toluene was evaporated under a gentle nitrogen flow, and redissolved in 1 mL MeOH:H_2O (1:1 v/v) for HPLC-HRMS analysis. The concentration of OTA ($ng \cdot mL^{-1}$) in toluene before and after the mixing was quantified.

4.2.5 Optimization of S-PEIRS for OTA in white wine

4.2.5.1 ATR-FTIR liquid deposition of OTA

A volume of 0.5 µL OTA standard solutions in MeOH (0, 0.2, 0.4, 0.6 and 1 mg·mL^{-1}) was deposited and dried on the ATR prism. The spectra were analyzed with ATR-FTIR as described in Sections 4.2.3.3 and 4.2.3.4.

4.2.5.2 PEIRS for OTA

A 2 mL Eppendorf tube was filled with 1.5 mL of MeOH containing 0, 2, 20, 200 and 2000 ng·mL^{-1} OTA (n=3 per concentration). Subsequently, a PEIRS paper tip was inserted in every tube with the tip pointing upwards. The tips were dried (>12 hours, until visibly dry), during which OTA molecules accumulated in the PEIRS tip area by evaporation-induced enrichment. The PEIRS tips were measured with ATR-FTIR as described in Sections 4.2.3.3 and 4.2.3.4.

4.2.5.3 S-PEIRS for OTA in standard solution

A mixture of pure ethanol and ultrapure water was prepared to obtain 15% (v/v) alcohol solution and mimic solvent conditions of wine samples. Then, a concentration range of 0, 20, 100, 250, 500, and 1000 ng·mL^{-1} OTA in 15% (v/v) alcohol was prepared. For every concentration level three individual IACs were loaded with 2 mL of solution, corresponding to 0, 40, 200, 500, 1000 and 2000 ng OTA, at a flowrate of ~1 mL·min^{-1}. Then, 5 mL of ultrapure water was applied to wash the IACs. The remaining water was carefully forced out of the IAC using an air-displacement pipette. Finally, 1.5 mL of pure methanol was applied to the IACs in 3 aliquots of 0.5 mL of which the first aliquot was allowed to settle into the IAC for 3 minutes. Then, the bound OTA molecules were dissociated and eluted into a 2 mL Eppendorf tube.

Next, the subsequent methanol aliquots were applied and eluted. A S-PEIRS tip was inserted into the eluate and put aside for evaporation-induced enrichment of OTA (>24 hours, until visibly dry). A total of 3 S-PEIRS tips per concentration level were analyzed with ATR-FTIR.

4.2.5.4 S-PEIRS for OTA in white wine

White wine containing 12.5% (v/v) alcohol was adjusted to a pH of approximately 7.1 by mixing 10 mL of wine with 1.5 mL of 0.5 M NaOH, and the resulting pH was recorded using a pH electrode. In total, five neutralized wine samples of 10 mL were prepared and spiked with OTA. The loading volumes (2 mL) contained concentrations of OTA of 0, 100, 250, 500 and 1000 ng·mL^{-1}, which corresponded to 0, 200, 500, 1000 and 2000 ng OTA. For every concentration level, three IACs were prepared as described under Section 4.2.5.3. A total of 3 S-PEIRS tips per concentration level were obtained and analyzed by ATR-FTIR.

4.2.6 Optimizated protocol of the combined solvent extraction assisted S-PEIRS method

Dealcoholized white wine (900 mL from a mixture of two wine bottles, 0.0 v/v%, pH = 2.5) was spiked at 0, 2, 6 or 20 ng·mL^{-1} OTA and transferred to a separatory funnel (1 L). Then, 100 mL of toluene was added and thoroughly mixed by shaking for 2 minutes. After phase separation, the toluene phase was collected and the funnel was rinsed with an additional 20 mL of toluene to maximize recovery. Then, the collected toluene was centrifuged at 3000 rpm for 8 minutes, after which the toluene layer was pipetted off from any residual aqueous solution. From the toluene layer, three aliquots of 0.5 mL of toluene were collected, each aliquot was evaporated with a gentle nitrogen flow and redissolved in 1 mL MeOH:H_2O (1:1 v/v), and analyzed with HPLC-HRMS. The concentration of OTA (ng·mL^{-1}) in the toluene phase was quantified to calculate the recovery of the first extraction step.

Then, the separated toluene phase was poured in a 100 mL separation funnel and thoroughly mixed with 10 mL 0.2 M carbonate buffer solution (alkaline aqueous phase, pH 9.5). After phase separation, the alkaline aqueous phase was collected in a falcon tube. Three 0.1 mL aliquots were taken from the alkaline aqueous phase and diluted in 0.9 mL MeOH:H_2O (1:1 v/v) to be analyzed with HPLC-HRMS, and the concentration of OTA (ng·mL^{-1}) was quantified to calculate the recovery of the second extraction step.

Subsequently, the enrichment factor (EF)[33] of the 2-step solvent extraction was calculated following Equation 4.3:

$$Enrichment\ \ factor = \frac{c_1}{c_0} \qquad \textit{Equation 4.3}$$

Where c_1 is the concentration of OTA in the final alkaline aqueous phase and c_0 is the concentration of OTA spiked in the wine.

Finally, the 10 mL alkaline aqueous extract was brought down to pH ~7 using 550 µL 10% FA. Three IACs per concentration level were loaded with 2 mL of neutralized extract and used as described under Section 4.2.5.3. From the eluate of each IAC, 0.1 mL was collected and diluted with 0.1 mL MeOH to be analyzed with HPLC-HRMS and the concentration of OTA (ng·mL^{-1}) in the eluate was quantified to determine the recovery of the IAC.

4.3 Results & discussion

4.3.1 Understanding the IR vibrational modes of OTA

The vibrational modes of OTA were evaluated by liquid deposition of different concentration levels of OTA analytical standard in methanol ranging from 0 – 1 mg·mL^{-1} (Figure 4.2). The molecular structure of OTA is characterized by a polyketide and an L-phenylalanine block linked to a chlorinated dihydroisocoumarin block via an amide [31,32,34]. The major vibrational modes of OTA are a ketone stretch from the carboxylic acid and the lactone (1. C=O ν, yellow) at 1735 cm^{-1}, a ketone stretch from the secondary amide (2. C=O ν, Amide I, blue) at 1673 cm^{-1}, a carbon-carbon double bond stretch of the aromatic rings (3. C=C ν, red) at 1614 cm^{-1}, a mixed vibrational mode from N-H bending and C-N stretching of the secondary amide (4. C-N ν, N-H δ, Amide II, grey) at 1533 cm^{-1}, a methylene and methyl bending doublet (5. CH2 δ, CH3 δ, orange) at 1425 cm^{-1} and 1390 cm^{-1}, and an ether stretch (6. C-O-C ν, green) at 1215 cm^{-1} (Figure 4.2). Therefore, the OTA molecule contained six vibrational modes that were of interest as potential molecular identifier of OTA for S-PEIRS.

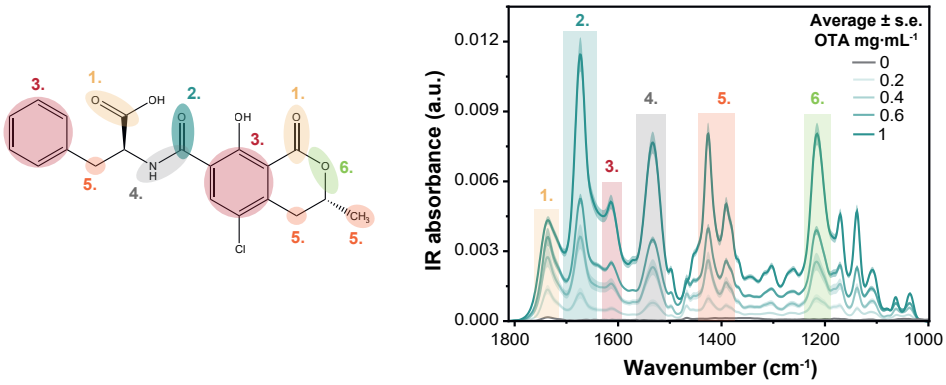


Figure 4.2: *ATR-FTIR vibrational modes of OTA. Analytical standard in methanol at concentrations between 0 – 1 mg·mL^{-1} were prepared. N=3 aliquots of 0.5 µL were applied to the ATR prism and n=3 technical replicates were measured and reported using ATR-FTIR. Except for 0.6 mg·mL^{-1} and 1 mg·mL^{-1}, here N=2 and n=3 were reported. OTA contained 6 major vibrational modes; a ketone stretch from the carboxylic acid and the lactone (1-yellow), an amide I (2-blue), a carbon-carbon double bond stretch (3-red), an amide II (4-grey), a methylene and methyl bending doublet (5-orange), and an ether stretch (6-green).*

4.3.2 PEIRS and S-PEIRS of OTA analytical standard

The enrichment of OTA molecules by PEIRS was achieved by simply inserting a pre-cut paper tip (Figure S4.2, 40 x 5 mm, tip ∠ = 28°) in 1.5 mL of methanol solution containing different OTA concentration levels. The PEIRS tip allowed the passive wicking and the continuous deposition of OTA molecules in the tip area as a result of capillary action and evaporation effects [30]. The evaporation of methanol and enrichment of the OTA molecules in the PEIRS tip takes at least 12 hours. The reason for this is the wicking of the 1.5 mL MeOH solution, which (i) is a substantial volume to wick into the paper tip, and (ii) is a passive process as the paper substrate acts as a passive pump. Of the six identified vibrational modes of OTA in the IR fingerprint range from 1800-1000 cm^{-1}, PEIRS was performed to identify which of those modes retained concentration dependency when enriched in the paper tip. First, the absolute absorbance spectra of PEIRS using OTA at a concentration of 0 and 2000 $ng{\cdot}mL^{-1}$ were compared (Figure S4.3). Here, three vibrational modes of OTA, as determined in Section 4.3.1, were clearly visible in the PEIRS spectra of 2000 $ng{\cdot}mL^{-1}$ (black) when compared to 0 $ng{\cdot}mL^{-1}$ (grey). These vibrational modes were the C=O of the Amide I at 1662 cm^{-1} (blue), the mixed mode of the C-NH of the Amide II at 1537 cm^{-1} (grey) and the C-O-C of the ether at 1205 cm^{-1} (green). Each of these three IR features were identified as a good candidate to be the molecular identifier of OTA. Still, the C=O at 1662 cm^{-1} was favored, as this feature gave the strongest absorbance which was important for the detection capability of S-PEIRS. Moreover, the C=O and the C-NH occurred in a region where paper shows minimal absorbance (1800 – 1500 cm^{-1}), while the C-O-C of OTA converges with the C-O-C feature of paper at 1205 cm^{-1}.

The IR feature used for the normalization of the paper background was determined to be 1315 cm^{-1} (Figure S4.3, arrow). At this wavenumber, OTA showed little absorbance while paper showed a distinct IR feature. After normalization of all the PEIRS spectra to 1315 cm^{-1} (Figure S4.4, indicated with *), 2nd derivative analysis was performed to deconvolve the C=O vibration at 1662 cm^{-1} (Figure 4.3a) [30,35–37]. The 2000 $ng{\cdot}mL^{-1}$ spectrum was excluded from Figure 4.3a to visualize the lower concentration range, but this spectrum was included in Figure S4.5. The 2nd derivative C=O feature was integrated between ~1680 – 1650 cm^{-1} and the result per concentration level was visualized in a boxplot (Figure 4.3b). A statistical evaluation first showed that the means were normally distributed. Additionally, the variance between the mean of 0 $ng{\cdot}mL^{-1}$ and the means of the OTA concentration levels were tested. Here, it was found that only the variance between 0 and 2000 $ng{\cdot}mL^{-1}$ was significantly different ($p=0.020$), which was taken into account for further statistical analysis. A Two-Sample t-test between the mean of 0 $ng{\cdot}mL^{-1}$ and the means of each OTA concentration level showed significant difference between 0 $ng{\cdot}mL^{-1}$ and 20 –

2000 ng·mL^{-1}, with $p<0.05$ (Figure 4.3b). Furthermore, the mean of 2 ng·mL^{-1} was not significantly different from the mean of 0 ng·mL^{-1} ($p=0.12$).

Similar to PEIRS, the performance of S-PEIRS was evaluated. The use of IACs allowed the selective capturing of OTA molecules from the loading solution, while most non-specific components that would otherwise possibly interfere with IR analysis are removed. This was especially important when moving to more complex matrices such as wine. The theoretical loading capacity for OTA given by the producer of the IACs was 2000 ng [38], this meant that samples containing >2000 ng were out of the linear range of the method and should be diluted [39]. Ethanol in water solutions (15% v/v) were spiked at different OTA concentrations (0 – 1000 ng·mL^{-1}). Therefore, loading of 2 mL at these concentration levels resulted in 0, 40, 200, 500, 1000 and 2000 ng OTA that was effectively loaded onto the IACs, and was equal to 0, 0.02, 0.1, 0.25, 0.5 and 1x the loading capacity as stated by the producer.

After normalization to 1315 cm^{-1} (Figure S4.4), the deconvolved C=O vibration at ~1662 cm^{-1} was clearly visible in the 2nd derivative spectra (Figure 4.3c). The integration of the area between 1680 – 1650 cm^{-1} is reported in Figure 4.3d. All means (N=3 per level) were normally distributed, and only the variance between 0 ng·mL^{-1} and 1000 ng·mL^{-1} was significantly different ($p=0.026$). Therefore, for the statistical analysis of the means using the Two-Sample t-test equal variance was assumed for all concentration levels except for 1000 ng·mL^{-1}. The t-test showed that the means of 20 and 100 ng·mL^{-1} OTA were not significantly different from 0 ng·mL^{-1}, with $p=0.51$ and $p=0.44$ respectively. This meant that the addition of the IAC for S-PEIRS decreases the detection capability when compared to PEIRS. The explanation for this difference was that the volume in which the S-PEIRS tip was inserted might contain some co-eluted water and column material.

Moreover, the inclusion of the IAC step for selectivity increased the evaporation time to at least 24 hours and altered the nature of the wicking solution, which could have led to a changed deposition mechanism of OTA compared to the pure methanol solution used in PEIRS. Still, the mean of 250 ng·mL^{-1} was different from 0 ng·mL^{-1} with a trend towards significance ($p=0.086$). The reason for this moderate difference was because one S-PEIRS tip had a relatively low response, in the region of the blank, compared to the other two (Figure S4.6, dashed circle). The means of both 500 ng·mL^{-1} and 1000 ng·mL^{-1} (1000 and 2000 ng) were statistically different, at p-values of 0.016 and 0.031 respectively (Figure 4.3d). Therefore, the detection capability of S-PEIRS for OTA was in a comparable range as S-PEIRS for DON [30], yet not in the relevant concentration range of the ML of OTA.

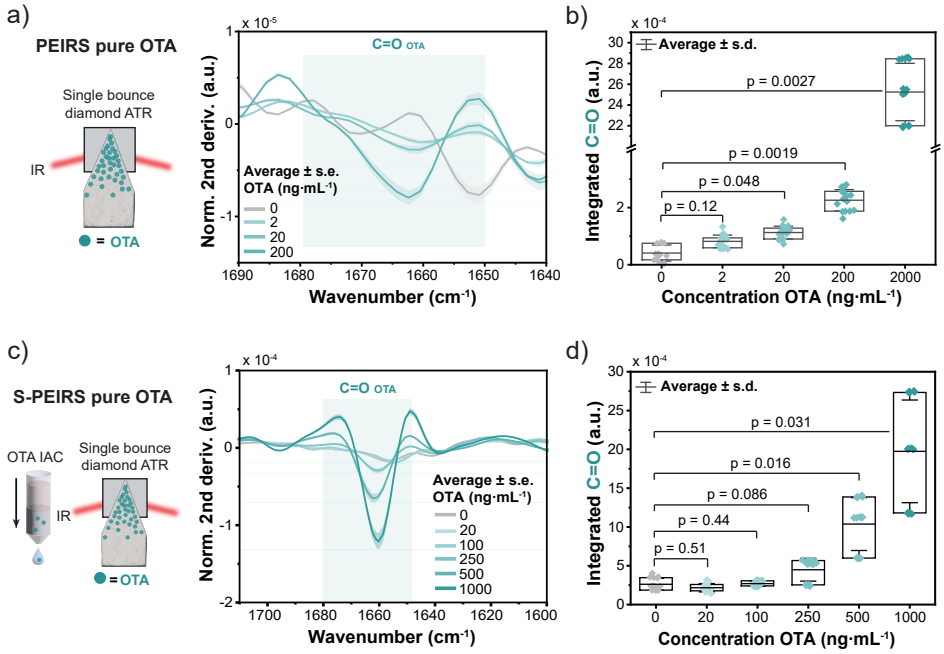


Figure 4.3: *Second derivative spectra (N=3 and n=5 per level) of normalized (to 1315 cm^{-1}) absorbance spectra and integrated data of the molecular identifier feature (C=O) of OTA for PEIRS and S-PEIRS in standard solutions. a) 2nd derivative results of the C=O range of OTA using PEIRS at concentrations between 0 – 200 ng·mL^{-1}. b) Integrated C=O area against concentration (0 – 2000 ng·mL^{-1}) of the PEIRS results. c) 2nd derivative results of the C=O range of OTA by loading solutions containing 15% (v/v) EtOH spiked at concentrations between 0 – 1000 ng·mL^{-1} onto IACs for OTA (S-PEIRS). d) Integrated C=O area against concentration (0 – 1000 ng·mL^{-1}) of the S-PEIRS results. The normality of the averaged data (N=3 per level) was confirmed by Shapiro-Wilk test, and the variance was evaluated prior to using a Two-Sample t-test to test statistical significance.*

4.3.3 S-PEIRS for OTA in white wine

The results above showed that OTA concentrations down to 250 ng·mL^{-1}, spiked in 15% (v/v) ethanol, could be detected using S-PEIRS. Therefore, a similar concentration range of OTA (0, 100, 250, 500 and 1000 ng·mL^{-1}) was used to evaluate S-PEIRS in white wine matrix (12.5% v/v, Figure 4.4). The white wine was neutralized (~pH 7.1) prior to spiking to assure compatibility with the antibodies of the IACs (Figure 4.4a). An acidic or alkaline pH can interfere with the binding between the antibodies and the OTA molecules in the IAC, since the binding capacity of antibodies is most efficient around physiological pH [40,41].

The C=O of OTA at ~1660 cm^{-1} showed a clear concentration dependent response in this feature (blue box, Figure 4.4b). The normalized S-PEIRS spectra were subjected to 2nd derivative analysis to deconvolve the C=O vibration from other

IR modes (blue box, Figure 4.4c). Subsequently, the C=O feature was integrated between ~1680 – 1650 cm^{-1} and the result per concentration level was visualized in a boxplot (Figure 4.4d). Again, the normality and the variance of the data was tested. The results of the Two-Sample t-test showed that the mean of 100 $ng{\cdot}mL^{-1}$ OTA was not significantly different from 0 $ng{\cdot}mL^{-1}$ (p=0.21), while the means of 250, 500 and 1000 $ng{\cdot}mL^{-1}$ were significantly different from 0 $ng{\cdot}mL^{-1}$, with p-values of <0.0001, 0.044 and 0.021 respectively (Figure 4.4d). These results were in line with the results for S-PEIRS of OTA standard in 15% (v/v) ethanol solution, described in Section 4.3.2. These results confirmed that OTA concentration levels of 250 $ng{\cdot}mL^{-1}$ (500 ng) in 2 mL neutralized wine could be directly detected using S-PEIRS. This was already a significant achievement in the field of IR spectroscopy, yet the regulatory limit that is relevant for food safety monitoring was still out of reach. Therefore, additional enrichment was needed prior to S-PEIRS to achieve molecular detection of OTA in e.g a bottle of wine contaminated at 2 $\mu g{\cdot}kg^{-1}$.

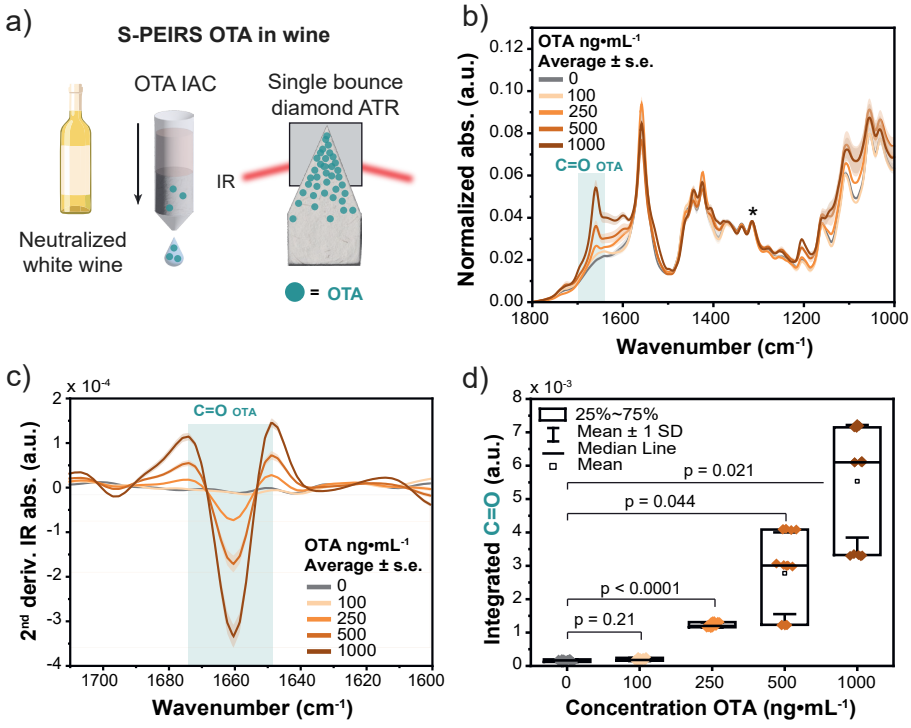


Figure 4.4: *S-PEIRS for OTA spiked in 2 mL neutralized white wine (12.5% v/v). Results of the normalized (to 1315 cm^{-1}) b) absorbance and c) 2nd derivative spectra (n=15 per level) of S-PEIRS for OTA concentrations of 0, 100, 250, 500 and 1000 $ng{\cdot}mL^{-1}$. d) integrated 2nd derivative areas of the C=O molecular identifier of OTA for every concentration, and statistical significance was tested using a Two-Sample t-test.*

4.3.4 Development of solvent-based purification prior to S-PEIRS

Solvent extraction involving a pH-sensitive component is a widely used approach in chemistry for sample workup and purification of ionizable molecules such as OTA, though less frequently by employing decreasing volumes to further pre-concentrate the sample [42,43]. In this work, a two-step pH-dependent solvent extraction was developed for the purification and enrichment of OTA prior to S-PEIRS (Figure 4.1b). Several experiments were performed to optimize the parameters of different steps of the solvent extraction. For the first solvent extraction different phase ratios were evaluated for partitioning of OTA from the acidic aqueous phase (0.1% FA, pH ~2.7) to the butyl acetate organic phase (Figure S4.7). In all cases, a phase ratio up to 16:1 resulted in similar absolute recoveries, yet an increasing volume of the aqueous phase was also increasingly difficult to seperate. Therefore, a phase ratio of 9:1 was chosen for all further experiments, to balance OTA enrichment with practicality of the sample handling.

The parameters of the second solvent extraction were optimized for OTA stability under different pH conditions ranging from neutral to alkaline conditions (pH 7 – 12.5, Figure S4.8). It was found that OTA was stable in solutions with alkalinity up to pH 10 for at least 16 hours. For the optimization of the second solvent extraction, the effect of alkaline pH on the partitioning of OTA from the organic to the alkaline phase was evaluated (Figure S4.9). Indeed, at alkaline pH the recovery of OTA in the alkaline aqueous phase was approximately 100%, and no residual OTA was detected in the organic phase (<LOD, HPLC-HRMS). Therefore, a pH of 9.5 was selected for the second solvent extraction.

Next to using butyl acetate, a more apolar organic phase was evaluated, as this could reduce the co-extraction of matrix constituents and water during the first extraction step. Therefore, the partitioning of OTA between toluene (2 mL) and acidic water (0.1% FA, 10 mL), wine (12.5% v/v, 10 mL) or dealcoholized wine (10 mL) was studied (Figure S4.10). It was observed that after mixing and subsequent phase separation, almost all OTA was found in the toluene layer suggesting that toluene could also be used as organic phase during the solvent extraction. Therefore, for the combined procedure of pH-dependent solvent extraction and S-PEIRS, toluene was used.

To obtain an estimation of the recoveries of the different extraction steps, subsamples were taken at different points in the workflow and analyzed by HPLC-HRMS. Here, an average recovery of 76 $\pm$ 3% was calculated for the first solvent extraction, and an average recovery of 68 $\pm$ 7% for the second solvent extraction (Figure S4.11). The observation that the average recoveries are lower than during the optimization of the method was expected to be related to the much larger volumes that were used here in combination with very low concentrations of OTA.

The experimental EF of the full pH-dependent solvent extraction procedure was calculated following Equation 4.3 (Section 4.2.6), and was approximately a factor 40 (Table S4.3). The experimental EF of the pH-dependent solvent extraction could be further improved, yet the combination of such pretreatment with direct IR detection of a mycotoxin is unique.

4.3.5 Application of solvent extraction assisted S-PEIRS for OTA detection in white wine in the ML range

The developed solvent extraction approach allowed for the enrichment of OTA in a small extract volume that could be directly used for S-PEIRS. To demonstrate the complete workflow of solvent extraction assisted S-PEIRS in the ML range of OTA, we spiked 900 mL of white wine (alcohol-free) at either 0, 2, 6 and 20 ng·mL^{-1} OTA and the complete procedure was followed (Figure 4.5a). The final extraction volume obtained from the solvent extraction was neutralized using 550 µL 10% FA. The estimated quantity of OTA per concentration level was 0, 850, 2300 and 7700 ng. The neutralized extraction volume was divided in aliquots of 2 mL for every OTA starting concentration level (0, 2, 6 and 20 ng·mL^{-1}). As a result, the OTA quantities that were present in the 2 mL loading volume were on average 160, 430, and 1400 ng. A subsample for HPLC-HRMS analysis was taken before and after the IAC and showed recoveries between 84 – 102%, suggesting that the IAC performed adequately. As a result, the paper tips contained OTA quantities of approximately 0, 140, 430 and 1370 ng for wine samples that were originally contaminated with 0, 2, 6 and 20 ng·mL^{-1} OTA respectively. These paper tips were analyzed using our ATR-FTIR method.

Identical to what was described for S-PEIRS (Section 4.3.3), the absorbance spectra were normalized to 1315 cm^{-1} (indicated by *, Figure 4.5b), and the average spectrum per concentration was calculated. The blue box indicated the C=O area of OTA, with a peak center at 1660 cm^{-1}, suggesting a concentration dependent IR signal in this feature. Second derivative analysis was performed, and it was observed that the C=O feature of OTA at 1660 cm^{-1} was present in all the samples containing OTA (2, 6 and 20 ng·mL^{-1}), while it was absent at 0 ng·mL^{-1} (Figure 4.5c). To quantify this difference, the area of the C=O signature was integrated for every spectrum and demonstrated in a boxplot (Figure 4.5d). The statistical evaluation showed that the means of 2, 6 and 20 ng·mL^{-1} OTA were significantly different from 0 ng·mL^{-1} with $p=0.015$, $p=0.017$ and $p=0.031$ respectively (Figure 4.5d). Moreover, the statistical evaluation showed that the means between the levels were also significantly different with $p=0.025$ (2 and 6 ng·mL^{-1}) and $p=0.037$ (6 and 20 ng·mL^{-1}). This confirmed that the C=O feature of OTA at 1660 cm^{-1} can be used for concentration dependent detection of OTA at and above the ML.

Finally, a linear regression analysis of the average areas detected per OTA concentration showed a relationship that followed the same monotonic trend for both S-PEIRS with solvent extraction and comparative HPLC-HRMS analyses (R^2=0.999 and R^2=0.964, Figure 4.5e). The LOD and LOQ were estimated following Equations 4.1-4.2 for S-PEIRS with solvent extraction (2.0 and 6.7 ng·mL^{-1}) and for comparative HPLC-HRMS (0.7 and 2.4 ng·mL^{-1}). These figures of merit are expected to be further improved by increasing the IAC loading volume, thereby maximizing the absolute OTA quantity in the eluate, as previously demonstrated for DON [30]. In Figure S4.12 the average integrated areas of i) the OTA C=O feature after S-PEIRS with solvent extraction and ii) the OTA m/z feature after comparative HPLC-HRMS showed a strong relationship (R^2=0.963, Figure S4.12).

These results prove that solvent extraction assisted S-PEIRS is able to achieve direct detection of OTA at the legal limit of 2 µg·kg^{-1} in white wine using IR spectroscopy for the first time. The only other reported direct spectroscopic detection method of OTA in white wine, which was based on supported liquid membrane extraction and SERS, achieved detection down to 115 µg·kg^{-1} and a reasonable relation to the LC-MS results (R^2=0.88) [44]. The SERS alternative circumvents the need of the expensive IACs (€17,-) and can be used in a high-throughput format. However, the preparation of the SERS substrates requires fabrication of gold nanopillars, functionalization of OTA-specific aptamers and a blocking layer for non-specific binding, whereas the S-PEIRS substrate is simply a paper tip that accumulates large quantities of OTA and is analyzed by regular ATR-FTIR. The methods are fundamentally different which makes true comparison challenging, yet our method shows a relevant detection limit (2 µg·kg^{-1}) and relationship with HPLC-HRMS (R^2=0.963, Figure S4.12).

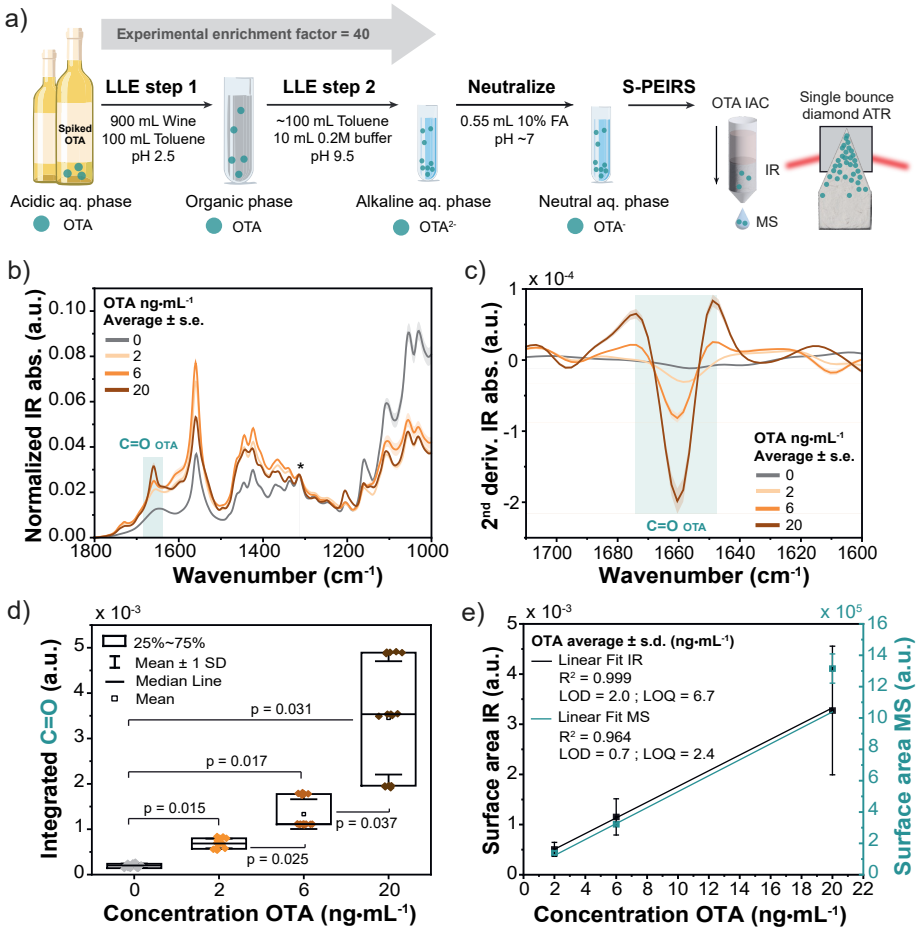


Figure 4.5: *Methodology of pH-dependent solvent extraction and S-PEIRS, for the sensitive detection of OTA at the legal limit of 2 µg·kg^{-1} in white wine. a) step-by-step illustration of the method starting from a large volume of wine containing low concentrations of OTA, to a relatively small volume containing high concentrations of OTA, leading to an experimental enrichment of a factor 40. Normalized (to 1315 cm^{-1}) b) absorbance and c) 2nd derivative spectra (N=3 full replicates and n=5 technical replicates per level) of pH dependent solvent extraction and S-PEIRS for OTA concentrations of 0, 2, 6, and 20 ng·mL^{-1}. d) Integrated 2nd derivative areas of the C=O molecular identifier of OTA for every concentration, and statistical significance was tested using a Two-Sample t-test. e) A linear regression resulted in strong relationship between the integrated OTA C=O feature (R^2=0.999), and the integrated OTA m/z feature (R^2=0.964), as a function of OTA concentration. Moreover, the IR and HPLC-HRMS results show the same monotonic trend following increasing OTA concentration.*

4.4 Conclusions

To achieve direct and label-free detection at the strict legal limit of harmful mycotoxins such as OTA, we have combined our S-PEIRS methodology [30] with a 2-step pH-dependent solvent extraction. Thereby, the concentration-dependent and molecular detection of OTA in white wine at the legal limit of 2 $\mu g \cdot kg^{-1}$ was achieved, for the first time using IR spectroscopy.

The direct and concentration-dependent character of the method does not necessitate large data sets for training and validation of prediction models that are needed for indirect prediction-based spectroscopy of OTA contamination. Moreover, solvent extraction assisted S-PEIRS offers an accessible spectroscopic platform for the direct and label-free detection of OTA that avoids any (nano)fabrication or functionalization of sensing substrates. The IACs and S-PEIRS tips are disposable after analysis, and a new sample could be immediately measured without needing to regenerate or dispose the entire substrate.

The IACs are a re-occurring cost per analysis (€17,-), which is why others have regenerated and reused IACs for OTA to reduce the total cost [45,46]. However, also alternative enrichment strategies that completely circumvent the need for an IAC are of interest for future advancement of the S-PEIRS method [47–51]. Additionally, the time-to-result (at least 24 hours) is a point of attention for future implementation and mainly originates from the passive preconcentration of solutes in the paper tips. This could be optimized by advancing to active enrichment, using e.g. localized evaporation enrichment [52], 3D-printed air-assisted enrichment [53], microfluidics-based enrichment [54,55] or heat. These horizons for future use and implementation of solvent extraction assisted S-PEIRS underline the method's potential as spectroscopic platform that can quantify the target analyte based on a molecular feature, and its application goes beyond the field of food safety analysis.

Acknowledgements

The authors thank the support and funding of the Shared Research Facilities (SRF) of Wageningen University and Research (The Netherlands). The authors gratefully acknowledge the facility NanoFACT (Wageningen, The Netherlands) for the support and assistance in undertaking this work.

References

1. WHO Global Strategy for Food Safety 2022-2030: Towards Stronger Food Safety Systems and Global Cooperation. (World Health Organization, Geneva, 2022).
2. Eskola, M. et al. Worldwide contamination of food-crops with mycotoxins: Validity of the widely cited 'FAO estimate' of 25%. Critical Reviews in Food Science and Nutrition 60, 2773–2789 (2020).
3. The European Commission. Commission Regulation (EU) 2023/915 of 25 April 2023 on maximum levels for certain contaminants in food and repealing Regulation (EC) No 1881/2006. (2023).
4. European Environment Agency. Mycotoxin exposure in a changing European climate. https://www.eea.europa.eu/en/analysis/publications/mycotoxin-exposure-in-a-changing-european-climate (2025).
5. World Health Organization. Food safety, climate change and the role of WHO. https://iris.who.int/handle/10665/376702 (2018).
6. Casu, A., Camardo Leggieri, M., Toscano, P. & Battilani, P. Changing climate, shifting mycotoxins: A comprehensive review of climate change impact on mycotoxin contamination. Comprehensive Reviews in Food Science and Food Safety 23, e13323 (2024).
7. Johns, L. E., Bebber, D. P., Gurr, S. J. & Brown, N. A. Emerging health threat and cost of Fusarium mycotoxins in European wheat. Nat Food 3, 1014–1019 (2022).
8. The European Commission. Commission Implementing Regulation (EU) 2023/2782 of 14 December 2023 laying down the methods of sampling and analysis for the control of the levels of mycotoxins in food and repealing Regulation (EC) No 401/2006. (2023).
9. The European Commission. Commission Regulation (EU) 2024/1022 of 8 April 2024 amending Regulation (EU) 2023/915 as regards maximum levels of deoxynivalenol in food. (2024).
10. Zimmerli, B. & Dick, R. Ochratoxin A in table wine and grape-juice: Occurrence and risk assessment. Food Additives and Contaminants 13, 655–668 (1996).
11. Visconti, A., Pascale, M. & Centonze, G. Determination of ochratoxin A in wine by means of immunoaffinity column clean-up and high-performance liquid chromatography. Journal of Chromatography A 864, 89–101 (1999).
12. Sulyok, M., Suman, M. & Krska, R. Quantification of 700 mycotoxins and other secondary metabolites of fungi and plants in grain products. npj Sci Food 8, 1–8 (2024).
13. Lemmink, I. B. et al. Chapter Two - Recent advances and challenges in the analysis of natural toxins. in Advances in Food and Nutrition Research. vol. 110 67–144 (Academic Press, 2024).
14. Csenki, E. et al. Stakeholder assessment for mycotoxin analysis: exploring the demand along the European food supply chain. World Mycotoxin Journal 16, 287–299 (2023).
15. Oliveira, S. et al. Advances in optical devices for the detection of contaminants in food and water. TrAC Trends in Analytical Chemistry 184, 118139 (2025).
16. Freitag, S., Sulyok, M., Logan, N., Elliott, C. T. & Krska, R. The potential and applicability of infrared spectroscopic methods for the rapid screening and routine analysis of mycotoxins in food crops. Comp Rev Food Sci Food Safe 21, 5199–5224 (2022).
17. Freitag, S. et al. Attenuated total reflection mid-infrared spectroscopy to screen Austrian and French wheat from multiple years for deoxynivalenol. Spectrochimica Acta Part A: Molecular and Biomolecular Spectroscopy 340, 126340 (2025).

18. Fomina, P. et al. Prediction of Deoxynivalenol Contamination in Wheat via Infrared Attenuated Total Reflection Spectroscopy and Multivariate Data Analysis. ACS Food Sci Technol 4, 895–904 (2024).
19. Meira, D. I. et al. Recent advances in nanomaterial-based optical biosensors for food safety applications: Ochratoxin-A detection, as case study. Critical Reviews in Food Science and Nutrition 64, 6318–6360 (2024).
20. Logan, N. et al. Advancing Mycotoxin Detection in Food and Feed: Novel Insights from Surface-Enhanced Raman Spectroscopy (SERS). Advanced Materials 36, 2309625 (2024).
21. Wu, Z., Pu, H. & Sun, D.-W. Fingerprinting and tagging detection of mycotoxins in agri-food products by surface-enhanced Raman spectroscopy: Principles and recent applications. Trends in Food Science & Technology 110, 393–404 (2021).
22. Kutsanedzie, F. Y. H., Agyekum, A. A., Annavaram, V. & Chen, Q. Signal-enhanced SERS-sensors of CAR-PLS and GA-PLS coupled AgNPs for ochratoxin A and aflatoxin B1 detection. Food Chemistry 315, 126231 (2020).
23. Song, L. et al. Highly sensitive SERS detection for Aflatoxin B1 and Ochratoxin A based on aptamer-functionalized photonic crystal microsphere array. Sensors and Actuators B: Chemical 364, 131778 (2022).
24. Li, J., Yan, H., Tan, X., Lu, Z. & Han, H. Cauliflower-Inspired 3D SERS Substrate for Multiple Mycotoxins Detection. Anal. Chem. 91, 3885–3892 (2019).
25. Oliverio, M., Perotto, S., Messina, G. C., Lovato, L. & De Angelis, F. Chemical Functionalization of Plasmonic Surface Biosensors: A Tutorial Review on Issues, Strategies, and Costs. ACS Appl. Mater. Interfaces 9, 29394–29411 (2017).
26. Deriu, C., Thakur, S., Tammaro, O. & Fabris, L. Challenges and opportunities for SERS in the infrared: materials and methods. Nanoscale Adv. 5, 2132–2166 (2023).
27. Wang, J. et al. Surface-enhanced infrared absorption spectroscopy (SEIRAS) for biochemical analysis: Progress and perspective. Trends in Environmental Analytical Chemistry 41, e00226 (2024).
28. Meira, D. I. et al. Label-free localized surface plasmon resonance (LSPR) biosensor, based on Au-Ag NPs embedded in TiO2 matrix, for detection of Ochratoxin-A (OTA) in wine. Talanta 284, 127238 (2025).
29. Kozuch, J., Ataka, K. & Heberle, J. Surface-enhanced infrared absorption spectroscopy. Nat Rev Methods Primers 3, 1–19 (2023).
30. Bosman, A. J. et al. Selective Paper-Enhanced Infrared Spectroscopy for Molecular Detection of Deoxynivalenol in Wheat. Preprint at https://doi.org/10.2139/ssrn.5182158 (2025).
31. EFSA Panel on Contaminants in the Food et al. Risk assessment of ochratoxin A in food. EFSA Journal 18, e06113 (2020).
32. Steinbrück, D., Rasch, C. & Kumke, M. U. Photophysics of Ochratoxin A in Aqueous Solution. Zeitschrift für Naturforschung B 63, 1321–1326 (2008).
33. Al-Saidi, H. M. & Emara, A. A. A. The recent developments in dispersive liquid–liquid microextraction for preconcentration and determination of inorganic analytes. Journal of Saudi Chemical Society 18, 745–761 (2014).
34. Cagnasso, I. et al. Comprehensive study on the degradation of ochratoxin A in water by spectroscopic techniques and DFT calculations. RSC Advances 9, 19844–19854 (2019).
35. Ruggeri, F. S. et al. Infrared nanospectroscopy characterization of oligomeric and fibrillar aggregates during amyloid formation. Nat Commun 6, 7831 (2015).
36. Dong, A., Huang, P. & Caughey, W. S. Protein secondary structures in water from second-derivative amide I infrared spectra. Biochemistry 29, 3303–3308 (1990).
37. Jansson, P. A. Deconvolution: With Applications in Spectroscopy. (Academic Press, 1984).
38. Romer Labs. OchraStar Immunoaffinity columns. Romer Labs https://www.romerlabs.com/at_en/shop/ochrastar-immunoaffinity-columns/ (2025).
39. MacDonald, S. J., Chan, D., Brereton, P., Damant, A. & Wood, R. Determination of deoxynivalenol

in cereals and cereal products by immunoaffinity column cleanup with liquid chromatography: interlaboratory study. J AOAC Int 88, 1197–1204 (2005).
40. Şenyuva, H. Z. & Gilbert, J. Immunoaffinity column clean-up techniques in food analysis: A review. Journal of Chromatography B 878, 115–132 (2010).
41. Moser, A. C. & Hage, D. S. Immunoaffinity chromatography: an introduction to applications and recent developments. Bioanalysis 2, 769–790 (2010).
42. Ashworth, I. W. & Meadows, R. E. A General Liquid–Liquid Partitioning Equation and Its Consequences: Learning from the pH Dependent Extraction of a Pharmaceutical Intermediate. J. Org. Chem. 83, 4270–4274 (2018).
43. Mariño-Repizo, L., Goicoechea, H., Raba, J. & Cerutti, S. A simple, rapid and novel method based on salting-out assisted liquid-liquid extraction for ochratoxin A determination in beer samples prior to ultra-high-performance liquid chromatography coupled to tandem mass spectrometry. Food Addit Contam Part A Chem Anal Control Expo Risk Assess 35, 1622–1632 (2018).
44. Rostami, S. et al. High-throughput label-free detection of Ochratoxin A in wine using supported liquid membrane extraction and Ag-capped silicon nanopillar SERS substrates. Food Control 113, 107183 (2020).
45. Liu, X. et al. Regeneration and Reuse of Immunoaffinity Column for Highly Efficient Clean-Up and Economic Detection of Ochratoxin A in Malt and Ginger. Toxins (Basel) 10, 462 (2018).
46. Reiter, E. V. et al. Sol–gel immunoaffinity chromatography for the clean up of ochratoxin A contaminated grains. Journal of Chromatography A 1218, 7627–7633 (2011).
47. Lemmink, I. B. et al. Modular Point-of-Need Tropane Alkaloid Detection at Regulatory Levels: Combining Solid–Liquid Extraction from Buckwheat with a Paper-Immobilized Liquid-Phase Microextraction and Immuno-Detection in Interconnectable 3D-Printed Devices. Anal. Chem. 96, 16462–16468 (2024).
48. Lemmink, I. B., Bosma, S., Bovee, T. F. H., Zuilhof, H. & Salentijn, G. IJ. Paper-immobilized liquid-phase microextraction for direct paper spray mass spectrometry and immuno-detection of atropine in baby food, buckwheat cereals, and edible oils at regulatory levels. Analytica Chimica Acta 343823 (2025).
49. Huang, S. et al. High enrichment and ultra-trace analysis of aflatoxins in edible oils by a modified hollow-fiber liquid-phase microextraction technique. Chem. Commun. 53, 8988–8991 (2017).
50. Zhang, D. et al. Recent advancements in the applications of separation and enrichment strategies towards SERS detection. TrAC Trends in Analytical Chemistry 184, 118136 (2025).
51. Shafaghi Khameneh, M., Afshar Mogaddam, M. R. & Azadmard-Damirchi, S. Development of an efficient sample pretreatment method for the extraction of aflatoxins from sesame oils before their determination with high-performance liquid chromatography-fluorescent detector. Microchemical Journal 214, 113879 (2025).
52. Park, M., Kim, Y.-S., Kim, S. & Lim, J. Y. Ultra-sensitive, on-site pesticide detection for environmental and food safety monitoring using flexible cellulose nano fiber/Au nanorod@Ag SERS sensor. Journal of Hazardous Materials 487, 137197 (2025).
53. Salentijn, G. Ij. & Hoekstra, M. H. Sensor cartridge for chemical assays of a liquid sample containing analyte molecules, WO2018226097 A1. (2018).
54. Ruggeri, F. S. et al. Microfluidic deposition for resolving single-molecule protein architecture and heterogeneity. Nat Commun 9, 3890 (2018).
55. Zhao, X. et al. Recent Advances in Microfluidics for the Early Detection of Plant Diseases in Vegetables, Fruits, and Grains Caused by Bacteria, Fungi, and Viruses. J. Agric. Food Chem. 72, 15401–15415 (2024).

Supplementary information to:

Detection of ochratoxin A in wine at the legal limit via solvent-based enrichment and paper-enhanced infrared spectroscopy

SI Tables

Table S4.1: *HRMS settings for OTA where the positive mode was used with a scan range of m/z 393-413 and a mass resolution of 70.000 FWHM.*

Compound	Elemental composition	Theoretical mass (*m/z*) [M + H^+]	Mass error (ppm)	Retention time
Ochratoxin A	$C_{20}H_{18}ClNO_6$	404.0901	2.09	6.14

Table S4.2: *Silhouette Studio settings for automatic cutting of paper-microfluidic PEIRS tips using Curio 2 precision cutter.*

Silhouette Studio parameter	Selected setting
Instrument	Curio 2
Tray	Auto (electrostatic bed)
Cutting mat	Protector sheet only
Media size	250 x 250 mm
Constrain media to cutting mat	On
Carriage tool 1	Autoblade
Carriage tool 2	None
Blade depth	1
Speed	15
Force	10
Passes	1
Acceleration	3
Pen-up height	30
Line segment overcut	Off
Intelligent Path Technology™	On

Table S4.3: *Calculation of the experimental enrichment factor of the solvent extraction procedure, based on HPLC-HRMS results.*

Solution	Volume (mL)	Concentration (ng·mL^{-1})		
Wine	900	2	6	20
After extraction 2	10	85	226	762
EF		43	38	38

SI Figures

Positive mode
$[M+H]^+$ adduct OTA
$C_{20}H_{19}ClNO_6^+$
Theoretical mass (m/z) = 404.0901

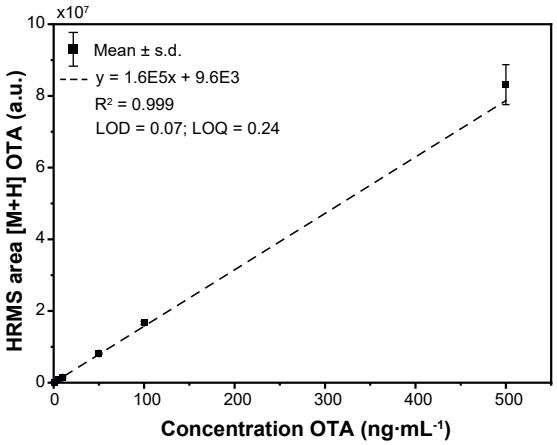


Figure S4.1: *Calibration curve between signal ochratoxin A (m/z 404.085-404.095), and concentration of ochratoxin A constructed by HPLC-HRMS. Error bars represent the standard deviation (n = 3).*

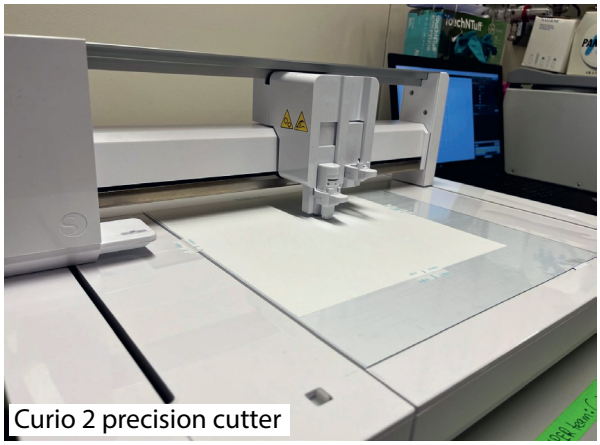




Figure S4.2: *The Silhouette Curio 2 precision cutter was used to cut 64 PEIRS tips within 5 minutes. The dimensions of the PEIRS tips were 40 x 5 mm, tip angle = 28°. The electrostatic bed held the paper in place without harming the paper. Four small pieces of tape were used to provide additional support on the edges of the paper.*

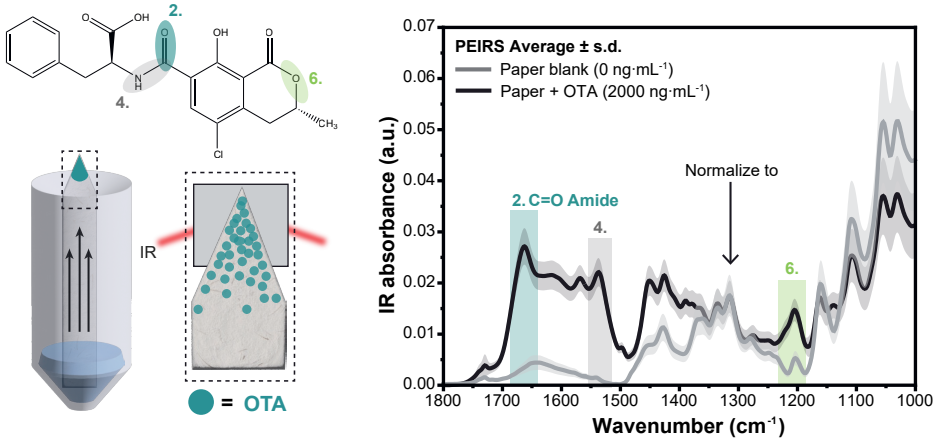


Figure S4.3: *Absolute PEIRS spectra comparing blank paper (0 ng·mL^{-1}) and paper with OTA (2000 ng·mL^{-1}). The three main vibrational modes of OTA are the C=O stretching of the amide I at 1662 cm^{-1} (blue), the C-NH stretching of the amide II at 1537 cm^{-1} (grey) and the C-O-C stretching of the ether at 1205 cm^{-1} (green). The numbering of the modes was related to the modes found in the liquid deposition spectra shown in Figure 4.2. The arrow indicates where the spectra could be normalized, this point at 1315 cm^{-1} originates mainly from paper and can be used to normalize all OTA containing papers specifically to the paper background.*

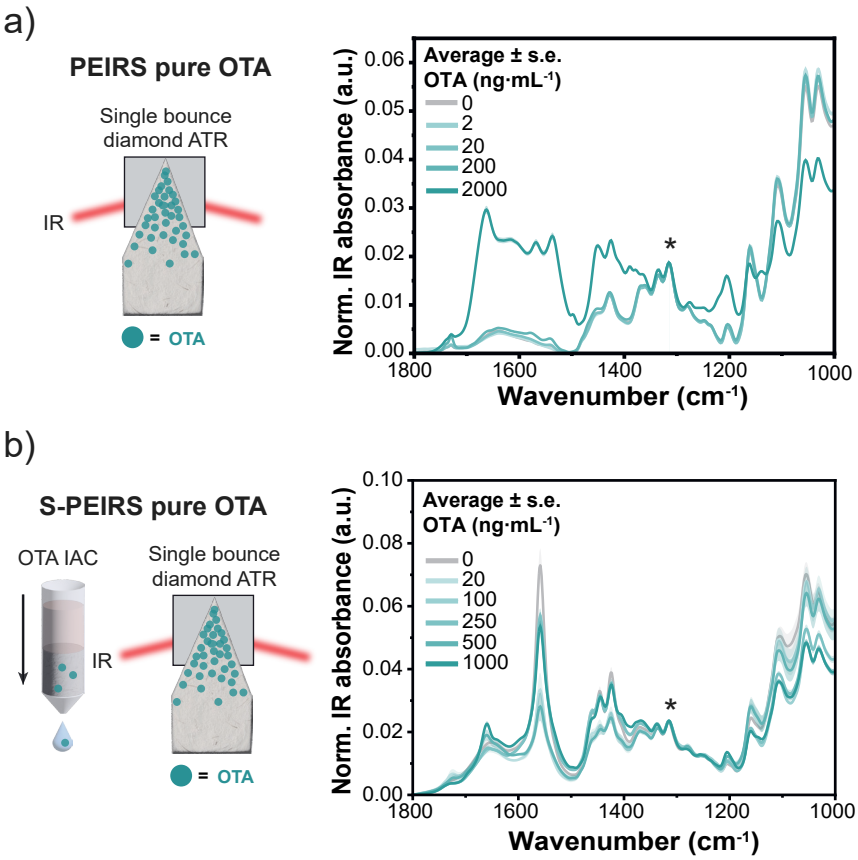


Figure S4.4: *PEIRS and S-PEIRS averaged IR absorbance spectra that were normalized to 1315 cm^{-1} (N=3, n=5). a) For PEIRS, the paper tips were inserted in different DON concentrations dissolved in pure methanol, and analyzed by ATR-FTIR when dry. b) For S-PEIRS, different concentrations of DON in 15% (v/v) ethanol were applied to the IACs, and the paper tips were inserted in the eluate from these samples and analyzed by ATR-FTIR when visibly dry.*

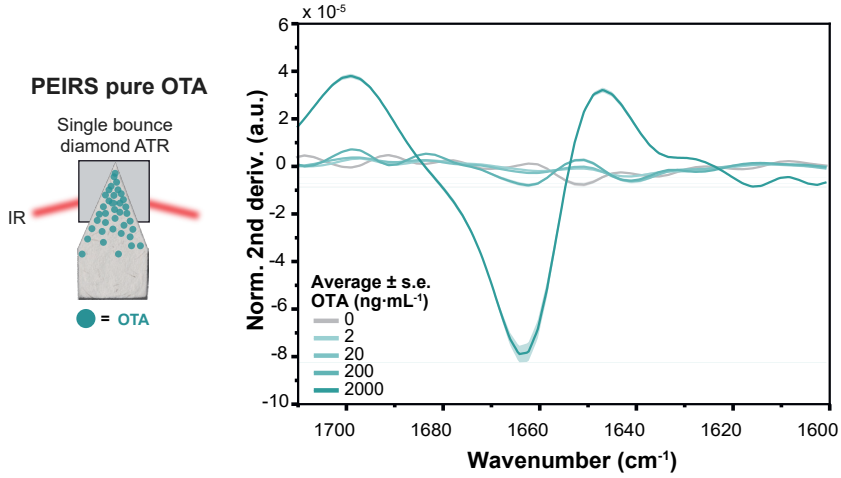


Figure S4.5: *Average PEIRS 2nd derivative spectra in the wavenumber region of the OTA C=O (Amide I, ~1662 cm^{-1}) for concentrations of 0, 2, 20, 200 and 2000 ng·mL^{-1} dissolved in methanol (N=3, n=5). Dried paper tips were analyzed by ATR-FTIR.*

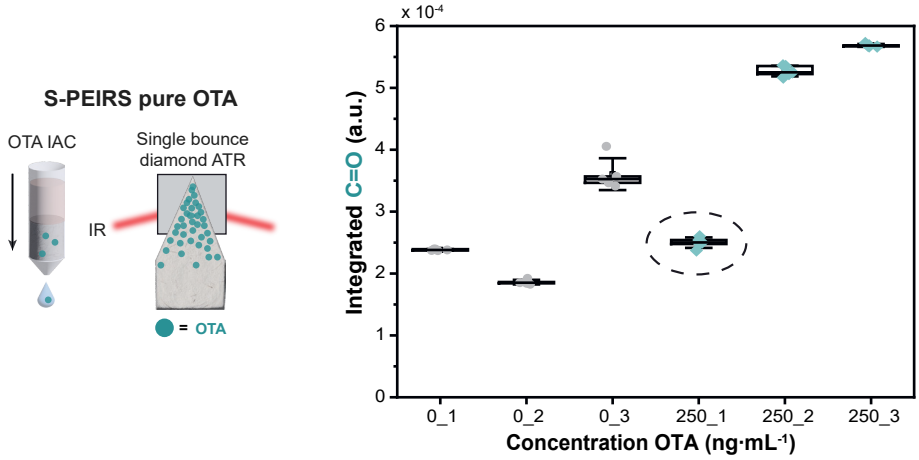


Figure S4.6: *Separate technical repeats (n=5) per analyzed S-PEIRS tip (N=3) for the concentration levels 0 and 250 ng·mL OTA in 15% (v/v) ethanol solution. The first paper tip of 250 ng·mL^{-1} (250_1) showed relatively low response in the region of the blank (0 ng·mL^{-1}), compared to sample 250_2 and 250_3.*

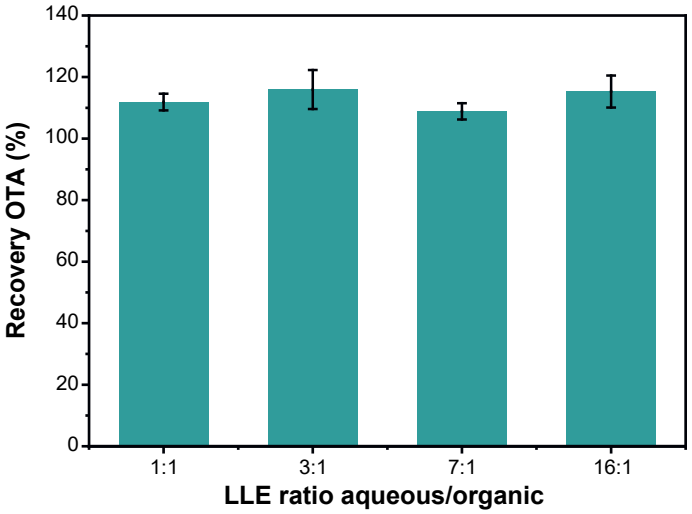


Figure S4.7: *Recovery of OTA following its extraction with different acid aqueous-to-organic volume ratios of 1:1, 3:1, 7:1, and 16:1, from water containing 0.1% formic acid (pH = ~2.7) to butyl acetate. The total volume of acidic aqueous and organic solution was fixed at 40 mL. Before the solvent extraction, the acidic aqueous solution contained OTA at 50 ng·mL. The recovery (%) was determined after HPLC-HRMS analysis. Error bars represent the standard deviation (n = 3).*

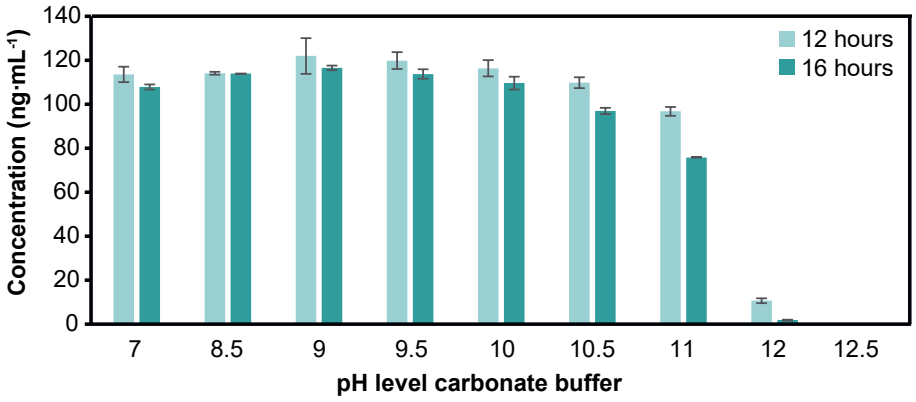


Figure S4.8: *Concentration of OTA in solution after storage of 12 or 16 hours at various neutral (pH = 7) and alkaline conditions (pH =8.5, 9, 9.5, 10, 10.5, 11, 12, or 12.5) at room temperature. The initial OTA concentration was 100 ng·mL^{-1}. The concentration (ng·mL^{-1}) was determined after HPLC-HRMS analysis. Error bars represent the standard deviation (n = 3).*

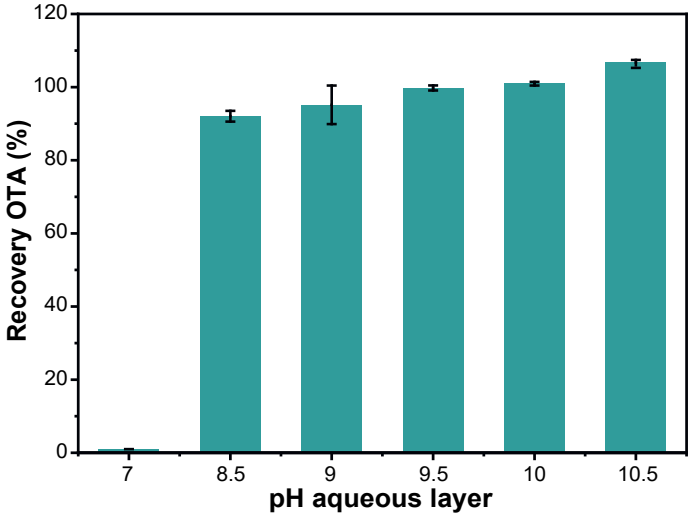


Figure S4.9: *Percentage of OTA in the alkaline aqueous layer after mixing 0.7 mL of organic phase (butyl acetate) with 0.7 mL of aqueous solution at different pH levels (pH = 7, 8.5, 9, 9.5, 10, or 10.5). Before the solvent extraction the OTA concentration in the alkaline aqueous solution was 125 ng·mL^{-1}. The percentage of OTA in the aqueous layer was determined after HPLC-HRMS analysis. Error bars represent the standard deviation (n = 3).*

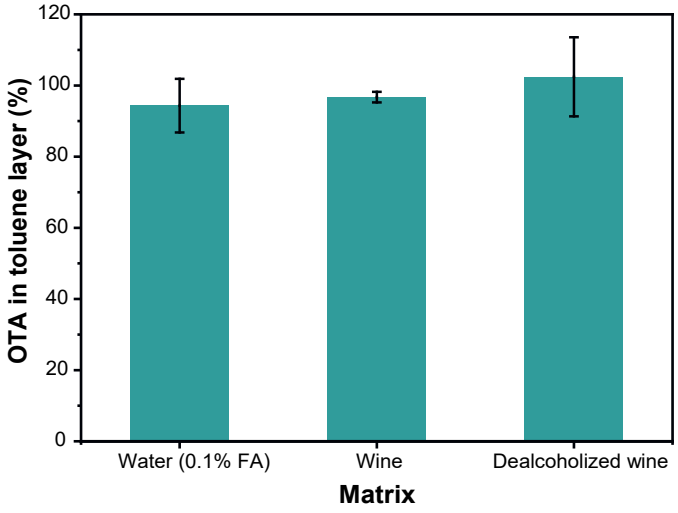


Figure S4.10: *Percentage of OTA in the toluene layer, after mixing 2 mL of toluene with 10 mL of acidic water, wine (12.5% v/v) or dealcoholized wine. Before the mixing the toluene layer contained 500 ng·mL^{-1} OTA. The percentage of OTA in toluene layer was determined after HPLC-HRMS analysis. Error bars represent the standard deviation (n = 3).*

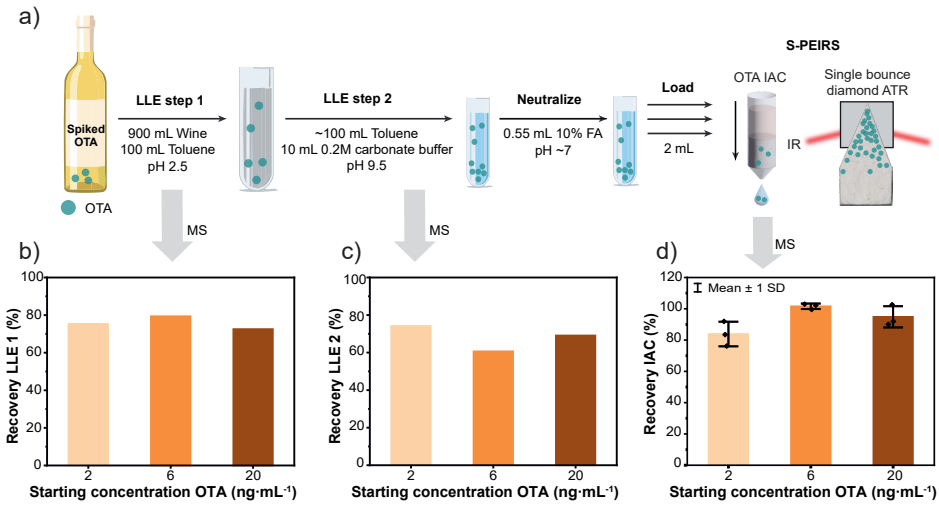


Figure S4.11: *HPLC-HRMS sub-samples taken at 3 different points and the recoveries were estimated for the individual workflow steps. An average recovery of 76 ± 3% was achieved during the first extraction, and 68 ± 7% during the second extraction. An immunoaffinity column (IAC) subsample (before and after) was taken for 2, 6 and 20 ng·mL^{-1}, and showed recoveries between 84 – 102%. Each paper tip contained absolute OTA quantities of approximately 140, 430 and 1370 ng for 2, 6 and 20 ng·mL^{-1} respectively. FA is formic acid.*

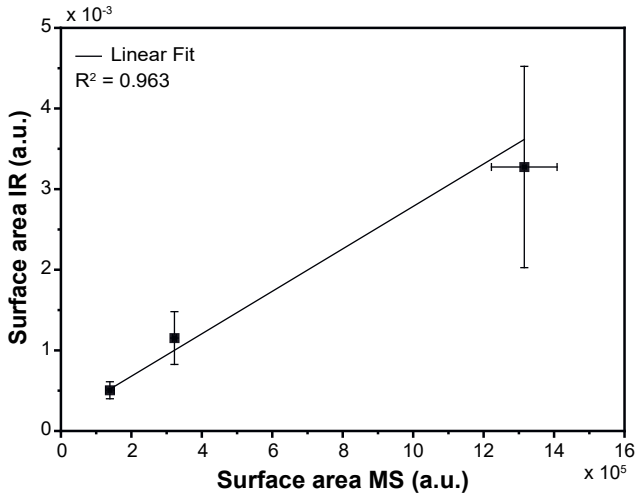


Figure S4.12: *Correlation results of the measurement of spiked wine samples at 2, 6 and 20 ng·mL^{-1} OTA using the developed solvent extraction assisted S-PEIRS method and comparative HPLC-HRMS analysis. The integrated OTA m/z area obtained by MS was plotted against the integrated OTA C=O vibrational mode obtained by IR. The error bars represent the standard deviations of both methods where in total n=3 for MS and n=15 for IR. Linear regression analysis between the data points showed correlation of R^2 = 0.963.*


5

General Discussion and Future Perspectives

5.1 General Discussion

The persistent occurrence of mycotoxins in our food value chain, as well as the migration of mycotoxin-producing fungi due to climate change present numerous challenges for their adequate detection. From the perspective of portable food analyzers for mycotoxin detection, the contents of this thesis focused on a methodological concept consisting of integrated sample preparation and direct mycotoxin detection with infrared (IR) spectroscopy (Figure 5.1). This was demonstrated for two regulated mycotoxins in different commodities and at different maximum levels (MLs), and laid the foundation for direct mycotoxin analysis. This thesis covers the entire range from the development of integrated and 3D-printed sample preparation tools for deoxynivalenol (DON) in wheat (Chapter 2), to a novel framework for direct mycotoxin detection where immunoaffinity chemistry, paper-based microfluidics and mid-IR spectroscopy were combined to establish selective paper-enhanced infrared spectroscopy (S-PEIRS, Chapter 3).

In order to improve the detection limit and detect the strictly regulated mycotoxin ochratoxin A (OTA) in white wine at the ML of 2 µg/kg, a pH-dependent solvent extraction was introduced (Chapter 4). Therefore, S-PEIRS can be used for the detection of these mycotoxins in hard and soft commodities, and at trace levels (Figure 5.1). In this final chapter, an overview is presented of the key results described in this thesis, linked to the original hypotheses (Chapter 1) and the associated challenges (Table 5.1). Subsequently, the methodological innovations of this thesis are evaluated in a broader and integrative context, to define and discuss remaining challenges, as well as ways to address them as a roadmap for future research.

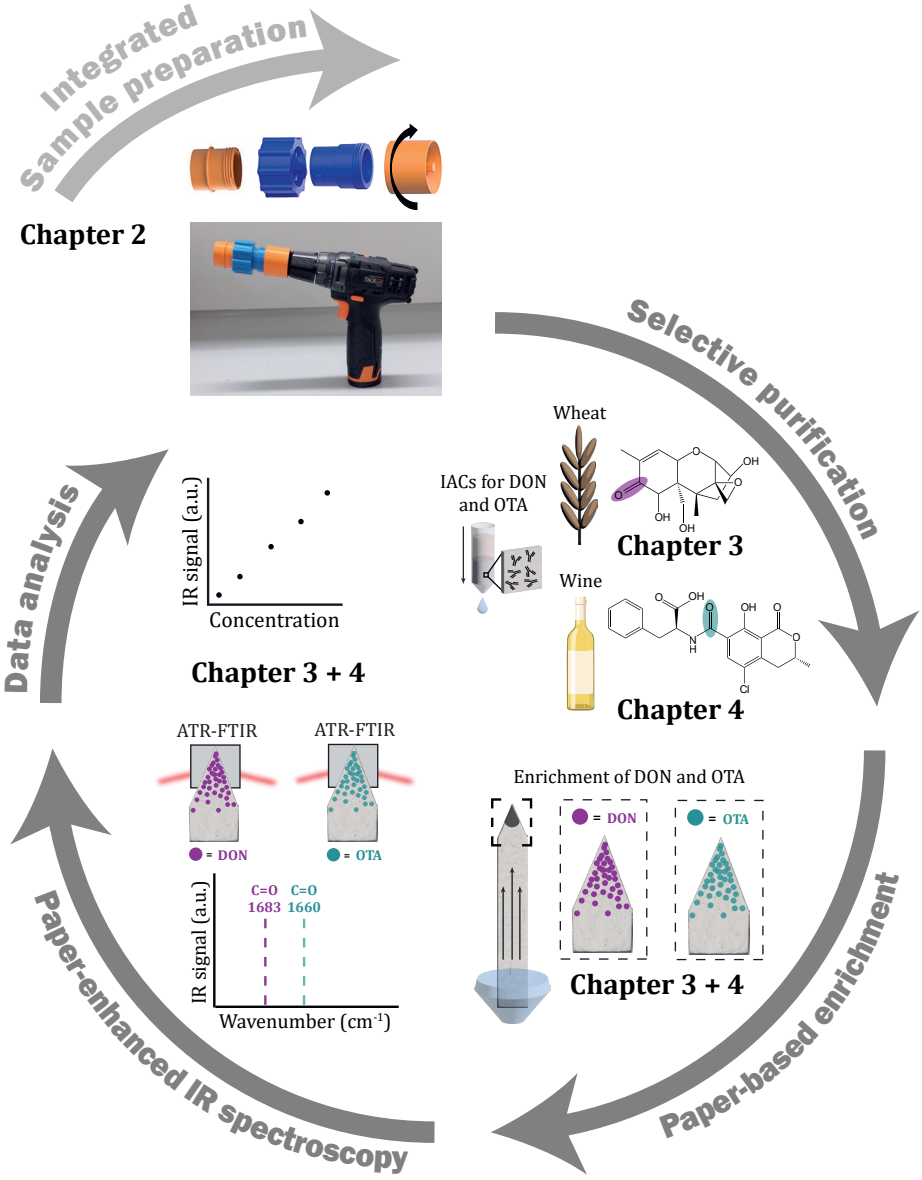


Figure 5.1: *Illustration of the scientific innovations described in this thesis.*

Table 5.1: *Challenges addressed and solutions provided in this thesis to develop integrated and direct infrared analysis of mycotoxins.*

Aim	Challenges	Solution(s), highlights and validation
Chapter 2 Investigation and development of new 3D-printed devices for integrated grinding and extraction of DON in wheat for mycotoxin screening	1. Complex and costly sample preparation. 2. Complete workflow validation with end-user generated particle sizes 3. Non-harmonized grinding of current commercial rapid tests. 4. Availability of appropriate reference materials.	- Integrated 3D-printed modules for grinding and extraction that are affordable (€2.50) and scalable. - Drill-operated grinding device. - Mixing of naturally contaminated wheat kernels to obtain a representative sample. - Prototype showed regulatory relevance for DON, is fit for a commercial portable food analyzer, and good correlation with LC-MS/MS (R^2 = 0.96). - Demonstrated user-friendliness by 10 first-time users that operated the device with minimal training.
Chapter 3 Develop a novel framework for direct mycotoxin analysis of DON in wheat at the maximum limit (1 mg/kg) using ATR-FTIR spectroscopy.	1. Insufficient sensitivity and selectivity of ATR-FTIR spectroscopy for mycotoxins in food. 2. Matrix-related absorbances convolute mycotoxin signal 3. Compensation for paper-related absorbances	- Selective paper-based IR framework (S-PEIRS) for the direct detection of DON in wheat in the regulatory range around 1 mg/kg. - Differentiation of DON specific C=O feature (1683 cm^{-1}) from background (matrix residue + paper). - Passive paper tip evaporation-based enrichment improved detection limit of ATR-FTIR. - Developed a standardized IR data analysis framework for mycotoxin feature selection and analysis. - Benchmarked S-PEIRS against state-of-the-art LC-MS/MS method that showed good agreement between IR and MS.

Aim	Challenges	Solution(s), highlights and validation
Chapter 4 Advance the paper-based IR framework to achieve the quantitative detection of OTA in white wine at the maximum limit of 2 µg/kg.	1. Detection in other (soft) commodities. 2. Detection limit S-PEIRS inadequate for trace level detection (low µg/kg range). 3. Reliable mycotoxin quantification based on molecular feature, at ML and in relevant matrix.	- S-PEIRS achieved the quantitative analysis of OTA in white wine (0 – 20 µg/kg) based on a specific molecular feature. - A 2-step pH-dependent solvent extraction for the purification and pre-enrichment of OTA in white wine. - Detection of OTA specific C=O feature (1660 cm^{-1}) from background (matrix residue + paper). - Strong relationship between solvent extraction assisted S-PEIRS and HPLC-HRMS (R^2 = 0.963) for the OTA levels 2, 6, and 20 µg/kg in white wine.

5.1.1 Integrated 3D-printed sample preparation for mycotoxin detection in hard commodities

3D-printing offers outstanding advantages due to the complete three-dimensional design freedom that aids customizability, rapid and low-cost prototyping. In addition, the on-demand production of parts anywhere in the world and the integration of parts to fabricate multifunctional devices are advantages as well. In order to develop sample handling tools that fit within a portable food analyzer workflow, the research described in Chapter 2 has utilized 3D-printing to develop an integrated grinding, particle selection and extraction device for mycotoxin detection in wheat kernels. This new device was combined with a commercially available lateral flow immunoassay (LFIA) method, to standardize the sample handling for on-site applications. Currently, the grinding practice of the LFIA method is not specified by the manufacturer and this leads to discrepancies in the end-result. The LFIA method was calibrated by the manufacturer with certified reference material that contains very finely ground and fully homogenized particles, which is not realistic for end-users with intact wheat samples. This introduced another challenge: the use of comminuted or certified reference material for calibration and validation avoids the assessment of the full screening method, as was also described by Tittlemier et al.[1]. Therefore, in Chapter 2, naturally contaminated intact wheat kernels were mixed to obtain several contamination levels which were ground by both the 3D-printed device and a standard laboratory mill. Reference analysis of the ground materials, as generated by the end user, indeed led to an underestimation in the end-result due to the difference in generated particle size between laboratory mill and 3D-printed grinder device.

In Chapter 1, it was described that many of the regulated mycotoxins occur in cereal products such as wheat. Therefore, in addition to detecting DON in wheat, the same workflow could be used to identify other regulated mycotoxins in wheat such as T-2/HT-2 toxin, zearalenone, fumonisins, ochratoxin A, and aflatoxins. Next to the successful implementation of the 3D-printed device in the LFIA workflow, it can be expected that the current device fits in an indirect, prediction-based IR screening method for mycotoxins such as those described in Chapter 1. In addition, it shows potential for implementation in the direct IR analysis method developed in this thesis (Chapter 3). Finally, whether commodities of similar size and hardness as wheat kernels can be processed using the current device needs to be further explored, as well as customization of the device for the processing of different hard (or soft) commodities. For example, to achieve the sample processing of peanuts, one of the major commodities in which aflatoxin B1 is found, the prototype needs to be customized [2]. The reason for that is because such oily commodities are typically processed as a slurry (processing in solution) [3,4]. The current device is not capable of slurry processing as the solvent would immediately drain into the collection module instead of blending with the peanuts. Therefore, redesign is needed that allows peanut processing with solvents using the device.

5.1.1.1 3D-printing for green analytical sample preparation

In Chapter 2 (Section S2,1), the sustainability and costs of the 3D-printed device were discussed in detail. In addition to that, increased focus on sustainability in chemistry have led to the development of test metrics that help estimate the greenness of analytical chemistry methods [5–9]. These metrics are based on the principles of green analytical chemistry (GAC) and examples include analytical greenness evaluation (AGREE) and green analytical procedure index [9]. In recent literature scientists found that AGREE was the most fitting metric to evaluate how 3D-printing can improve the analytical greenness of novel devices [10]. A variant of the AGREE metric was developed specifically to assess the greenness of analytical sample preparation, named AGREEprep. The online testing tool of AGREEprep (https://agreeprep.anvil.app) was used to estimate the greenness of the current 3D-printed sample handling device in combination with the LFIA workflow for the detection of DON in wheat (Table 5.2, Figure 5.2). This metric consists of 10 criteria that were used for the determination of greenness scores. The prototype developed in Chapter 2 scored particularly good (1.00 out of 1.00) on criteria 2, 9, and 10. Criterion 2 describes the use of hazardous materials during sample preparation and because only water and a dissolvable buffer bag were used, the value for hazardous materials was zero. Criterion 9 describes the format of analysis and in the LFIA workflow the sample was transferred to a paper test strip and the read-out was done automatically by a dedicated reader. Criterion 10 describes the safety of the

operator from the perspective of the sample preparation reagents, which were all safe. However, this metric does not consider the toxicity of the analyte and adequate safety measures must be taken when working with material that is potentially contaminated with mycotoxins.

Table 5.2: *Overview of the AGREEprep results including the criteria, answers and obtained score. All criteria were equally weighted and the score scale goes from 0.00 to 1.00.*

#	Criterion	Answer	Score
1	Sample preparation placement	On-site	0.33
2	Hazardous materials	0 [g or mL]	1.00
3	Sustainability, renewability, and reusability of materials	50-75% of reagents and materials are sustainable or renewable, but can only be used once	0.50
4	Waste	50 [g or mL]	0.00
5	Size economy of the sample	Mass or volume of the sample: 10 [g or mL]	0.33
6	Sample throughput	6 [samples/h]	0.42
7	Integration and automation	Sample prep steps: 3 steps, semi-automated systems	0.38
8	Energy consumption	30 [W]	0.72
9	Post-sample preparation configuration for analysis	Simple, readily available detection: smartphones, desktop scanners, paper strips etc.	1.00
10	Operator safety	No hazards or no exposure	1.00

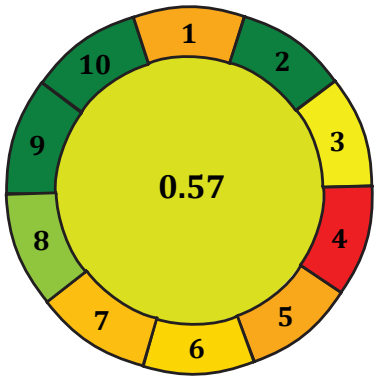


Figure 5.2: *Overall AGREEprep result for the developed 3D-printed sample preparation tool with greenness color indication per criterion, red signifies a low score and green a high score on a scale from 0.00 to 1.00.*

The improvement of criteria 4, 5 and 7 requires the minimization of waste, sample size and sample preparation steps. To improve criterion 7, the number of sample preparation steps need to be further minimized by for example facilitating in-device LFIA testing as demonstrated for the unibody lab-on-a-chip in Chapter 1 (Figure 1.4) [11]. The minimization of waste and size economy of the sample requires a smaller extraction volume and a smaller sample weight, because currently a volume of 50 mL and a weight fraction of 10 g are used. For example, if the AGREEprep metric would be used again for an extraction volume of 5 mL and a sample size of 1 gram, the overall metric score would further improve from 0.57 to 0.64. However, such metric improvements come at the cost of a reliable result, because a smaller sample size is generally less representative [12–14]. The reason for that is the high degree of heterogeneity of mycotoxin contamination, as the mycotoxins occur in so-called 'hot-spots' [13,14]. Therefore, in the field of mycotoxin analysis, adequate sampling is one of the most (if not the most) difficult aspects of the whole measurement procedure and is typically the largest contributor to the total variance [13,14]. In the EU, official sampling plans are in place that state the minimal sample size for a specific lot and indicate how many small increments need to be sampled, the typical weight of the increment sample is 100 g [15]. As an example, for lot sizes smaller than 100 tons, up to 100 incremental samples are taken that result in aggregate sample weights between 1 – 10 kg [15]. That means that minimizing the size economy of the sample during sample preparation to improve the AGREEprep metric, is not analytically responsible.

5.1.1.2 3D-printing for user-friendly sample preparation

In Chapter 1 it was stressed that the operability of portable food analyzers should match the level of expertise and intended purpose of the envisioned user. This was underlined by the findings of Chapter 2, where the variability in grinding method significantly influenced the end result due to the lack of standardized grinding practices. For the 3D-printed device developed in Chapter 2, a user-centric approach was taken. This included design considerations such as a drill-attachment that was created for easy grinding without needing manual labor, an interconnected device that improved operator safety and, an ergonomic design of the parts that are held by the user. 3D-printing also allows for the color coding of parts and the inscription of texts for a more intuitive user interface. The grinding operation of the device was tested with ten new users (age between 21 and 66) and all of them were able to obtain sufficient wheat particles in 30 seconds with minimal instructions (average $\pm$ RSD $= 1.37$ g $\pm$ 38%). Nevertheless, the user-friendliness of the device could be further improved by providing a pictogram guide and movie with instructions, similar to the work described by Ross et al [11]. Finally, after further device optimization, the usability of the full workflow should be evaluated with different end-users and a

dedicated metric. While some criteria of AGREEprep are linked to user-friendliness such as criteria 7, 9 and 10, this metric is not meant to assess it critically. Notably, there is not one quantitative or qualitative tool which is the 'golden standard' for the assessment of user-friendliness of portable analytical devices. However, there is one concept that could be transformed in such a tool which is the concept of (RE)-ASSURED, also described in Chapter 1 [16–19].

5.1.2 S-PEIRS for direct mycotoxin detection in hard and soft commodities

As described in Chapter 1, IR spectroscopy is a versatile technology and provides rapid, non-destructive and environment-friendly chemical analysis of food products. In combination with chemometrics, it becomes a powerful tool to translate spectral data into valuable information on the quality, authenticity or safety of foodstuffs. In the context of indirect mycotoxin analysis, information on the safety of a certain food is obtained via the correlation of fungal-induced matrix changes to mycotoxin contamination [20,21]. While this can be used as pre-screening strategy that can predict the possibility of a sample exceeding the maximum limit (ML), it does not offer the level of certainty needed for direct mycotoxin screening nor for confirmatory analysis. In Chapter 1, several challenges were identified that have prevented the direct detection of mycotoxins using IR spectroscopy. These included; (i) the low, yet harmful abundance of mycotoxins in complex food matrices, (ii) the lack of IR method specificity and, (iii) the inadequate detection limit of routine IR spectrometers for ML concentrations.

The work described in this thesis explored a novel strategy that strengthens the chemical elucidation power of mid-IR spectroscopy with the specificity of immunoaffinity chemistry and detection advancements by paper-based microfluidics. In Chapter 3, this strategy was introduced and the direct detection of DON in wheat at the ML (1 mg/kg) was achieved. This strategy was named 'selective paper-enhanced infrared spectroscopy (S-PEIRS)' and highlights the first demonstration of direct mycotoxin detection with mid-IR spectroscopy allowing the molecular identification of DON in wheat. In Chapter 4, the capabilities of S-PEIRS were further explored and the direct detection of OTA in white wine at the ML (2 µg/kg) was achieved. For this work, a pH-dependent solvent extraction was needed to preconcentrate a sufficient amount of OTA molecules from wine prior to performing S-PEIRS. In addition, S-PEIRS was adapted to identify the characteristic vibrational mode of OTA. Therefore, the S-PEIRS concept allows for the specific enrichment of mycotoxin molecules in a paper substrate, and a characteristic IR feature of the mycotoxin is measured on the paper directly.

The novel concept of S-PEIRS shows the power of IR spectroscopy for direct

mycotoxin analysis and is based on characteristic IR features, which leads to increased measurement certainty over indirect screening methods. These aspects and the major components of the S-PEIRS methodology are evaluated and discussed in the following sub-sections.

5.1.2.1 Selective purification

Initially, it was explored if selectivity could be achieved by realizing an immunocapturing area on a paper substrate, which follows the work of Geballa-Koukoula et al. [22]. In this work, an immunocapturing area for DON was realized on nitrocellulose paper, after washing the immunocapturing area with water the DON was dissociated in 200 µL solution ($MeOH/NH_3$, 2% v/v) and directly measured with mass spectrometry. The absolute quantity of DON that could maximally be captured in this area was approximately 4 ng, leading to a maximum concentration of 20 ng/mL, which is sufficient for MS analysis [22]. However, the absolute quantity of mycotoxin molecules that was needed for ATR-FTIR analysis (by liquid deposition) was at least 50 ng (in 0.5 µL), which is equivalent to 100000 ng/mL. Therefore, this strategy was impractical for the capturing of sufficient DON molecules for ATR-FTIR. Alternative capturing strategies were considered and column-based formats showed more potential because of their increased capturing capacity for mycotoxins. Another advantage of column-based formats was their widespread use and commercial availability for most regulated mycotoxins. Three major column-based capturing formats are available for mycotoxins; immunoaffinity columns (IACs), molecularly imprinted polymer (MIP) columns and solid-phase extraction (SPE) columns [23–28]. SPE columns do not show specificity towards the target mycotoxin and are mainly used for sample clean-up prior to instrumental methods that rely on internal analyte separation and sensitive detection such as LC-MS/MS. Therefore, SPE-columns were not suitable for direct mycotoxin analysis using ATR-FTIR spectroscopy. The other two column formats, IACs and MIPs, show specificity towards the target mycotoxin by affinity through biological interactions (antibodies) or shape selectivity, respectively [25].

MIP-based selective enrichment relies on the manufacturing of synthetic binding cavities in a polymer matrix in which the target mycotoxin can be captured through intermolecular forces. Compared to IACs, MIP-columns show advantages such as increased loading capacity, are stable in organic solvents, can be stored at room temperature and are generally less expensive [25,28,29]. Moreover, affinity through synthetic interactions is interesting from a research and development perspective of novel mycotoxin methods because of the European Union (EU) Directive 2010/63/EU that advices a shift towards non-animal derived affinity elements [28,30,31]. However, commercially available MIP-columns generally suffer from low affinity and column

leaching (yielding false results), and are therefore mostly fit for applications where the capacity is more important than the specificity [29]. In addition, compared to the IACs, a commercial MIP-column workflow consists of more steps and includes multiple organic solvents which makes such procedures less suitable for on-site applications. While advances in nanotechnology have enabled the fabrication of nanoMIPs which can compete with antibodies in terms of specificity and show other improvements, the availability of nanoMIP affinity columns is limited and was therefore not chosen as affinity approach for the work described in this thesis [25,29].

In Chapter 3 and 4, IACs were chosen for the capturing of DON and OTA because of their widespread availability and, superior specificity and operability [25]. Moreover, IACs are an important purification tool in analytical chemistry and are recognized as official method for reliable food safety testing [23]. Next to the IACs for DON and OTA, there are IACs available for many other mycotoxins and harmful residues in food. Therefore, S-PEIRS can be adapted to measure these other mycotoxins and residues. This can be realized by simply exchanging the IAC as was also demonstrated in Chapter 4 where S-PEIRS was adapted from DON to OTA. Therefore, it is possible to use multiple IACs for the same sample allowing the detection of co-occurring mycotoxins in food products such as cereals, in which co-occurrence can be problematic [2,32–34]. Next to single mycotoxin columns, multi-mycotoxin IACs are also available and could potentially be used to detect multiple mycotoxins in one measurement using S-PEIRS. Still, the multi-IAC loading capacities, the natural presence of co-occurring mycotoxins and the broad range of MLs they are regulated at require further optimization of S-PEIRS in order to achieve multi-mycotoxin detection in the future.

While the use of IACs is part of the success of S-PEIRS, several challenges remain (partly) unaddressed. One of the central challenges that was faced in Chapter 3 was the loading capacity of the IACs, which affects the absolute quantity of mycotoxin molecules that can be captured from the sample solution. Essentially, the loading volume and the loading capacity have an immediate effect on the detection capability and linearity of the method. Commercial IAC protocols are optimized for instrumental detection methods such as LC-FLD or LC-MS, which are much more sensitive than IR (or S-PEIRS) and for those methods it suffices to use 2 mL of 20% w/v extracts to detect DON contamination. In Figure 5.3, a theoretical demonstration of the challenges encountered in Chapter 3 is illustrated. In this figure, the absolute DON quantities that can maximally be present in different IAC loading volumes (2, 4, 6, 8 and 10 mL) for samples contaminated at 0.5, 1.0, 2.0 and 3.0 mg/kg DON are shown. Here, it can be observed that 2 mL loading volumes of samples contaminated at $\leq$ 3 mg/kg do not allow the capturing of sufficient DON molecules for IR detection. In addition, only the loading volumes of 8 and 10 mL allow the capturing of sufficient

DON molecules from wheat samples contaminated at ML (1 mg/kg, blue symbols), as these quantities fall within the operation window of S-PEIRS. Therefore, in Chapter 3, a loading volume of 10 mL was used to consider this operation window and which allowed the detection of DON in wheat contaminated at ML.

In order to optimize the current S-PEIRS method for DON, two strategies can be explored to enlarge the operation window. One of the strategies is to develop IACs that have at least double the loading capacity of the current column (2500 ng). This should lead to a larger operating window for S-PEIRS. However, this would also increase the cost per analysis significantly, which is already relatively high (approx. €20,- per column), as more antibodies are needed. Another strategy to enlarge the operating window is to improve the detection limit of S-PEIRS by further enhancing the paper-based enrichment and IR detection (5.1.2.2 and 5.1.2.3). Moreover, an alternative approach to achieve selectivity was explored that avoids the use of an affinity column completely, via paper-based enrichment (5.1.2.2.1).

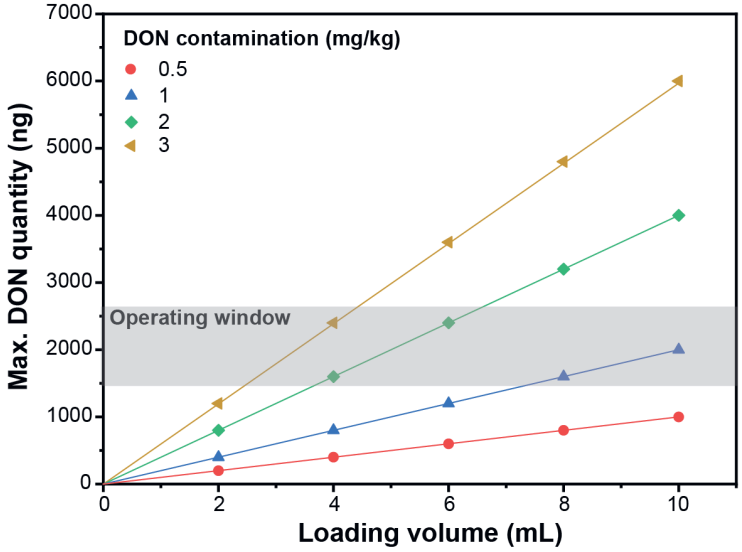


Figure 5.3: *Theoretical demonstration of the S-PEIRS operation window for DON. The maximum DON quantity in the sample is shown for different loading volumes and contamination levels of samples extracted following 20% w/v. The operating window in which mycotoxin analysis is possible (grey box) is determined by the S-PEIRS detection limit and the maximum capacity of the IAC columns for DON.*

5.1.2.2 Paper-based enrichment

During the work described in Chapter 3, it became evident that significant enrichment (enrichment factor >100) was needed to achieve the detection of mycotoxins at relevant concentrations with ATR-FTIR. In addition, the active IR

sensing area was restricted by the single-bounce format of the ATR unit (2 x 2 mm diamond crystal interface). Therefore, one of the central challenges for mycotoxin analysis was to find an approach that allowed the accumulation of a high quantity of molecules in a focused substrate area. In Chapter 1, the choice of paper as enrichment substrate was substantiated and was related to its analytical versatility, spontaneous flow and affordability. In Chapter 3, first, a small paper disc was used to enrich DON by drop-casting of the sample solution. While this method could detect high concentrations of DON and marked the first measurement of mycotoxin molecules on paper with IR, the method was not suitable to enrich a high quantity of DON from ML solutions in a focused paper area. This was partly related to the shape of the paper, as illustrated in Figure 5.4. Here, the circularity of the paper induced a ring-shaped enrichment profile (e.g. coffee-ring effect) instead of a focused area, which was governed by evaporation [35–37].

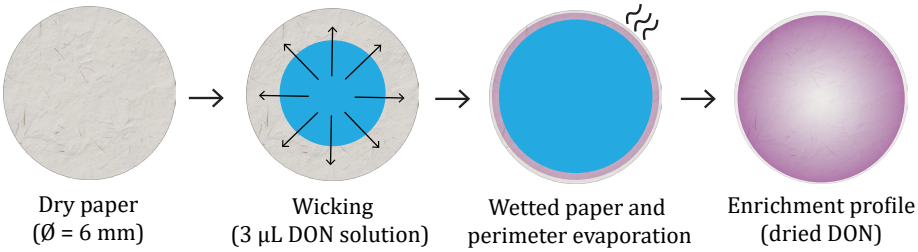


Figure 5.4: *Schematic of paper-microfluidic process on the paper disc. The wicking of DON solution in the outward direction leads to a fully wetted paper and evaporation of the solvent is fastest at the perimeter, inducing a ring-shaped enrichment profile.*

To overcome this, the evaporation process became a means to steer the enrichment of DON in paper. Therefore, a tip shape was explored because then the evaporation is driving capillary flow to the tip area, leading to focused enrichment of solutes. The use of paper tips not only solved the challenge of mycotoxin enrichment for IR but also facilitated the positioning of the paper on the small ATR interface. In the case of the paper discs, the paper needed to be slightly moved between each repeated IR measurement to consider the ring-shaped distribution of DON. For the paper tips this was not necessary, because the highest IR response for DON was found in the tip area. Moreover, the use of paper tips allowed the wicking and evaporation of a larger volume of DON solution than the paper discs, leading to the enrichment of sufficient quantities for IR analysis. One of the remaining challenges is the speed of the evaporation, which needs to be increased for on-site applicability. Currently, a 1.5 mL methanol solution takes at least 12 hours to evaporate and a 1.5 mL IAC eluate solution takes at least 24 hours to evaporate. The evaporation of eluate solution takes longer than the pure methanol because of the presence of residual

water from the IAC washing procedure. Moreover, environmental factors such as humidity played a role in the speed of the evaporation process as well.

To speed up the evaporation and enrichment of solutes in the paper tip, one approach is to shift from passive to active evaporation and enrichment by applying heat or compressed air [38], as discussed in Chapter 3 and 4. Iterative design of several active evaporation set-ups have led to the development of a 3D-printed heat-induced enrichment prototype (Figure 5.5). Using this prototype, a 1.5 mL solution of diluted food dye (in methanol) was enriched in the paper tips in 45 minutes, which is significantly faster than the passive evaporation. Still, this prototype needs further optimization and validation before it is suitable for implementation in the S-PEIRS workflow. The following aspects require further research; (i) the wicking of uncured polymer resin from the 3D-printed prototype in the paper tips, (ii) adsorption of target molecules onto the surface of the 3D-printed prototype which influences recovery, (iii) adsorption of glue from the copper tape in the paper and, (iv) influence of heat on the solutes present in the IAC eluate (e.g. wheat proteins), which all possibly affect IR analysis.

In addition to shifting towards active evaporation, a complementary approach to study the physical-chemical parameters that govern the enrichment of analytes in paper would be interesting. In this way the deposition of mycotoxin molecules can be further improved towards the paper tip area, and preferably also on one side of the paper, to improve the detection limit. Therefore, the paper-based enrichment process of S-PEIRS could be computed and further optimized using COMSOL Multiphysics software [39–42].

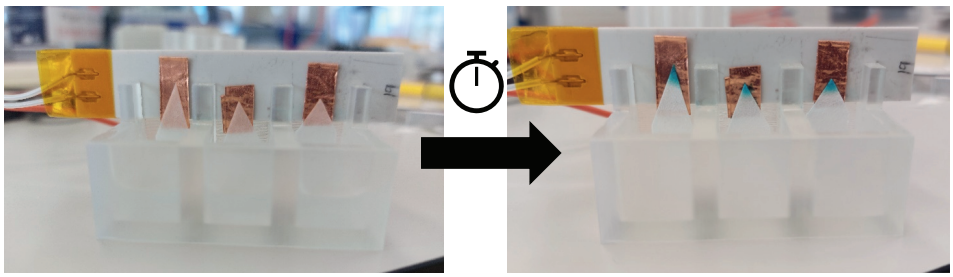


Figure 5.5: *3D-printed prototype of a heat-induced active evaporation set-up. The prototype consists of a ceramic heating element that is controlled by a USB power supply (step up/down module) and was set to 9.5 V. This heating element was inserted in a 3D-printed holder that contained three cavities for liquids. Copper tape was used to optimize the contact and heat transfer between heating element and paper tip. A diluted blue food dye solution in methanol (1.5 mL) was evaporated and the dye molecules enriched in the paper tips in 45 minutes.*

One of the reasons that the passive evaporation was slow and the active format was proposed, is the relatively large volume (1.5 mL) that needs to wick into the paper and evaporate. This volume is linked to the IAC procedure, where the minimal amount of elution volume that can be used to remove the captured mycotoxin from the IACs was 1.5 mL. It might be possible to reduce the elution volume and consequently also the evaporation time, yet the use of IACs brings about additional challenges as discussed in Section 5.2.1. Therefore, an alternative approach to using affinity columns was explored, to achieve selective paper-based enrichment.

5.1.2.2.1 Paper-immobilized liquid-phase microextraction

In order to achieve selective and paper-based enrichment of mycotoxins without the use of affinity columns, an approach based on the work of Lemmink et al. was explored [43,44]. This approach is named paper-immobilized liquid-phase microextraction (PI-LPME), and has been developed to enrich tropane alkaloids (TAs) in paper from different food samples [43,44]. Characteristic to this approach was that no affinity element (e.g. antibody or MIP) was used, only a pre-wetted acidified paper strip that acts as the microextraction substrate. In PI-LPME, the acidic aqueous solution becomes immobilized in the paper more readily than butyl acetate because of capillary action. At low pH, the TAs are protonated and therefore favor partitioning from the apolar organic solution to the polar acidified solution, immobilized in the paper. The large phase ratio between the organic solvent and immobilized acidic solution leads to the enrichment of TAs in the paper, while most non-ionizable matrix constituents remain in the butyl acetate [43].

To adapt PI-LPME for OTA enrichment, an alkaline aqueous solution for paper immobilization was used because OTA becomes deprotonated at high pH, as discussed in Chapter 4. Therefore, OTA favors partitioning to the immobilized alkaline solution and this leads to OTA enrichment in the paper. Thereafter, PI-LPME was combined with PEIRS for the selective enrichment of OTA (Figure 5.6). Essentially, here, the selective aspect of S-PEIRS is the PI-LPME method instead of the IACs. The first extraction step of this combined workflow would be similar to that of Chapter 4, a solvent extraction of wine, yet was initially left out to study the combination of PI-LPME and S-PEIRS without matrix interference. Samples of 10 mL butyl acetate containing either 0, 180 or 1000 ng/mL OTA (n=6 per concentration) were prepared (Figure 5.6a). A S-PEIRS paper tip (in a 3D-printed holder) was prewetted with alkaline solution, inserted in the butyl acetate and was left overnight (PI-LPME). The butyl acetate volume was analyzed using HPLC-HRMS before and after PI-LPME, and showed OTA removal of 80 $\pm$ 4% for the 180 ng/mL samples and 62 $\pm$ 3% for the 1000 ng/mL samples (Figure 5.6b). Subsequently, the papers were dried and inserted in 100 µL of clean methanol in order to transfer the enriched OTA

to the tip area. The dried tips (n=3 per concentration) were analyzed following the S-PEIRS protocol of Chapter 4, which included spectral processing procedures such as baselining and normalization (*) to 1315 cm^{-1} (Figure 5.6c). The characteristic amide I vibration of OTA was visible in the absorbance spectra of 180 and 1000 ng/mL at 1665 cm^{-1} (indicated with arrow) and was different from the blank. The ether stretch vibration of OTA was found at 1203 cm^{-1}, and was an additional indication of the presence of OTA on the paper. A 2^{nd} derivative analysis of the OTA region around 1665 cm^{-1} showed the difference of the OTA containing samples from the blank paper signal in this region (Figure 5.6d).

The integration of the area of the 2nd derivative spectra showed that the average areas of 180 and 1000 ng/mL were indeed different from the blank, yet one of the papers from the 1000 ng/mL set showed a relatively low response compared to the other two papers in this set, which requires further research (Figure 5.6e). In addition, what also requires further research is the full workflow including the acidic wine matrix.

One of the challenges that needs further research is the co-extraction of wine residues in the butyl acetate phase that can influence the partitioning of OTA to the alkaline paper as well as cause IR interference. Therefore, to reduce matrix co-extraction, we shifted from butyl acetate to toluene in Chapter 4. While the use of toluene may work for PI-LPME as well, toluene is not very suitable for on-site methods, and therefore PI-LPME for OTA in wine requires further studies. Nevertheless, these results do show that the adapted PI-LPME approach can be used to enrich OTA in paper, and subsequently detect it using S-PEIRS. Moreover, this highlights the potential of enrichment without the need of affinity columns for paper-based IR spectroscopy.

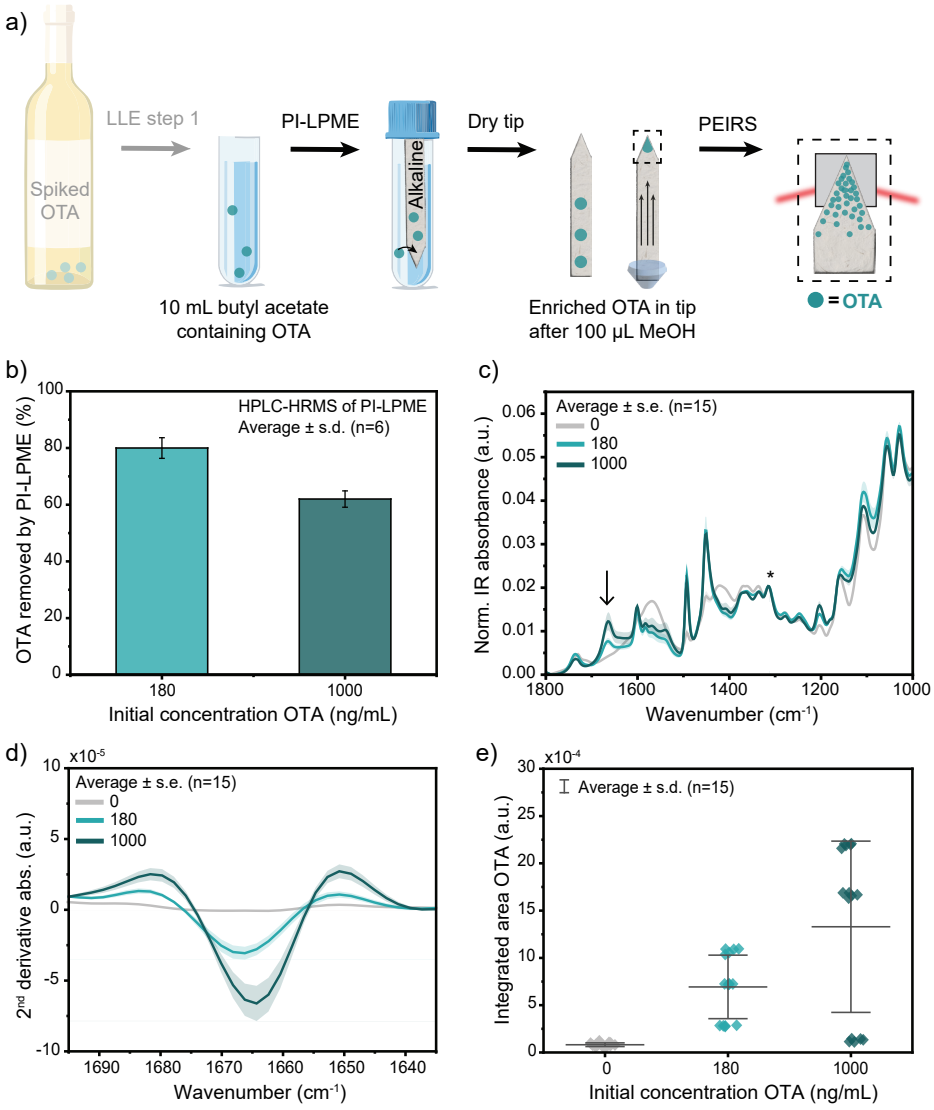


Figure 5.6: *Combined method of PI-LPME and PEIRS for the selective enrichment and detection of OTA using paper. a) Workflow was performed without the first extraction step to prevent matrix interference. b) HPLC-HRMS analysis of PI-LPME showed OTA removal of 80 ± 4% and 62 ± 3% for 180 ng/mL and 1000 ng/mL samples, respectively. c) Preprocessed IR absorbance spectra (* indicates normalization point and arrow indicates the OTA amide I vibration). d) 2nd derivative spectra of OTA region around 1665 cm^{-1}. e) Integrated areas of 2nd derivative spectra.*

5.1.2.3 Selective paper-based IR spectroscopy for mycotoxin analysis

As described in Chapter 1, the implementation of IR spectroscopy for food safety analysis was limited to the prediction of mycotoxin contamination based on fungal-induced matrix changes, and was therefore categorized as indirect screening method [45]. Therefore, in this thesis, one of the central objectives was to develop a method that would allow the direct detection of mycotoxin molecules with mid-IR spectroscopy, for which S-PEIRS was established. The mid-IR spectroscopy principle behind S-PEIRS exploits Attenuated-Total-Reflection Fourier-Transform (ATR-FTIR) spectroscopy, a well-established spectroscopic tool to study the surface ($\leq$ 2 µm) of samples. In S-PEIRS, the sample surface (paper) is enriched with mycotoxin molecules and other solutes from the different method components, as described in Chapter 3 and 4. Therefore, the typical spectrum of a S-PEIRS paper tip consists of vibrational modes originating from the paper substrate, the enriched mycotoxin molecules and other potential solute-related interferences. It was therefore important to study the spectral features of paper and the mycotoxin in detail, as was demonstrated in Chapter 3 and 4.

To standardize S-PEIRS analysis, a framework was established that builds-up in method complexity while continuously examining the IR spectral changes (Table 5.3). In Chapter 3 and 4 this framework was exploited for the detection of DON and OTA in wheat and white wine respectively, but can also be used to study other analytes and matrices.

Table 5.3: *General framework components of the developed S-PEIRS method.*

Major framework items	**Why**	**How**
1: Paper	To elucidate the vibrational modes and chemical variability of the substrate.	Measurement of individual clean paper substrates with ATR-FTIR.
2: Analyte	To elucidate the vibrational modes of the mycotoxin.	Measurement of highly concentrated standard solutions with ATR-FTIR (by liquid deposition). Compare with blank.
3: Enrichment (PEIRS)	To examine the detection limit and concentration-dependency for paper-based IR analysis using standard solution.	Enrichment of high volumes at concentrations approaching detection limit. Compare with blank.
4: Identification molecular signature	To differentiate between mycotoxin and paper background.	Select the strongest mycotoxin related vibrational mode, showing a concentration dependent signal, in a region where paper minimally interferes.
5: Point of normalization	To standardize the spectra and correct for small measurement errors.	Select a point in the spectrum where paper absorbs and the mycotoxin does not (or minimally).
6a: S-PEIRS of standard solution	To examine influence of selectivity element (e.g. IAC) on spectra/ results.	Run complete method using detectable concentration levels of standard solution. Investigate newly appearing absorbances.
6b: S-PEIRS of reference material (e.g. quality control or fortified food samples)	To proof the concept using well-characterized samples with known contamination levels in controlled matrices.	Run method using reference material. Deconvolve identifier vibration and examine performance parameters.

Major framework items	Why	How
6c: S-PEIRS of naturally contaminated samples	To validate method using real-world samples and contamination levels. To consider natural matrix variability.	Run complete method using naturally contaminated samples. Deconvolve identifier vibration and examine the method performance parameters. Evaluate reliability of method.
7 (optional): Chemometric analysis of S-PEIRS spectra	Multivariate assessment of spectra and sample differences	Principle component analysis of spectra. Loadings show which variables are responsible for separation in PCA.

While S-PEIRS allowed the direct detection of mycotoxins in matrix and at ML for the first time using IR spectroscopy, several challenges remain unaddressed. One of the challenges is reproducibility. So far, S-PEIRS was only performed by one person in one laboratory. Therefore, to assess reproducibility, the S-PEIRS method needs to be externally validated, first by different scientists in different laboratories, and subsequently by end-users on-site. Thereby, a good understanding of the reproducibility and reliability of the method in real user settings can be obtained. However, before proceeding with external validation the S-PEIRS method requires further optimization and simplification, as was already discussed in the other sections.

Another challenge is the automation of the data analysis. While the current data analysis protocol can be partly automated in the OriginPro software, full automation is required when moving to on-site devices. Ideally, the on-site user places the paper tips on the IR interface and starts the analysis. When all papers are measured the spectra should be processed and analyzed in the back-end of the software and only return the final result to the end-user. The analysis can be mid-fidelity or high-fidelity depending on the user's preferences. For example, a mid-fidelity analysis can be faster for high-throughput screening. Here, the result can be a range in which the contamination level of the sample was found, and can be obtained by scoring the spectra from safe to unsafe in several segments. Whenever the result is in the ML segment or higher (=unsafe), the high-fidelity analysis can be used to determine the exact contamination level (e.g. confirmation). Thereby, portable screening and confirmation in one device could be possible. Still, this requires further improvements of the complete S-PEIRS method.

The work described in this thesis shows the potential of IR spectroscopy for the direct analysis of regulated mycotoxins. Next to regulated mycotoxins IR spectroscopy also shows potential to differentiate modified mycotoxins such as the

acetylated forms of DON, which are also positional isomers, and is discussed in the following sub-section 5.1.2.3.1.

5.1.2.3.1 Differentiating DON and acetylated forms using IR

IR technologies such as ATR-FTIR have been used to differentiate positional isomers of e.g. psychoactive substances [46]. In the field of mycotoxin analysis, positional isomers are found as well. They can occur when the 'parent' mycotoxin is structurally altered by factors such as the plant's defense mechanism with the aim to detoxify fungal toxins [47–51]. While there are comprehensive analytical methods that can differentiate positional mycotoxin isomers, their detection and unambiguous discrimination remain a major challenge for the field. An example of modified mycotoxins, that are also positional isomers, are the acetylated forms of DON; 3-acetyl-DON and 15-acetyl-DON. These acetylated DON molecules are equally relevant for food safety since the acetyl groups can be cleaved off during digestion in humans and animals, leading to the free DON molecule. Moreover, these acetylated DON molecules frequently co-occur with DON in cereal-based products and are a contributing factor to the total dietary DON exposure and intake [47–51].

To demonstrate the potential of ATR-FTIR for the differentiation of DON and its acetylated forms, different concentrations (1, 2, 5, 7 mM) of standard solution in methanol were prepared of DON, 15-Ac-DON and 3-Ac-DON. The liquid samples were deposited on the ATR prism and dried prior to analysis by ATR-FTIR (Figure 5.7). The full mid-IR range (4000 – 400 cm^{-1}) of the preprocessed and averaged spectra were combined to examine the differences in IR signal between DON, 15-Ac-DON and 3-Ac-DON (Figure 5.7a). The spectra of DON and the acetylated forms show clear differences between 1800 – 900 cm^{-1}. Compared to DON, the acetylated forms show an additional vibrational mode at ~1741 cm^{-1} (i – grey box), which originates from the C=O of the acetyl group. In addition, 15-Ac-DON shows a vibration at ~1230 cm^{-1} and 3-Ac-DON at ~1243 cm^{-1} originating from the C-O-C of the acetyl group (ii – grey box). The reason that they occur at slightly different wavenumbers is due to the different position of the acetyl group on the DON molecule. In addition, these acetyl C-O-C vibrations occur in a medium intensity absorbance region of the paper spectrum. Therefore, these vibrational modes show potential for the differentiation of all three molecules on paper. Moreover, the region round 960 cm^{-1} also shows unique absorbances for all three toxin forms (iii – grey box).

To critically evaluate the IR-based differentiation between DON, 15-Ac-DON and 3-Ac-DON a principal component analysis (PCA) was performed using the 2nd derivative spectra (n=15 per concentration, per analyte) in the region between 1800 – 900 cm^{-1} (Figure 5.7 b-c). The loading plot showed that PC2 mainly separates the acetyl DON forms and PC3 mainly separates DON from the acetyl forms. The

concentration dependency of the responses was observed in the score plot, and was indicated by the different symbols for each concentration. These preliminary results, combined with the successful development of S-PEIRS for DON, show the potential of IR spectroscopy for the direct analysis of modified mycotoxins in food at relevant levels.

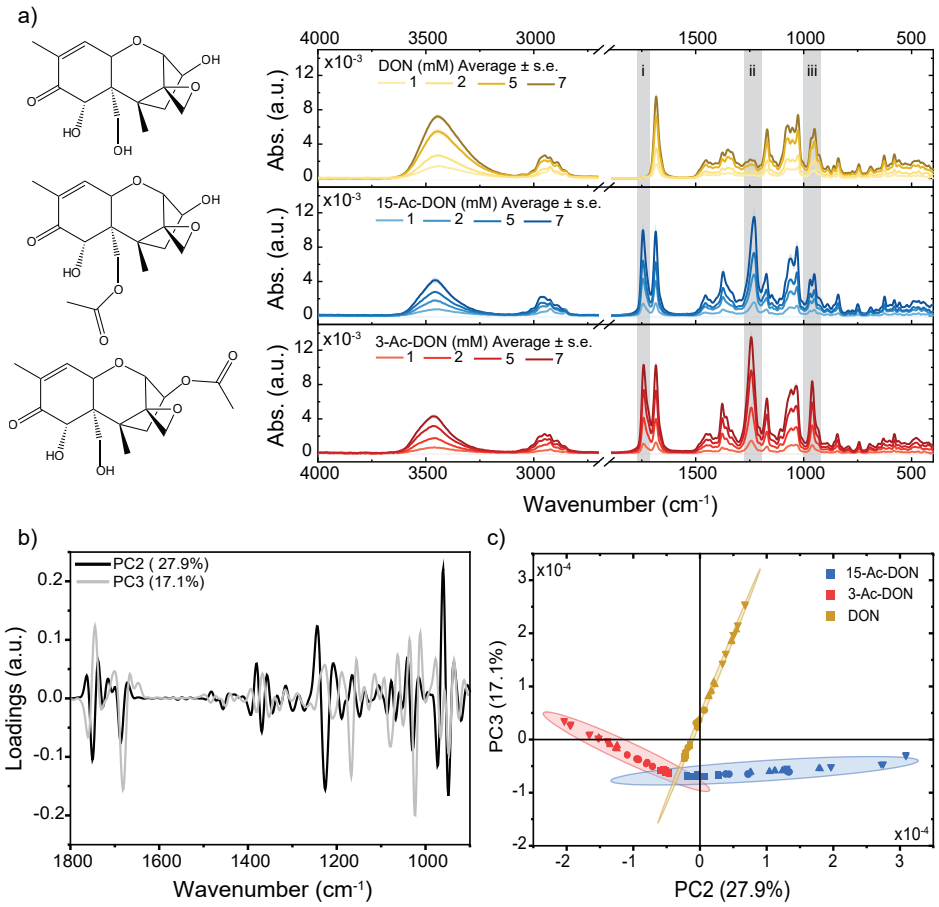


Figure 5.7: *Differentiation of DON and its acetylated forms, 15-Ac-DON and 3-Ac-DON, that are also positional isomers. a) absorbance spectra (4000 – 400 cm^{-1}) of all three molecules. Sample solutions containing 1, 2, 5 and 7 mM of concentration were deposited and analyzed by ATR-FTIR (n=15 per concentration). b) PCA loading plot (1800 – 900 cm^{-1}) and c) PCA score plot of 2nd derivative spectra between 1800-900 cm^{-1}. Symbols in score plot related to concentration level.*

5.2 A roadmap for DIY sample preparation and IR spectroscopy-based portable food analyzers, and beyond

The work described in this thesis has focused on the development of a novel methodological concept for direct mycotoxin detection, as illustrated in Figure 5.1. This concept consists of two main components; 1- integrated sample preparation and 2- direct analysis with mid-IR spectroscopy. As discussed in detail already, 3D-printing, immunoaffinity chemistry and paper-microfluidics were the key technologies that allowed the envisioned concept to become a reality. Moreover, the careful development of the S-PEIRS framework, including the data analysis protocol, have led to a strong foundation for future research. While the current approach could be characterized as a group 4 method (instrumental screening), it shows potential to become a portable targeted analysis method (group 5) in the future [45]. Still, several scientific and technological challenges need to be addressed, which were summarized in Table 5.4 and briefly discussed.

Ultimately, one of the short-term aims is to bring together the 3D-printed sample preparation and the developed S-PEIRS method, as one workflow for hard food commodities. Therefore, first, the 3D-printed sample preparation and S-PEIRS need to be further optimized based on what was discussed in this Chapter. This includes (i) the extension of 3D-printed sample preparation to other (semi-)hard food commodities, (ii) the establishment of active paper-based enrichment and a better understanding of the enrichment/evaporation process through computation and experimentation and, (iii) the demonstration of S-PEIRS for other mycotoxins and commodities. Additionally, the detection of modified mycotoxins such as 3-Ac-DON and 15-Ac-DON with IR spectroscopy should be further explored. Finally, the full workflow should be transferred to a portable ATR-FTIR instrument such as the Mobile-IR II (Bruker) and tested at location by experienced users.

Once the full workflow can be performed at location, a full validation at multiple locations and with a large cohort of non-expert users needs to be set up (mid-term). Next to the chemical aspect of workflow validation, a comprehensive user-assessment is required to understand the technology acceptance and possible implementation at specific points in the food value chain. In the mid-term, further exploration and development of a workflow that enables selective enrichment without the use of affinity columns is recommended, to solve the issues regarding capacity. Other recommendations for the mid- and long-term include the expansion of 3D-printed sample preparation capabilities, to establish a toolkit for sample preparation based on 3D-printed and interconnectable components. In addition, such a toolkit may comprise of robotics-assisted technologies in order to partly or fully automate the sample preparation. In the perspective of upcoming IR sensor technologies it could be interesting to adapt the S-PEIRS method to photonic IR devices [53–56], as well as

explore multi-spectroscopic platforms for complementary assessment of the sample [57,58]. This may lead to the development of methodologies that enable screening and confirmation of mycotoxins in one 3D-printed IR-based device [59–61].

Table 5.4: *A roadmap of the developed methodological concept described in this thesis. This roadmap can be used to guide future research on the two main components; 3D-printed integrated sample preparation and direct analysis with paper-enhanced mid-IR spectroscopy.*

	Short-term (1 year)	**Mid-term (1-5 years)**	**Long-term (5+ years)**
3D-printed integrated sample preparation	- Optimization of current device and customization to different commodity groups - Implement in current S-PEIRS workflow	- Expanding of 3D-printed sample preparation capabilities (e.g. dilution, selective enrichment) [52] - Comprehensive user-assessment at location with dedicated (RE)-ASSURED tool	- Robotics-assisted sample preparation kit with exchangeable 3D-printed and paper-microfluidic components tailored to different analytes and commodities
Direct analysis with selective paper-enhanced mid-IR spectroscopy	- Study physical-chemical enrichment and (active) evaporation for optimization - Demonstration of S-PEIRS for more regulated mycotoxins - further explore IR detection of modified mycotoxins -Transfer method to portable ATR-FTIR (e.g. Bruker Mobile-IR II) and validate S-PEIRS at location	- Move to selective enrichment without affinity columns and further enhance S-PEIRS detection capabilities - Achieve full on-site workflow with non-expert users - Exploration of, and transfer to portable photonic mid-IR device [53–56]	- Multi-spectroscopic detection [57,58] with complementary sensors for high level of certainty - In-device screening and confirmation of food contaminants on-site - Real-time risk management through portable IR mycotoxin platform with connected application - 3D-printing of complete detection device using advanced and multi-material printer approaches [59–61]

References

1. Tittlemier, S. A. et al. Design of a quality control scheme to assess sample preparation performance for the determination of deoxynivalenol in wheat. World Mycotoxin J. 18, 145–153 (2025).
2. Alshannaq, A. & Yu, J.-H. Occurrence, Toxicity, and Analysis of Major Mycotoxins in Food. Int. J. Environ. Res. Public. Health 14, 632 (2017).
3. Whitaker, T. B., Dickens, J. W. & Monroe, R. J. A water slurry method of extracting aflatoxin from peanuts. J. Am. Oil Chem. Soc. 57, 269–272 (1980).
4. Dhanshetty, M., Elliott, C. T. & Banerjee, K. Decontamination of aflatoxin B1 in peanuts using various cooking methods. J. Food Sci. Technol. 58, 2547–2554 (2021).
5. Wojnowski, W., Tobiszewski, M., Pena-Pereira, F. & Psillakis, E. AGREEprep – Analytical greenness metric for sample preparation. TrAC Trends Anal. Chem. 149, 116553 (2022).
6. Nowak, P. M. & Arduini, F. RGBfast – A user-friendly version of the Red-Green-Blue model for assessing greenness and whiteness of analytical methods. Green Anal. Chem. 10, 100120 (2024).
7. Sajid, M. & Płotka-Wasylka, J. Green analytical chemistry metrics: A review. Talanta 238, 123046 (2022).
8. Pena-Pereira, F., Wojnowski, W. & Tobiszewski, M. AGREE—Analytical GREEnness Metric Approach and Software. Anal. Chem. 92, 10076–10082 (2020).
9. Hammad, S. F., Hamid, M. A. A., Adly, L. & Elagamy, S. H. Comprehensive review of greenness, whiteness, and blueness assessments of analytical methods. Green Anal. Chem. 12, 100209 (2025).
10. Mestre-Manrique, F., Payà-Pou, R., Beneito-Cambra, M., Simó-Alfonso, E. F. & Carrasco-Correa,E.J. Is 3D printing a good alternative to prepare novel devices for Green Analytical sample preparation? Adv. Sample Prep. 6, 100062 (2023).
11. Ross, G. M. S., Filippini, D., Nielen, M. W. F. & Salentijn, G. IJ. Interconnectable solid-liquid protein extraction unit and chip-based dilution for multiplexed consumer immunodiagnostics. Anal. Chim. Acta 1140, 190–198 (2020).
12. Agnes Champeil, Jean-Francois Fourbet, and & Doré, T. Effects of Grain Sampling Procedures on Fusarium Mycotoxin Assays in Wheat Grains. ACS Publications https://pubs.acs.org/doi/pdf/10.1021/jf049374s (2004) doi:10.1021/jf049374s.
13. Whitaker, T. B. Detecting mycotoxins in agricultural commodities. Mol. Biotechnol. 23, 61–71 (2003).
14. Whitaker, T. B. Sampling Foods for Mycotoxins. Food Addit. Contam. 23, 50–61 (2006).
15. The European Commission. Commission Implementing Regulation (EU) 2023/2782 of 14 December 2023 laying down the methods of sampling and analysis for the control of the levels of mycotoxins in food and repealing Regulation (EC) No 401/2006. (2023).
16. Jafari, S. et al. ASSURED Point-of-Need Food Safety Screening: A Critical Assessment of Portable Food Analyzers. Foods 10, 1399 (2021).
17. Mabey, D., Peeling, R. W., Ustianowski, A. & Perkins, M. D. Diagnostics for the developing world. Nat. Rev. Microbiol. 2, 231–240 (2004).
18. Smith, S., Korvink, J. G., Mager, D. & Land, K. The potential of paper-based diagnostics to meet the ASSURED criteria. RSC Adv. 8, 34012–34034 (2018).
19. Land, K. J., Boeras, D. I., Chen, X.-S., Ramsay, A. R. & Peeling, R. W. REASSURED diagnostics to inform disease control strategies, strengthen health systems and improve patient outcomes. Nat. Microbiol. 4, 46–54 (2019).
20. Freitag, S. et al. Attenuated total reflection mid-infrared spectroscopy to screen Austrian and French wheat from multiple years for deoxynivalenol. Spectrochim. Acta. A. Mol. Biomol. Spectrosc. 340, 126340 (2025).
21. Fomina, P. et al. Prediction of Deoxynivalenol Contamination in Wheat via Infrared Attenuated Total Reflection Spectroscopy and Multivariate Data Analysis. ACS Food Sci. Technol. 4, 895–904 (2024).

22. Geballa-Koukoula, A., Gerssen, A. & Nielen, M. W. F. Direct analysis of lateral flow immunoassays for deoxynivalenol using electrospray ionization mass spectrometry. Anal. Bioanal. Chem. 412, 7547–7558 (2020).
23. Şenyuva, H. Z. & Gilbert, J. Immunoaffinity column clean-up techniques in food analysis: A review. J. Chromatogr. B 878, 115–132 (2010).
24. MacDonald, S. J., Chan, D., Brereton, P., Damant, A. & Wood, R. Determination of deoxynivalenol in cereals and cereal products by immunoaffinity column cleanup with liquid chromatography: interlaboratory study. J. AOAC Int. 88, 1197–1204 (2005).
25. Sun, Q. et al. Molecularly imprinted polymers for mycotoxin biosensing: Rational design, advanced applications, and future horizons. Biosens. Bioelectron. 292, 118111 (2026).
26. Tang, Z. et al. Solid-phase extraction techniques based on nanomaterials for mycotoxin analysis: An overview for food and agricultural products. J. Sep. Sci. 45, 2273–2300 (2022).
27. Romero-González, R., Martínez Vidal, J. L., Aguilera-Luiz, M. M. & Garrido Frenich, A. Application of Conventional Solid-Phase Extraction for Multimycotoxin Analysis in Beers by Ultrahigh-Performance Liquid Chromatography—Tandem Mass Spectrometry. J. Agric. Food Chem. 57, 9385–9392 (2009).
28. Vivaldi, F., Torrini, F., Spiaggia, F., Di Francesco, F. & Minunni, M. Exploring affinity receptors in bioanalysis: from natural binders to biomimetics. Sens. Actuators Rep. 10, 100359 (2025).
29. Garg, S. et al. Future Perspectives on the Automation and Biocompatibility of Molecularly Imprinted Polymers for Healthcare Applications. Macromolecules 58, 1157–1168 (2025).
30. Gray, A. C. et al. Animal-derived-antibody generation faces strict reform in accordance with European Union policy on animal use. Nat. Methods 17, 755–756 (2020).
31. Geballa-Koukoula, A. et al. Best practices and current implementation of emerging smartphone -based (bio)sensors - Part 2: Development, validation, and social impact. TrAC Trends Anal. Chem. 161, 116986 (2023).
32. Malachová, A. et al. Advanced LC–MS-based methods to study the co-occurrence and metabolization of multiple mycotoxins in cereals and cereal-based food. Anal. Bioanal. Chem. 410, 801–825 (2018).
33. Corrêa, A. N. R. & Ferreira, C. D. Mycotoxins in Grains and Cereals Intended for Human Consumption: Brazilian Legislation, Occurrence Above Maximum Levels and Co-Occurrence. Food Rev. Int. 39, 5920–5933 (2023).
34. Palumbo, R. et al. Occurrence and Co-Occurrence of Mycotoxins in Cereal-Based Feed and Food. Microorganisms 8, E74 (2020).
35. Guo, Z. et al. Rapid enrichment detection of patulin and alternariol in apple using surface enhanced Raman spectroscopy with coffee-ring effect. LWT 152, 112333 (2021).
36. Aksoy, C., van Kesteren, I., Zuilhof, H. & Salentijn, G. I. Broad Tuning of Paper Microfluidic Properties by Covalent Surface Modification for Precise Flow Control and Sensing. ACS Appl. Bio Mater. 8, 3748–3761 (2025).
37. Bhattacharya S., Kumar S., Agarwal A.K., Paper Microfluidics: Theory and Applications. (Springer, Singapore, 2019). doi:10.1007/978-981-15-0489-1.
38. Salentijn, G. Ij. & Hoekstra, M. H. Sensor cartridge for chemical assays of a liquid sample containing analyte molecules, WO2018226097 A1. (2018).
39. Liu, Y. et al. A Bioinspired, Reusable, Paper-Based System for High-Performance Large-Scale Evaporation. Adv. Mater. 27, 2768–2774 (2015).
40. Patari, S. & Sinha Mahapatra, P. Imbibition of Liquids through a Paper Substrate in a Controlled Environment. Langmuir 38, 4736–4746 (2022).
41. Bozorgmehr, B. & Murray, B. T. Numerical Simulation of Evaporation of Ethanol–Water Mixture Droplets on Isothermal and Heated Substrates. ACS Omega 6, 12577–12590 (2021).
42. Zhang, W., Yang, J. & Knopf, G. K. Numerical Simulation of Solvent Evaporation in a Reactive Silver Ink Droplet Deposited on a Heated Substrate. ACS Omega 8, 38991–39003 (2023).

43. Lemmink, I. B. et al. Modular Point-of-Need Tropane Alkaloid Detection at Regulatory Levels: Combining Solid–Liquid Extraction from Buckwheat with a Paper-Immobilized Liquid-Phase Microextraction and Immuno-Detection in Interconnectable 3D-Printed Devices. Anal. Chem. 96, 16462–16468 (2024).
44. Lemmink, I. B., Bosma, S. J., Bovee, T. F. H., Zuilhof, H. & Salentijn, G. I. Paper-immobilized liquid-phase microextraction for direct paper spray mass spectrometry and immuno-detection of atropine in baby food, buckwheat cereals, and edible oils at regulatory levels. Anal. Chim. Acta 1349, 343823 (2025).
45. Lemmink, I. B. et al. Chapter Two - Recent advances and challenges in the analysis of natural toxins. in Advances in Food and Nutrition Research (ed. Toldrá, F.) vol. 110 67–144 (Academic Press, 2024).
46. Verhoeven, M., Bonetti, J., Kranenburg, R. & van Asten, A. Chemical identification and differentiation of positional isomers of novel psychoactive substances – A comprehensive review. TrAC Trends Anal. Chem. 166, 117157 (2023).
47. Vidal, A. et al. Humans significantly metabolize and excrete the mycotoxin deoxynivalenol and its modified form deoxynivalenol-3-glucoside within 24 hours. Sci. Rep. 8, 5255 (2018).
48. Nešić, K., Habschied, K. & Mastanjević, K. Modified Mycotoxins and Multitoxin Contamination of Food and Feed as Major Analytical Challenges. Toxins 15, 511 (2023).
49. EFSA Panel on Contaminants in the Food Chain. Risks to human and animal health related to the presence of deoxynivalenol and its acetylated and modified forms in food and feed. EFSA J. https://doi.org/10.2903/j.efsa.2017.4718 (2017)
50. Malachová, A. et al. Critical evaluation of indirect methods for the determination of deoxynivalenol and its conjugated forms in cereals. Anal. Bioanal. Chem. 407, 6009–6020 (2015).
51. De Boevre, M., Ediage, E. N., Van Poucke, C. & De Saeger, S. Untargeted Analysis of Modified Mycotoxins using High-resolution Mass Spectrometry. in Masked mycotoxins in food 50–72 (2015).
52. Zargaryan, A., Farhoudi, N., Haworth, G., Ashby, J. F. & Au, S. H. Hybrid 3D printed-paper microfluidics. Sci. Rep. 10, 18379 (2020).
53. Ghoname, A. O., Sabry, Y. M., Anwar, M. & Khalil, D. Attenuated total reflection (ATR) MEMS FTIR spectrometer. in MOEMS and Miniaturized Systems XIX vol. 11293 170–175 (SPIE, 2020).
54. Femenias, A. et al. Portable tunable interband cascade laser spectrometer using thin-film waveguides for food contaminant analysis. AIP Adv. 14, 125209 (2024).
55. Kazakov, D. et al. Driven bright solitons on a mid-infrared laser chip. Nature 641, 83–89 (2025).
56. Kong, B., Brandsrud, M. A., Karki, P., Mizaikoff, B. & Kohler, A. Variable refractive index waveguides for mid-infrared sensing. Optik 347, 172662 (2026).
57. Klingler, S. et al. Simultaneous Infrared Spectroscopy, Raman Spectroscopy, and Luminescence Sensing: A Multispectroscopic Analytical Platform. ACS Meas. Sci. Au 2, 157–166 (2021).
58. Hashimoto, K., Badarla, V. R., Kawai, A. & Ideguchi, T. Complementary vibrational spectroscopy. Nat. Commun. 10, 4411 (2019).
59. Carrasco-Correa, E. J., Simó-Alfonso, E. F., Herrero-Martínez, J. M. & Miró, M. The emerging role of 3D printing in the fabrication of detection systems. TrAC Trends Anal. Chem. 136, 116177 (2021).
60. Wang, H. et al. Two-Photon Polymerization Lithography for Optics and Photonics: Fundamentals, Materials, Technologies, and Applications. Adv. Funct. Mater. 33, 2214211 (2023).
61. Baumgartner, B., Freitag, S. & Lendl, B. 3D Printing for Low-Cost and Versatile Attenuated Total Reflection Infrared Spectroscopy. Anal. Chem. 92, 4736–4741 (2020).


A

English Summary

Protecting the food supply and minimizing harmful mycotoxin contamination are closely linked. Recent evidence indicates that mycotoxin occurrence and exposure are rising worldwide, with significant variation across different regions and populations. Ensuring access to reliable, fit-for-purpose detection methods is therefore essential. Portable food analyzers enable timely decision-making at critical points in the food supply chain and allow for more frequent monitoring and risk management. Consequently, the demand for portable mycotoxin detection tools is growing across the food supply chain. Previous research has shown the suitability of mid-infrared (MIR) spectroscopy for portable mycotoxin detection, but limitations remain due to the lack of measurement certainty and detection capability. The work described in this thesis addresses this limitation by introducing methodological innovations that integrate sample preparation and enhance MIR spectroscopy for direct detection at regulatory levels. These innovations focused on the development of a novel 3D-printed sample handling device and the establishment of 'selective paper-enhanced infrared spectroscopy' (S-PEIRS). In **Chapter 1**, the motivation and scientific background for the work described in this thesis were introduced, covering the topics of mycotoxin analysis, integrated sample preparation using 3D-printing, paper-based microfluidics and IR spectroscopy.

In **Chapter 2**, the suitability of a newly developed low-cost 3D-printed sample handling device that fits in an on-site mycotoxin screening workflow was evaluated. Contaminated wheat kernels were milled using the device with universal battery-drill extension and were internally sieved, enabling milling and particle size selection within five minutes. Ten first-time users operated the device with minimal instructions. The modular character of the device allowed for the immediate, in-device extraction of deoxynivalenol (DON). After extract transfer, DON was detected using a lateral flow test, completing the workflow in 15 minutes. The efficiency of the 3D-printed device was characterized against a typical laboratory mill, and the complete screening workflow showed strong correlation with reference analysis. These developments have demonstrated the potential of 3D-printing for portable and integrated sample preparation.

In **Chapter 3**, a novel framework to overcome the limitations of MIR spectroscopy for the detection at relevant levels was introduced. In the European Union, the maximum level (ML) set for DON in unprocessed wheat is 1000 µg/kg. At these low concentrations, the DON molecules are undetectable with standard MIR spectroscopy, especially when present in a complex matrix like wheat. The final framework called S-PEIRS relies on the following steps; (i) wheat extract purification using simple immunoaffinity columns (IACs), (ii) enrichment of the DON molecules from the purified extract in a paper tip, (iii) paper-based MIR analysis of the enriched solutes in the paper tip and (iv) in-depth data analysis to detect the concentration-

dependent DON molecular feature at a specific wavenumber and down to 1000 µg/kg in various types of wheat. S-PEIRS illustrates the potential of paper-based IR spectroscopy for portable food safety analysis, as innovative detection method with molecular certainty.

In **Chapter 4**, the S-PEIRS framework established in **Chapter 3** was advanced to achieve the quantitative detection of another, more strictly regulated mycotoxin; ochratoxin A (OTA). OTA occurs in many food products such as cereals, wines, coffee and spices and the ML set by the EU for wines is only 2 µg/kg, which is 500 times lower than the ML of DON in wheat. OTA molecules exhibit different charge states at varying pH. This characteristic was used to transfer OTA from a large wine volume into a small extract, significantly increasing its concentration. Then, S-PEIRS was adjusted to detect the concentration-dependent OTA feature at a specific wavenumber. Due to further purification of the extract and enrichment of the OTA molecules in the paper tip following the S-PEIRS framework, the quantitative detection of OTA down to 2 µg/kg in wine was achieved. This is the first time that such low concentrations could be measured quantitatively using MIR spectroscopy and broadens the further application of MIR for strictly regulated compounds, also beyond the field of food safety.

In **Chapter 5**, a general discussion on the key thesis topics of integrated 3D-printed sample preparation and S-PEIRS was provided, including major challenges and achievements, and an outlook for future research with prelimenary results.


A

Nederlandse Samenvatting

Het beschermen van de voedselvoorziening en het minimaliseren van schadelijke mycotoxine besmetting zijn nauw met elkaar verbonden. Recente gegevens wijzen erop dat de sociaaleconomische impact van deze stoffen wereldwijd toeneemt, met aanzienlijke verschillen tussen regio's en bevolkingsgroepen. Toegang tot betrouwbare, doelgerichte detectiemethoden is daarom essentieel. Draagbare detectiesystemen maken tijdige besluitvorming mogelijk op kritieke punten in de voedselvoorziening en verbeteren het monitoren en risicobeheer. Hierdoor groeit de vraag naar draagbare detectiesystemen voor mycotoxinen. Eerder onderzoek heeft aangetoond dat mid-infrarood (MIR) spectroscopie geschikt is voor draagbare mycotoxine detectie, maar er blijven beperkingen bestaan door het gebrek aan meetzekerheid en detectie capaciteit. Het onderzoek in deze thesis beschrijft hoe deze beperking kan worden opgelost door innovatieve methodes te introduceren die monstervoorbereiding integreren en MIR-spectroscopie verbeteren. Daardoor wordt directe detectie van mycotoxinen in voeding op gereguleerde niveaus mogelijk. Deze innovaties richten zich op de ontwikkeling van een nieuw, 3D-geprint apparaat voor monstervoorbewerking en op de ontwikkeling van 'selective paper-enhanced infrared spectroscopy' (S-PEIRS). In **Hoofdstuk 1** werden de motivatie en de wetenschappelijke achtergrond van het werk in dit proefschrift geïntroduceerd, waarbij de onderwerpen mycotoxineanalyse, geïntegreerde monstervoorbereiding met behulp van 3D-printen, papiergebaseerde microfluidica en IR-spectroscopie aan bod kwamen.

In **Hoofdstuk 2** beschreef ik de ontwikkeling van een betaalbaar 3D-geprint apparaat dat past in een bestaande methode voor het meten van mycotoxinen buiten het laboratorium. Besmette tarwekorrels werden gemalen met het apparaat, daartoe uitgerust met een universele accuboormachine, en de deeltjes werden intern gezeefd. Het vermalen en verkrijgen van gezeefde tarwedeeltjes duurde slechts vijf minuten. Daarnaast konden tien nieuwe gebruikers het apparaat bedienen met minimale instructies. Door het modulaire ontwerp kon extractie van deoxynivalenol (DON) direct worden uitgevoerd in het apparaat. Na het opbrengen van het extract op een laterale flowtest kon DON worden gedetecteerd, en de volledige workflow kon in 15 minuten worden afgerond. De efficiëntie van het 3D-geprinte apparaat werd vergeleken met een molen uit het laboratorium, en de nieuwe workflow toonde een sterk verband met de laboratoriumanalyse. Deze ontwikkelingen laten duidelijk het potentieel van 3D-printen zien voor geïntegreerde monstervoorbereiding buiten het laboratorium.

In **Hoofdstuk 3** werd een nieuw methodologisch kader geïntroduceerd om de beperkingen van MIR-spectroscopie voor detectie op gereguleerde niveaus te overwinnen. In de Europese Unie is de toegestane limiet voor DON in onbewerkte tarwe vastgesteld op maximaal 1000 µg/kg. Bij deze lage concentraties zijn DON-

moleculen niet detecteerbaar met standaard MIR-spectroscopie instrumenten, en zeker niet in complexe matrices zoals tarwe. De nieuwe methode, S-PEIRS, omvat de volgende stappen: (i) zuivering van tarwe-extracten met eenvoudige immuno-affiniteitschemie, (ii) ophopen van DON-moleculen in een papieren strip, (iii) MIR-analyse van de opgehoopte stoffen op de papieren strip en, (iv) diepgaande data-analyse om het moleculaire kenmerk van DON bij een specifieke golflengte te detecteren, zo laag als 1000 μg/kg in verschillende tarwesoorten. Daarmee, toont S-PEIRS het potentieel van IR-spectroscopie met papier als innovatieve methode voor voedselveiligheidsanalyse met moleculaire meetzekerheid.

In **Hoofdstuk 4** werd S-PEIRS uitgebreid om een andere, nog veel strenger gereguleerde mycotoxine kwantitatief te detecteren; namelijk ochratoxine A (OTA). OTA komt vaak voor in voedingsmiddelen zoals granen, wijn, koffie en specerijen. De toegestane limiet die door de EU is vastgesteld voor wijn is slechts 2 μg/kg, wat 500 keer lager is dan de limiet voor DON in tarwe. OTA-moleculen vertonen verschillende ladingen bij variërende pH. Deze eigenschap werd gebruikt om OTA over te brengen van een groot wijnvolume naar een klein extract, waardoor de concentratie aanzienlijk werd verhoogd. Vervolgens werd S-PEIRS aangepast om het moleculaire kenmerk van OTA bij een specifieke golflengte te detecteren. Door verdere zuivering van het extract en verrijking van OTA-moleculen in de papieren strip werd kwantitatieve detectie van OTA tot 2 μg/kg in wijn mogelijk. Dit is de eerste keer dat zulke lage concentraties kwantitatief konden worden gemeten met MIR spectroscopie en dit verbreedt de verdere toepassing van MIR voor streng gereguleerde stoffen, ook buiten het gebied van voedselveiligheid.

In **Hoofdstuk 5** beschreef ik in een algemene beschouwing de belangrijkste onderwerpen van het proefschrift, namelijk geïntegreerde 3D-geprinte monsterpreparatie en S-PEIRS, inclusief de belangrijkste uitdagingen en successen, en een vooruitblik op toekomstig onderzoek met voorlopige resultaten.


A

Curriculum Vitae

About the author



Anouk Julia Bosman was born on June 1st, 1997, in Doetinchem the Netherlands. She obtained her Bachelor's degree in Chemistry from HAN University of Applied Sciences while also completing the national Analytical Sciences Talent Program. For her BSc thesis on the development of a portable fluorescence-based bioassay platform targeted at trace material detection at crime scenes, she received an award from the Royal Netherlands Chemical Society.

Anouk earned her Master's degree in Applied Nanotechnology from Saxion University of Applied Sciences, where she specialized in lab-on-a-chip systems, portable detection platforms, and ethics of technology. For her MSc thesis, she worked on the development of a chip-based point-of-care platform at a University of Twente spin-off, where she was also employed part-time. During her time at the company, she introduced an ethics of technology framework to strengthen the societal integration of nanotechnological innovations.

In 2021, Anouk began her PhD research at Wageningen University & Research as part of the European Union Horizon 2020 project PHOTONFOOD. Collaborating with three other universities and nine industry partners, the project developed novel photonic infrared-based platforms for detecting food contaminants and implemented these methods across partners. Most of Anouk's work was conducted within the Organic Chemistry chair group and at Wageningen Food Safety Research. Her research primarily focused on developing a sample-to-result workflow for direct, label-free mycotoxin detection in foods at regulatory levels using 3D printing, immunochemistry, paper-based microfluidics and mid-infrared spectroscopy.

Since April 2026, she is a postdoctoral researcher at Radboud University (Analytical Chemistry & Chemometrics group) working in the project CHOWSAI (Control of Household Waste Sorting by Artificial Intelligence). This interdisciplinary project aims to improve plastic waste sorting by integrating advanced sensor technologies (including spectral imaging) with artificial intelligence for real-time material characterization, quality assessment, and digital twin development.

Contact: ajbosman@outlook.com

List of publications

This thesis

A.J. Bosman, S. Freitag, G.M.S. Ross, M. Sulyok, R. Krska, F.S. Ruggeri, G.IJ. Salentijn. Interconnectable 3D-printed sample processing modules for portable mycotoxin screening of intact wheat. *Analytica Chimica Acta*, 2023, 1285, 342000

A.J. Bosman, G.M.S. Ross, S. Freitag, M. Sulyok, R. Krska, G.IJ. Salentijn, F.S. Ruggeri. Selective paper-enhanced infrared spectroscopy for molecular detection of deoxynivalenol in wheat. *Food Chemistry.* Volume 516. 2026. 149360.

A.J. Bosman, I.B. Lemmink, F.S. Ruggeri, G.IJ. Salentijn. Detection of Ochratoxin A in wine at the legal limit via solvent-based enrichment and paper-enhanced infrared spectroscopy. *Journal of Hazardous Materials.* Volume 511. 2026. 142248.

Others

G.M.S. Ross, Y. Zhao, A.J. Bosman, A. Geballa-Koukoula, H. Zhou, C.T. Elliot, M.W.F. Nielen, K. Rafferty, G.IJ. Salentijn. Best practices and current implementation of emerging smartphone-based (bio)sensors – Part 1: Data handling and ethics. *Trends in Analytical Chemistry*, 2022, 158, 116863

A. Geballa-Koukoula, G.M.S. Ross, A.J. Bosman, Y. Zhao, H. Zhou, M.W.F. Nielen, K. Rafferty, .T. Elliott, G.IJ. Salentijn. Best practices and current implementation of emerging smartphone-based (bio)sensors – Part 2: Development, validation and social impact. *Trends in Analytical Chemistry*, 2023, 161, 116986

E. Csenki, V. Mikulas, S. Freitag, P. Fomina, M. Hlavatsch, A. Femenias, A.J. Bosman, F.S. Ruggeri, M. Smirnova, G.IJ. Salentijn, B. Mizaikoff, R. Krska, J. Scholderer, A. Kohler, G. Kasza. Stakeholder assessment for mycotoxin analysis: exploring the demand along the European food supply chain. *World Mycotoxin Journal*, 2023, 16(4), 287-299

A. Femenias, M. Erdem, P. Fomina, J. Scheuermann, U. Blazhko, S. Freitag, A.J. Bosman, R. Weih, J. Koeth, A. Kohler, R. Krska, G.IJ. Salentijn, F.S. Ruggeri, B. Mizaikoff. Portable tunable interband cascade laser spectrometer using thin-film waveguides for food contaminant analysis. *AIP Advances*. 2024. 14. 125209

Overview of completed training activities

Discipline specific activities	Organizer	Place	Year
Advanced food analyisis[2]	VLAG	Wageningen	2022
Advanced organic chemistry	VLAG	Wageningen	2021-2024
Bio-spectroscopy summerschool	NMBU	Ås (NO)	2022
FASTest[2]	TI-COAST	Amersfoort	2021
EuroFAST	TI-COAST	Nijmegen	2022
RAFA	UCT Prague/WUR	Online	2021
RAFA[3]	UCT Prague/WUR	Prague (CZ)	2022
Young researcher workshop PHOTONFOOD	BOKU	Tulln (AT)	2022
Secondment	BOKU	Tulln (AT)	2022
Young researcher workshop PHOTONFOOD[1]	WUR	Wageningen	2023
ILSI - food contaminants[3]	WUR	Wageningen	2023
Young researcher workshop PHOTONFOOD[1]	WUR	Wageningen	2024
PHOTONFOOD symposium[3]	BOKU	Tulln (AT)	2024
FAST[3]	TI-COAST	Maastricht	2025
Talent Network Symposium[3]	TI-COAST	Utrecht	2025

1 = I organized event; 2 = Poster; 3 = Oral

General courses	Organizer	Place	Year
PhD competence assessment	WGS	Wageningen	2021
Project & time management	WGS	Wageningen	2021
Introduction to LaTeX	WGS	Wageningen	2021
PhD week	VLAG	Baarlo	2022
Chemometrics (multivariate statistics)	VLAG	Wageningen	2022
Philosophy & Ethics of food science and technology	VLAG	Wageningen	2022

Assisting in teaching and supervision	Organizer	Place	Year
Analytical methods in organic chemistry	ORC	Wageningen	2022-2024
Bio-organic chemistry for life sciences	ORC	Wageningen	2022-2024
Supervision of BSc thesis student	ORC	Wageningen	2022-2023

Other activities	Organizer	Place	Year
Colloquia	ORC	Wageningen	2021-2025
PhD research proposal	ORC	Wageningen	2021
PhD study tour (chair of trip)	ORC	Ulm (DE), Konstanz (DE), Zurich (CH), Gent (BE), Leuven (BE)	2023
TEKNOWLOGY	NWO	Utrecht	2023
EU project meetings	PHOTONFOOD	Europe	2021-2025
WFSR team meetings	Team biosensors/ bioassays	Wageningen	2021-2025


A

Acknowledgements

I am hesitant to write this last part of the thesis and that is not because I do not know who to thank. I am hesitant because writing these final words means that my time as a PhD has come to an end, which feels fulfilling and melancholic at the same time. I dedicate these last words to all the people that have supported me through these years; your energy, advice, laughs and tears have made this a ride that I will never forget. I (and you) can now proudly close this book and cheer to this achievement that I could not have accomplished without you.

To my supervision team

Han, while you were not my supervisor, you did play an important role in this story as you were the one to introduce me to this project via a message on LinkedIn. Thank you for reconnecting and welcoming me to the chair group with a memorable T-shirt.

Michel, I had the pleasure of being supervised by you (and Maurice) during an internship when I was a bachelor student. Knowing that you would become my promotor reassured me I was in good hands. Even though you enjoyed your retirement during most of my PhD time, you were always quick to respond to my emails and provided me with useful advice. I treasure our 'meeting' in Nijmegen where we walked, talked and enjoyed some beers on a boat. I felt heard by you, which was exactly what I needed at that moment. Thank you for that. As your last PhD to defend, you are now a 'free elf' (as Dobby would say). Enjoy your well-deserved retirement!

Hans-Gerd, you were not only my 'back-up' promotor, you were also my 'bonus' promotor. I had the luxury of having your bonus advice and feedback during the writing of this thesis, which you communicated to me with enthusiasm and a kind attitude. Thank you for spotting spelling mistakes and grammatical errors; you really have a great eye for that. Like Michel, you also provided me with feedback very quickly, which allowed me to keep the pace when writing the chapters of this thesis. I enjoyed our meetings at Unilever and I hope we can stay in touch.

Simo, both of us were new employees at WUR when you started to supervise me and it took some time to find each other's 'wavelength', but luckily we did and this resulted in a successful PhD journey. Without your expertise in infrared spectroscopy and data analysis we could not have achieved the level of success with S-PEIRS that we now did. You have taught me, amongst others, how to properly analyze IR spectra, how to spot errors in the spectra, how to decide whether we were looking at noise or actual mycotoxin signals, how to properly represent IR data and how to make publication-worthy figures. Thank you for being a caring supervisor, especially in the times that were difficult for me personally. One of your philosophies that I will keep remembering is that "Error is your friend". In fact, it is of high importance in

my next career step. Let's stay in touch!

Gert, you have played a central role in the supervision and guided me with due diligence through this PhD journey. I look up to you as a mentor and your words of wisdom always stuck with me. I most enjoyed the moments, often during travels or consortium meetings, where we talked about anything (science, life, society etc.) over a nice beer or two. Thank you for inviting us (your PhD babies) to your home every Christmas to meet your actual babies (and lovely wife), and enjoy homecooked food together. Your honest advice and authentic personality were things I valued a lot in you as my supervisor, thank you for that. Surely, we will stay in touch through, e.g. the COAST network.

To my colleagues

My paranymphs Clementina and Stijn, I am very grateful and proud that I am backed by the two of you on D-day. Throughout my PhD you have been a constant support and I valued that a lot. I had countless of funny and memorable moments with you. Thank you for the coffees, the chitchats and the understanding.

Clementina, you have been my sister in science throughout the PhD and the office and WUR were not the same when you left for an awesome job in Brussels. Luckily, fate has brought you back to the Netherlands and I foresee many memorable activities as doctors together. Let's make wine our first study object.

Stijn, you and me have been sharing the same struggles towards the end of our PhD. Finishing publications, the thesis and finding a job. Not easy. It was very comforting to talk with you about all these things. Both of us have found ourselves a new challenge, Python... While that is again not easy, I think we will do nice things with it. Thanks hosselaar, op naar jou defense!

Júlia, while you are not my paranymph today, you have basically been paranymphing throughout my PhD time. You have been a constant support, a great office decorator, a creative genius, and a funny and lovely friend. Thank you for everything, you rock!

Gina, thank you for having been my bonus mentor throughout the first steps in my PhD and staying in touch with me over the years. Your support gave me the confidence that I could manage this PhD. Also, I like your vibe, it resonates with me. Thank you for coming all this way to celebrate!

The PhotonFood consortium, it was a pleasure to get to know all of you and do science together. I always looked forward to the next consortium meeting due to all the nice people, thanks to NMBU and in particular **Prof Kohler and Margo** for leading this great consortium. In addition, thanks to **Prof Krska**, for the opportunity to work in his lab, which I very much enjoyed. Finally, thanks to **Stephan, Miriam, Polina and Toni** with whom I shared many fun moments during meetings, trainings,

dinners and other activities.

Stephan, Dr F, next to being a lovely colleague who played a significant role in the research described in this thesis, I also much appreciate the friendship we have built over the years. This friendship solidified when I came to work at BOKU with you on our 3D-printed grinder prototype and we spent many hours in- and outside the lab together. You are funny, you give good advice and you appreciate beer as much as I do. I will never forget our first RAFA, our skiing trip in Norway, our Barcelona adventures, your time in NL and your homemade shakshuka. It is a pity that you cannot be at the defense because you are doing super cool fire fighter stuff but I am certain we stay in touch, in- and outside of science.

The ORC chair group, I met some of you already during my time as an intern back in 2017 and with all the new people that joined, you have been great colleagues during my PhD time. I would like to specifically thank the teaching staff that I worked most with (**Hans, Frank, Hendra, Tjerk**). Your enthusiasm for teaching and the coordination of the courses I assisted in made me enjoy the teaching a lot and it became one of my favorite non-research related activities. In addition, thanks to **Hans, Frank, Sidhu and Barend** for maintaining the equipment in the labs. **Maurice, Louis, Dieuwertje,** thank you for checking in with me occasionally, these small acts of kindness made me feel seen. Also a BIG thank you to the secretary of ORC, **Marjolein, Eveline, Elly and Aleida**, you were/are the beating heart of the chair group and I much appreciate all the support with administrative difficulties (and many other things). Next to that, you were great company during lunchtime and also checked in with me from time to time; thank you for the sincere conversations and attention. These 4.5 years of working with **all of you** have been my pleasure and I look back on so many memorable moments that taught me a lot in life.

Office 7035; Clementina, Stijn, Júlia, Thijmen, Xuecong, Julian, Elisa. I could not have picked a better office to work in because all of you made it a pleasure to come to work. Especially when times were difficult you made the office a safe space to share thoughts and feelings, which were always received with a kind attitude. Thank you for all the funny moments, for the shared coffee, walks, talks, beers and office decorations.

Paper- and Spectro-team; Gina, Si, Canan, Peiheng, Ids, Klaudia, Alissa, Clementina, Xuecong, Bas, Visakh, Giacomo, Masbah, Mengsha and Lutger. Thank you for all the shared moments over the years, the shared struggles and the shared successes. Having the same PhD supervisor is a special kind of connection as colleagues and I have felt much support from all of you. Some of you are a Dr already and some of you are well on their way, I wish you all the best in your future careers.

Ids, a special thanks to you for our great collaboration together. Long lab days with

you were always enjoyable. Also, I am still amazed by the size of your lunch box.

Susannah, no shared office or supervisor; nevertheless I got to know you as a great person and colleague who works hard and fights for what is right. Thank you for the talks, coffees, beers and all the things you have organized for the PhDs. You might not know what you will do after finishing your PhD yet, but I am sure good things will come to you. Trust yourself, you are doing great.

WFSR, A big thank you goes out to all my colleagues from Wageningen Food Safety Research, and especially to the ones from the Biosensor team. **Toine, Nathalie, Jeroen, Erik, Alexander, Liza, Richard, Linda, Ariadni, Andries, Geert and Ids**. The lab of the Biosensor team was my favorite lab to work in. Here, I prepared all the samples before they were analyzed with IR in the other building. In addition, during the Young Researcher Workshops that I organized we could always count on you for some extra lab space. Everyone was always ready to help and it made working at WFSR an absolute pleasure. I want to thank **Erik** in particular for all the technical help in the lab. I could always count on your creativity and enthusiasm. Thank you for developing the evaporation device with which I could finally show that the extensive drying time of the S-PEIRS method could be decreased. I wish everyone all the best!

Aan mijn vrienden

Suus, Joyce, Rob, Daan, Rens, Thomas, Florien, Max, Susan mijn lieve oud-huisgenootjes uit Enschede. Met jullie kwam ik de corona periode gelukkig wel door. Ik heb zo veel plezier met jullie gehad in mijn Enschedese studententijd en ben erg blij dat we elkaar nog met enige regelmaat zien. Het is altijd als van ouds.

Henk-Willem, ik ben ontzettend blij dat je mij tijdens mijn laatste hbo-stage bij de UTwente achter mijn bureau vandaan hebt getrokken om ook een vrijdagmiddagborrel te drinken in jullie PhD kantoor. De bank in jullie kantoor werd mijn nieuwe favoriete werkplek en ik kon altijd bij je terecht voor vragen over wetenschap en het leven. Ik kijk enorm tegen je op (letterlijk haha) en ik waardeer de vriendschap die is ontstaan heel erg.

Brigitte, in dezelfde periode dat ik Henk-Willem leerde kennen was jij de supervisor van mijn hbo-stage. Dit was zo'n fijne en succesvolle samenwerking dat mijn scriptie zelfs genomineerd werd voor de Gouden Spatel prijs. Gelukkig stopte ons contact daar niet. We spraken en zagen elkaar met enige regelmaat bijvoorbeeld bij projecten die jij met onze vakgroep hebt. Ook enorm bedankt voor de hulp tijdens het solliciteren!

Dames 7 (nu weer 6!), sinds ik bij jullie in het team ben gekomen is volleybal iedere week weer een feestje. Ik krijg altijd zo veel energie van de trainingen en wedstrijden met jullie! Dit seizoen zijn we ook nog eens kampioen geworden en

gepromoveerd, mega trots op ons! Op naar een nieuw seizoen vol hard geslagen ballen en mooie derde helften.

Lara, Sjors, Nick, Pelle, Nikkie, Rosalinde, Yanni, Colin, Kjel. Lieve vrienden uit Nimma. Sommige van jullie ken ik al een hele tijd, sinds onze hbo studietijd. Anderen juist wat korter, maar dat heeft de pret niet gedrukt haha. We hebben zo veel leuke dingen gedaan samen en volop van het leven genoten. Bedankt voor alle support en liefde.

Laar, ik wil jou in het bijzonder bedanken voor alle steun, vriendschap en memorabele momenten. Ik level altijd fijn met jou en ik waardeer je echt heel erg als vriendin. Onze avonturen in Thailand staan nog vers in mijn geheugen (behalve die van Khao San Road…) en ik weet zeker dat we nog veel meer avonturen gaan beleven samen. Dankjewel lieverd.

Denise, ik herinner het mij nog als de dag van gisteren toen wij tegelijk in het huis aan de Cardasstraat kwamen wonen. Ik dacht in eerste instantie niet dat wij zulke goede vriendinnen zouden worden. Gelukkig zag ik snel in dat jij echt een fantastisch en uniek persoon bent en we werden al snel onafscheidelijk. Al onze kookmomenten in de keuken en borrelplanken bij jou op de bank maakten thuiskomen van werk een feestje. Ik moet altijd ontzettend veel met je lachen en ben je erg dankbaar voor je steun. Ik ben blij dat we nu ook met zijn vieren (met Rob en Sophie) zo veel schik hebben, op naar meer!

Miek, Nad en Nik, lieve meiden, ik schiet direct vol nu ik aan dit stukje begin met schrijven. Niet van verdriet maar van dankbaarheid. Jullie zijn mijn harde kern, een grote support door de jaren heen en ik heb altijd onwijs veel plezier met jullie. Woorden schieten eigenlijk tekort om te beschrijven hoeveel jullie voor mij betekenen. Naast al onze festival avonturen zijn we inmiddels ook aan 'volwassen' uitjes begonnen waarin we allerlei, vaak creatieve, kunstwerkjes maken of andere gekke activiteiten ondernemen. Ik kan inmiddels (een beetje) steenhouwen, keramiek schilderen, tepelflossen maken, DJ-en, koken, bootje varen, en er staat nog veel meer op de planning. Ik hoop dat we over 50 jaar terug kunnen kijken op een onvergetelijke tijd samen. Dat gaat wel goed komen denk ik! Dankjewel lieverds. We proosten op vrienden die familie zijn!

Aan mijn familie

Hanneke, Fleur, Joost en Anne-Magriet (& de kids), je weet natuurlijk nooit wie je schoonfamilie wordt als je begint te daten met iemand, maar ik kwam er al snel achter dat ik me gelukkig mag rekenen met een onwijs fijne schoonfamilie. Jullie warmte en gezelligheid maken familiedagen iets om naar uit te kijken en ik ben erg blij dat jullie mij zo opgenomen hebben in de familie. Hanneke, een speciaal bedankje voor alle lekkere diners bij jou thuis en dat je altijd een biertje in huis hebt dat ik lekker vind.

Pap en mam, wie had dat gedacht, doctor Bosman. De weg naar het behalen van deze titel had ik absoluut niet voltooid zonder jullie onuitputtelijke support. Vanaf het begin hebben jullie mij gestimuleerd om hard te werken, mijn eigen pad te kiezen en te gaan voor mijn dromen. De motivatie en het doorzettingsvermogen dat ik nodig heb gehad om hier te komen is ongetwijfeld jullie verdienste en ik ben jullie daar eeuwig dankbaar voor. De laatste periode van mijn PhD heb ik motivatie geput uit jouw doorzettingsvermogen pap. Hoe jij ondanks alle narigheid van het ongeluk je toch hebt weten in te zetten voor het revalidatieproces is bewonderingswaardig. Dankzij die inzet loop jij straks met mij, mama, sophie en deze titel de deur uit, chapeau. Dankjewel voor alles, altijd.

Sophie, lieve Soof, ik zou nog wel zo'n boekje vol kunnen schrijven over jou, ons, het verleden en alles wat nog komen gaat. Zo veel ruimte is er helaas niet, dus die houd je nog van mij tegoed. Sinds jij (weer) in mijn leven bent is het allemaal veel lichter en makkelijker geworden. Dat geldt ook zeker voor het afronden van dit onderzoek en boekje. Door jouw rust, liefde en zorgzaamheid kon ik de druk veel beter aan en herstelde ik langzaam maar zeker van het overspannen zijn. Je deed (en doet) zoveel liefs voor me. Wanneer ik bijvoorbeeld moeite had met opstaan zorgde jij voor een lekker ontbijtje, want ontbijten deed ik anders niet. Daarnaast zorgde je er voor dat ik met een goed gevulde tas naar werk ging, zodat ik ook daar genoeg en gezond at. Je hebt zelfs een dag in het lab geholpen toen dat nodig was, je bent echt van alle markten thuis. Je luistert naar mijn frustraties en hersenspinsels met een open houding, en hebt altijd een goed advies en/of een stevige knuffel paraat. Gelukkig weet je me ook te vertellen wanneer ik gewoon even normaal moet doen, dat voel je allemaal piekfijn aan. Ik denk dat we wel kunnen stellen dat ik dankzij jou support en liefde door heb kunnen gaan en dit tot een goed einde kon brengen. Jij bent echt mijn alles en ik hou ontzettend veel van je. Dankjewel schat, voor alles.

The research described in this thesis has received funding from the European Union's Horizon 2020 research and innovation programme under grant agreement No. 101016444. And Photonics21. Photonics Public Private Partnership. https://www.photonics21.org.
and by the Dutch Ministry of Agriculture, Nature and Food Quality through the Knowledge development program 'Healthy and safe food systems' (project KB-37-002-023).

Cover design and layout by Anouk Bosman

Printed by proefschriftmaken.nl

